BIOLOGICAL AND ROBOTIC STUDIES TOWARDS INTELLIGENT PHYSICAL INTERACTION WITH COMPLEX TERRAIN

by

Yaqing Wang

A dissertation submitted to Johns Hopkins University in conformity with the requirements for the degree of Doctor of Philosophy

Baltimore, Maryland

October 2024

Abstract

Terrestrial animals are amazingly good at traversing complex 3-D terrain with large obstacles by physically interacting with them and transitioning across various locomotor modes. In stark contrast, even the most advanced legged robots struggle to do so, possibly because they lack a fundamental framework to model robot-obstacle physical interaction paralleling artificial potential fields for obstacle avoidance. To remedy this, previous studies on cockroaches and robophysical models established a novel framework—potential energy landscape modeling—that explains and predicts the destabilizing mode transitions from physical interactions between animal/robot and obstacles, which governs a wide range of complex locomotion. This framework inspired new body shapes and feedforward control strategies to improve robot performance in traversing familiar obstacles. Despite this advance, the framework needed further development to better understand biological adjustments, to be applicable to unknown terrains, and to guide robotic mode transitions.

We further study locomotor-obstacle physical interaction using the potential energy landscape modeling framework in our biological and robotic model systems, where a cockroach or a cockroach-inspired robot traverses a pair of stiff, grass-like beams as cluttered, large obstacles. The animal or robot usually transitions from pitch to roll mode to traverse. This transition on a potential energy landscape over the body roll-pitch space requires escaping the entrapment in a pitch basin, crossing a potential energy barrier, and reaching a roll basin. The least-resistance transition occurs when crossing the barrier at a saddle point.

We observed that cockroaches adjust appendages in the locomotor transition. On a refined landscape, some adjustments substantially reduce the transition barrier, whereas others did not. We developed a minimalistic robot capable of sensing contact forces and torques. Using them as the gradient, we reconstructed the potential energy landscape of an unknown terrain. Finally, we proposed a bio-inspired control strategy that enabled a robot to use feedback control to find unknown modes and transition with the least-resistance path. We verified this strategy using a simulated robotic system. Building on the potential energy landscape modeling framework, our findings advanced the understanding of animal behaviors, enlarged robot's accessible terrain, and improved robots' mobility.

Primary Reader and Advisor: Chen Li

Secondary Readers: Noah J. Cowan, Shai Revzen

Acknowledgment

I am deeply grateful to my advisor, Prof. Chen Li, for his patient guidance, warm encouragement in my scientific research, and invaluable support and recommendations in my career development. His enthusiasm and commitment to research and mentorship have greatly inspired me, serving as a role model to follow as I work toward becoming an independent researcher.

I am deeply grateful to Prof. Noah Cowan for teaching me knowledge of animal locomotion and nonlinear systems in two courses, for his advice on my research, for his support in my career development, and for serving as my thesis reader. I am also deeply grateful to Prof. Shai Revzen for his insightful discussions on saddle-seeking methods and for serving as my thesis reader.

I sincerely thank many professors and colleagues for their helpful discussions and suggestions. I thank Prof. Ioannis Kevrekidis and Anastasia Georgiou for discussions on saddle-finding algorithms, Prof. Noah Cowan, Prof. Jean-Michel Mongeau, Prof. Jeremy Brown, Prof. Mitra Hartmann, Prof. Floris Van Breugel and Dr. Benjamin Cellini for discussions on biological sensing behavior, Prof. Dan Negrut, Dr. Radu Serban, and Dr. Luning Bakke for ProjectChrono simulation software support.

I would like to especially thank Prof. Simon Sponberg and his group members, Prof. Jean-Michel Mongeau and his group members, Prof. Daniel Goldman and his group members, Prof. Bo Cheng and his group members, Prof. George Lauder, Prof. Noah Cowan, Prof. Joshua Dudman, and Prof. Bradley Dickerson for their interviews in my post-doc applications. Your suggestions on my career development provided valuable insights,

helping me reflect on and summarize my past work. They broadened my scientific perspective and inspired and motivated me to set clear goals for my future career.

I would especially like to thank Prof. Dan Wu, Prof. Wenzeng Zhang, and Prof. Ying Liu from Tsinghua University for their support and recommendations, which allowed me to join the Terradynamics lab for a summer internship and ultimately embark on my Ph.D. journey.

I thank Prof. Noah Cowan, Prof. Jeremy Brown, Prof. Joseph Moore, Prof. Ioannis Kevrekidis, Prof. Shai Revzen, and Prof. Simon Leonard for serving on my Graduate Board Oral Examination (GBO) committee. I thank Prof. Noah Cowan, Prof. Louis Whitcomb, and Prof. Gretar Tryggvason for serving on my Department Qualifying Examination (DQE) committee.

I thank the scientific communities for their welcome and feedback: the Society for Integrative and Comparative Biology, the American Physical Society, and the Dynamic Walking Conference.

I felt fortunate to meet with the talented colleagues in the Terradynamics Lab. I thank Dr. Ratan Othayoth, Dr. Yuanfeng Han, Dr. Qihan Xuan, Dr. Qiyuan Fu, Xiao Yu, Dr. Divya Ramesh, Eugene Lin, Kangxin Wang, Gargi Sadalgekar, and many others for their warm help and thoughtful discussions. Special thanks to Dr. Ratan Othayoth and Dr. Yuanfeng Han for helping me start during the early days. Special thanks to Dr. Ratan Othayoth and Dr. Yuanfeng Han for their advice on animal experiments. Special thanks to Dr. Ratan Othayoth and Dr. Qihan Xuan for their advice on robot design, robotic experiments, and simulation setup. Special thanks to Xiao, Eugene, Divya, Gargi, and many others for the help with animal care. I am privileged to mentor Xiao Yu, Jonathan

Mi, Ling Xu, Xiyuan Wang, Kyungmo Choi, Zheyu Zhou, Kangxin Wang, Maosen Tang, Eric Lara, Kapi Ketan Meta, Wenxuan Zheng, Stefan Hustrulid, Yue Qin, Shruthika Kandukiri, Nicholas Harrell, Milla Ivanova, Taliyah Huang, Terry Qu, Qian Kun Liu, and many others, which are rewarding experiences and warm memories to me.

I thank the funding resources that supported my studies: the Burroughs Wellcome Fund, the Arnold and Mabel Beckman Foundation, the Johns Hopkins University Whiting School of Engineering, and the Tsinghua University Department of Mechanical Engineering (for supporting my summer internship before my Ph.D. studies).

I thank the administrative staff at the Department of Mechanical Engineering and the Laboratory for Computational Sensing and Robotics for their support: Mike Bernard, Kevin Adams, John Soos, Patrick Caufield, Lorrie Dodd, Jordan Card, Ashley Moriarty, and Dr. Alison Morrow.

I thank my other friends for their warm communication in daily life, especially the ones in the lab: Yifeng Zhang, Xiangyu Peng, Yishun Zhou, Kaiwen Wang, Siyuan Sun, Lei An and many others, around the campus: Yu Yang, Di Cao, Dr. Siming Deng, and many others, in Maryland Zoo: Joseph Golden, Allison Schwartz, and Yensabro Kanashiro.

Finally, I thank my parents, Changchun Wang and Jihong Wu, my grandparents, Zhenwang Wu and Wei Wu, and my uncle's family, Jibing Wu, Yuling Jia, and Jiaqi Wu, for their unconditional love and support over the past 28 years.

Table of Contents

List of Tables

List of Figures

Chapter 1 Introduction

1.1 Motivation and overview

Animals' legged locomotion occurs daily across diverse natural terrains ranging from savanna grassland to rainforest floor [1–3]. Some of these terrains are highly complicated and cluttered with obstacles of various sizes and properties, such as rocks, tree roots, shrubs, burrows, etc. They raise significant locomotor challenges for legged animals [4,5]. However, the animals appear to traverse complex terrain agilely by using and transitioning between various locomotor modes [6,7] (e.g., climbing [8], leaping [9], crawling [10], self-righting [11], etc.). This is achieved by robustly making effective physical interactions with the terrain [1,2,4] (**Figure 1-1**).

Figure 1-1: Terrestrial animals physically interact with complex terrain using various locomotor modes. (**A**) American cockroaches crawling out of a crevice. (**B**) A mountain goat walking on cliffs. (**C**) A squirrel climbing on a tree. Images courtesy of (A) Tom Libby, Kaushik Jayaram and Pauline Jennings from PolyPEDAL Lab, (B) Marshall Bannister on Pexels, and (C) Maddie Franz on Pexels.

Thanks to the advances over the last few decades, legged robots can run and walk stably on modest ground with no or small unevenness [12–14]. The most advanced robots from Boston Dynamics [15,16], Agility Robotics [17], ANYbotics [18], and Ghost

Robotics [19] demonstrate impressive ability to transition to jumping and somersaulting. However, such mode transitions are far from robust in complex terrain with obstacles as large as the robots [15,20]. Unlike animals, robots still struggle when physically interacting with complex terrain (**Figure 1-2**). Because most existing simple models for legged locomotion focused on stable, steady-state or limit-cycle gaits without contact with obstacles [21–25], robots lack a fundamental framework to model the complex physical interactions [26]. This diminished the usefulness of robots in many important applications, such as search and rescue in rubble [27], environmental monitoring in mountain boulders and forest debris [28], and planetary exploration through large Martian and Lunar rocks [29].

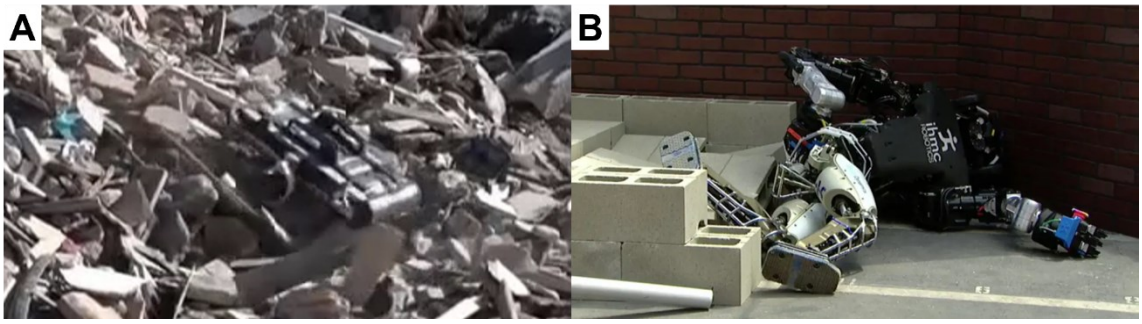

Figure 1-2: Legged robots (struggle to) physically interact with complex terrain. (**A**) An X-RHex robot fails to climb up a rubble pile. (**B**) IHMC's Atlas flips when walking on uneven ground. Images courtesy of (A) Kodlab on YouTube and (B) DARPA [30].

To understand how legged animals and robots should modulate direct physical interaction with complex terrain and make robust locomotor transitions, recent studies in our lab began to establish a potential energy landscape modeling [26,31]. Although this framework has not yet captured the full dynamics of systems, it began to serve as a fundamental conceptual model of terradynamics [32] that simplifies the detailed dynamic analyses (i.e., composing and solving equations from Newton's laws) and leads to an easier

and more intuitive understanding of physical interactions, similar to the inverted pendulum model for walking [22] and the spring-loaded inverted pendulum model (SLIP) model for running [21]. This framework has already been applied to the animal's (**Figure 1-3A**) and robot's (**Figure 1-3B**) legged locomotion in traversing multiple types of obstacles [31,33–36] and ground self-righting [11,37–39]. In each scenario, the model explains and predicts stereotyped modes and transitions (**Figure 1-3C**) using the potential energy landscapes (**Figure 1-3D**) and inspires feedforward robotic control strategies (**Figure 1-3E**) that increase the rate of transition to a favorable mode and traversal [26]. Despite these achievements, potential energy landscape modeling as a new framework needs further exploration. For example, we should understand better how to measure it on unknown terrain. Also, it could be useful in better understanding biological adjustments and guiding robots in traversing large obstacles.

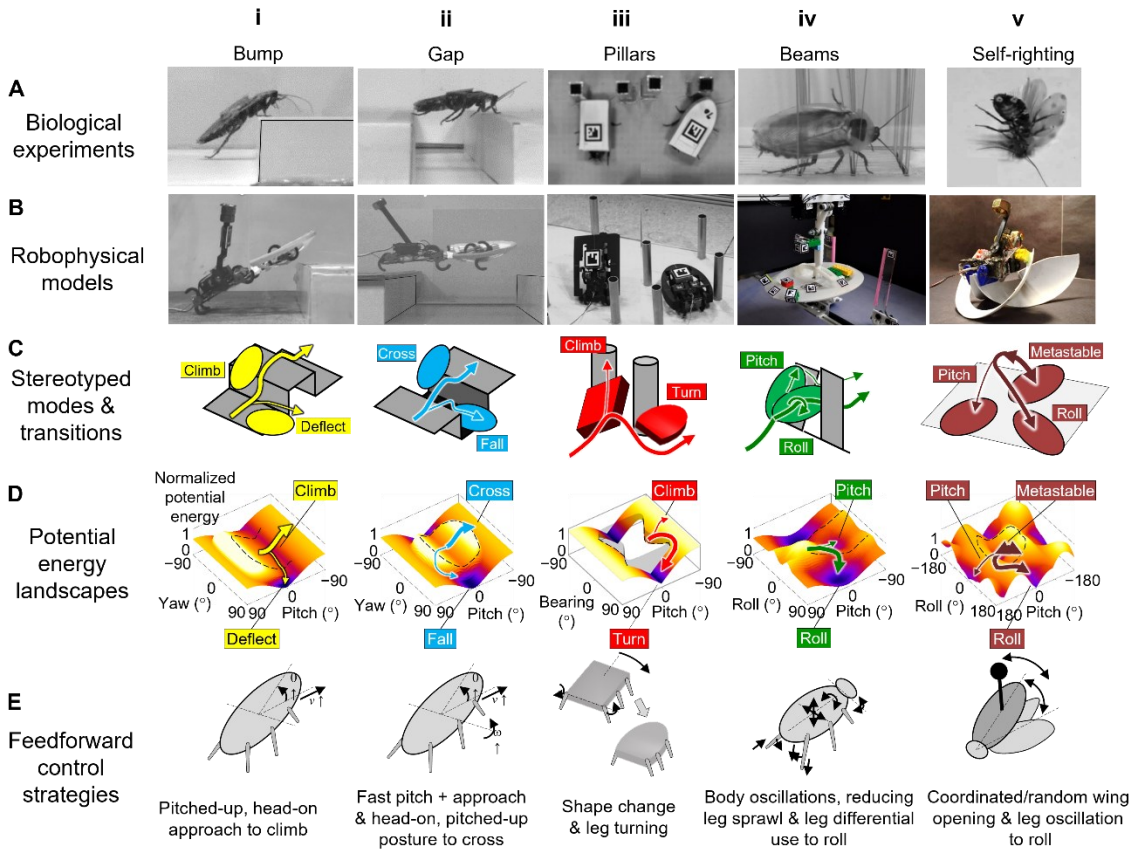

Figure 1-3: Potential energy landscapes explain and predict animals' and robots' locomotor modes and transitions and inspire control strategies. (**A**) Biological experiments of cockroaches traversing model terrain and self-righting. (**B**) Simplest robophysical models. (**C**) Stereotyped locomotor modes and transitions of model systems. (**D**) Potential energy landscapes. The system is attracted in a distinct basin in each locomotor mode. Locomotor transitions are destabilizing, barrier-crossing maneuvers. Black dashed curves show potential energy barriers. Arrows in (C, D) show representative system state trajectories; thicker arrows show more desirable modes. (**E**) Feedforward strategies that facilitate transitions to favored modes and increase traversal probabilities. Example locomotor challenges are traversing (i) a bump, (ii) a gap, (iii) pillars, (iv) beams, and (v) ground self-right. (A, B) Images courtesy of Terradynamics lab. (C-E) Adapted from [11,26,33–36].

This dissertation is the next step in the development of potential energy landscape modeling. We continued to bridge the knowledge gap using an interdisciplinary approach integrating biology, robotics, and physics [37] (**Figure 1-4**). We observed the detailed adjustments of biological organisms and analyze how they change the shape of the potential energy landscape (biology to physics). In return, we used the changes in transition barriers on the landscape to explain the usefulness of these adjustments (physics to biology). Inspired by the animal's shape, sensor distribution, and potentially active sensing behavior, we developed a new robot capable of contact force and torque sensing (biology to robotics). Using this robot, we better understood how the robot can model physical interaction with the terrain (robotics to physics) and proposed the possible usefulness of animals' active behavior in sensing (robotics to biology). We proposed a landscape-based control strategy for robots to make least-resistance transitions (physics to robotics). We tested this strategy using a simulation that was verified by comparing it with physical robotic data (robotics to physics). The results of this dissertation should further enlarge the accessible terrain and enrich the usefulness of the potential energy landscape modeling.

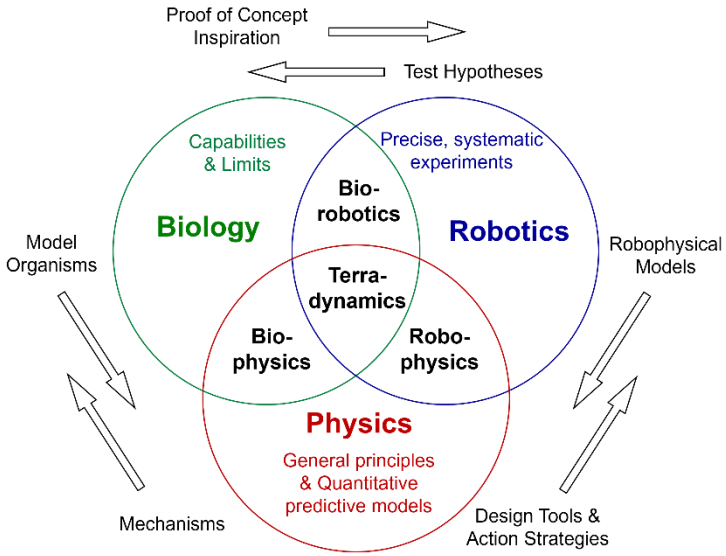

Figure 1-4: Terradynamics as an interdisciplinary field integrating biology, robotics, and physics. Observations of model organisms inspire robot morphology and motion [40,41]. Robophysical models inspire and test biological hypotheses and allow control and variation of parameters to discover general physics principles [42–44]. Physics principles and predictive models explain animal locomotion mechanistically and inspire robotic control strategies [21,22,45]. Adapted from [26].

1.2 Background: biological and robotic legged locomotion

1.2.1 On the ground ranging from flat to large unevenness

Two basic gaits of biological, legged locomotion are walking and running. Studies of animals on flat ground (i.e., unevenness = 0) revealed the simplest models of the two gaits. Walking was modeled as an "inverted pendulum," where the body mass swings over a rigid leg in each step [22] (**Figure 1-5A, i**). Running was modeled as a "spring-loaded inverted pendulum," where the body mass bounces on an elastic leg like a pogo stick [21,46] (**Figure 1-5A, ii**). Both models are the simplest templates [45], explaining the energy conservation [21,47–52] and dynamic stability of the passive mechanism [53–58]. They inspired the development of passive or feedforward-controlled (with minimal sensors and central pattern generators (CPGs) to conduct leg motion) yet dynamically stable robotic walkers and runners [13,59–67] (**Figure 1-5B**). They also inspired walking and running models for legged walking and running gaits in 3-D, such as the "3D inverted pendulum" model for waddling [68,69] and the "lateral leg spring" model for sprawled runners [70].

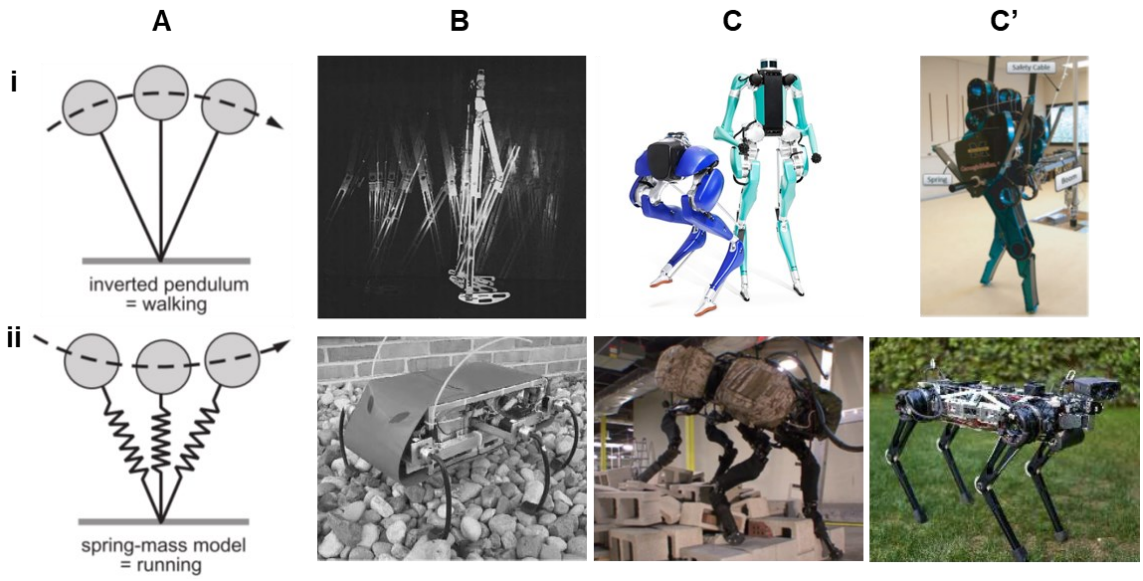

Figure 1-5: Simplest models and robotic examples for walking and running. (**A**) (i) Inverted pendulum model and (ii) Spring-mass model (or spring-loaded inverted pendulum, SLIP) model are the simplest models for walking and running. (**B**) Example passive or feedforward-controlled robots. (i) McGeer's walker. (ii) RHex. (**C** and **C'**) More developed robots with sensory and control systems. (C) (i) Cassie and Digit. (ii) BigDog. (C') (i) MABEL. (ii) MIT Cheetah. Adapted from [4,13,14,17,71–73].

When the ground unevenness is small (unevenness << leg length), animals and robots can still rely on dynamic stability from the passive mechanism or mechanical feedback to keep the gaits [13,23,74–76] (**Figure 1-6A, B**). However, such dynamic stability is limited (especially for robots) [58]. As the unevenness beyond a certain threshold, successful locomotion likely depends more on sensory feedback to sense the ground unevenness [4,77–81] and modulate their CPGs accordingly to remain stable [4,77,82–87] (**Figure 1-6C**).

Figure 1-6: Animals and robots maintain the stability when traversing rough terrains. (**A**) A cockroach traverses rough terrain with only mechanical feedback. (**B**) A RHex robot traverses rough terrain without sensory feedback. (**C**) A Raibo robot traverse deformable terrain with sense-based modulations. Image courtesy of (B) Agile Systems Lab at Georgia Tech on YouTube. (A, C) Adapted from [74,77].

1.2.2 Through a field of large obstacles

When the terrain is more 3-D complex and cluttered (unevenness ≈ or even > leg length [88]) and exceeds the stability region walking and running gaits, the animals or the robot cannot use a single gait to traverse the obstacle field. Instead, the animals facilitate various locomotor modes [1,4] by physically interacting with the terrain (or obstacles). They also often transition between them [6,36,89] to traverse, showing high robustness and agility. Even if the animal loses stability and flips upside down sometimes, it often can rapidly self-right [11,90–94] to recover.

On the other hand, even the most advanced robots (**Figure 1-5C, C'**) often show less agility than animals. They struggle to interact with large obstacles [15,20] (**Figure 1-2**). As a result, the dominant approach for navigating an complex terrain is to avoid obstacles. For example, a robot can use visual sensing (e.g., cameras, LiDAR) to create a geometric map of the terrain. Using this map, the robot can construct an artificial potential field

[95,96] (**Figure 1-7**), with its goal modeled at a global minimum and obstacles modeled at high potential regions. The robot then can plan and follows a gradient descent, collision-free path towards the goal around the obstacles [97]. Algorithm inspired by this already overcame the necessity of prior knowledge of the terrain [98] .With advanced planning and control, the legged robots can jump over single stairs or gaps to make up small discontinuities in the collision-free path [15,16,99,100].

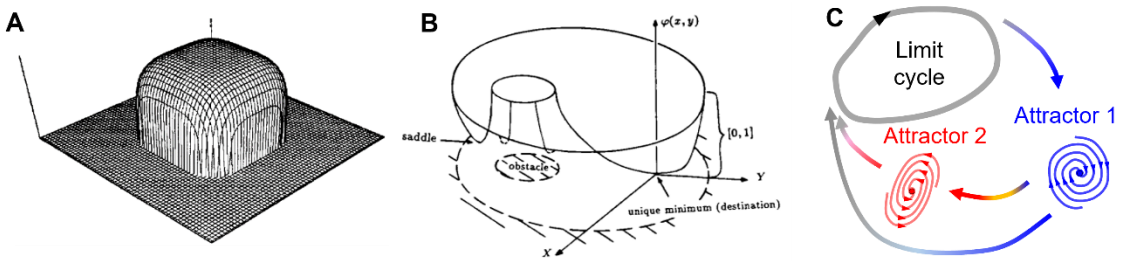

Figure 1-7: Models to avoid or physically interact with obstacles. (**A, B**) Artificial potential fields as fundamental models for obstacle avoidance. (A) A potential function of the artificial repulsive force. (B) Artificial potential functions over a free configuration space. (**C**) Scheme that robots physically interact with obstacles to destabilize and transition between locomotor modes (limit cycles and attractors) similar to animals. Adapted from [26,95,96].

Although difficult, many robots can traverse obstacles by physically interacting with them. One common strategy is empirically designing special gaits to interact with designated obstacles [101–105]. Another common strategy is to obtain a learning-based controller from simulation to maintain stable gaits [77,82,84,87,106,107] and transition between them [108–110].

Above studies on robots locomoting through a field of large obstacles mainly assumed that the robot should use stabilized, limit-cycle-like walking or running gait, and

some enhanced the stability of the gaits using sensory information. Locomotor transitions were not involved or triggered by the descending robot control. We lack an understanding of how robots should physically interact with the terrain to destabilize from limit cycles to transition between various locomotor modes similar to animals (**Figure 1-7C**). Recent studies in our lab began to establish a potential energy landscape modeling that models how locomotor-terrain physical interactions induces such destabilizing locomotor transitions. Inspired by this modeling and observation of animal behavior, the lab proposed robots to have specially designed outfits and generate simple actuation other than legs [31,33–35,37,111]. With these simplest feedforward control strategies, the robots could dynamically traverse large obstacles by physically interacting with them and transitioning between various locomotor modes.

1.2.3 Locomotor transitions and landscape approaches

As introduced above, animals transition between locomotor modes to navigate. These transitions emerge from interactions between the animal and the terrain across the neural, postural, navigational, and ecological levels [112–114]. At the neural level, legged animals use sensory information [23,115,116] to modulate central pattern generators [83] to switch locomotor modes. At the postural level, animals transition between locomotor modes (e.g., between walking and running) to save energy [117]. At the ecological level, animals switch locomotor modes to forage across natural landscapes with minimal metabolic cost [118].

Landscape approaches are used to explain and visualize biological transitions. For example, a potential function (as a 1-D landscape) is artificially defined to explain the walk-to-run transition of humans [119]. A potential landscape is obtained from Bayesian

model selection criteria to explain the walk-to-trot transition of dogs [120]. Metabolic energy landscapes are inferred from oxygen consumption to explain locomotor modes switching over natural landscapes [118]. Aside from explaining locomotor transitions, landscape modeling is also widely used to explain mode transitions in other domains, such as protein folding [121–123], biological phase transitions [124], and robotic manipulation [125].

Robotic mode transitions emerge across postural control, navigational, and cross-media levels. At the postural control level (similar to neural and postural levels in biology), robots use sensory information to modulate central pattern generators to switch locomotor modes [83,87,126–133]. At cross-media scale (similar to the ecological level in biology), robots transition across aerial, aquatic, and terrestrial locomotion [6,7,134].

For both animals and robots, few studies focus on how locomotor transitions emerge from physical interaction with the terrain at the navigational level. The robotic studies on locomotor transitions at the postural control level mostly focused on the gaits on flat ground that facilitate obstacle avoidance but did not explain how locomotor transitions emerge from physical interaction with obstacles. The landscapes proposed above are either artificially defined or inferred by measured energy consumption, which lacks a connection with the first principle of dynamics.

1.2.4 Potential energy landscape modeling

Recent studies in our lab began to establish a potential energy landscape modeling framework [26] (**Figure 1-3**). This simple landscape approach from first principles explains and predicts how locomotor modes and multi-pathway transitions emerge from physical interaction with the terrain (usually an obstacle that blocks animals or robots) at

the navigational level. It currently applies to hard-shell animals (terrestrial insects with exoskeletons like cockroaches, turtles, etc.) and robots' locomotion traversing large obstacles [26,31,33–36] in a regime where large potential energy barriers are comparable to or exceed kinetic energy and/or mechanical work generated by each propulsive cycle or motion. Analogous to artificial potential fields for geometry-based obstacle avoidance, these real potential energy landscapes provide a physics-based foundation for robots to conceptualize locomotor transitions.

Specifically, a self-propelled animal's or robot's body physically interacts with obstacles, resulting in a potential energy landscape (the system's real potential energy as a function of body 3-D position and rotation), with attractive basins of stability separated by potential energy barriers (**Figure 1-3D**). Due to continual self-propulsion resulting in frequent body-obstacle contacts that break continuous friction, the system's state tends to settle to these basins. As the robot or animal is attracted to each stability basin on the landscape, its motion emerges as a distinct locomotor mode (which often involves large body rotations, not just translation) (**Figure 1-3C**). Given the limited propulsive forces and torques of the animal or robot, the modes lead to different outcomes (e.g., traversing the obstacle, climbing the obstacle, being trapped, etc.). The animal or robot should propel to destabilize itself from attraction by the basins/modes of entrapment and overcome potential energy barriers to transition to the favored basins/modes. A large enough but non-feedback-controlled kinetic energy fluctuation from oscillatory self-propulsion can induce such a transition. For a review, see [26].

Despite these achievements, the potential energy landscape modeling needs further development to understand animals' locomotion. Animals use both quick mechanical

feedback [135,136] that relatively slow sensory feedback [137,138] during physical interaction with obstacles [4]. The potential energy landscape modeling mostly captures the mechanical feedback part—for example, self-propulsive oscillation modulated by mechanical feedback transformed into kinetic energy fluctuations and induced barrier-crossing transitions [31]. On the other hand, multiple pieces of evidence have shown that animals can make adjustments (presumably using sensory feedback control) to aid locomotor transitions [31,33–35,89,115,116]. For example, the animal transitioned before the kinetic energy level exceeded the transition barrier, indicating that mechanical feedback alone does not lead to this transition [31].

Sensory feedback control is reflected in the animal's adjustments [139] on its body and appendages (we mean the motions that cause some parts of the body part or appendages to move relative to the body frame, such as flexing the head, abdomen, or moving legs, but not overall body motion like the whole animal moving forward or rotating). These adjustments may have various functions, such as enhancing sensing, steering system state, or generating oscillations to explore. Aside from these, the potential energy landscape modeling offered a new possibility for understanding the usefulness of these adjustments.

Other than this, the potential energy landscape modeling needs further development to apply to unknown terrains. The establishment of the potential energy landscape modeling is heavily based on large quantities of empirical observation of the locomotion of animals and their robophysical models [26]. Such a bio-inspired process naturally combined with specific model systems with regular, controlled obstacles (e.g., pillars of perfect circular or square cross-sectional shapes [35], rigid beams [31]). We lack methods

for a robot to obtain the potential energy landscape of an unknown terrain with arbitrary obstacles, which limits the modeling to be applied in natural and new terrains.

1.2.5 Sensing physical contact

Biological locomotion is modulated by both sensory feedback from the nervous system and mechanical feedback from the musculoskeletal system [4]. During rapid physical interaction with the obstacles, sensory feedback becomes more important in guiding the timing and motion direction for locomotor mode transitions [26]. To monitor the physical contact with obstacles, animals are equipped with a hierarchical tactile sensory system. For example, insects like cockroaches have exteroceptors like bristles and campaniform sensilla to sense contact position and force and proprioceptors like hair plates and chordotonal organs to sense relative position/velocity between joints to infer contact positions and forces [140,141] (**Figure 1-8A**). These sensors form clusters or groups [142,143] to compute local signals collected and used by the central neural system. These redundant mechanosensing streams provide robustness against sensor damage.

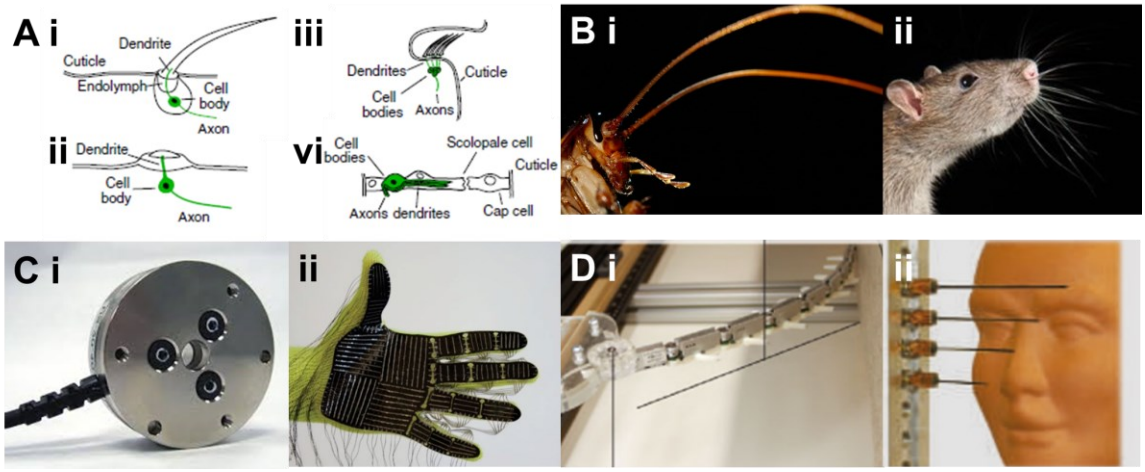

Figure 1-8: Biological and robotic sensors. (**A**) Biological sensors. (i) Bristle. (ii) Campaniform sensillum. (iii) Hair plate. (iv) Chordotonal organ. (**B**) Biological sensory

organs. (i) antennae of an American cockroach. (ii) Whiskers of a rat. (**C**) Robotic sensors. (i) Commercial multi-axis force/torque sensor. (ii) Flexible sensory arrays on a glove. (**D**) Robotic sensory parts. (i) Robotic antenna. (ii) Robotic whisker array. Images courtesy of (B, i) Erik Karits on Pexel, (B, ii) Nikolett Emmert on Pexel, and (C, i) ATI Industrial Automation. Others are adapted from [140,144–146]

Aside from numerous sensors, animals exhibit contact-based active sensing behavior [147–149], especially using specialized sensory organs (e.g., antennae and whiskers, **Figure 1-8B**). For example, when encountering an obstacle, a cockroach uses its antennas to repeatedly touch the obstacle [145,150–152]. A stick insect does an antenna search and sample behavior aided by body and head rotating [153,154]. A rat actively whisks (i.e., moving the whiskers back and forth) against obstacles [155–157]. These behaviors enable the animal to locate the obstacle and extract its contours.

Similar to animals, robots are also equipped with sensors to monitor physical contact with obstacles. The most common are strain gauge-based, single- or multi-axis force/torque sensors (e.g., from ATI, OnRobot, FUTEK) (**Figure 1-8C, i**). These commercial sensors are well-developed and robust, have high sensory frequency, and offer multiple choices of size, sensory range, and sensitivities. They are usually installed between the body and foot or end effectors like proprioceptors, which are sufficient to sense foot–ground interaction [158–160] that help stabilize upright running and walking on the ground with small unevenness (<< leg length) [88]. To enable obstacle contact monitoring over a large region on the surface, flexible sensory arrays [144,161–165] (**Figure 1-8C, ii**) are installed on the robot surface like exteroceptors. Although currently, these sensors are usually fragile and have low sensory frequency and accuracy, they promise to provide richer information about the physical contact that infers obstacle

properties. Inspired by the animals, some robotic contact-based sensory parts have also been developed [136,145,146,166] (**Figure 1-8D**). However, contact-based active sensing behaviors for legged locomotion are rarely reported.

Because the potential energy landscape emerges from physical interaction between the locomotor and the obstacles, we propose that a robot should obtain the landscape of an unknown terrain by monitoring the physical contact, i.e., measuring the contact forces and torques. However, existing sensors do not suit this purpose. Especially, a commercial multi-axis sensor is usually too expensive, bulky, and fragile for a small self-propelled robot to frequently collide with obstacles. Force sensory arrays on robot surfaces only provide 1-D force sensation [144,161–165], which cannot measure 6-D forces and torques. Robotic antennae and whiskers always have large deformations. We lack a method to achieve cheap and durable 6-D force and torque sensing on a small robot.

In biological and robotic experiments, researchers can also monitor the locomotor-terrain physical contact externally (i.e., embedding the sensors in the terrain), such as sensing contact positions using touch sensors [167], and contact forces using force plates [52,168] or photoelastic substrate techniques [169–171] (**Figure 1-9**).

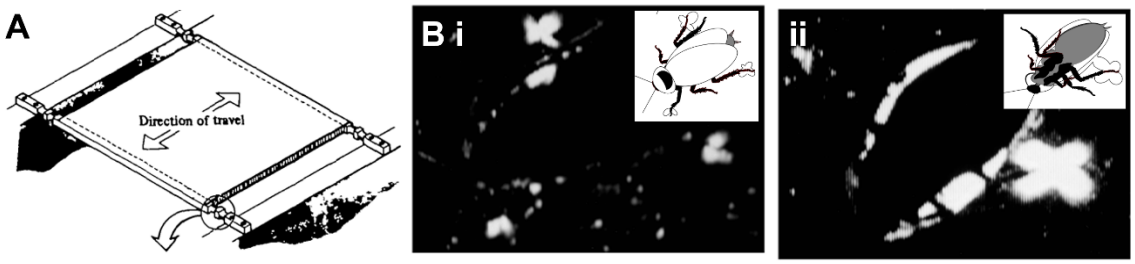

Figure 1-9: External sensors to monitor physical contact. (**A**) Force plate. (**B**) Photoelastic substrate. The optical patterns produced during (**i**) a running trial and (**ii**) a right attempt, showing in inserts. Adapted from [168,171].

1.2.6 Path planning and saddle-seeking on landscapes

The potential energy landscape modeling has already inspired some empirical robotic control strategies to facilitate mode transitions and obstacle traversal [26]. However, such strategies are often feedforward or triggered manually and are seemingly excessive in ensuring enough desired motion (e.g., enough pitch angles [33,34], enough kinetic energy fluctuation [31,37]), which is energy-consuming. We lack an understanding of how to use the potential energy landscapes to guide robots to make a mode transition and traverse obstacles with the least effort. One approach would be to identify a least-resistance barrier-crossing path on the potential energy landscape. As a saddle point on the landscape is the lowest point on the transition barrier, identifying it may also provide a rough least-resistance path.

Many terrestrial animals can plan paths on a geological landscape [172,173]. To do this, an animal obtains cognitive maps [174–176] of the environment. These maps are from past experience and current sensory inputs [177], allowing them to recall the locations of resources and obstacles [178]. Based on the cognitive map, the animal can plan paths by searching through and evaluating possibilities [179,180] or learn paths from trial and error [9,181–183]. The selected path is also affected by difficulty [184], energy consumption [118], predation risk [180], etc.

Animals' paths are sometimes altered by the need for sensing. Specifically, some animals are observed to generate motion angled in the desired direction. For example, a cockroach "alternated turning left and right" in the wind of sex pheromone [185,186] (**Figure 1-10A**). An eastern American mole's head oscillates in lateral directions toward the odorants [187] (**Figure 1-10B**). These trajectory changes are also observed in flying

insects [188–191] (**Figure 1-10C**). They hypothetically enhance detecting the stimuli directions [192–195].

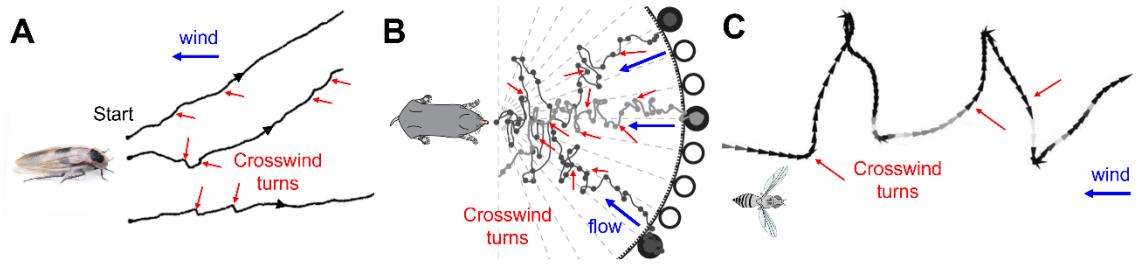

Figure 1-10: Biological paths altered by the need for sensing. (**A**) Trajectory of a cockroach tracking sex pheromone in wind. (**B**) Trajectory of an eastern American mole's head tracking odorants. (**C**) Trajectory of a fly tacking a plume in wind. All animals exhibited significant crosswind turning from anemotaxis. Adapted from [185,187,189].

Many artificial (compared to biological) algorithms can plan a least-resistance path from the start to the goal in a presumed known geological or configurational landscape [196]. The "effort" of a path is usually quantified by the energy cost or accumulated control force amplitude, represented as cost functions in these algorithms. To first find feasible paths, an agent can construct an artificial potential field (**Figure 1-7**) and follow a gradient descent trajectory as previously introduced. An agent can also generate probabilistic roadmaps (PRM) [197], an expansive space tree (EST) [198], or a rapidly exploring random tree (RRT) [199–202] to represent feasible trajectories between adjacent states in the space. And then, it can use a graph search algorithm (e.g., Dijkstra's algorithm [203], A* algorithm [204]) to find an optimal trajectory. The agent can further fine-optimize the trajectory using algorithms such as dynamic programming or Pontryagin's minimum principle [205], ant colony optimization [206], and genetic algorithms [207].

Many artificial algorithms developed in computational chemistry can find saddle points on a landscape [208]. One class exhaustively explores the whole space in the initial

minimum basin to finally find the saddle point, such as the metadynamics method [209], the adaptive biasing force method [210], etc. Another class traces a curve between two known minima and minimizes the energy along it, such as the nudged elastic band method and its variants [211–213]. The last class approaches a saddle point from a minimum following a continuous curve, such as following Newton trajectories [214], orthogonal trajectories [215], gradient extremals [208,216], dimer method trajectories [217], gentlest ascent dynamics [218], etc.

1.3 Model system: cockroaches and robots traversing grass-like beam obstacles

1.3.1 Model biological organism

The discoid cockroach (*Blaberus discoidalis*) (**Figure 1-11**) naturally dwells on the floor of tropical rainforests in Central America. It encounters and negotiates various cluttered obstacles daily, some of which are of the same or much larger than its body size [219]. The discoid cockroach is also a common model organism for legged locomotion studies. Previous studies showed that it uses a tripod running gait, which is robust against perturbation [25,220] and limb loss [221] to run stably on modest and cluttered terrain [74,75]. It uses and transitions between various locomotor modes to traverse complex terrain with large obstacles [8,11,33,34,36], benefiting from both neural sensory [222,223] and mechanical feedback [224,225] control.

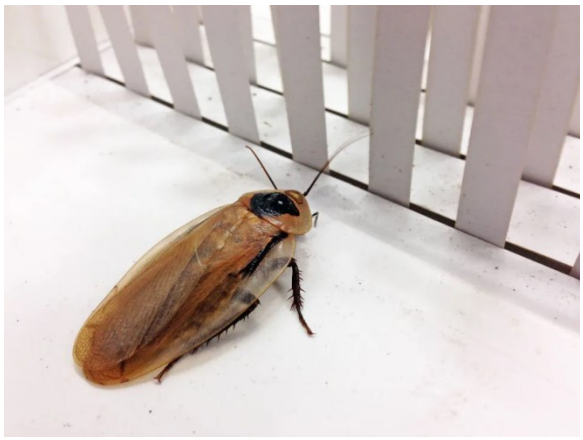

Figure 1-11: Discoid cockroach (*Blaberus discoidalis*) as a model organism. The cockroach is in front of a set of grass-like beam obstacles. Image courtesy of Chen Li.

1.3.2 Robophysical models

The first robophysical model to study grass-like obstacle traversal was a legged robot developed from a VelociRoACH robot [64] with changeable shells added on the top (**Figure 1-12A**) running into multiple layers of grass-like beams made by flexible acrylic sheets [36]. The gaps between the two beams were narrower than the shell width, so the robot could not traverse them with avoidance. To test whether and how the roundness of the shell affects robot locomotion, the shell varied to three levels of roundness, from the most rounded ellipsoid slice to the flat oval and the least rounded flat rectangle. The results showed that the shell roundness affects the probability of locomotor modes. Specifically, shells with higher roundness are more likely to lead to a roll motion (rolling the body to either side and maneuvered through the gap) to traverse the obstacle field. In contrast, the others are more likely to lead to either a pushing (maintaining a horizontal body orientation and pushing against the beams) or climb (pitching body up and pushing against the beams) motion and being trapped.

Figure 1-12: Robophysical models. (**A**) Legged robots with (i) ellipsoid slice, (ii) flat oval, and (iii) Flat rectangle shells. (**B**) Simplest robophysical model. Adapted from [31,36].

A minimalistic robophysical model (**Figure 1-12B**) was developed to further study the mechanics of locomotor mode emergence and transitions [31]. An ellipsoid-like robot resembling a cockroach without legs was hung via a gyroscope mechanism that allowed free body rotation in roll and pitch directions. The robot was propelled forward with unlimited force and could be oscillated in vertical directions at various frequencies with feedforward control. The body was constrained not to yaw or move laterally. One layer of beams was used. Each beam is a rigid, flat acrylic bar with torsional joints at the base that only allow rotation in the fore-aft direction. In this model robotic system, the robot could traverse the beam obstacles either in a pitch mode (pitched body up and pushed through the beams, similar to the climb and pushing motion in [36]) or to transition to a roll mode (rolled the body and maneuvered through the gap, similar to the roll motion in [36]). The locomotor transition emerged from physical interaction between the body and the beams, whose direction is from a more strenuous (pitch) to a less strenuous, more favorable (roll) mode. Systematic experiments using this system also show that an oscillation at a high frequency statistically induces this locomotor transition.

In Chapters 3 & 4, to measure the physical contact, we upgraded the minimalistic robophysical model (i.e., a hanging robot without legs traversing rigid beams) [31] to a new robotic system that was capable of force and torque sensing, and modeled it in simulation.

1.3.3 Simplest model and potential energy landscape

The simplest model of the cockroach or an ellipsoidal robot traversing a beam obstacle was proposed in a previous study [36] (**Figure 1-13A**). The locomotor (animal or robot) is simplified as a rigid ellipsoid (**Figure 1-13B, C**). Two adjacent beams are simplified as two massless rigid plates with torsional springs at their bases. They rotate due to physical contact with the body. The total potential energy of the system is the sum of the gravitational potential energy from the body and the elastic potential energy from torsional springs. The body was assumed to rotate freely to reach the minimal system potential energy in its rotational dimensions. The potential energy landscape was the potential energy as a function of robot fore-aft and lateral displacements (**Figure 1-13D**). This initial landscape model showed that the body orientations of the lowest potential energy resemble that observed from animals/robots.

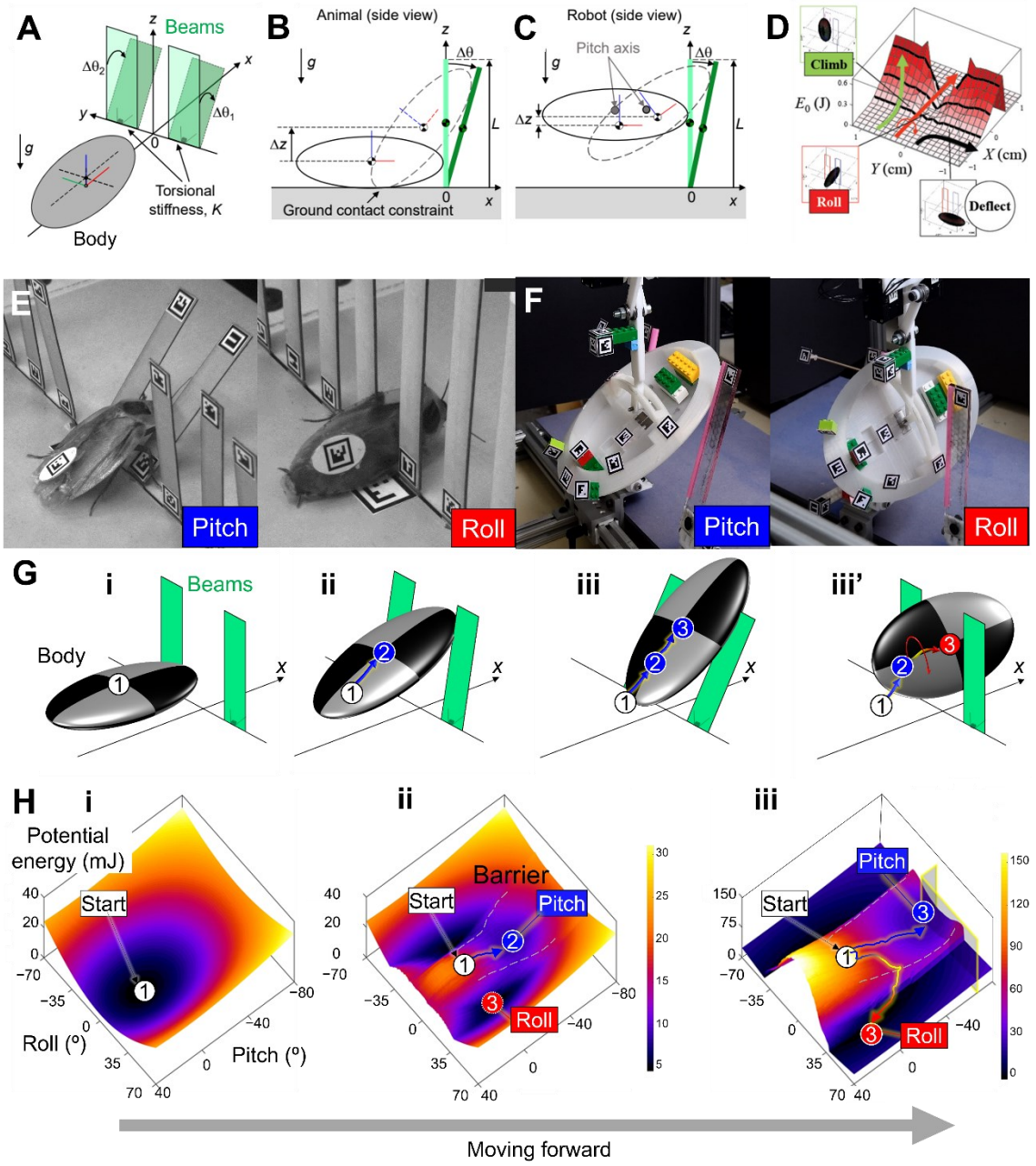

Figure 1-13: Simplest model and potential energy landscapes. (**A**) Simplest model of the system where the animal/robot body is a rigid ellipsoid, and beams are rigid plates with torsional springs at the base. (**B, C**) Side view of the model for (B) animal and (C) robot showing the body rotation and beam deflection before (solid) and after (dashed) contact. (**D**) This model's first potential energy landscape as a function of body position in the horizontal plane. Insets in the green, red, and black boxes and arrows show the lowest

potential energy orientations at three representative positions. (**E, F**) When (E) a cockroach and (F) a minimalistic, feedforward robot traverse cluttered grass-like beams with small gaps (< body width), they either use a strenuous pitch mode to push across (left, blue) or a less strenuous roll mode, where after rolling they maneuver through the gap (right, red). (**G, H**) show the latest model and potential energy landscape. (G) Schematics of animal or robot's body interacting with two beams. The body was an ellipsoid (checkered). The beams were rigid rectangle plates (green) attached to the ground with torsional springs at the bottom. After coming close to the beams (i), the body interacts with beams either using the pitch mode (ii, iii) or transitioning to the roll mode (iii'). (H) Snapshots of the updated potential energy landscape over roll-pitch (α-β) space. Before physically interacting with the beams (i), the landscape has a global basin. During interaction (ii**,** iii), a pitch basin and left- and right-roll basins emerge on the landscape, separated by potential energy barriers (gray dashed curves). The start (running), pitch, or roll locomotor mode (white, blue, or red circles in (G)) emerges as the system is attracted to the global, pitch, or roll basin (white, blue, or red circle in (H)), separately. Arrows on the landscape show examples of state trajectory. Adapted from [26].

An improved potential energy landscape of the same simplest model (with small differences elaborated below) was proposed in a previous study [31]. The largest improvement is to calculate the landscape also as a function of the body roll and pitch rotational dimensions instead of only the intuitive translational dimensions. This demonstrate the self-propelled system does not always reach minimal potential energy orientation as assumed in [36], but is strongly attracted to it [35]. This also enabled the entire movement trajectory to be fully and continuously projected onto the landscape and enabled the landscape to intuitively explain and predict locomotor modes and transitions between them. Some other small improvements and changes include considering the beam's gravitational potential energy to make the system potential energy more accurate, assuming the animal and robot to be bottom heavy so that the horizontal posture is favored,

and canceling the ground contact constraint for the hanging robot based on the robophysical model (**Figure 1-13C)**.

To traverse relatively stiff, cluttered beam obstacles with gaps narrower than its body width, the discoid cockroach or a cockroach-inspired robot often transitions from a strenuous pitch mode (pushing forward across beams with large body pitching) (**Figure 1-13E, F**, blue), to a much easier roll mode (rolling into beam gaps and maneuvering through) (**Figure 1-13E, F**, red). The potential energy landscape is viewed in the cross-section on body roll and pitch rotational dimensions. Before the body physically interacts with the beams, the landscape has a global basin at zero roll and pitch (**Figure 1-13G, H, i**). The state at the minimum corresponds to the horizontal posture (**Figure 1-13G, H**, white). During the interaction (**Figure 1-13G, H, ii**). a pitch basin and left- and right-roll basins emerge on the landscape, separated by potential energy barriers. The states in these basins correspond to the motion of pitch and roll modes, separately (**Figure 1-13G, H**, blue and red). When the beams are stiff, the roll mode is more favorable than the pitch mode because it needs to accumulate less potential energy and is, therefore, more likely to lead a traversal with limited self-propulsion. The pitch-to-roll mode transition requires escaping entrapment in a pitch basin, crossing a potential energy barrier, and reaching a roll basin. These basins emerge and morph as the body moves forward, changing the pitch-to-roll transition potential energy barrier (**Figure 1-13G, H, iii, iii'**).

1.3.4 Rationale for selecting this model system

Among all obstacle types as possible model systems [26], we chose to use cockroaches and robots traversing grass-like beam obstacles as the model system for multiple reasons. Firstly, the obstacles are deformable in this system, making it more

challenging for the animal and the robot to become familiar with them and modulate their motion. Secondly, the locomotor modes and transitions between them were well-defined and easily identified (compared to other systems when the projects started). Lastly, previous studies provided rich biological and robotic experiment results as references [31,36].

For both biological and robotic experiments, we select to use rigid beams that only deflect at the bottom. Because this matches the simplest model, and we already have a mature method to manufacture beams with controlled geometry and stiffness [31]. We choose a stiff beam stiffness so that transitioning to roll mode is always preferred [31]. For the robotic experiment, we choose the robotic model without legs (**Figure 1-12B**) instead of one with physical legs to avoid complex leg design and integration. We constrain the robot to yaw or move laterally or vertically to match the simplest model and simplify its motion.

1.4 Project Summaries

1.4.1 Better understanding of biological body and appendage adjustments

In Chapter 2, we present a biological study to better understand the usefulness of a cockroach's body and appendage adjustments during beam traversal. Cockroaches were challenged to traverse the beam obstacles. We quantified the adjustments in the head, abdomen, and legs. To do this, we further sectioned the cockroach model instead of using a rigid body in the previous potential energy landscape modeling [31,33–35]. We measured the adjustment metrics in the video recordings from a group of synchronized high-speed cameras. We refined the simplest model described in Section 1.3.3 by adding the head,

abdomen, and legs and refined the method to calculate the transition barriers. To test whether and how these motions facilitated the barrier-crossing mode transition, we calculated the potential energy landscape and transition barriers change according to the metrics. This project has been published in the *Journal of Experimental Biology*, entitled *Cockroaches adjust body and appendages to traverse cluttered large obstacles*, authored by Yaqing Wang, Ratan Othayoth, and Chen Li [226].

1.4.2 Reconstructing potential energy landscapes in unknown terrains

In Chapter 3, we present a robophysical study that tests if a robot can reconstruct the potential energy landscape by sensing obstacle contact forces and torques in an unknown terrain. We proposed that robots could sense accurate 6-D forces and torques to do so, as they may infer the conservative forces and torques as the derivative of potential energy by translation or rotation. We developed a minimalistic, cockroach-inspired robot capable of sensing contact forces and torques with obstacles. To test whether the sensed contact forces and torques resemble the potential energy landscape gradient, we systematically varied the robot's rotational roll and pitch angles and propelled the robot forward to traverse beam obstacles while sensing contact forces and torques. We compared the results with the landscape gradient from the theoretical model. To test if the robot could obtain the potential energy landscape based on force and torque sensing, we reconstructed the landscape from the sensory data and compared it with the theoretical model. This project explored the feasibility of introducing potential energy landscape modeling to unknown terrains. This project was posted on *arXiv* entitled *Sensing environmental interaction physics to traverse cluttered obstacles*, authored by Yaqing Wang, Ling Xu, and Chen Li [227].

1.4.3 Seeking a minimum-effort path for obstacle traversal

In Chapter 4, we present a potential energy landscape-based bio-inspired strategy to control a robot to traverse obstacles with the least effort that we tested it on a simulated robot traversing beam obstacles. We proposed that following a gradient minimal path (i.e., the gradient extremal path [208,216] following the smallest gradient) on the potential energy landscape leads to least-resistance mode transition and obstacle traversal, because the landscape gradient on a gradient minimal path is locally minimal, indicating that the terrain resistive force is roughly minimal (yet still affected by hard-to-model frictions and other effects). We proposed that the robot should sense the obstacle contact forces and torques and follow the direction of the gradient minimal path in real-time. To test the performance of this strategy, we built a simulation of the robot traversing beam obstacles system and verified its realism by comparing it with the robotic experiment results from previous studies. We simulated the robot to try to traverse the beam obstacle using the new strategy. We quantified the strategy's performance using the traversal time and accuracy of crossing the transition barrier at the saddle point. We also systematically varied key parameters in the strategy to test whether and how they modulate the performance. This project was the first attempt to use the potential energy landscape modeling to guide a robot to do precise control and make locomotor transitions.

Chapter 2 Cockroaches adjust body and appendages to traverse cluttered large obstacles

This chapter was previously published as an article entitled *Cockroaches adjust body and appendages to traverse cluttered large obstacles*, authored by Yaqing Wang, Ratan Othayoth, and Chen Li, in *Journal of Experimental Biology* [226]. We re-used the article in this chapter with slight changes of the format under CC BY 4.0 and with permission from all authors.

2.1 Author contributions

Yaqing Wang, Ratan Othayoth, and Chen Li designed research; Yaqing Wang performed research; Yaqing Wang and Ratan Othayoth developed algorithms; Yaqing Wang analyzed data; and Yaqing Wang, Ratan Othayoth, and Chen Li wrote the article.

2.2 Acknowledgment

We thank Yuanfeng Han and Qiyuan Fu for help with imaging setup, Yuanfeng Han and Qihan Xuan for discussion, and Xiao Yu for help with animal care and manually correcting the marker tracking.

This research was funded by an Arnold & Mabel Beckman Foundation Beckman Young Investigator Award, a Burroughs Wellcome Fund Career Award at the Scientific Interface, and the Johns Hopkins University Whiting School of Engineering start-up funds to Chen Li. Yaqing Wang was partially supported by funds for an undergraduate research internship from the Department of Mechanical Engineering at Tsinghua University.

2.3 Summary

To traverse complex terrain, animals often transition between locomotor modes. It is well-known that locomotor transitions can occur by switching neural control patterns or to minimize metabolic energetic cost. Recent work discovered that locomotor transitions in terrain cluttered with large obstacles can emerge from physical interaction with the terrain controlled by the nervous system. For example, to traverse cluttered, stiff grass-like beams, the discoid cockroach often transitions from a strenuous pitch mode pushing across to a less strenuous roll mode rolling into and through the gaps. This transition can save mechanical energetic cost substantially ($\sim 10^{0}$-10^{1} mJ) but requires overcoming a potential energy barrier ($\sim 10^{-3}$-10^{-2} mJ). Previous robotic physical modeling demonstrated that kinetic energy fluctuation of body oscillation from self-propulsion helped overcome the barrier and facilitate this transition. However, the animal transitioned even when the barrier still exceeded kinetic energy fluctuation. Here, we studied whether and how the cockroach makes adjustments to further facilitate this transition to traverse beams. During the transition, the animal repeatedly flexed its head and abdomen, reduced hind leg sprawl, and depressed one hind leg and elevated the other, which were absent when running on a flat ground. Using a refined potential energy landscape with additional degrees of freedom to model these adjustments, we found that head flexion did not substantially reduce the transition barrier (by $\sim 10^{-3}$ mJ), whereas leg sprawl reduction did so dramatically (by $\sim 10^{-2}$ mJ). We speculate that head flexion helped sense the terrain to guide the transition via sensory feedback control.

2.4 Introduction

Animal locomotion emerges from direct physical interaction with the terrain controlled by the nervous system via both feedforward preflexes facilitated by morphology and feedback control modulated by sensing [4]. To move across complex terrains, animals often use and transition between multiple modes of locomotion [1,4,6,7,36]. Most terrestrial locomotion studies focused on how animals use neuromechanical control to generate or stabilize near-steady-state, single-mode locomotion (e.g., walking, running [21,22]). Previous work explored how gait transitions result from changes in the rhythmic output of central pattern generators [83], sensed information of the terrain [115,116], or the need to minimize metabolic energy cost over large spatiotemporal scales [117,118].

Recent research in our lab has begun to offer insight into how locomotor transitions can emerge from animals' direct physical interaction with the terrain [11,31,33–39,228,229]. In particular, these studies have established a potential energy landscape approach to understanding stochastic yet stereotyped animal locomotor transitions in complex 3-D terrain with many large obstacles [26,31]. In such terrain, physical interaction of the animal with the terrain results in a potential energy landscape with distinct basins. Because the animal's self-propulsion breaks continuous frictional terrain contact, the system is statically unstable and drifts down the potential energy basin. This attraction towards distinct landscape basins results in the system having stereotyped locomotor modes. Thus, transitions between locomotor modes can be generated by taking actions to destabilize the system across potential energy barriers separating landscape basins. The barrier height measures the difficulty of making a transition. Most of these studies focused on how locomotor transitions can be induced by feedforward self-propulsive mechanisms

[31,33–35,37–39,228]. Not surprisingly, some of them also found evidence that animals can make adjustments (presumably using sensory feedback control) to aid locomotor transitions [31,33–35].

Here, we take the next step in quantifying and understanding how animals use adjustments to better make locomotor transitions in complex 3-D terrain. Our study was motivated by and built upon a recent study of the discoid cockroach (*Blaberus discoidalis*) traversing a layer of cluttered grass-like beam obstacles [31]. When encountering stiff beams, the animal often first pushes against the beams resulting in the body pitching up (the pitch mode, **Figure 2-1**, thick blue arrow), but then it often rolls its body into a gap between beams (the roll mode, **Figure 2-1**, red arrow) to traverse and rarely pushed down the beams to traverse (**Figure 2-1**, thin blue arrow). The animal may also be deflected sideways when exploring in front of the beams (the deflect mode, **Figure 2-1**, purple dashed curve) [36]. Potential energy landscape modeling revealed that the pitch and roll modes emerge as the system is attracted to distinct pitch and roll basins of the potential energy landscape, respectively. Both the pitch and roll modes are more strenuous than running on a flat ground (with a minimal mechanical energetic cost of 7.9 and 0.2 mJ, respectively, for the stiff beams tested in this study, Section 2.8.1; these are 130 × and 3 × that needed per stride during medium-speed running at 5 body lengths s^{-1} [230], respectively). Transition from the pitch to the roll mode can substantially reduce mechanical energic cost (by $\sim 10^{0}$-10^{1} mJ), but it requires overcoming a potential energy barrier between the pitch and roll basins ($\sim 10^{-3}$-10^{-2} mJ, Section 2.8.1). Systematic experiments using a feedforward-controlled robot demonstrated that kinetic energy fluctuation from body oscillations resulting from self-propulsion can induce transitions

from the pitch to the roll mode (**Figure 2-1**, orange arrow), when it exceeds the potential energy barrier. However, despite qualitatively similar overall findings, the animal's pitch-to-roll transition happens even when its body kinetic energy fluctuation is insufficient to overcome the barrier. This means that the animal must also be making adjustments to facilitate the transition.

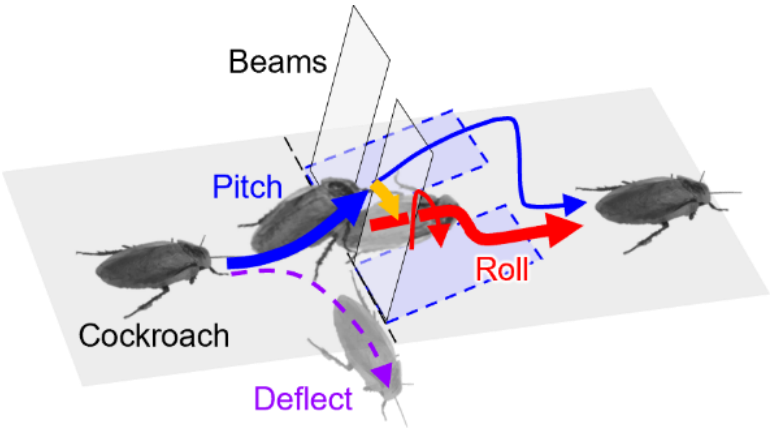

Figure 2-1: Stereotyped pitch and roll modes and pitch-to-roll transition during cluttered grass-like beam traversal of discoid cockroaches. A possible deflect mode is also shown (see Section 2.5.11). Adapted from [31].

To achieve our goal, we challenged the discoid cockroach to traverse a layer of stiff beams and used high-speed imaging to measure detailed body and appendage kinematics during pitch-to-roll transition. We discovered that the animal makes several adjustments: (1) Head flexion: the animal repeatedly flexed its head while interacting with the beams. (2) Abdomen flexion: the animal flexed its abdomen while interacting with the beams and after the animal rolled into the beam gap. (3) Leg sprawl: the animal spread both its hind legs further outward when pitching against the beams, but it tucked one hind leg inward when rolling into the beam gap. (4) Differential leg use: the animal depressed one hind leg

(moved the foot further away from the thorax) and elevated the other (moved the foot closer to the thorax) when rolling into the beam gap.

We hypothesized that the animal's head flexion and leg sprawl adjustment facilitate pitch-to-roll transition. Specifically: When the animal is pitched up against the beams, (1) head flexion and (2) tucking in the legs reduces the pitch-to-roll transition barrier and facilitates rolling into the gap. (3) After the animal body has rolled into the gap, head flexion helps it stay in the gap.

To test hypotheses (1) and (2), we used potential energy landscape modeling to analyze whether and how much the observed use of head flexion and leg tucking in changed the potential energy barrier that must be overcome to transition from the pitch to roll mode (which measures the difficulty of the transition). We found that leg tucking in reduced the pitch-to-roll transition barrier, supporting hypothesis (2), but head flexion did not, rejecting hypothesis (1). To test hypotheses (3), we analyzed whether and how much the observed head flexion changed the potential energy barrier that prevented the animal from transitioning from the rolled body being within the gap between the beams to being out of the gap and deflecting sideways. We found that head flexion did not substantially increase the roll-to-deflect barrier, rejecting hypothesis (3). Finally, we discuss the likely functions of the observed body and appendage adjustments and suggest future directions.

2.5 Methods

We first performed animal experiments and obtained kinematics data (Section 2.5.1-2.5.8). Then, we constructed the potential energy landscape of the system along the observed average trajectory and analyzed cross-sections of the landscape relevant to the animal's body pitch and roll. We identified local minimum basins corresponding to the

pitch and roll modes in the pitch-roll cross section. Next, we identified saddle points between the pitch and roll basins, and quantified the potential energy barrier (Section 2.5.9-2.5.11). Finally, we varied head flexion and total sprawl of the two hind legs and assessed how the barrier changed compared to that using the constant average values to test hypotheses (1) and (2) about the functions of head and leg adjustments during the pitch-to-roll transition (Section 2.5.12, 2.5.13). We also performed these analyses on a yaw cross section of the landscape (Section 2.5.11) to test the hypothesis (3) about the function of head adjustment to keep the animal within the beam gap (Section 2.5.12).

2.5.1 Animals

We used three adult male *Blaberus discoidalis* cockroaches (Joe's BUGz LLC, Atlanta, GA, USA). Before the experiments, each animal was kept in a plastic container in a room with a controlled temperature of 22°C, moisture of 70%, and lighting on a 12h:12h light-dark cycle. Dry dog food (Purina Beneful, Largo, FL, USA) and water jelly made from water and polymer crystal (Tasty Worms Nutrition Inc., USA) were provided *ad libitum*. The animals weighed 2.7 ± 0.6 g (with marker items) and measured 5.3 ± 0.3 cm in length, 2.3 ± 0.1 cm in width, and 0.73 ± 0.08 cm in thickness. All data reported are means ± 1 s.d.

2.5.2 Obstacle track

For controlled, repeatable experiments, we constructed a testbed (**Figure 2-2A**) similar to that in the previous study [31], with a layer of beam obstacles that consisted of seven beams. Each beam was 10 mm wide, 100 mm tall, and 0.8 mm thick. The lateral distance between two adjacent beams was 10 mm, and the lateral distance between the

left/right-most beams and the walls was 5 mm. We used the same method to construct beam obstacles and characterize their stiffness as described in the previous study [31]. The beams can only deflect about a hinge just above the ground. The beam torsional stiffness was $K = 2.5 \pm 0.4$ mN·m·rad^{-1} (mean ± s.d. of 7 loading cycles), which was between the two most stiff beams in the previous study. We chose this high stiffness to induce a high pitch-to-roll transition probability [31] to increase experimental yield.

2.5.3 Imaging setup

Eight synchronized high-speed cameras (N5A-100, Adimec, Netherlands) recorded the experiment from different views: one from top view, two from the side view, one from the top-down oblique view, and four from isometric views (**Figure 2-2A**). All the cameras recorded at a frame rate of 100 Hz, a shutter time of 50 μs, and a resolution of 2592 × 2048 pixels. Even with eight cameras, we had to carefully tune camera positioning and orientation to achieve reliable tracking of the animal and beams (Section 2.5.5), because the animal had large 3-D body rotations (max absolute yaw = 100°, max absolute pitch = 62°, max absolute roll = 98°, defined in Section 2.5.6) and markers were frequently occluded by the beams. Four halogen work lights (Coleman Cable, Waukegan, IL, USA) provided lighting from the top and side. During experiments, the ambient temperature around the arena was around 36°C. To prevent the cockroaches from overheating, we turned off the work lights between trials.

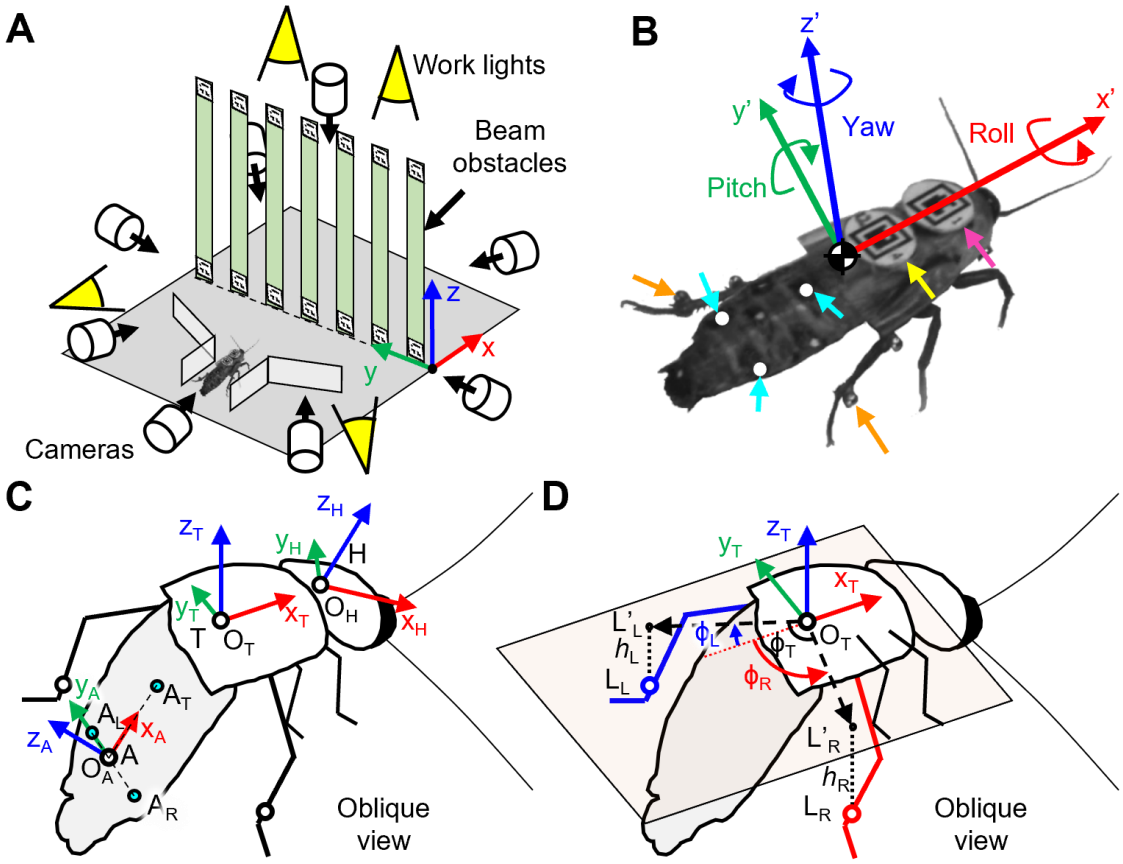

Figure 2-2: Experimental setup and cockroach schematic diagrams. (**A**) Schematic of beam obstacle track and multi-camera imaging system. (**B**) Marker placement on animal and definition of body (thorax) frame. Magenta: head marker. Yellow: thorax marker. Cyan: abdomen markers. Orange: leg markers. (**C**) Definition of thorax, head, and abdomen frames. Coordinate $X_TY_TZ_T$: body (thorax) frame. Coordinate $X_HY_HZ_H$: head frame. Coordinate $X_AY_AZ_A$: abdomen frame. (**D**) Definition of leg sprawl and leg height. Light-colored plane: body coronal plane. L_L: Left leg marker. L_R: Right leg marker. $L'_{L,R}$: Projections of leg markers on body coronal plane. ϕ_L: left leg sprawl angle. ϕ_R: right leg sprawl angle. ϕ_T: total leg sprawl angle. h_L: left leg height. h_R: right leg height. A negative leg height means leg marker is below the thorax coronal plane, and a positive leg height means leg marker is above.

2.5.4 Experiment protocol

During each trial, we first placed the animal at the start of the track, covered it with a piece of cardboard, and let it settle down. We recorded the ambient temperature around the obstacle field and reset the beams upright. Then we started camera recording, lifted the cardboard to expose the animal to bright light, and prodded its abdomen with a tape-wrapped straw to induce running through the funnel towards the beams. After the animal traversed the beams, it entered a shelter of egg cartons (not shown in **Figure 2-2A**) at the other end of the track. Then, camera recording was stopped, and videos were saved. The animal was allowed at least 3 minutes to rest after each trial. For each animal, we recorded 18-19 trials.

For each animal, we rejected the trials in which at least one of the following situations occurred: (1) The animal used at least one locomotor mode [36] other than the pitch and roll modes [31] to traverse the beams. (2) The animal touched the arena wall in the roll phase (defined in Section 2.5.7). (3) At least one marker (BEEtags, white-outs, or beads) fell off. From the remaining trials, we selected the 12 trials with the shortest traversal time for each animal, with a total of 36 trials (N = 3, n = 36). This sample downsizing was done due to the significant time cost of digitizing (next section).

2.5.5 Tracking and 3-D reconstruction

To overcome the challenge in tracking from large 3-D body rotation and frequent occlusions, we used several types of markers (**Figure 2-2B**). (1) We glued the animal's wings into a natural folded shape using hot glue and exposed the abdomen by trimming the posterior half of the wings. Then we used hot glue to attach a BEEtag [231] to the anterior

half of the fixed wings covering the thorax as the thorax marker (**Figure 2-2B**, yellow). (2) We used hot glue to attach a BEEtag onto the animals' pronotum as the head marker (**Figure 2-2B**, magenta). (3) We used white-out to paint point markers on the dorsal surface of the abdomen as abdomen markers (**Figure 2-2B**, cyan). We did not use BEEtags to track the abdomen, because they often fell off when the animal interacted with the beams with large abdomen flexion. (4) We used ultraviolet curing glue (Bondic, Aurora, Ontario, Canada) to attach two small, lightweight (12 mg each, 0.4% body weight, 15% hind leg weight [230]) aluminum beads (McMaster-Carr, Elmhurst, IL, USA) to each hind leg at two locations close to the femoral-tibial and tibia-tarsal joints as leg markers (**Figure 2-2B**, orange). (5) We attached BEEtags [231] to the top and the bottom of each beam's frontal side as beam markers (**Figure 2-2A**). The added mass from the BEEtags (1 mg, 0.03% body mass) was comparable to or less than that of backpacks used in previous studies of dynamic locomotion of discoid cockroaches (e.g., 0.8× body mass [75], 1.1× body mass [35], 5.2× body mass [220]. We attached all BEEtags and beads under room temperature without cold anesthetizing the animal, because both the hot glue and ultraviolet curing glue used could solidify within a few seconds. We verified that these additional modifications did not significantly affect the animal's traversal performance and behavior compared to our previous study [31] where only one BEEtag was attached to the wings (Section 2.6.1).

Then, we tracked the markers on the animal and beams in each recorded video from all eight cameras. We tracked all the BEEtag markers automatically using a customed MATLAB code modified from the BEEtag master code [231]. To track the abdomen and leg markers efficiently, we used DeepLabCut [232]. For each camera view, we first manually digitized these markers in 10 trials, with 100 video frames from each camera

view, and used these data as a training sample to train the neural network. After training, DeepLabCut tracked the markers in these videos. We then visually examined the sample tracking results, manually fixed obvious tracking errors, and re-trained the training sample. After several cycles of manual corrections and reinforcement learning, DeepLabCut could automatically track markers in all videos with high accuracy. We visually checked the tracking result carefully and manually corrected the remaining tracking errors. Using this tracking method, we achieved a high maker tracking performance: the head, thorax, abdomen, and leg markers were all tracked in 100% of all the frames of all trials. We emphasize that, even with 8 cameras covering a large angular range and using DeepLabCut, tracking detailed kinematics in such a densely cluttered terrain is a very laborious and time-consuming process, due to the large body rotation in 3-D and frequent occlusions of markers. In total, it took an experienced experimenter 20 hours of manual digitizing, 72 hours of automatic tracking, followed by another 150 hours of manual correction, to track 36 trials averaging 280 frames each with 8 camera views.

Finally, we reconstructed 3-D kinematics of all tracked markers using the direct linear transformation method and DLTdv digitizing tool [233]. To facilitate 3-D calibration, we built a calibration object with 60 BEEtag markers using Lego bricks (The Lego Group, Denmark).

2.5.6 Kinematics and kinetic energy fluctuation analyses

With the 3-D reconstruction of tracked markers, we quantified the motion of the animal's head, thorax, abdomen, and two hind legs. For simplicity, we laterally mirrored kinematic data of the trials in which the animal rolled to the left (negative body roll) to

become rolling to the right (positive body roll) to simplify the analysis, considering lateral symmetry.

We first approximated the thorax frame (which is the body frame in [31]) and head frame using the BEEtags on them. To do this, we projected a model of the animal (Section 2.5.9) to a set of eight synchronized camera views and adjusted its pose to visually match it to the animal figure in the video. We checked this matching between the model and the animal figure in at least five other frames in the videos. Then we defined the animal's thorax frame ($X_T Y_T Z_T$) and head frame ($X_H Y_H Z_H$) as the model's thorax frame and head frame, respectively, and used homogeneous transformation between the tags and the models to represent the spatial relationship between the tags and the animal's thorax and head. For the abdomen frame ($X_A Y_A Z_A$), we defined the origin (O_A) as the foot of the perpendicular from the top marker (A_T) to the segment of left (A_L) and right markers (A_R), defined the *x*-axis as the direction from the origin (O_A) pointing at the top marker (A_T), defined the *y*-axis as the direction from the origin (O_A) pointing at the left marker (A_L) (**Figure 2-2C**). Thus, we obtained the head, thorax, and abdomen frames, each with 3-D position (*x*, *y*, *z*) and orientation (yaw α, pitch β, roll γ, *Z*−*Y*'−*X*" Tait-Bryan convention) (**Figure 2-2C**). Note that a negative pitch angle means the body is pitched up.

We then calculated the following kinematic variables as a function of time in each trial. (1) Head flexion β_h: the pitch of the head frame in the thorax frame. (2) Abdomen flexion β_a: the additive inverse of the pitch of the abdomen frame in the thorax frame. The additive inverse (positive becoming negative, and negative becoming positive) was used so that β_a is positive when the animal flexes the abdomen down. (3) Leg sprawl $\phi_{L,\,R,\,T}$: the angles from the vector from the thorax frame origin (O_B) to the leg markers' projection into

the body coronal plane (L'_L, L'_R) to the *x* direction of thorax frame is defined as left and right leg sprawl angle (ϕ_L , ϕ_R), respectively. Total leg sprawl ϕ_T is the sum of the two (**Figure 2-2D**). (4) Leg height difference Δh: The leg height of the right hind leg (h_R) minus the leg height of the left hind leg (h_L) (after mirrored). Hind leg height was defined as the distance of the leg marker from the thorax coronal plane (**Figure 2-2D**). A negative leg height means that the leg marker is below the thorax coronal plane, and a positive leg height means that it is above. All the Equations are summarized below.

The rotation matrix of the thorax (R_T), head (R_H), and abdomen (R_A) frames in the world frame:

$$R = \begin{bmatrix} c_\alpha c_\beta & c_\alpha s_\beta s_\gamma - s_\alpha c_\gamma & c_\alpha s_\beta c_\gamma + s_\alpha s_\gamma \\ c_\alpha s_\beta & c_\alpha s_\beta s_\gamma + s_\alpha c_\gamma & c_\alpha s_\beta c_\gamma - s_\alpha s_\gamma \\ -s_\beta & c_\beta s_\gamma & c_\beta c_\gamma \end{bmatrix}, \tag{2-1}$$

where $s_{\alpha,\beta,\gamma}$ and $c_{\alpha,\beta,\gamma}$ are abbreviations for sine and cosine terms, respectively, and α, β, and γ are the Euler angles (yaw, pitch, and roll).

The rotation matrix of head and abdomen frames in the thorax frame:

$$R_{TH} = R_T^T R_H, \tag{2-2}$$

$$R_{TA} = R_T^T R_A. \tag{2-3}$$

The head flexion and abdomen flexion:

$$\beta_h = \beta(R_{TH}), \tag{2-4}$$

$$\beta_a = -\beta(R_{TA}), \tag{2-5}$$

where $\beta(\cdot)$ means to obtain the pitch of a rotational matrix:

$$\beta(R) = \text{atan2}(\sqrt{r_{31}^2 + r_{32}^2}\,, r_{33}),$$

where r_{ij} is the ith row, the jth column element in the matrix R.

Leg sprawl:

$$\phi_L = \text{sign}\left[y_T\left(\overrightarrow{O_T L'_L}\right)\right] \cdot \cos^{-1}\left[\left(\overrightarrow{O_T L'_L} \cdot \overrightarrow{x_T^-}\right) / \left|\left| \overrightarrow{O_T L'_L} \right|\right|\right], \quad (2\text{-}6)$$

$$\phi_R = -\text{sign}\left[y_T\left(\overrightarrow{O_T L'_R}\right)\right] \cdot \cos^{-1}\left[\left(\overrightarrow{O_T L'_R} \cdot \overrightarrow{x_T^-}\right) / \left|\left| \overrightarrow{O_T L'_R} \right|\right|\right], \quad (2\text{-}7)$$

$$\phi_T = \phi_L + \phi_R, \quad (2\text{-}8)$$

where $y_T(\cdot)$ means to obtain y element of a vector in the frame ($X_T Y_T Z_T$), x_T^- means the unit vector along x_T negative direction.

Leg height difference:

$$\Delta h = h_R - h_L. \quad (2\text{-}9)$$

To obtain average kinetic energy fluctuation, we first calculated the time average of the animal's kinetic energy due to translational and rotational velocity components other than the forward velocity [31] in the explore + pitch and roll phases for each trial, then averaged the means of all trials. Kinetic energy fluctuation ΔE_K was calculated as:

$$\Delta E_K = \frac{1}{2}\left(m v_y^2 + m v_z^2 + I_{xx}\omega_x^2 + I_{yy}\omega_y^2 + I_{zz}\omega_z^2\right) = E_K - \frac{1}{2} m v_x^2,$$

where m, I_{xx}, I_{yy}, I_{zz} are mass and moment of inertia along x, y, and z axes, v_x, v_y, v_z, ω_x, ω_y, ω_z are the translational and rotational velocities along the x, y, and z axes, and E_K is the animal's total kinetic energy.

During experiments, the animal's hind legs moved at 0.17 ± 0.05 m·s^{-1} (temporal average across all trials), resulting in an estimated kinetic energy of 0.005 ± 0.003 mJ from both hind legs. We neglected this contribution because it was much smaller than the potential energy barrier reduction from leg flexion (0.06 mJ, Section 2.6.9).

2.5.7 Definition of traversal phases

To compare the animal's motion in different stages of the traversal, we divided each trial into five distinct phases:

(1) Approach: From when the animal ran into the camera view to when it collided with the beams.

(2) Explore + pitch: From when the animal collided with the beams to when it started the final, successful roll attempt. Because the animal sometimes attempted to roll its body more than once, here we separated this phase and the next phase with the start of the last, successful attempt. The start of an attempt was defined as the instance when the animal's body roll changed sign from negative to positive (after mirrored, Section 2.5.6).

(3) Roll: From when the animal started the final, successful body roll attempt to when body roll was maximal.

(4) Land: From when body roll was maximal to when the animal landed with all its six legs had touched the ground again.

(5) Depart: From when the animal landed with all its six legs touching the ground to when it exited the camera views.

Note that the pitch + explore and roll phases here are not the same as the pitch and roll modes in our previous study [31]; instead, these two phases and the subsequent land phase are consecutive stages of the overall process of the animal transitioning from the pitch to the roll mode. The approach and depart phases correspond with the animal running on flat ground.

Our goal was to quantify and understand what adjustments the animal made to facilitate the pitch-to-roll transition. To achieve this, we focused on analyzing whether there were significant changes in kinematics in the explore + pitch and roll phases, compared with the approach and depart phases. We did not focus on analyzing the complex kinematics in the land phase because the pitch-to-roll transition was completed by then.

2.5.8 Statistics

To compare across traversal phases, for each trial, we averaged most kinematic variables (body roll γ, body pitch β, total leg sprawl ϕ_T, and leg height difference Δh) over time in each phase. For head flexion β_h and abdomen flexion β_a, for each trial, we instead calculated their standard deviation in each phase. This was because the animal often repeatedly flexed its head and abdomen (Section 2.6.4, 2.6.5), and the head and abdomen flexion angles each often nearly cancelled itself out when being averaged over time. On the other hand, their standard deviation better reflected the animal's repeated head and abdomen flexion amplitudes.

Then, we pooled the averages of most kinematic variables and standard deviations of head flexion and abdomen flexion from all trials. Using these data, for each pair of phases, we performed a mixed-effects ANOVA, with the phase as a fixed factor and the individual as a random factor to account for individual variability, to determine if there was a significant difference between phases. These data are reported as mean ± s.d. across trials (Section 2.6.3-2.6.6).

To check whether the animal's overall performance and behavior in this study were similar to those in our previous study [31], we performed a fixed-effects ANOVA, with

whether the data were from this study or previous study as the factor, and traversal time and maximal body roll as the variables (Section 2.6.1).

Because the duration of each phase in each trial varied substantially, plotting kinematics of all the trials as a function of time results in substantial overlap of data of different phases and obscures the trends of kinematics during each phase. To better visualize how body, head, abdomen, and leg kinematics change during each phase (**Figure 2-6B, D**, **Figure 2-7B, Figure 2-8B, Figure 2-9B, D**), for each trial, we offset the time of each phase to zero at its beginning and then normalized it to the duration of the phase to be percentage of each phase. In this way, we aligned the beginning and end of each phase across all the trials. This time normalization allowed clear visualization of the trends of the kinematics and did not affect the results of any other analysis.

All analyses except for statistical tests were performed using MATLAB (MathWorks, Inc., MA, USA). All statistical tests were performed using JMP 16 (SAS Institute Inc., NC, USA).

2.5.9 Potential energy landscape model definition

In the previous study, to generate the potential energy landscape, the animal body was modeled as a single rigid ellipsoid [31]. Here, to further study how the adjustments facilitated the beam traversal, we refined the animal body model to consist of a head, a thorax, and an abdomen (**Figure 2-3A**). Antennas, front and middle legs, and other body parts were neglected (totaling 7% body weight). The hind legs were neglected (6% body weight) when studying the usefulness of head flexion (Section 2.5.12), considering that they are not in contact with beams when the pitch-to-roll transition happened. The hind legs were added when studying the use of leg adjustments (Section 2.5.13). The thorax was

modeled as a half ellipsoid (**Figure 2-3A**, orange, length: 19.9 mm, width: 27.6 mm, thickness: 6.4 mm). The head was modeled as a massless ellipsoid-like rigid body (**Figure 2-3A**, red, length: 9.1 mm, width:14.4 mm, thickness: 6.0 mm). The abdomen was modeled as half of an ellipsoid (**Figure 2-3A**, yellow, length: 30.5 mm, width: 20.6 mm, thickness: 6.5 mm). All the dimensions above were the averages of the measured animal dimensions. When added, the hind legs were modeled as rigid rods with one side fixed to the thorax center (**Figure 2-3A**, blue and red lines with circle for left and right legs, respectively), because we only tracked the tibia-tarsal joint of the legs. The length of each leg was 27 mm (the average maximal leg length was 27 ± 2 mm in the explore + pitch and roll phases over all trials). For simplicity, we assumed that the head and abdomen could each only flex about a lateral axis fixed to the thorax (i.e., only the pitch degree of freedom was allowed). We set the body center of mass at the middle of the rotation axes between the thorax and the abdomen, which is a reasonable approximation [230]. We intentionally designed overlapping between the thorax and the head or abdomen (**Figure 2-3A**, **Figure 2-11A**) to reduce unrealistic concavity between these segments.

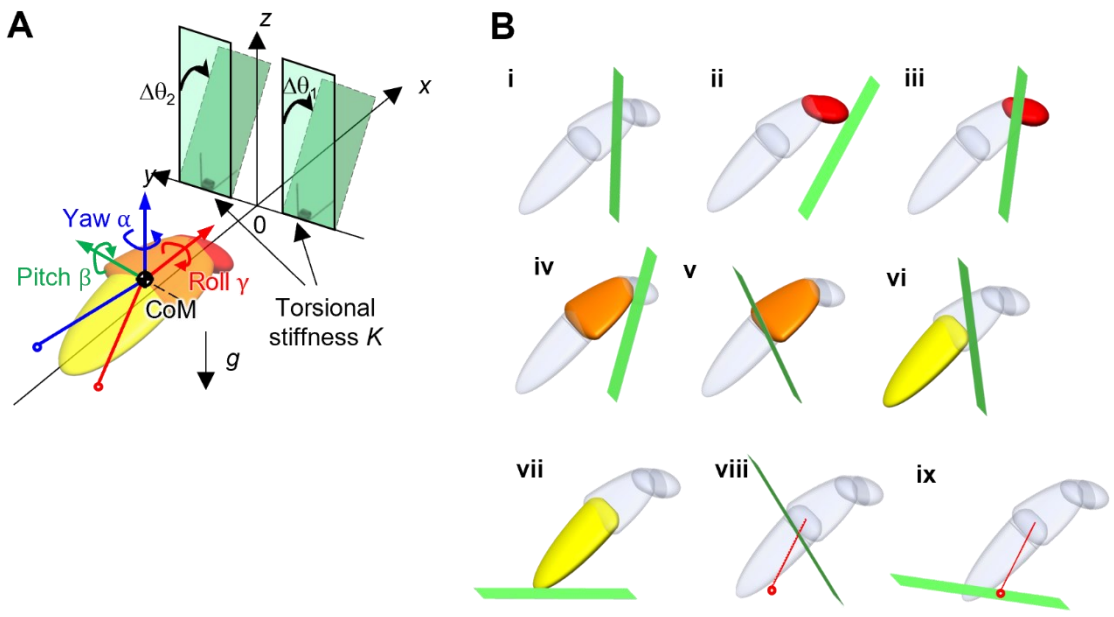

Figure 2-3: System modeling for potential energy landscape approach. (**A**) Model of animal and beams and definition of variables. (**B**) Schematic examples to choose between multiple possibilities of beam deflection. Hind legs (blue and red segments originating from the center of mass (CoM) in (A), red segments in (B), viii, ix) are neglected for analyses on head flexion (Section 2.5.12, **Figure 2-11A**) and are only included in analyses on leg adjustments (Section 2.5.13, **Figure 2-11B**).

The beams were modeled as rigid rectangular plates attached to the ground with Hookean torsional joints at the bottom. Their orientations without animal interaction were set vertically (**Figure 2-3A**, green with solid contour). In the previous study, the beams were only allowed to deflect forward, and the largest possible deflection angle was always selected [31]. This resulted in overestimated beam deflection. In particular, when the cockroach had already traversed the beams using roll mode, the estimated beam deflections were still calculated as if the beams blocked in front of the cockroach when the animal used a pitch mode. Here, to refine the model, we allowed the beams to deflect either forward or backward during the interaction, and we determined each beam's deflection ($\Delta\theta_1, \Delta\theta_2$) as

the angle with minimal absolute value at which the beam did not overlap with any part of the animal. This revised protocol ensured that, when the cockroach is sufficiently far away from the beam, either not having entered the beam area or having already traversed, beam deflection is zero; when the animal is interacting but has not traversed the beams, the beams deflect forward; when the animal has traversed the beams, the beams deflect backward. Note that this revised protocol does not affect the transition barrier analysis, because the pitch-to-roll transition happened when the animal body was only beginning to enter the gap (average body $x = -13.6 \pm 4.4$ mm when the pitch-to-roll transition happened over all trials); in that case, both protocols gave the same result.

Below we give an example of how to determine beam deflection (**Figure 2-3B**). When hind legs are neglected, we first identified seven possible deflection angles, i.e., 0° deflection (**Figure 2-3B, i**), deflections where the beam is tangential to the head in the front or back (**Figure 2-3B, ii, iii**), to the thorax in the front or back (**Figure 2-3B, iv, v**), or to the abdomen in the front or back (**Figure 2-3B, vi, vii**). Sometimes, there are no deflections where the beam is tangential to any body part; in that case, the two possible deflection angles where the beam is tangential to this part are set to be 0°. Then, we rejected the beam deflections where the beam overlaps with any body part (**Figure 2-3B, i, iii, iv, v, vi**), and finally selected the deflection angle with minimal absolute value (**Figure 2-3B, ii** is selected, **Figure 2-3B, vii** is rejected). When hind legs were added for analyzing the function of leg adjustments (Section 2.5.13, **Figure 2-11B**), compared with that neglecting hind legs, two additional possible deflection angles were identified for each hind leg, i.e., deflections where the beam contacts the leg in the front or back (**Figure 2-3B, viii, ix**, with only the right leg shown for simplicity). The remaining procedure was the same as that

neglecting hind legs. Beam deflection calculated from this method better matched experimental measurements than in the previous study [31], reducing the error from 15° ± 32° to −1° ± 13° ($P < 0.001$, repeated-measures ANOVA).

The potential energy of the system E_p is the sum of animal and beam gravitational potential energy and beam elastic energy:

$$E_p = m_c g z + m_b g \frac{L}{2}(\cos \Delta\theta_1 + \cos \Delta\theta_2) + \frac{1}{2} K(\Delta\theta_1^2 + \Delta\theta_2^2), \quad (2\text{-}10)$$

where m_c is the animal mass, g is gravitational acceleration, z is the height of body center of mass from the ground, m_b is the beam mass, L is the beam length, K is the beam torsional stiffness, and $\Delta\theta_1$ and $\Delta\theta_2$ are beam deflection from vertical. Given the constraints above, it was fully determined by the animal's position, orientation, and head and abdomen flexion and did not depend on the trajectory (i.e., determined by configuration with no history dependence). This is crucial for applying the potential energy landscape approach, because it simplifies the problem to be within a finite number of dimensions and further makes the variation of variables practical.

2.5.10 Potential energy landscape generation

We generated the potential energy landscape similarly to the previous study [31]. The model system has eight degrees of freedom, including the animal position (forward x, lateral y, vertical z) and orientation (yaw α, pitch β, roll γ) of thorax and head (β_h) and abdomen (β_a) flexion. So, the potential energy of the system should be a function of these eight independent variables:

$$E_p = E_p(x, y, z, \alpha, \beta, \gamma, \beta_h, \beta_a), \quad (2\text{-}11)$$

We calculated the potential energy landscape over the 8-D space by varying these eight variables, their ranges, and increments are listed in **Table 2-1**. We did not vary the abdomen flexion β_a for two reasons. First, the head and leg adjustments likely facilitated transition to the roll mode, whereas the abdomen which interacted with the beams after the body had already rolled into the gap and likely contributed less to this transition. Second, adding one more dimension to our potential energy landscape calculations was computationally costly. The first seven dimensions that we varied systematically already took three weeks of computation on a 32-core 2.93 GHz workstation. It would take ~20 times more (~a year) if we varied abdomen flexion like head flexion. To simplify landscape analysis, we focused on two cross sections of the entire 8-D landscape by collapsing less relevant dimensions. We first collapsed the landscape along the z dimension. For each combination of the other seven variables, potential energy is a function of z. We varied z from z_{min} (when the body touched the ground) to z_{min} + 15 mm and chose the z value for which potential energy is minimal, assuming that the unstable (due to self-propulsion) system was attracted to the local minimum. This method was different from that used in the previous study [31], where the animal's lowest point was constrained to always touch the ground (i.e., ground contract constraint). The body z obtained from this refined method better matched observations: with the ground contact constraint, to reach the average measured z when the animal interacted with the beams (x = –9 to –3 mm, **Figure 2-12B**) would require the animal to pitch up by an average of 20°, much greater than the observation (< 10°, **Figure 2-12D**) which was only possible without the ground contact constraint.

Next, we collapsed the landscape along other less relevant dimensions by analyzing landscape cross sections that follow the average animal trajectory. To extract an average animal trajectory as a function of forward position x, we first discretized x within [−26, 33] mm into 296 bins, each spanning 0.2 mm. We checked whether the animal passed any of these x bins between each two adjacent time steps in each trial. For each bin where this occurred, we determined the values of kinematic variables other than x using linear interpolation over x and recorded them under this bin. Finally, we averaged these recorded variables for each x bin, the evolution of which over x gave the average animal trajectory (**Figure 2-12**). For the pitch-roll cross section analysis, we always kept body y and yaw α to follow the average trajectory. For the yaw cross section analysis below, we always kept body y, body pitch β, and roll γ to follow the average trajectory. For both analyses, we constrained the abdomen pitch β_a fixed at 7° (temporal average of abdomen flexion was $\beta_a = 7° \pm 4°$ in the approach phase over all trials). Head flexion β_h was a variable in Section 2.5.12 and was set to follow the average trajectory in Section 2.5.13. See **Table 2-1** for a summary of the ranges and increment of parameter variation and dimension collapsing protocol.

To study how the head and leg adjustments affected pitch-to-roll transition (Section 2.5.12, 2.5.13), we extracted a pitch-roll cross section of the landscape, where potential energy is a function of body pitch β and roll γ. In addition, to study if the head flexion helped the animal stay within the gap after the animal rolled (Section 2.5.12), we extracted a body yaw cross section of the landscape, where potential energy is a function of body yaw α.

2.5.11 Quantifying difficulty of transition using potential energy barrier

To transition from one mode to another, the animal had to overcome a potential energy barrier (i.e., transition barrier) on the landscape cross section. A higher transition barrier means that it is more difficult to transition. We can measure whether and how the transition barrier changed with an observed adjustment (i.e., head flexion, leg tucking in) to evaluate whether it facilitated or hindered a transition. To quantify the difficulty to transition between two modes (i.e., from the pitch to the roll mode, from the roll to the deflect mode), for each x position during traversal ([−26, 33] mm), we generated the relevant cross section of the landscape, identified the basins corresponding to the two modes, and calculated the transition barrier.

First, we looped through all points on the landscape to identify the local minima and their basins corresponding to the locomotor modes. To quantify pitch-to-roll transition barrier, on the pitch-roll landscape cross section, we located the pitch minimum (**Figure 2-4B**, blue point) with a finite body pitch and a body roll near 0° (**Figure 2-4A**, **i-iii**) and the roll minimum (**Figure 2-4B**, red point), with a body pitch near 0° and a body roll around 90° (**Figure 2-4A, iii'**). When no roll minimum existed (i.e., when the animal was far from the beams, **Figure 2-4B, i**), we defined (pitch, roll) = (0°, 90°) as the roll minimum.

To quantify the roll-to-deflect barrier, on the yaw landscape cross section, we located the roll minimum (**Figure 2-4D**, red point), which corresponded to the body rolled into the gap with a body yaw around 0° (**Figure 2-4C, i, ii**), and the two deflect minima (**Figure 2-4D**, purple points), which corresponded with the body deflected towards the left or right with a body yaw around ± 90° (**Figure 2-4C, ii', ii''**). Note that the same roll mode (**Figure 2-4A, iii', Figure 2-4C, i, ii**) corresponded with the roll basin on the pitch-roll

cross section and the roll basin on the yaw cross section, which appeared as different basins. This is because the potential energy landscape exists in a high-dimensional space, with five degrees of freedom (x, y, pitch, roll, yaw) when not considering head, abdomen, and leg adjustments. At the same (x, y), the same roll basin in the higher-dimension pitch-roll-yaw landscape cross section appears as different basins on the lower-dimension pitch-roll cross section and yaw cross section.

Once we located the pitch and roll basins on the pitch-roll cross section and roll and deflect basins on the yaw cross section, we used breadth-first search to calculate the transition barrier from one basin to another. Breadth-first search is a computational algorithm for searching on graph data structure [234]. We fed the gridded potential energy landscape cross section as the graph data, with the starting minimum as the start point, the destination minimum as the goal point, and the highest potential energy on the traversing route as the cost function. In the breath-first search algorithm, each searched point remembered its parent (the point that this point was developed from), so tracing the parent and further ancestors from the goal point (i.e., parent backtracking) gave an imaginary route from the starting to the destination minimum that crossed the lowest energy barrier (**Figure 2-4B, D**, green curve). We defined the point with the highest energy on this route as the saddle point (**Figure 2-4B, D**, orange points on the cross sections). Note that this "saddle point" is only a true saddle point on the 2-D pitch-roll cross section and when both the pitch and roll minima are actual local minima on this cross section. When no roll minimum existed (see last paragraph, roll minimum definition), the "saddle point" on this cross section was calculated as the roll minimum defined, because the potential energy increases monotonically along the imaginary route from pitch to roll minimum. On the 1-

D yaw cross section, the “saddle point” is actually a local maximum. We refer to them all as “saddle point” for simplicity.

We then defined the transition barrier as the potential energy increase from the starting minimum to the saddle point. Note that the imaginary route was only for defining the saddle point, and during the transition the animal did not necessarily start from a local minimum or transition by crossing the saddle point. Despite this, our barrier estimation still provided useful insight as it quantified the level of the difficulty to transition.

Intuitively, the breadth-first search approach resembled injecting water slowly at the start minimum and tracking the expansion of the water-covering area. The potential energy landscape resembled an uneven surface (**Figure 2-14A**), and each basin on the surface corresponded with a locomotor mode, such as pitch and roll modes [31] (**Figure 2-14A**, blue and red points, **Figure 2-14B**, blue and red area, separately). Increasing the cost resembled injecting water in the starting basin (**Figure 2-14B**, blue area) and increasing the water level. As the water level increased, there was a moment that the water level was sufficiently high to overcome a barrier between two basins (**Figure 2-14B**, the boundary between blue and red areas), and the water flowed via the saddle point of the barrier (**Figure 2-14B**, orange point) into the destination basin. The water level measured from the starting minimum at the time of this onset of flow resembled the potential energy barrier height (**Figure 2-14C**, yellow).

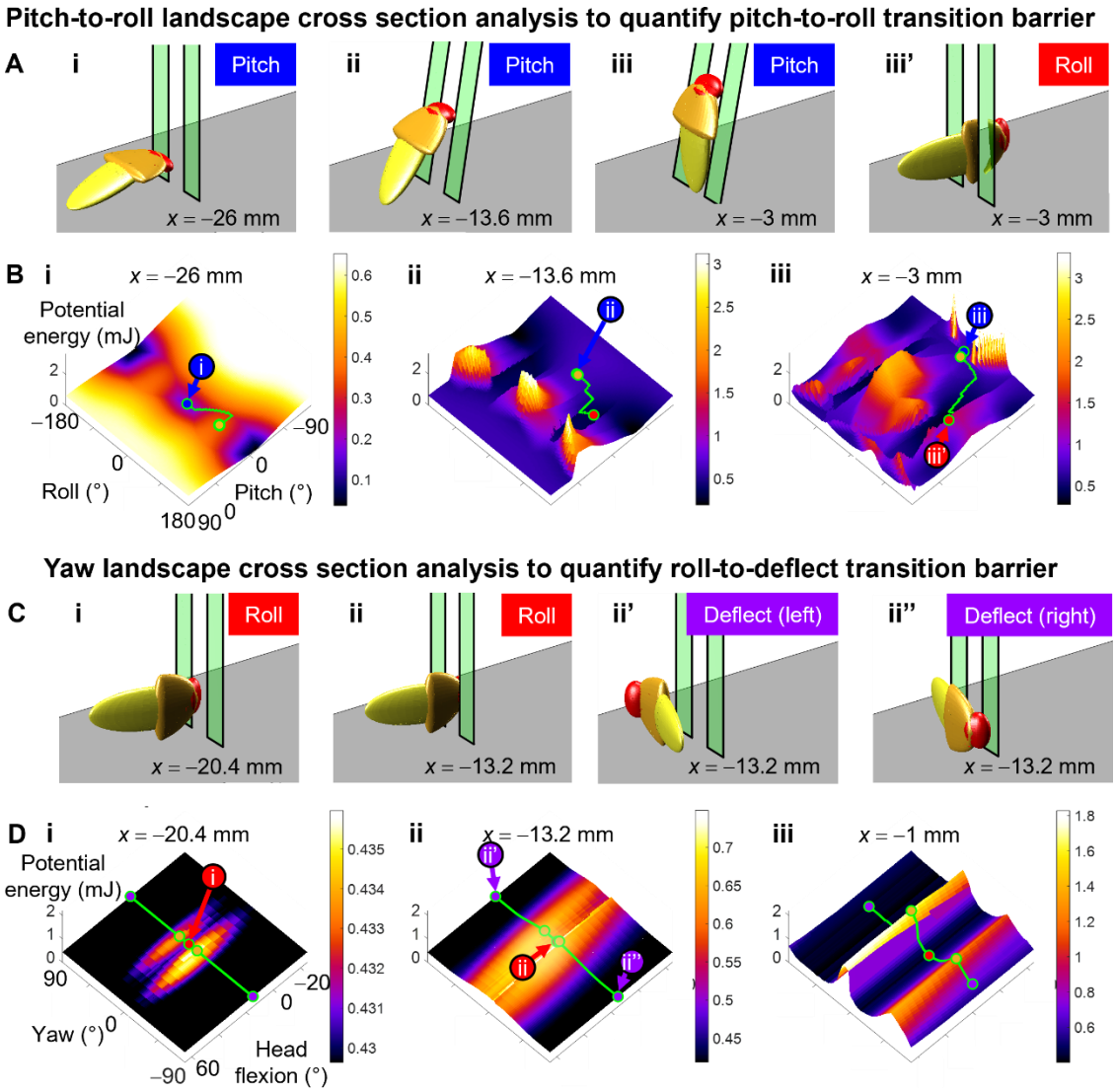

Figure 2-4: Potential energy landscape analyses to quantify transition barriers. Top (A, B): Illustration of pitch-roll landscape cross section analysis to test hypotheses (1) and (2). Bottom (C, D): Illustration of yaw landscape cross section analysis to test hypothesis (3). (**A**) Illustration of locomotor modes for pitch-roll cross section. (i) Pitch mode at $x = -26$ mm, (pitch, roll) = (0°, 0°). (ii) Pitch mode at $x = -13.6$ mm, (pitch, roll) = (−38°, 0°). (iii) Pitch mode at $x = -3$ mm, (pitch, roll) = (−73°, 0°). (iii') Roll mode at $x = -3$ mm, (pitch, roll) = (−8°, 92°). (**B**) Pitch-roll landscape cross section at different x for quantifying pitch-to-roll transition barrier. Blue point is pitch local minimum. Red point is roll local minimum. Orange point is saddle point. Green curves are imaginary routes. (i) $x = -26$

mm. Note that roll minimum and saddle point overlap here. (ii) $x = -13.6$ mm. Pitch minimum and saddle point are close. (iii) $x = 0$ mm. (**C**) Illustration of locomotor modes for yaw cross section. (i) Roll mode at $x = -20.4$ mm, yaw = 0°. (ii) Roll mode at $x = -13.2$ mm, yaw = 0°. (ii') Deflect mode at $x = -13.2$ mm, to the left, yaw = 90°. (ii") Deflect mode at $x = -13.2$ mm, to the right, yaw = −90°. (**D**) Yaw landscape cross sections stacked along head flexion dimension at different x for quantifying roll-to-deflect transition barrier. Red point is roll local minimum. Purple points are deflect local minima, with positive yaw deflected to the left and negative yaw to the right. Orange points are saddle points. Green curves are imaginary routes. Only routes at head flexion $\beta_h = 15°$ are marked. (i) $x = -20.4$ mm. (ii) $x = -13.2$ mm. (iii) $x = -1$ mm. In (B, D), i, ii, ii', ii'', iii, iii' in circles refer to locomotor modes in (A, C). Note that the imaginary route is only for defining the saddle point, and during the transition the animal did not necessarily start from a local minimum or transition by crossing the saddle point. In (B), body y and yaw at each x follow those of average trajectory (Section 2.5.10, **Figure 2-12**). In (D), body y, pitch, and roll at each x follow those of average trajectory (Section 2.5.10, **Figure 2-12**). In both (B, D), head flexion is fixed at 15°, and abdomen flexion is fixed at 7°. In all illustrations and landscapes shown here, legs are neglected; however, legs are modeled when testing hypothesis (2) (Section 2.5.13, **Figure 2-10B**, **Figure 2-11B**). Also see **Movie 3** for an illustration of how the landscapes evolve as a function of x.

2.5.12 Test usefulness of head flexion

To test hypothesis (1), we analyzed whether head flexion in the range observed reduced the pitch-to-roll transition barrier compared to if the animal simply held its head in the typical orientation (average head flexion during running on flat ground). We varied head flexions within [−25°, 65°] (covering the observed head flexion range of [−24°, 64°] over all the trials) with an increment of 5° (**Figure 2-11A**), calculated the pitch-to-roll transition barrier as a function of x, and compared the transition barrier at each head flexion

with that at head flexion $\beta_h = 15°$, which represents the case without head flexion (temporal average of head flexion was $\beta_h = 15° \pm 4°$ in the approach phase over all trials).

To test hypothesis (3), we analyzed whether the head flexion in the range observed increased the roll-to-deflect transition barrier compared to without head flexion. We varied the head flexion like above, calculated the roll-to-deflect transition barrier as a function of *x*, and compared the transition barrier at each head flexion with that at head flexion $\beta_h = 15°$.

2.5.13 Test usefulness of leg tucking in

To test hypotheses (2), we analyzed whether the leg sprawl changes affected the pitch-to-roll transition barrier. We added two hind legs (length = 27 mm, Section 2.5.9) into the model symmetrically to the left and right sides of the body, with a leg height of −5 mm (temporal average of leg height was -5 ± 3 mm in the explore + pitch phase over all trials, Section 2.6.6), and varied total leg sprawl within [0°, 180°] with an increment of 45° (**Figure 2-11B**). We compared the transition barrier at each total leg sprawl with that at total leg sprawl $\phi_T = 160°$ (average maximal total leg sprawl was $\phi_T = 156° \pm 21°$ in the explore + pitch phase over all trials) and $\phi_T = 20°$ (average minimal total leg sprawl was $\phi_T = 21° \pm 17°$ in the roll phase over all trials). Note that the animal also elevated and depressed its hind legs asymmetrically in pitch and roll phases (Section 2.6.6). For simplicity, here we kept the two legs symmetric to provide a rough estimate of the effect of leg sprawl change on the barrier.

2.6 Results

2.6.1 Similar overall performance and behavior to previous study

The animals displayed similar locomotor performance as that in the previous study [31], with a similar traversal time (3.0 ± 1.0 s vs. 3.9 ± 3.9 s previously, $P = 0.18$, fixed-effects ANOVA). The animal also always transitioned to the roll mode to traverse (100% of all 36 trials), similar to the previous study (97% of all previous trials for slightly less stiff beams $K = 1.7$ mN·m·rad^{-1}), with a similar maximal body roll during traversal (81° ± 10° vs. 84° ± 20° previously, $P = 0.30$, fixed-effects ANOVA). Note that even counting the 28 trials not included in the dataset (Section 2.5.4), which had slightly longer duration, these metrics were still similar (traversal time: 4.5 ± 1.8 s vs. 3.9 ± 3.9 s, $P = 0.71$, fixed-effects ANOVA; roll mode use: 98% vs. 97% of all trials; maximal body roll: 90° ± 20° vs. 84° ± 20°, $P = 0.09$, fixed-effects ANOVA).

2.6.2 Animal uses complex motion to transition from pitch to roll mode

After running with an alternating tripod gait and colliding with the beams (approach phase, **Figure 2-5**, green), the animal traversed the beam obstacles with complex body, head, and leg motions. In the explore + pitch phase (**Figure 2-5**, blue), the animal often moved along the beam layer (y-direction) and turned left or right to search around the beams, pitched up its body against the beams, repeatedly flexed its head, and rubbed its pronotum against the beams, sometimes pushed the beam using its fore or middle legs, and swept its antennas in the gaps. In the roll phase (**Figure 2-5**, red), the animal rolled its body into the gap and struggled its legs to try to push against the back side of the beams. It sometimes flexed its head repeatedly. It also sometimes flexed and twisted its abdomen. In the land phase (**Figure 2-5**, orange), the animal continued to do these, eventually passed

the beams in the roll mode, and resumed an upright body orientation. Finally, in the depart phase (**Figure 2-5**, purple), the animal ran away in an alternating-tripod gait. These observations were consistent with those in the previous study [31].

Similar to the previous study, body oscillation was observed [31]. The average kinetic energy fluctuation was 0.01 ± 0.01 mJ. This was smaller than that in the previous study (0.02 ± 0.01 mJ). We speculate that this was caused by the additional modifications on the animal (wing trimming, adding one more tag on the pronotum, and beads on hind legs) that slightly resisted the animal motion.

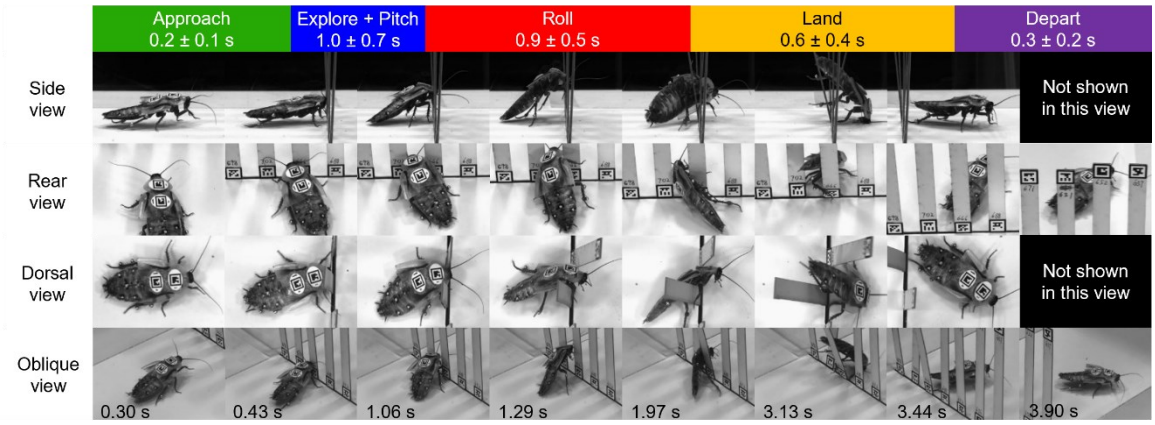

Figure 2-5: Five phases of traversal. Values under phase labels are means ± s.d. of the duration of each phase across all trials.

2.6.3 Body rotations

The animal's body pitched up in the explore + pitch phase and rolled into the gap in the roll phase (**Figure 2-6A, Movie 1**). In the approach phase, the body only slightly pitched up (**Figure 2-6A, v, Figure 2-6D**, green, average pitch $\beta = -8° \pm 7°$; note that a negative body pitch angle means the body pitched up). In the explore + pitch phase, the body pitched up substantially (pitch angle became more negative, minimal pitch $\beta = -36°$

± 9°, **Figure 2-6A, ii, vi, Figure 2-6D**, blue). In the roll phase, as the animal rolled its pitched-up body substantially into the gap (maximal roll $\gamma = 81° \pm 10°$, **Figure 2-6A, iii, vii, Figure 2-6B**, red), the body became less pitched (pitch angle less negative, **Figure 2-6A, iii, vii, Figure 2-6D**, red) and eventually horizontal. Average body roll γ was higher in the roll phase ($44° \pm 8°$) than in the approach ($-2° \pm 3°$), explore + pitch ($-3° \pm 6°$), and depart ($-2° \pm 4°$) phases (**Figure 2-6C**, $P < 0.0001$, repeated-measures ANOVA). Average body pitch β was lower (meaning the body was more pitched up) in the explore + pitch ($-14° \pm 9°$) and roll ($-14° \pm 9°$) phases than in the approach ($-8° \pm 7°$) and depart ($-7° \pm 5°$) phases (**Figure 2-6E**, $P < 0.05$, repeated-measures ANOVA).

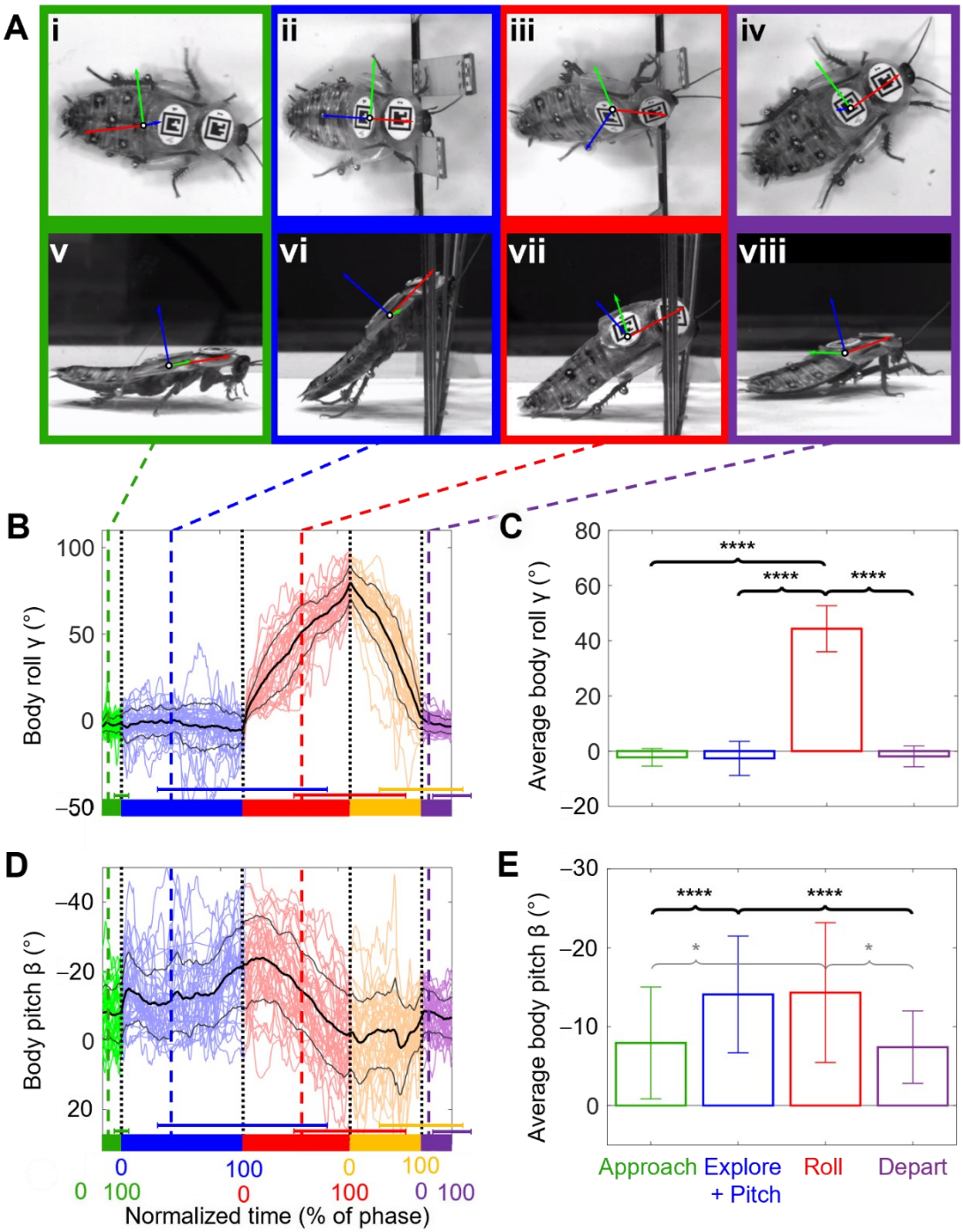

Figure 2-6: Body rotations. (**A**) Representative snapshots for each phase. Top and bottom rows show thorax frame from top and side view in approach (i), explore + pitch (ii), roll (iii), and depart (iv) phases, respectively. Animal's body orientation is represented by Euler angles of thorax frame (yaw α, pitch β, roll γ, *Z*–*Y*'–*X*" Tait-Bryan convention, Section

2.5.6). For simplicity, we laterally mirrored kinematic data of the trials in which the animal rolled to the left to become rolling to the right to simplify the analysis, considering lateral symmetry (Section 2.5.6). (**B, D**) Body roll and pitch as a function of time, with time of each phase offset to zero at its beginning and then normalized to its duration to be percentage of each phase (Section 2.5.8). Colors are for five phases defined in **Figure 2-5**. Length of horizontal colored thick bars and error bars are proportional to means ± s.d. of the duration of each phase of all trials shown in **Figure 2-5**. Black vertical dotted lines separate consecutive phases. Colored dashed lines show moments of snapshots in (A). Colored curves are individual trials. Thick and thin black curves are mean ± s.d. across all trials. (**C, E**) Average body roll and pitch in different phases. Bars and error bars are means ± s.d. of the temporal averages of all trials in (B, D) for each phase. * $P < 0.05$, **** $P < 0.0001$, repeated-measures ANOVA. Bold brackets and asterisks show important comparisons described in Results. In (D, E), *y*-axis is inversed to better show body pitching up more or less, because a negative body pitch angle means body is pitched up.

2.6.4 Head flexion

During both the explore + pitch and roll phases, the animal sometimes repeatedly flexed its head dynamically and sometimes flexed its head down and held it statically (**Figure 2-7A ii, iii, Figure 2-7B**, blue and red, **Movie 1**). This motion was absent during the approach and depart phases when the animal ran on flat ground (**Figure 2-7A i, iv, Figure 2-7**B, green and purple). The standard deviation of the head flexion β_h, which reflects how much the head flexed (Section 2.5.6), was higher in the explore + pitch (7° ± 3°) and roll (8° ± 3°) phases than in the approach (1.7° ± 0.5°) and depart (2° ± 1°) phases (**Figure 2-7C**, $P < 0.0001$, repeated-measures ANOVA).

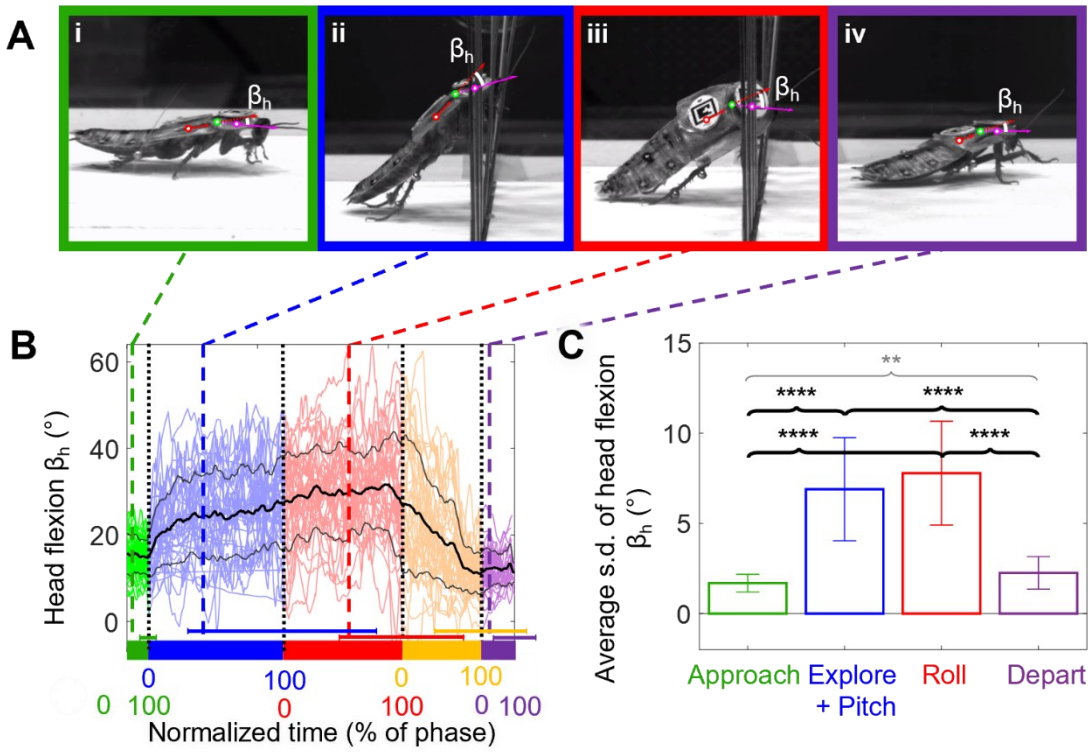

Figure 2-7: Head flexion. (**A**) Representative snapshots for each phase. Four panels show head flexion β_h (defined as pitch angle of head in thorax frame, Section 2.5.6) in approach (i), explore + pitch (ii), roll (iii), and depart (iv) phases. For simplicity, we laterally mirrored kinematic data of the trials in which the animal rolled to the left to become rolling to the right to simplify the analysis, considering lateral symmetry (Section 2.5.6). (**B**) Head flexion as a function of time, with time of each phase offset to zero at its beginning and then normalized to its duration to be percentage of each phase (Section 2.5.8). Colors are for five phases defined in **Figure 2-5**. Length of horizontal colored thick bars and error bars are proportional to means ± s.d. of the duration of each phase of all trials shown in **Figure 2-5**. Black vertical dotted lines separate consecutive phases. Colored dashed lines show moments of snapshots in (A). Colored curves are individual trials. Thick and thin black curves are mean ± s.d. across all trials. (**C**) Average standard deviation of head flexion in different phases. Bars and error bars are means ± s.d. of the temporal standard deviations of all trials in (B) for each phase. ** $P < 0.01$, **** $P < 0.0001$, repeated-measures ANOVA. Bold brackets and asterisks show important comparisons described in Results.

2.6.5 Abdomen flexion

During both the explore + pitch and roll phases, the animal sometimes repeatedly flexed its abdomen dynamically and sometimes flexed its abdomen down and held it statically (**Figure 2-8A ii, iii, Figure 2-8B**, blue and red, **Movie 1**). This motion was absent during the approach and depart phases when the animal ran on flat ground (**Figure 2-8A i, iv, Figure 2-8B**, green and purple). The standard deviation of the abdomen flexion β_a, which reflects how much the abdomen flexed (Section 2.5.6), was higher in the roll (7° ± 3°) and explore + pitch (4° ± 2°) phases than in the approach (2° ± 1°) and depart (3° ± 1°) phases (**Figure 2-8C**, $P < 0.0001$, repeated-measures ANOVA).

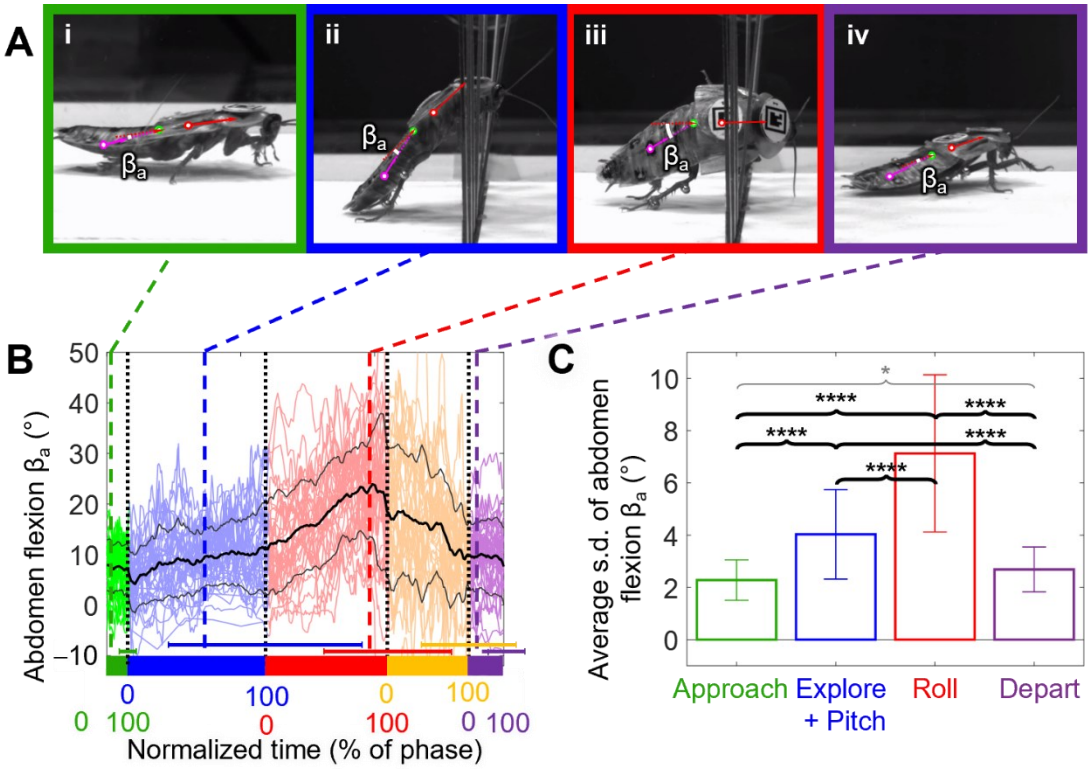

Figure 2-8: Abdomen flexion. (**A**) Representative snapshots for each phase. Four panels show abdomen flexion β_a (defined as pitch angle of abdomen in thorax frame, Section 2.5.6) in approach (i), explore + pitch (ii), roll (iii), and depart (iv) phases. For simplicity,

we laterally mirrored kinematic data of the trials in which the animal rolled to the left to become rolling to the right to simplify the analysis, considering lateral symmetry (Section 2.5.6). (**B**) Abdomen flexion as a function of time, with time of each phase offset to zero at its beginning and then normalized to its duration to be percentage of each phase (Section 2.5.8). Colors are for five phases defined in **Figure 2-5**. Length of horizontal colored thick bars and error bars are proportional to means ± s.d. of the duration of each phase of all trials shown in **Figure 2-5**. Black vertical dotted lines separate consecutive phases. Colored dashed lines show moments of snapshots in (A). Colored curves are individual trials. Thick and thin black curves are mean ± s.d. across all trials. (**C**) Average abdomen flexion angle in different phases. Bars and error bars are means ± s.d. of the temporal standard deviations of all trials in (B) for each phase. * $P < 0.05$, **** $P < 0.0001$, repeated-measures ANOVA. Bold brackets and asterisks show important comparisons described in Results.

2.6.6 Leg adjustments

The animal adjusted its hind legs in two ways (**Figure 2-9A, Cockroach Flexed its Head and Abdomen while Traversing Beams.** Top: zoomed top (left) and side (right) views. White points with red, magenta, cyan, green, and orange edges are the origins of thorax frame, head frame, abdomen frame, middle point of thorax-head joint, and middle point of the thorax-abdomen joint, respectively. Solid and dotted arrows show +*x* and +*x*' direction of body (red), head (magenta), and abdomen (cyan) frames, respectively. Head and abdomen flexion are the angles between body +*x*' direction and head or abdomen +*x* direction. Bottom left: isometric view. Bottom right: head and abdomen flexion as a function of time.

Link: https://youtu.be/bc4hdj_a1_A.

Movie 2). First, it adjusted its hind leg sprawl in the explore + pitch and roll phases. During the explore + pitch phase, the animal spread both its hind legs further outward (**Figure 2-9A, ii**) compared to the approach phase (**Figure 2-9A, i, Figure 2-9B**, average left leg sprawl angle $\phi_L = 63° \pm 15°$ vs. $55° \pm 10°$, average right leg sprawl angle $\phi_R = 64°$

± 13°vs. 55° ± 11°). As body rolling began, the animal tucked in its depressed (left) hind leg (**Figure 2-9A, iii, Figure 2-9B**, blue, average left leg sprawl angle $\phi_L = 27° \pm 21°$) while keeping the right leg sprawl relatively unchanged (**Figure 2-9A, iii, Figure 2-9B**, red, average right leg sprawl angle $\phi_R = 62° \pm 13°$). Average total leg sprawl ϕ_T was greater in the explore + pitch phase ($\phi_T = 127° \pm 19°$) and smaller in the roll phase (90° ± 23°) than in the approach (110° ± 13°) and depart (115° ± 11°) phases (**Figure 2-9C**, $P < 0.0001$, repeated-measures ANOVA).

In addition, the animal depressed one hind leg relative to the body and elevated the other in the roll phase. In the explore + pitch phase, both hind legs had similar heights (**Figure 2-9A, vi, vi', Figure 2-9D**, average left leg height $h_L = -4 \pm 2$ mm, average right leg height $h_R = -5 \pm 2$ mm, average leg height difference $\Delta h = -1 \pm 2$ mm). In the roll phase, the animal usually kept both feet on the ground (**Figure 2-9A, vii, vii'**), with one hind leg depressed further (**Figure 2-9D**, blue, average leg heights $h_L = -11 \pm 3$ mm), appearing to push against the ground (**Figure 2-9A, vii, vii'**), while the other elevated (**Figure 2-9D**, red, average leg heights $h_R = -2 \pm 2$ mm), appearing to support the body (**Figure 2-9A, vii, vii'**), which increased the leg height difference (**Figure 2-9E**, red). As the animal moved further through the gap and reached maximal body roll, it elevated its depressed (left) leg up to around the body coronal plane (maximal leg height $h_L = 4 \pm 3$ mm) in the land phase (**Figure 2-9D**, blue). The average leg height difference Δh was higher in the roll phase (9 ± 3 mm) than in the approach (−1 ± 1 mm), explore + pitch (−1 ± 2 mm), and depart (−1 ± 1 mm) phases (**Figure 2-9E**, $P < 0.0001$, repeated-measures

ANOVA). Both these observations demonstrated that the animal used its left and right hind legs differentially in the roll phase.

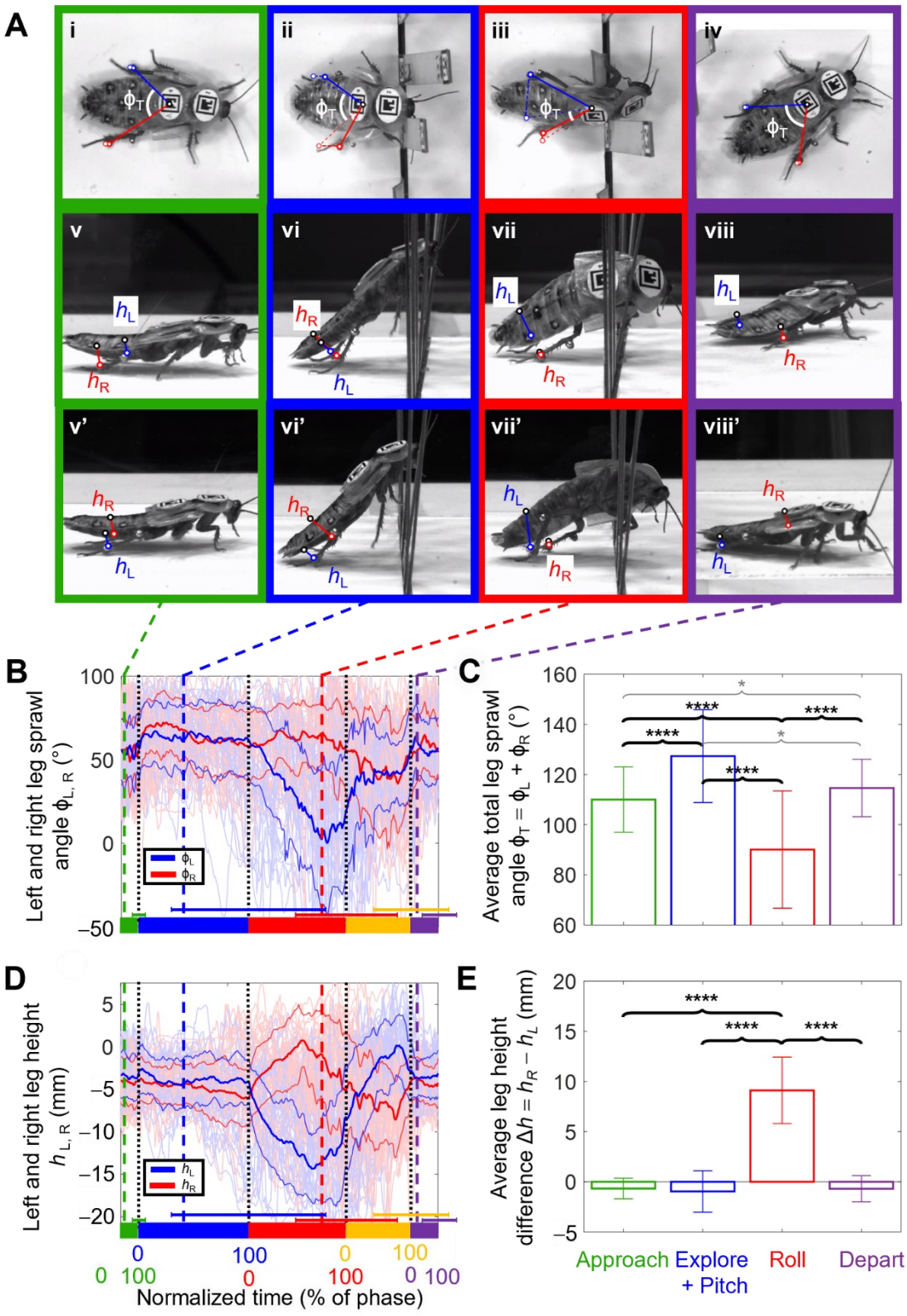
A
i
ii
iii
iv
v
vi
vii
viii
v'
vi'
vii'
viii'
B
Left and right leg sprawl angle $\phi_{L,R}$ (°)
100
50
0
−50
ϕ_L
ϕ_R
C
Average total leg sprawl angle $\phi_T = \phi_L + \phi_R$ (°)
160
140
120
100
80
60
*
****
****
****
****
*
D
Left and right leg height $h_{L,R}$ (mm)
5
0
−5
−10
−15
−20
h_L
h_R
0 100 0 100 0 100 0 100
Normalized time (% of phase)
E
Average leg height difference $\Delta h = h_R - h_L$ (mm)
20
15
10
5
0
−5
****
****
****
Approach
Explore + Pitch
Roll
Depart

Figure 2-9: Leg adjustments. (**A**) Representative snapshots for each phase. Top row shows total leg sprawl ϕ_T (defined as angle between two leg vectors in body coronal plane, Section 2.5.6) in approach (i), explore + pitch (ii), roll (iii), and depart (iv) phases, respectively. Middle row shows left leg height h_L (blue) and right leg height h_R (red) (defined as leg distance to body coronal plane, Section 2.5.6) in approach (v), explore + pitch (vi), roll (vii), and depart (viii) phases, respectively. For simplicity, we laterally mirrored kinematic data of the trials in which the animal rolled to the left to become rolling to the right to simplify the analysis, considering lateral symmetry (Section 2.5.6). Bottom row (v', vi', vii', viii') shows mirrored lateral views from cameras opposite to the middle row ones (v, vi, vii, viii) to better show legs on the opposite side. (**B, D**) Leg sprawl angle and leg height of hind legs as a function of time, with time of each phase offset to zero at its beginning and then normalized to its duration to be percentage of each phase (Section 2.5.6). A negative leg height means that the leg marker is below body coronal plane, and a positive leg height means leg marker is above it. Length of horizontal colored thick bars and error bars are proportional to means ± s.d. of the duration of each phase of all trials shown in **Figure 2-5**, whose colors are for five phases defined in **Figure 2-5**. Black vertical dotted lines separate consecutive phases. Colored dashed lines show moments of snapshots in (A). Light-colored curves are individual trials. Thick and thin solid-colored curves are mean ± s.d. across all trials. Blue and red colors are for left and right legs, respectively. (**C, E**) Average total leg sprawl and leg height in different phases. Bars and error bars are means ± s.d. of the temporal averages of all trials in (B, D) for each phase. * $P < 0.05$, **** $P < 0.0001$, repeated-measures ANOVA. Bold brackets and asterisks show important comparisons described in Results.

2.6.7 Refined potential energy landscape consistent with and more accurate than coarse landscape in previous study

The topology and evolution of the refined potential energy landscape (**Movie 3**) as viewed in the pitch-roll cross section were consistent with that in the previous study [31]. Initially, when the animal was far from the beam, the energy landscape had a local

minimum at zero pitch and roll, a basin was formed near the minimum; as the body moved close to the beam, the basin moved along pitch direction, becoming the pitch basin, while the roll basin formed at about zero pitch and about 90° roll. The similarity of the topology of potential energy landscape indicated that it was insensitive to minor differences in shape modeling (e.g., using refined body shape vs. using a simple ellipsoidal body; varying head and abdomen flexion; including hind legs or not). We also found that the pitch-to-roll transition barrier calculated from the refined potential energy landscape model here is similar to that from the simple model in the previous study (Supplementary Information, Section 2.8.2), further demonstrating the model's consistency and applicability with both coarse-grained and fine-grained model approximations (see Discussion in [31]).

Because we allowed the beam to deflect backward, the pitch basin finally went back to near zero pitch, and the roll basin eventually disappeared. The landscape became the initial landscape as the animal had traversed and moved far from the beam. This showed that the beam deflection calculation was more reasonable than the previous study.

2.6.8 Head flexion does not facilitate pitch-to-roll transition

To test hypothesis (1) that head flexion reduces the pitch-to-roll transition barrier and facilitates rolling into the gap, we analyzed whether adjusting head flexion can reduce the pitch-to-roll transition barrier. The transition barrier from the pitch to the roll mode with different head flexion is shown in **Figure 2-10A**. At the average $x = -13.6$ mm where the animals transitioned from pitch to roll mode, the maximal transition barrier reduction with head flexion within [−25°, 65°] was 0.0027 mJ (**Figure 2-10A**, a). This mechanical energy that could be saved by head flexion was small (27%) compared with the average

kinetic energy fluctuation level (0.01 mJ) and small (4.5%) compared to the energy saved by leg tucking in (0.06 mJ, Section 2.6.9). Also, achieving this saving would require the head to flex by 65°, which was rarely observed in the experiment. This suggested that the head adjustment did not reduce the transition barrier substantially to facilitate pitch-to-roll transition. This rejected our hypothesis that the head adjustment facilitated the mode transition by lowering the pitch-to-roll transition barrier on the potential energy landscape.

To test hypothesis (3) that head flexion facilitates the animal staying within the gap after rolling into it, we analyzed whether adjusting head flexion can increase the roll-to-deflect transition barrier. The transition barrier from the roll to the deflect mode with different head flexion is shown in **Figure 2-10C, D**. At the average $x = -13.6$ mm where the animal transitioned from the pitch to the roll mode, the maximal increase in transition barrier with head flexion within [−25°, 65°] was 0.012 mJ (**Figure 2-10C**, c) to deflect to the left and 0.008 mJ (**Figure 2-10D**, d) to deflect to the right. The transition barrier only increased by a maximum of 12%, which required the head to hyperextend (head flexion $\beta_h = -25°$), which was rarely observed in the experiment. This suggested that the head adjustment did not increase the transition barrier substantially to prevent the animal from yawing to deflect the beams. This rejected our hypothesis that the head adjustment facilitates the body staying within the gap.

2.6.9 Leg sprawl adjustments facilitate body rolling

To test hypothesis (2) that tucking in a hind leg reduces the pitch-to-roll transition barrier and facilitates rolling, we analyzed how adjusting leg sprawl changes the pitch-to-roll transition barrier. The transition barrier from pitch to roll mode with different total leg

sprawl is shown in **Figure 2-10B**. At the average $x = -13.6$ mm where the animals transitioned from the pitch to roll mode, the transition barrier at 20° total leg sprawl was less than that at 160° total leg sprawl by 0.06 mJ (**Figure 2-10B**, b), which is six times larger than the average kinetic energy fluctuation level. These indicated that tucking a hind leg in helped the animal substantially reduce the pitch-to-roll transition barrier when rolling. Together, these findings supported our hypothesis that leg sprawl adjustment facilitated the pitch-to-roll transition.

Curiously, at $x = -20$ mm, where the animals pitched against the beams (the mean of temporal average of x over the pitch + explore phase across all trials was -20 ± 3 mm), the transition barrier at 160° total leg sprawl was larger than that at 20° total leg sprawl by 0.35 mJ, which was 35 times larger than the animal's average kinetic energy fluctuation (0.01 mJ). Because a larger potential energy barrier indicates higher stability, this suggested that further spreading out hind legs during the pitch + explore phase helped the animal stay pitched up against the beams more stably and resisted rolling into the gap. We speculate that in this phase the larger leg spread here helped the animal's pitched up body stay aligned to the gap rather than yaw and fall sideways under gravity.

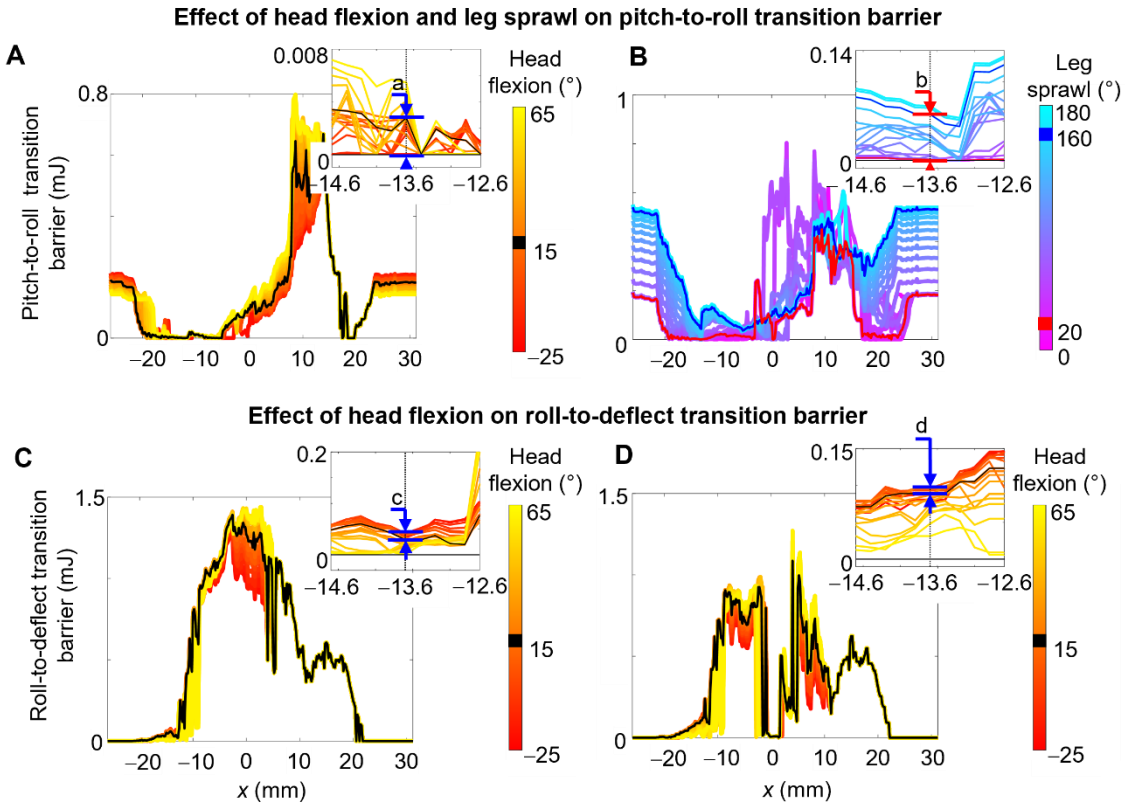

Figure 2-10: Effect of head flexion and leg sprawl on transition barriers. (**A, B**) Pitch-to-roll transition barrier as a function of x for different head flexion and total leg sprawl. (**C**, **D**) Roll-to-deflect transition barrier as a function of x under for different head flexion. (C) Deflect to the left. (D) Deflect to the right. In (A, C, D), black curves show transition barrier at average animal head flexion $\beta_h = 15°$. In (B), red and blue curves show transition barrier at total leg sprawl $\phi_T = 20°$ and 160°, respectively. Insets in (A-D) are close-up views at in the x range of [−14.6, −12.6] mm, respectively. Dashed lines show $x = -13.6$ mm, which is the average location when roll phase begins. (a-d) show the maximal transition barrier increase or reduction by using adjustments. See **Movie 3** for an illustration of how barrier as a function of x is obtained. In (A, B), body y and yaw at each x follow those of average trajectory (Section 2.5.10, **Figure 2-12**). In (C, D), y, pitch, and roll at each x follow those of average trajectory (Section 2.5.10, **Figure 2-12**). In (A, C, D), hind legs are neglected, and abdomen flexion is flexed at 7°. In (B), head flexion is fixed at 15°, and abdomen flexion is fixed at 7°.

2.7 Discussion

As a first step to understand how animals control physical interaction with complex 3-D terrain to transition between locomotor modes, we quantified adjustments by the discoid cockroach to make the pitch-to-roll transition while traversing beam obstacles. The major adjustments included body rotations (**Figure 2-6**), head flexion (**Figure 2-7**), abdomen flexion (**Figure 2-8**), and differential hind leg use (**Figure 2-9**). Because it was strenuous to traverse the stiff beams by pushing across (the pitch mode), the animal likely made these adjustments to facilitate transitioning to the less strenuous roll mode. Below we discuss the likely function of each adjustment and suggest future directions.

2.7.1 Role of head flexion

To find the function of head flexion in both the explore + pitch and roll phases, we first hypothesized that by changing the overall body shape, it (1) lowered the pitch-to-roll transition barrier and (2) increased the roll-to-deflect transition barrier. However, we found that the head flexion did not change the transition barrier substantially in both cases. Therefore, we rejected these two hypotheses (Section 2.6.8). We speculate that this is because the cockroach's head is small and relatively more spherical (thickness/length = 0.66) compared to the thorax (thickness/length = 0.30) and abdomen (thickness/length = 0.21), so its orientation does not change overall body shape substantially, resulting in too small of a change in the potential energy landscape.

We speculate that the animal flexed its head to sense obstacle properties in the explore + pitch phase. Groups of campaniform sensilla and sensory hairs embedded in the cockroach's pronotum can sense the magnitude, direction, and position of the terrain

reaction force [235]. The chordotonal organ in the animal's neck can detect the forces pushing against the head [140,236]. These could help the animal estimate the obstacle's physical properties (stiffness, surface friction coefficient, etc.) [237] and guide its adjustments to better traverse. We speculate that the occasional dynamically changing head flexion is a form of tactile sensing [145,148,152]. We observed that the animal seemed to hyperextend the head upward in order to find the top end of the stiff beam obstacles (to initiate climbing) and flexed the head downward in order to find a gap to move into.

In addition, we speculate that the animal flexed its head in the land phase (after the center of mass had passed the beams) to help its fore legs reach the ground to help propel forward, while its middle and hind legs were still interacting with the beams and were likely less effective at generating propulsion within the narrow gap. This is similar to cockroaches flexing the head to help fore legs reach the top surface when climbing a large step [223].

Although head flexion is not driven by the same muscle group as abdomen flexion or hind leg movement [238], it is possible that it can be indirectly triggered by the abdomen motion (e.g., via sensory feedback for coordination). Further analysis of the correlation between adjustments will test these possibilities.

2.7.2 Role of abdomen flexion

We speculate that the animal flexed its abdomen frequently in the roll and land phases to generate kinetic energy fluctuation to break resistive frictional and interlocking contact as it pushed through the beams when the body has rolled into the gap. Because the beam gap was narrow and barely larger than the animal body thickness (average body thickness not including legs is only 73% of gap width), the animal had to elevate its legs closer to the body to fit them within the gap. This made it difficult to generate thrust force

from the legs. Meanwhile, the spines and other asperities on the thorax, abdomen, and legs added resistance, similar to a cockroach crawling in a confined space [10]. This kinetic energy fluctuation from abdomen flexion helps the animal become unstuck and facilitates traversal (i.e., likely overcoming very small barriers on a very fine-grained potential energy landscape, if one considers the effects of these small features; see discussion in [31]).

2.7.3 Role of leg adjustments

We speculate that the animal spread its hind legs further outward to stabilize the pitched-up body against the beams in the pitch + explore phase and tucked in the depressed hind leg (the left one during body rolling to the right) to destabilize it to roll in the roll phase. Geometrically, the stable support polygon of the animal was formed among contacts between its hind feet and the ground and contacts between its head or thorax and the beams. In the explore + pitch phase, the animal spread its hind legs out widely, with a large distance between the two hind feet touching the ground, which increased the animal's roll stability (**Figure 2-13A**). We speculate that this helped the animal's pitched up body stay aligned to the gap rather than yaw and fall sideways under gravity. In the roll phase, as the animal tucked in its depressed hind leg, the support polygon shrank and roll margin of stability reduced (**Figure 2-13B**), and the roll stability reduced. These effects can be quantified by the potential energy landscape. The potential energy barrier from the pitch to the roll basin measures the difficulty of the transition. In the explore + pitch phase, further leg spreading increased the transition barrier, which helped the animal stay pitching up against the beams. During pitch-to-roll transition, tucking in a leg reduced the transition barrier and made rolling easier. We also observed that the animal spread out its elevated hind leg (the right

one during body rolling to the right) in the land phase. We speculated that this was to better engage with the ground to propel itself forward when its body was still in the gap.

Aside from leg sprawl, the differential leg uses also played an important role. We speculated that in the beginning of the roll phase the animal depressed one hind leg and elevated the other while keeping both feet on the ground to generate a roll torque. In the land phase, it elevated both hind legs closer to the body after the body has rolled into the gap, likely to reduce the resistance on the legs from the beams while pushing through.

2.7.4 Role of body flexibility

Our results further suggested that the flexibility from multiple body parts and articulated leg joints of the entire animal also reduces the efforts of locomotor transition and traversal [10,223]. The animal's body is more flexible and compliant than our rigid body model. This will likely result in a smaller beam flexion than estimated by the model and reduce the transition barrier. Soft, segmented exoskeleton structure also likely reduced interlocking and frictional resistance and facilitated traversal.

2.7.5 Likely involvement of sensory feedback control

Studies on insects negotiating large obstacles have revealed that the changes in kinematics are often modulated by sensory inputs. For example, when climbing large stairs, stick insects switch from using long to short steps when they have sensed a lack of substrate engagement [239]; when climbing a large step, cockroaches flex the head to help fore legs reach the top step surface when its head has sensed that it has risen above the step [223]. During traversal of cluttered beams in our study, the cockroach's adjustment to make the pitch-to-roll transition, which were absent when running on a flat ground, was almost

certainly driven by sensory input of its terrain-interaction. During traversal, it took the animal an average time of 1.3 ± 0.7 s to explore and pitch up against the beams before rolling occurred. This is well above the ~100 ms that cockroaches need to complete a feedback control loop (6-40 ms for the sensory delay [116] and 47 ms for neuromuscular delay [74]). We posit that the animal sensed the terrain and used this information to determine that pushing across was too strenuous and guide transitioning to the less strenuous roll mode. We have recently explored the feasibility of this strategy in a simple simulated robotic physical model [237].

2.7.6 Future work

Future work should test the speculated mechanisms of how each kind of adjustment facilitates the observed locomotor transition. (1) To understand whether and how the flexing head facilitates terrain sensing and how to take advantage of this, we can build a robot with head flexion and force sensing [227] and study it systematically with and without feedback control using the sensed forces. (2) To understand whether and how the abdomen flexion helps the animal become unstuck, we can build a robot with a flexing abdomen (or tail [111]) to test if the flexing of the massive lateral part helps in beams traversal. (3) To test whether leg adjustment indeed generates a roll torque, we can add highly sensitive yet low-cost force sensors [240,241] to the ground in front of the beams to measure the ground reaction force on each foot.

To further understand the neural mechanisms involved in such cluttered large obstacle traversal, we can measure the animal's sensory neural signals [116,242] and muscle activity (i.e. electromyogram) [74,224] and alter motor activation signal to change adjustments and test their effect on the body dynamics [225,243]. The first challenge is to

identify what sensors are involved in these cluttered adjustments for large obstacle traversal. Like other insects, cockroaches should have many sensors that can obtain information about the terrain [140,141,222,235], including: (1) visually observe the geometry of the terrain. (2) use exteroceptors like tactile hairs to sense the position of an object; (3) proprioceptors to sense relative position/velocity between joints to infer object position; and (4) campaniform sensilla to detect force and torque exerted on exoskeleton and joints. A first step to identify the relevant sensing modalities is to disable some of these sensing sources, such as blinding the eyes [244] and disabling the campaniform sensilla [245], and observe changes in locomotor behavior and performance. Based on animal observations, computational modeling of neural control (such as in [246]) may be fruitful for understanding feedback principles governing body and appendage adjustments to traverse cluttered large obstacles. In addition, it may be interesting to study whether animals perform active sensing [139,145,147,153,247–249] in the less-considered modality of contact force sensing.

Our case study illustrated how to use fine-grained potential energy landscape modeling to understand locomotor-terrain interaction that involves adjustments of more body and appendage degrees of freedom, which may lead to the discovery of attractive basins that result in distinct nuanced locomotor modes (see discussion in [31]). Given these advancements, the potential energy landscape modeling still does not fully describe system dynamics, as it only describes conservative forces of the system that can be expressed as gradients of the potential energy landscape. Future work should systematically measure and model non-conservative and random forces and add them to make the modeling approach predictive. These measurements and a predictive potential energy landscape

theory capturing dynamics will reveal how the animal generates propulsive forces and torques to overcome resistive ones in order to destabilize itself from undesired modes (basins) of attraction and steer into the desired modes (basins) and how this process can be guided by terrain force sensing [237].

2.8 Supplementary Information

2.8.1 Minimal mechanical energetic cost in pitch and roll mode

To quantify how strenuous the pitch and roll modes are, we estimated the minimal mechanical energetic cost of the pitch or roll mode by calculating the maximal potential energy increase of the system during the traversal process using either mode.

For the pitch mode, we assumed that the animal kept a horizontal body orientation (zero body pitch and roll, neglecting legs), moved forward in the middle of the two beams with the lowest point of the body always contacting the ground, and pushed the beams down to traverse. The maximal potential energy increase of 7.9 mJ occurred when both beams deflected by nearly 90°.

For the roll mode, we assumed that the animal started with a horizontal body orientation and rolled by 90° to move through between the beams without deflecting them, with the lowest point of the body always contacting the ground. The maximal potential energy increase of 0.2 mJ occurred when the body roll was 90°.

2.8.2 Pitch-to-roll transition barrier

The pitch-to-roll transition barrier can be calculated from the potential energy landscape model, and it is a function of the forward position x [31]. In our previous study that used a simple ellipsoid to model the animal, when traversing beams of K = 1.7

mN·m·rad^{-1}, the pitch-to-roll transition barrier was 0.04 mJ at $x = -21$ mm where the animal was observed to transition [31] (**Figure 2-6A, iv**), and it was 0.0021 mJ at $x = -13.6$ mm. In this study that used a refined animal model, when traversing beams of K = 2.5 mN·m·rad^{-1}, the pitch-to-roll transition barrier was 0.052 mJ at $x = -21$ mm, and it was 0.0027 mJ at $x = -13.6$ mm where the animal transitioned. These similar values between the two studies demonstrated that our potential energy landscape approach is consistent and useful either with the simplest or refined animal model.

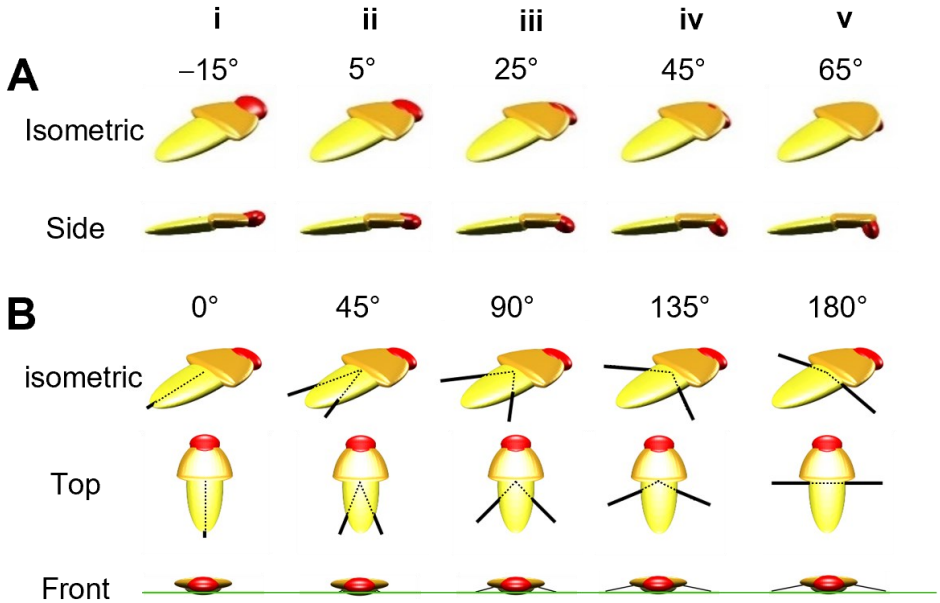

Figure 2-11: Example variation of head flexion and total leg sprawl to test the use of head and leg adjustments in potential energy landscape model. (A) Head flexion. (B) Total leg sprawl. Green line in (B) front view is leg height = −5 mm.

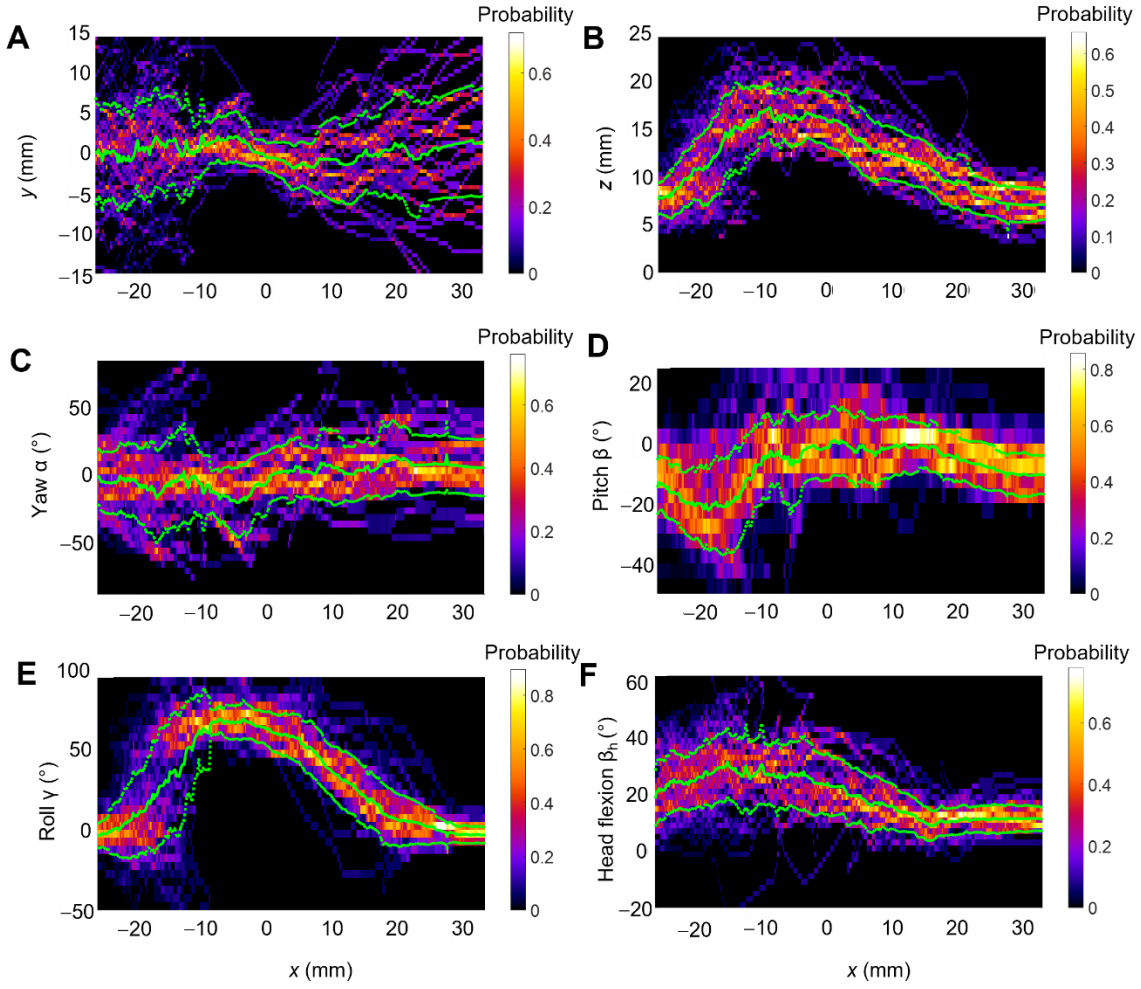

Figure 2-12: Average trajectory as a function of forward position *x*. (**A**) Lateral position *y*. (**B**) Vertical position *z*. (**C**) Yaw α. (**D**) Pitch β. (**E**) Roll γ. (**F**) Head flexion β_h. Solid and dashed green curves are mean ± s.d. from averaging data of all trials. Each column of the heat map is a normalized histogram showing probability distribution of the data (sum of each column is 1) at corresponding forward position *x*.

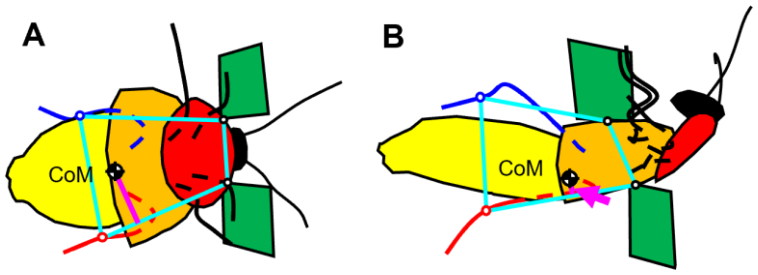

Figure 2-13: Representative support polygon evolution from top view during pitch-to-roll transition. (**A**) Explore + pitch phases. (**B**) Roll phase. Cyan closed shapes show support polygons, and magenta lines show the distance from center of mass (CoM) to nearest lateral edge of the support polygon, which measures roll stability. In (**B**), the distance is small and indicated by a magenta arrow.

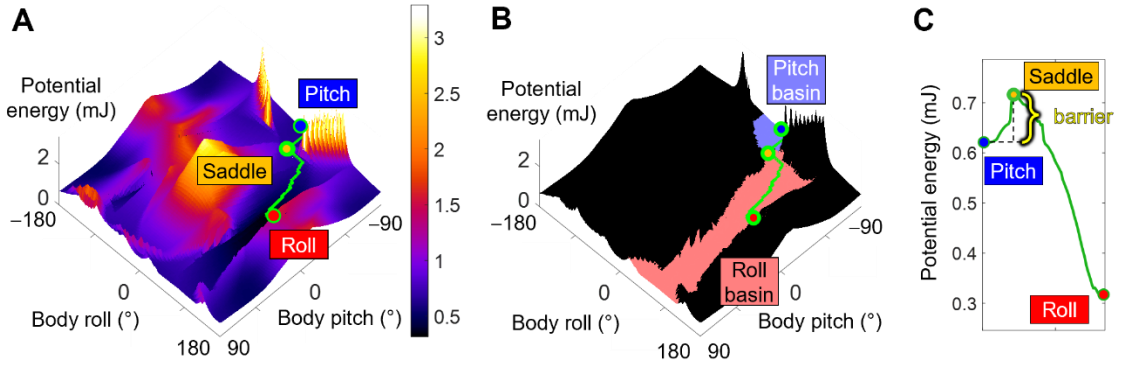

Figure 2-14: Demonstration of breath-first search result on potential energy landscape. (**A**) Potential energy landscape pitch-roll cross section at $x = 0$ along the average animal trajectory, with hind legs neglected. Blue and red dots are pitch and roll local minima, respectively. Orange dot is saddle point. Green curve is imaginary route obtained from parent backtracking (Section 2.5.11). (**B**) Basins identified from breath-first search. Blue and red areas are pitch and roll basins, respectively. Boundary of basins is iso-height contour with the same potential energy as saddle point. Black area is rest of landscape. (**C**) Potential energy along imaginary route. Potential energy barrier is increase in potential energy from pitch minimum to saddle point. Note that imaginary route is only for defining saddle point, and during transition, animal did not necessarily start from a local minimum or transition by crossing saddle point.

Table 2-1 Ranges and increment of landscape variation and dimension collapse protocol

Variable	Unit	Min	Max	Increment	Dimension collapsing protocol	
					Pitch-roll cross section	Yaw cross section
Forward position x	mm	–26	33	0.2	Not collapsed	Not collapsed
Lateral position y	mm	–3	3	1	Follow average trajectory	Follow average trajectory
Vertical position z	mm	z_{min}	z_{min} + 15	1	Minimize potential energy	Minimize potential energy
Yaw α	deg	–90	90	5	Follow average trajectory	Not collapsed
Pitch β	deg	–90	90	2	Not collapsed	Follow average trajectory
Roll γ	deg	−180	180	2	Not collapsed	Follow average trajectory
Head flexion β_h	deg	–25	65	5	Not collapsed or follow average trajectory	Not collapsed
Abdomen flexion β_a	deg	7	7	-	-	-

z_{min}: vertical position z when the body touched the ground.

Table 2-2 Frequently used averaged variables and range

Variable	Time range	Measured value	Used value
Forward position x	Pitch-to-roll transition	−13.6 ± 4.4 mm	−13.6 mm
Maximal leg length	Explore + pitch and roll phase	27 ± 2 mm	27 mm
Temporal averaged abdomen flexion β_a	Approach phase	7° ± 4°	7°
Head flexion range β_h	Whole trial	[–24°, 64°]	-
Temporal averaged head flexion β_h	Approach phase	15° ± 4°	15°
Temporal averaged leg height	Explore + pitch phase	–5 ± 3 mm	–5 mm
Maximal total leg sprawl ϕ_T	Explore + pitch phase	156° ± 21°	160°
Minimal total leg sprawl ϕ_T	Roll phase	21° ± 17°	20°
Kinetic energy fluctuation	Explore + pitch and roll phase	0.01 ± 0.01 mJ	0.01 mJ
Temporal averaged forward position x	Explore + pitch phase	–20 ± 3 mm	–20 mm

Chapter 3 Sensing environmental interaction physics to traverse cluttered obstacles

This chapter was posted as a preprint entitled *Sensing environmental interaction physics to traverse cluttered obstacles* authored by Yaqing Wang, Ling Xu, and Chen Li on *arXiv* [227]. We re-used the article in this chapter with slight changes of the format under CC BY 4.0 and with permission from all authors.

3.1 Author contributions

Yaqing Wang and Chen Li designed research; Yaqing Wang performed research; Ling Xu contributed new methods; Yaqing Wang analyzed data; and Yaqing Wang and Chen Li wrote article.

3.2 Acknowledgment

We thank Ratan Othayoth for sharing CAD files for previous robot system design and discussion on experiment conduction; Xiao Yu for help in assembling the experimental setup and preliminary testing; Qihan Xuan for discussion on experiment design and conduction; Shai Revzen for discussion on experiment design and saddle finding algorithms; Ioannis Kevrekidis, and Anastasia Georgiou for discussions on saddle finding algorithms; Noah Cowan, Jean-Michel Mongeau, Jeremy Brown, and Mitra Hartmann for discussion on active sensing.

This work was supported by a Beckman Young Investigator Award from Arnold and Mabel Beckman Foundation for Chen Li, a Career Award at the Scientific Interface from Burroughs Wellcome Fund for Chen Li, a Bridge Grant from Johns Hopkins

University Whiting School of Engineering for Chen Li, and a Research Experience for Undergraduates in Computational Sensing and Medical Robotics (CSMR REU) from National Science Foundation for Ling Xu and Chen Li.

3.3 Summary

When legged robots physically interact with obstacles in applications such as search and rescue through rubble and planetary exploration across Martain rocks, even the most advanced ones struggle, possibly because they lack a fundamental framework to model the robot-obstacle physical interaction similar to the artificial potential fields for obstacle avoidance. To remedy this, recent studies established a novel framework—potential energy landscape modeling—that explains and predicts the destabilizing transitions across locomotor modes from physical interaction between robots and obstacles, and governs a wide range of complex locomotion. However, this framework was previously confined to the laboratory due to a lack of methods to obtain the potential energy landscape in unknown terrains. Here, we explore the feasibility of introducing this framework to such terrains. We show that a robot can reconstruct the potential energy landscape for unknown obstacles by measuring the obstacle contact forces and resulting torques. To elaborate, we present a minimalistic robot capable of sensing contact forces and torques when propelled against a pair of grass-like obstacles. Despite the forces and torques not being fully conservative, they match the potential energy landscape gradients, and the reconstructed landscape matches the ground truth calculation. In addition, we find that using normal forces and torques and head oscillation inspired by cockroach observations further improves the estimation of conservative forces and torques. Our study may inspire future research in which free-running robots achieve low-effort, prior-free traversal of clustered, large obstacles in real-world applications by sampling contact forces and torques and reconstructing the landscape around its neighboring states in real time.

3.4 Introduction

Sensing their surrounding environment helps animals and robots move through the complex world. Animals (including humans) combine vision and other sensory modalities (mechanosensing, chemosensing, etc.) to sense, plan, and control their interaction with obstacles to *traverse* them [250–252]. By contrast, robots heavily rely on visual information to navigate complex environments while *avoiding* obstacles [253] (**Figure 3-1**, top row). For example, robots often use long-ranged visual sensing (e.g., cameras, LiDAR) (e.g., **Figure 3-1A**) to create a geometric map of the environment (e.g., **Figure 3-1B**). Using this map, the robots could construct an artificial potential field [95,96], with its goal modeled by a global minimum and obstacles modeled by high potential regions. The robots then plan and follow a gradient descent path towards the goal while avoiding the obstacles [97] (**Figure 3-1C**), often transitioning between various locomotor modes (e.g., **Figure 3-1D**).

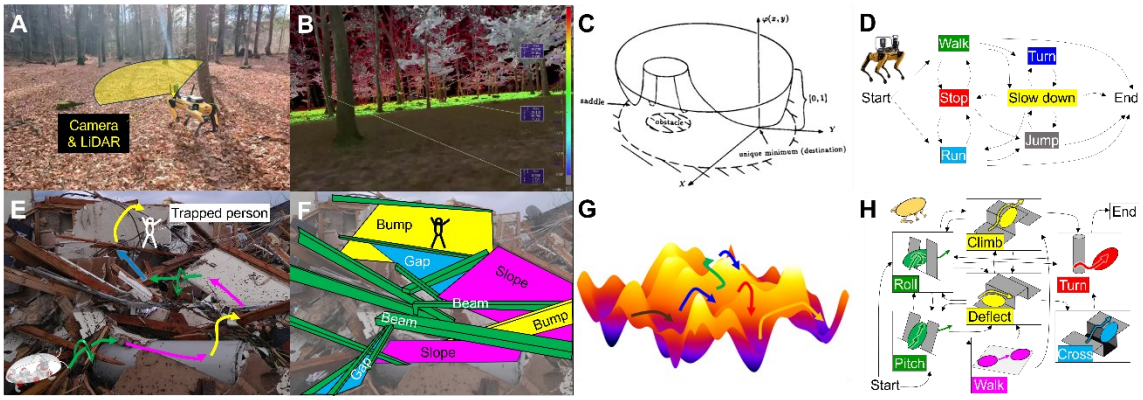

Figure 3-1: Envisioned potential energy landscape approach enabling legged obstacle traversal analogous to artificial potential field enables obstacle avoidance. (**A**) A legged robot leverages vision-based sensory to navigate a flat, sparse forest terrain with scattered trees. (**B**) Geometric map scanned using LiDAR from the robot in (A). (**C**) Artificial potential field approach for obstacle avoidance. (**D**) Multi-pathway driving

transitions to avoid obstacles. (**E**) Envisioned traversal of cluttered large obstacles to be enabled (e.g., earthquake rubble for search and rescue). (**F**) Identified locomotor challenges from large, diverse obstacles, whose environmental interaction physics needs to be sensed to enable robust traversal. (**G**) Potential energy landscape approach for obstacle traversal. (**H**) Multi-pathway locomotor transitions to traverse via sensing and controlling physical interaction with obstacles. (A, B) Image courtesy of Intuitive Robots on YouTube. (C, E, G, H) Adapted from [26,31,95].

However, this vision-based approach to robot navigation fails in terrains with densely cluttered (spacing ~ body size), large (~ body size) obstacles, where a collision-free trajectory to the goal simply may not exist. Instead, a robot must physically interact with obstacles and/to generate appropriate forces and torques. However, a lack of sensing physical interaction with obstacles leads to poor control of locomotion through them. Also, most motion planning methods for avoidance (e.g., using artificial potential fields) cannot plan effective paths for robots to physically interact with obstacles to traverse. These challenges have diminished the usefulness of robots in many important applications, such as search and rescue in rubble [27] (**Figure 3-1E**), environmental monitoring in mountain boulders and forest debris [28], and planetary exploration through large Martian and Lunar rocks [29].

To traverse densely cluttered terrains, a robot must sense not only environmental geometry but also physical interaction, so that it can control its self-propulsion to generate appropriate forces and torques to overcome obstacles, planning and following least-resistant paths guided by environmental models that take into account physical interaction as well as geometry [26,31]. Towards this vision, our lab recently established a new approach to modeling environmental interaction, using potential energy landscapes

resulting from physical interaction of robots (and animals) (**Figure 3-1**, bottom) with a diversity of large obstacles that present distinct locomotor challenges (e.g., **Figure 3-1F**) [26,31,33–36,226]. Analogous to artificial potential fields for geometry-based obstacle avoidance, these real potential energy landscapes (**Figure 3-1G**) provide a physics-based foundation for robots to conceptualize locomotor transitions (**Figure 3-1H**) to traverse (for a review, see [26]).

Specifically, a self-propelled robot's (or animal's) body physically interacts with obstacles, resulting in a potential energy landscape (the system's real potential energy as a function of body 3-D position and rotation), with attractive basins of stability separated by potential energy barriers (**Figure 3-1G**). Due to continual self-propulsion breaking continuous frictional contacts, the system's state tends to settle to these basins. As the robot (or animal) is attracted to each stability basin on the landscape, its motion emerges as a distinct locomotor mode (which often involves large body rotations, not just translation) (**Figure 3-1H**). Given the limited propulsive forces and torques of the robot (or animal), some modes can lead to traversal, while others lead to being trapped. Thus, to traverse, the robot (or animal) must propel to destabilize itself from attraction by the basins/modes of entrapment and overcome potential energy barriers to transition to the basins/modes that lead to traversal. Because these barrier-crossing transitions are highly strenuous (requiring the generation of large propulsion and work compared to the robot's (or animal's) capacity), it is beneficial to sense the potential energy landscape, find saddles (lowest points) on the barriers, and cross the barriers via saddles, as doing so has the least resistance and requires the least effort [26].

Our lab's recent simulation study supports the usefulness of obstacle contact force and torque sensing in real robots [237]. By sensing the total obstacle interaction force from a known type of obstacle, a simulation robot can escape from entrapment in a more strenuous locomotor mode and transition to a less strenuous mode, thereby traversing with less effort or even enabling traversal given limited propulsion.

Given these advances in modeling environmental physical interaction in densely cluttered terrains using potential energy landscapes, as well as simulation evidence of the usefulness of sensing physical interaction, how to sense the potential energy landscape is unsolved. A system's potential energy landscape gradients are the conservative forces and torques, so, to sense the potential energy landscape, the robot must sense forces and torques. However, obstacle contact forces and torques also have contributions from non-conservative forces (frictional forces, damping forces, inertial forces, etc.) and torques. Yet, our lab's previous works demonstrated that the system's locomotor mode transition dynamics are strongly governed by the potential energy landscape in densely cluttered terrains [26]. This suggests that the conservative forces and torques (landscape gradients) dominate, and the non-conservative forces and torques are small. In other words, the total contact forces and torques should well approximate the conservative forces and torques. Thus, we hypothesized that the potential energy landscape can be reconstructed from obstacle contact forces and torques.

Testing our hypothesis requires a robot with custom onboard sensors to measure obstacle contact forces and torques on its body. Many robots already equipped one force/torque sensor in each leg to sense foot–ground interaction [158,159], which may help stabilize upright running and walking on the ground with small unevenness (<< leg length)

[82,106,254]. However, traversing cluttered large obstacles (i.e., terrain unevenness ~ leg length) requires sensing the more general body–terrain interaction. To traverse densely cluttered terrain, the robot transitions across locomotor modes with large body rotations, changing where the body contacts obstacles. Sensing every contact requires multiple sensors distributed over the body. Moreover, self-propulsion during interacting with cluttered large obstacles always induces continual collisions with the obstacles [26], where sophisticated commercial sensors capable of measuring both forces and torques (e.g., ATI F/T sensors, OnRobot HEX-E series, FUTEK LCF series) are too fragile for this purpose (and too expensive to have multiple ones). Recent studies began to address this problem by developing flexible sensory arrays [144,161–165]. However, these sensors only provide 1-D force (normal force) sensation, have long sensory cycles (for sequentially measuring a voltage on each cell), have obvious dead zones and delay, and require substantial effort and special equipment to manufacture. All these challenges encouraged us to develop new custom sensors and sensing strategies.

Here, we take the next step towards our vision by creating a robot equipped with custom distributed force and contact sensors on its body for sensing obstacle contact forces and torques, and using the robot to test how well the potential energy landscape can be estimated from the sensed forces and torques. Specifically, the robot senses contact force and position with each obstacle from two kinds of custom sensors, and calculates the resulting torque. We controlled the robot to traverse cluttered obstacles with prescribed trajectories over a broad range of relevant states (including both transitions and rotations) while sensing forces and torques, and tested how well the sensed obstacle contact forces and torques matched the landscape gradients and how well the potential energy landscape

was estimated. We also tested whether using normal forces (i.e., eliminating friction) and torques improved the landscape gradient estimation.

Attempting to further improve the landscape gradient estimation, we considered robotic active sensing behavior. It is well-known that many animals use active sensing behavior when physically interacting with obstacles [226,255]. However, the mechanics of how this modulates the sensed signal and benefits obstacle estimation are not fully understood. To begin to understand animal behavior and learn how to apply this to robots, we controlled the robot to make a feedforward motion similar to a prospective active sensing motion observed from an animal, and tested how this modulates the sensed forces and torques.

3.5 Results

3.5.1 Model system

Our study focuses on the model system of grass-like beam obstacle traversal, building on our lab's previous works [31,36,226] (**Figure 3-2A, B**). To traverse relatively stiff, cluttered beam obstacles with gaps narrower than its body width, the discoid cockroach or a cockroach-inspired robot often transitions from a strenuous pitch mode (pushing forward across beams with large body pitching), which requires a large propulsive force and mechanical energy cost (**Figure 3-2A, B**, blue), to a much easier roll mode (rolling into beam gaps and maneuvering through), which requires a much smaller propulsion and mechanical energy cost (**Figure 3-2A, B**, red). When the trajectory of the system (**Figure 3-2C**) is viewed on the potential energy landscape over the animal's or robot's body roll-pitch space (**Figure 3-2D**), this pitch-to-roll transition (**Figure 3-2C, iii'**)

requires escaping the entrapment in a pitch basin (**Figure 3-2D, ii, iii**, blue), crossing a potential energy barrier, and reaching a roll basin (**Figure 3-2D, ii, iii**, red). These basins emerge and morph as the body moves forward, changing the pitch-to-roll transition potential energy barrier (**Figure 3-2D, ii, iii**, gray dashed curve).

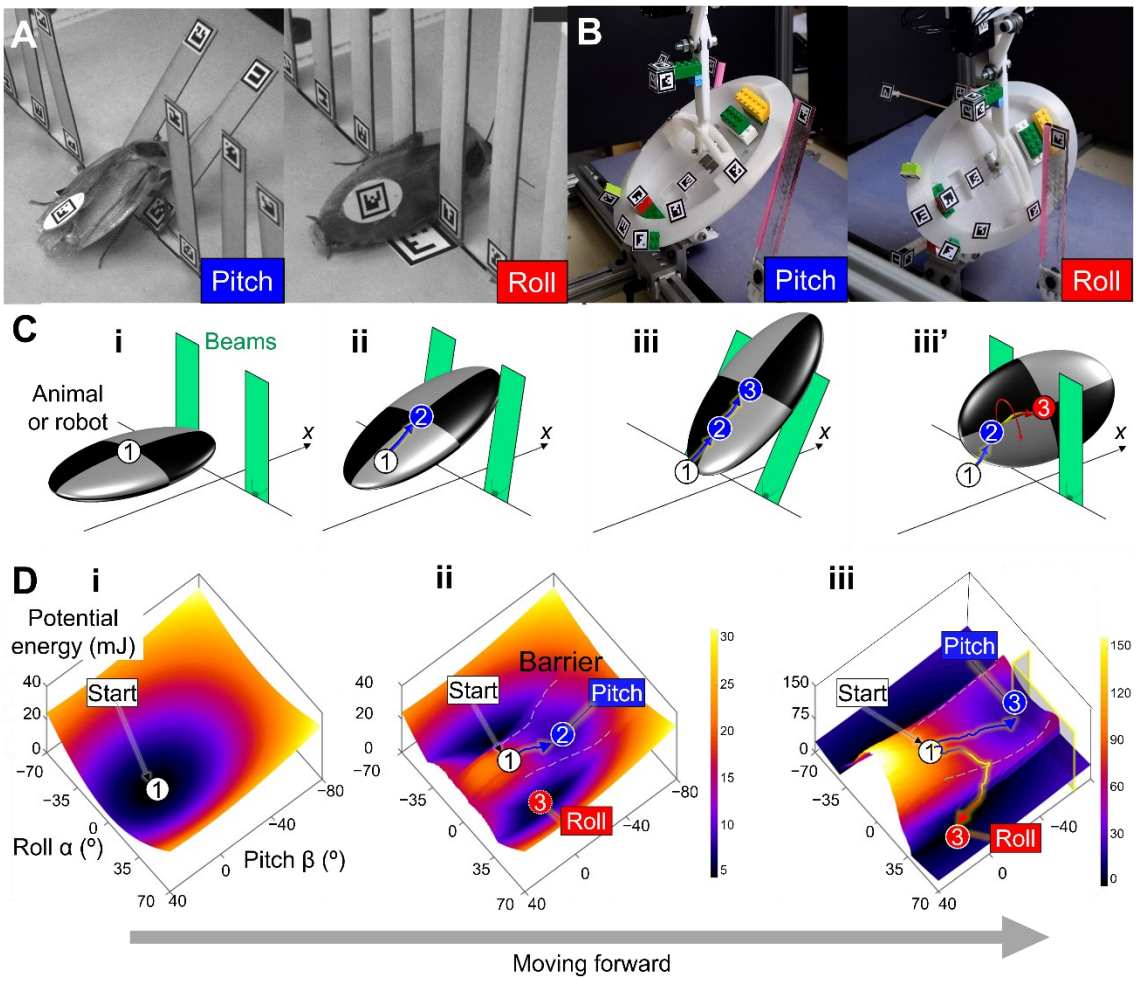

Figure 3-2: Model system of cluttered beam obstacle traversal. (**A**, **B**) When (A) a cockroach and (B) a minimalistic, feedforward robot traverse cluttered grass-like beams with small gaps (< body width), they either use a strenuous pitch mode to push across (left, blue) or a less strenuous roll mode, where after rolling they maneuver through the gap (right, red) [31]. (**C**) Schematics of animal or robot's body interacting with two beams. The body was an ellipsoid (checkered). The beams were rigid rectangle plates (green) attached to the ground with torsional springs at the bottom. After coming close to the beams (i), the

body interacts with beams either using the pitch mode (ii, iii) or transitioning to the roll mode (iii'). (**D**) Snapshots of the potential energy landscape over roll-pitch (α-β) space. Before physically interacting with the beams (i), the landscape has a global basin. During interaction (ii, iii), a pitch basin and left- and right-roll basins emerge on the landscape, separated by potential energy barriers (gray dashed curves). The start (running), pitch, or roll locomotor mode (white, blue, or red circles in (C)) emerges as the system is attracted to the global, pitch, or roll basin (white, blue, or red circle in (D)), separately. Arrows on the landscape show examples of state trajectory. Adapted from [31].

3.5.2 New robot capable of obstacle contact force and torque sensing

To systematically study obstacle contact force and torque sensing and landscape reconstruction, we iteratively developed (**Figure 3-10**) a minimalistic, cockroach-inspired robot (**Figure 3-3**) with the ability to sense contact forces and torques while moving forward at a constant speed, with prescribed body roll and pitch that was varied across trials.

Our robotic system is upgraded from the previous sensor-less robot for studying the passive dynamics of the system [31], consisting of a robot with an outer shape similar to the discoid cockroach traversing a pair of deflectable beams (**Figure 3-3A**), mimicking the cockroach traverses grass-like obstacles. Upon the previous design, the robot was further cropped from a full shape (**Figure 3-3B**, translucent green) to only keep the regions that contact the beams. To sense contact forces and torques, we separated the robot into body and shells, added customed 3-D force sensors between the body and shells (**Figure 3-3B**, magenta), and added contact sensors to the shell surface (**Figure 3-3B**, yellow and orange). The body was driven forward (**Figure 3-3A**, white) by an external translational motor (**Figure 3-3B**, black) to emulate the forward propulsion generated by legs, but without adding legs. For systematically measuring obstacle contact forces and torques over a broad

range of roll and pitch, which are needed to reconstruct the potential energy landscape, we added two motors (**Figure 3-3B**, red and blue) that rigidly attached to the robot rotational axes (**Figure 3-3A**, red and blue), to prescribe body roll and pitch.

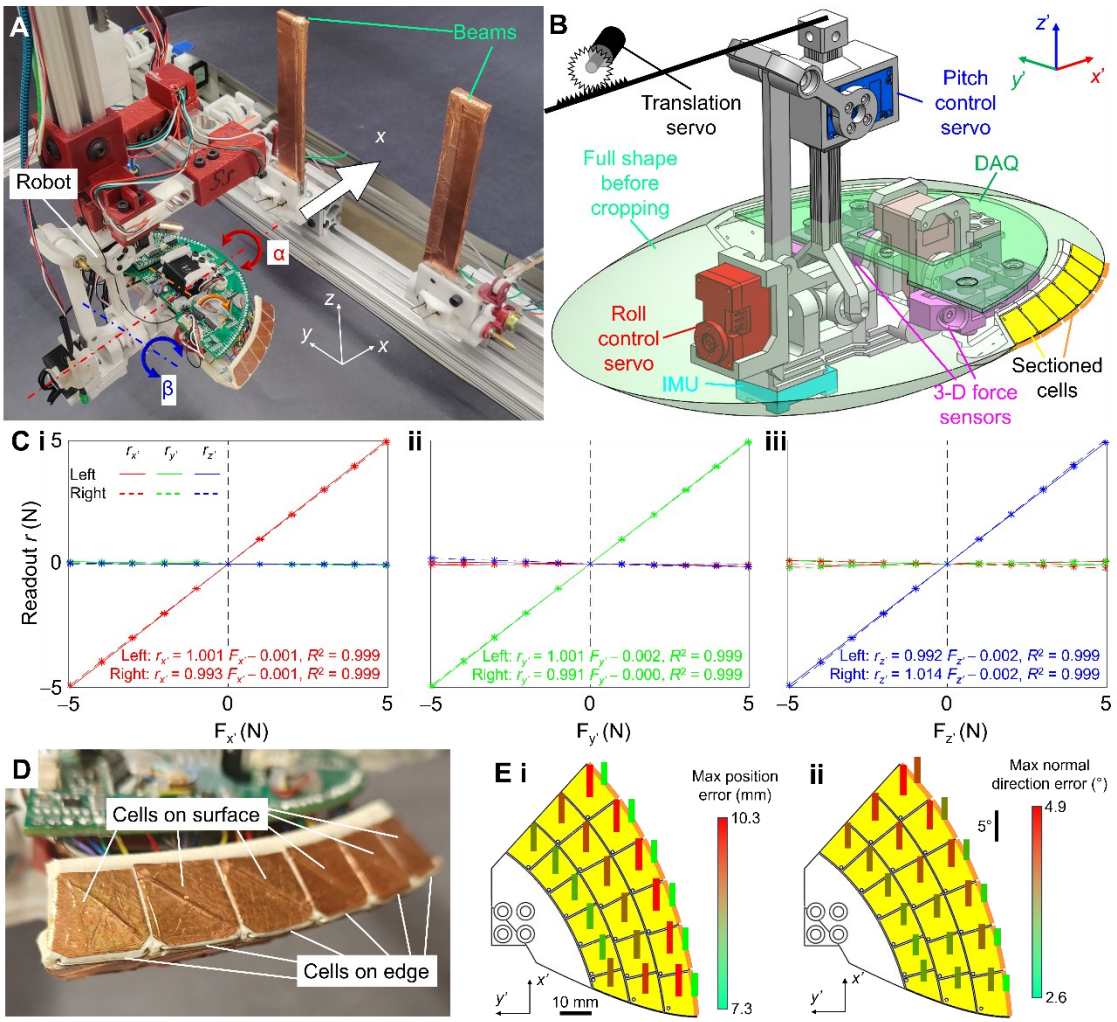

Figure 3-3: New robotic system for sensing obstacle contact forces and torques. (**A**) Photo of the system consisting of a robot with force and contact sensors and two beams. *x*, *y*, and *z* axes show the lab frame. White, red, and blue arrows show translation in fore-aft (*x*), and rotation in roll (α) and pitch (β) directions, separately. (**B**) CAD model of the robot. The shells were cropped from a full shape (translucent green). The robot is propelled forward along +*x* direction at a constant speed (white arrow in (A)) by a servo motor via gear-rack mechanism (black). Body roll and pitch (red and blue arrows in (A)) are

controlled by servo motors (red and blue). To sense contact forces and torques on the body, 3-D force sensors (magenta) and touch sensory cells (yellow and orange) are added. To verify the robot rotation, an inertial measurement unit (IMU, cyan) is added. *x*'-, *y*'-, and *z*'- axes show the robot body frame. (**C**) Custom 3-D force sensor calibration. Curves show the sensor readout *r* (red: *x*', green: *y*', blue: *z*') as a function of applied force *F* in body (i) *x*'-, (ii) *y*'-, and (iii) *z*'- axes, separately. Solid and dashed curves are from the left and right sensors, separately. It is hard to differentiate the left and right curves, because the two sensors are highly identical. Formula shows linear regression results between sensor readout *r* and applied force *F* in the same axes, which all show high linearity ($R^2 = 0.999$). (**D**) Touch sensory cells on the surface and edge, detecting contact positions. They enable contact torque calculation when combined with force sensing. (**E**) Maximal (i) position and (ii) normal direction error on each touch-sensitive cell. The pattern of cells is from robot bottom view. *x*'- and *y*'-axes show robot body frame. Because the left and right shells are mirrored, only the right shell is shown. Because the cells above the edge are mirrored from those beneath the edge, only the bottom cells are shown. Bar rooting at the center of a cell shows error on that cell, whose height and color shows error magnitude. With a careful cell pattern design, the maximal position and normal direction errors are small and roughly constant across the shell surface.

3.5.3 Contact force and torque sensor design and calibration

To sense obstacle contact forces and torques, we added force and contact sensors to the robot. Specifically, to measure the contact force with either beam, the robot's outer shell was separated into left and right parts. We connected each piece of shell with the body frame via a custom small (58 mm × 44 mm × 22 mm), low-cost 3-axis force sensor (**Figure 3-3B**, magenta), each consisting of three load cells serially connected and orthogonal to one other. Each load cell provided a separate force measurement along the robot body *x*'-, *y*'-, or *z*'-axis, with a labeled range of ± 20 N and precision of ± 0.004 N, which suited our experiment where the contact forces were < 10 N. A force calibration (**Figure 3-3C**) shows

that both left and right custom force sensors have high linearity between their readouts and applied forces in the same body frame axes ($R^2 = 0.999$) and small crosstalk between their readouts and applied forces in different axes (< 4%). See Section 3.8.4 for force sensor calibration method. To get contact torque, we detected the contact position with each beam by attaching sectioned touch-sensitive cells (**Figure 3-3D**) made of copper tape [256] on the shell surface (**Figure 3-3B,** yellow) and metal wires (0.5 mm in diameter) on the shell edge (**Figure 3-3B,** orange), and calculated the contact torque combining the contact force and position data. The pattern of the touch sensory cell distribution was carefully designed so that the measurement resolutions of contact position and normal direction were within small thresholds (i.e., position resolution < 11 mm, normal direction resolution < 5°, see Section 3.7.3 for definitions) (**Figure 3-3E**), which is achieved by gradually revising touch sensor pattern design in the iterative development process (**Figure 3-10**).

3.5.4 Trends of contact forces and torques matched with the landscape gradients

To estimate the potential energy landscape over the state space (x-α-β, corresponding to fore-aft position, roll, and pitch angles) in the model system of beam traversal, we let the robot systematically vary the fore-aft position and roll and pitch angles. Before each trial, the roll and pitch angles were set to the desired values, and then the body was driven forward to traverse the beam obstacles, while the force sensors recorded the 3-D contact forces (**Figure 3-4A**, red) and the contact sensors recorded the contact positions with each beam on the body (**Figure 3-4A**, orange) at 50 Hz. Contact roll and pitch torques from each beam were calculated based on contact forces and positions (see Section 3.7.3).

We observed several trends of the measured forces and torques (**Figure 3-4B, C**) in the x-α-β space, namely, the fore-aft force F_x, roll torque T_α, and pitch torque T_β. (1) The

fore-aft force was always negative (averaged F_x = –2.0 ± 0.4 N) when the robot contacted the beams. (2) For a small roll angle (α = 0° – 30°), the roll torque was near-zero (averaged T_α = 7 ± 17 N·mm). (3) For a large roll angle (α = 35° – 40°), the roll torque was positive (maximal T_α = 98 ± 66 N·mm) at first, but then suddenly reduced to negative (minimum T_α = –41 ± 45 N·mm). (4) For a small pitch angle (|β| = 10° – 20°), the pitch torque was positive (maximal T_β = 27 ± 22 N·mm) at first, but then reduced to negative (minimum T_β = –98 ± 46 N·mm). (5) For a large pitch angle (|β| = 25° – 40°), the pitch torque was always negative (averaged T_β = –45 ± 20 N·mm).

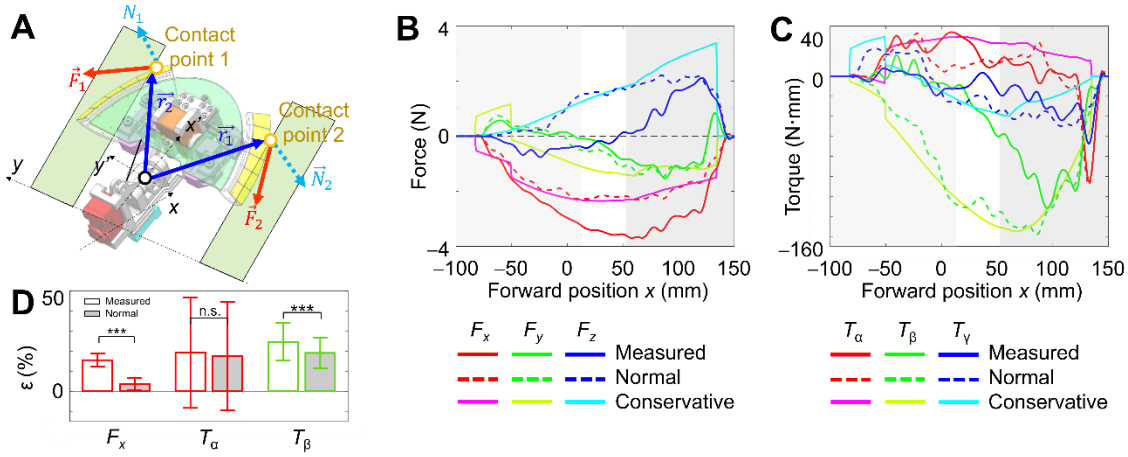

Figure 3-4: Estimating the potential energy landscape gradients using measured contact forces and torques. (**A**) Schematic of force analyses. The robot directly obtained the measured contact forces F_i (red arrows) from custom 3-D force sensors and contact positions (orange points) from touch sensors. Normal forces N_i (cyan arrows) were defined as the component of contact forces along surface normal directions measured by the contact sensors. Force arms r_i (blue arrows) were the distance from the geometric center to the contact point. Measured or normal torques were the cross of force arms and measured ($T_i = r_i \times F_i$) or normal forces ($T_{i,N} = r_i \times N_i$), separately. (**B** and **C**) Measured, normal, and conservative contact (B) forces and (C) torques as functions of forward position x from a representative trial. Light and dark gray show where contacts with both beams are surface

and edge contact cases, separately. (**D**) Relative error ε of using fore-aft force Fx, contact force roll torque T_α, and pitch torque T_β as the landscape gradients in surface contact cases. White and gray bars show measured and normal forces/torques, separately. See Section 3.5.7 for definition of normal forces/torques. Bars and error bars are means ± 1 standard deviation of the average relative error of all average trials. *** $P < 0.001$, n.s.: not significant $P > 0.05$, Student's t-test.

Here, we further describe the evolution of the potential energy landscape as the robot traversed the beam obstacles (**Figure 3-2D**) to help understand how these observed trends matched those expected from the landscape. We defined the potential energy landscape similarly as in [31] (see Section 3.7.1). Before encountering the beams, the system's potential energy was simply the robot's gravitational potential energy. Because the robot was bottom-heavy, the potential energy landscape formed a global basin in the roll-pitch (α-β) section, whose global minimum was at zero roll and zero pitch (i.e., the horizontal posture, α = β = 0°) (**Figure 3-2D, i**). As the robot encountered and interacted with the beams, the average potential energy landscape in α-β section lifted, because more beam elastic energy was stored, and the system potential energy increased. The global basin evolved into a "pitch" basin, whose local minimum was at a negative pitch (|β| = 0° – 70°) and zero roll. At the same time, two "roll" basins emerged, whose local minima were at near-zero pitch and a positive or negative roll (around α = ± 50°) (**Figure 3-2D, ii, iii**). The pitch and roll basins separated by barriers (around α = ± 35°) (**Figure 3-2D, ii, iii**).

Comparing the trends of measured forces and torques with landscape evolution, we found that the direction of contact forces and torques along x, α, and β directions were always inverse to the corresponding landscape gradients. Specifically, (1) the system potential energy increased with x (**Figure 3-2D**), suggesting a positive gradient along the

x direction. (2) The landscape gradients were near-zero when the robot's state fell in the pitch basin and was near the local minimum (**Figure 3-2D, ii, iii**, blue) at a small roll angle. (3) The landscape gradient along α direction was initially negative when the robot's state was in the roll basin to the +α side of the barrier (**Figure 3-2D, ii, iii**, red) at a large roll angle. (4) The landscape gradient along β direction was initially negative when the robot's state was to the −β side of the local pitch or roll minimum. As the robot moved forward, if |β| was small, the landscape gradients along the β direction changed to positive as the landscape minimum shifted along −β direction and passed the robot's state.

The match between the trends of forces and torques and the landscape evolution suggested that the contact forces and torques were strongly related to the corresponding landscape gradients.

3.5.5 Measured contact forces and torques roughly matched landscape gradients

We further quantitatively compared the measured contact forces and torques with the conservative forces and torques (i.e., potential energy landscape gradients) from modeling, and found that they roughly matched each other (**Figure 3-4B, C**, measured vs. conservative). The measured forces and torques matched conservative ones with a small relative error of $\varepsilon_x = 15\% \pm 3\%$ in the *x* direction, $\varepsilon_\alpha = 19\% \pm 28\%$ in the α direction, and $\varepsilon_\beta = 25\% \pm 9\%$ in the β direction (**Figure 3-4D**, measured).

These results showed that, despite not being fully conservative, the measured contact forces and torques enabled potential energy landscape gradient estimation. We speculated that the mismatch between the sensed forces and torques and the landscape gradients was caused by friction, collisions, inertial effects, etc. See Section 3.8.2 for

theoretical proof that the contact forces and torques should be the landscape gradients without these factors.

3.5.6 Reconstructed potential energy landscape matched with ground truth calculation

To test whether the measured contact forces and torques can infer the potential energy landscape, we performed Helmholtz decomposition [257] on them to reconstruct the landscape (see Section 3.7.5). We found that the reconstructed landscape (**Figure 3-5A**) and its gradients matched the ground truth calculations from modeling (**Figure 3-5B**) with a low relative error of ε_{PE} = 14.0% in potential and ε_{Grad} = 21.6% in gradients (**Movie 4**). By comparison, we also reconstructed the potential energy landscape using vision-based geometry sensing by assuming that beams are rigid (see Section 3.8.3), which had a much poorer reconstruction accuracy (relative error ε_{PE} = 180% in potential).

These results showed that the measured contact forces and torques enabled potential energy landscape reconstruction. We speculated that although the measured forces and torques were not fully conservative, the Helmholtz decomposition compensated the non-conservative parts and extracted a potential whose gradients best matched the measured forces and torques.

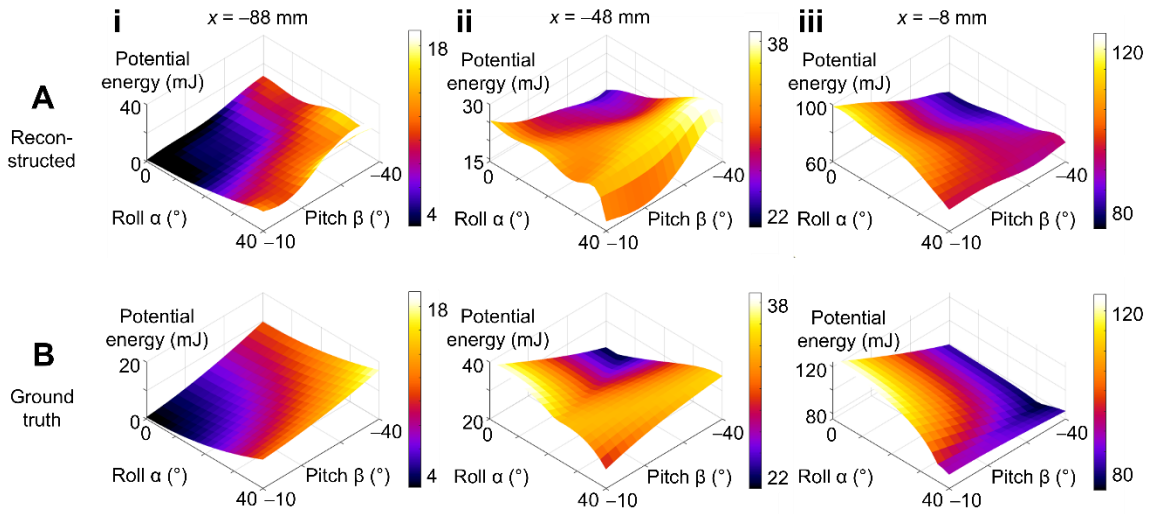

Figure 3-5: Potential energy landscape reconstruction. (**A**) Reconstructed and (**B**) ground truth potential energy landscape evolved as the robot moved forward. The presented landscapes are from the trials without head oscillation (f = 0 Hz) as a demonstration. (i) x = –88 mm, (ii) x = –48 mm, (iii) x = –8 mm. The landscape figures in the same column share the same colormap range.

3.5.7 Using normal forces and torques improves estimation of conservative ones in surface contact cases

The contact between the robot and obstacles can be of two kinds: surface contact and edge contact, where the contact point is on a 2-D surface (**Figure 3-3B,** yellow) or a 1-D edge (**Figure 3-3B,** orange) of the robot, separately. The robot can easily identify the contact cases because it knows the triggered touch-sensitive cell. Both contact cases appear frequently (surface: 56% ± 16%, edge: 44% ± 16% among all trials).

In the surface contact cases, because friction was one of the factors that caused a mismatch between sensed forces and torques and the conservative ones, we hypothesized that estimating the surface normal direction and using normal forces (i.e., the component of measured forces along the surface normal direction) and their torques to estimate

conservative ones eliminated the effect from friction (component along the surface tangential direction) (see Section 3.7.3). To verify this, we obtained the measured normal direction (**Figure 3-4A**, same direction as cyan) as that of the triggered touch-sensory cell. We found that the measured normal directions matched well with the ground truth calculations, with a small estimation error of 8% ± 4% in surface contact cases. We further calculated the normal forces and torques as the estimation of conservative ones. We found that the normal forces and torques better matched the conservative ones in the surface contact cases, reducing the estimation errors in the x direction to ε_x = 4% ± 3% from 16% ± 3%, and β direction to ε_β = 19% ± 8% from 25% ± 9% ($P < 0.001$, Student's t-test). However, we found no significant improvement in the α directions ($P = 0.37$, Student's t-test) (**Figure 3-4D**, normal vs. measured).

These results showed that using normal forces and torques improved landscape gradient estimation in surface contact cases. Besides, we also found that further improving the normal direction measurement accuracy promised better conservative forces and torques estimation (see Section 3.8.6). Further discussion on why using normal torques does not improve conservative torque estimation in α direction is in Section 3.6.8.

3.5.8 Active robotic head oscillation improves estimation of conservative forces and torques in edge contact cases

Although contact forces and torques are already good landscape gradient estimates, a robot or an animal benefit from a more precise landscape gradient estimation when traversing obstacles (See Section 3.6.5). We attempt to learn from the animal behaviors to improve landscape gradient estimation. Curiously, the discoid cockroach often exhibits up/down head oscillations (more than on flat ground [226]) (**Figure 3-6A, B**) while

pushing against large obstacles before transitioning to easier modes to traverse [31,35,36,226]. We speculate that such motions may be "exploratory" [195] to help an animal or robot sense landscape gradients over a small neighborhood of its current state.

Specifically, we hypothesized that with a fast enough oscillation, the frictions in the back-and-forth motion cancel out each other when the oscillation frequency is filtered out. To verify this hypothesis, we controlled the robot to actively oscillate its head at a frequency of 2 Hz (which emulates the animal behavior after scaling, see Section 3.8.7) while traversing the beams, and compared the measured contact forces and torques with the conservative ones. We found that as the head oscillation involved, the measured forces and torques (after flitting out the head oscillation frequency) usually converged to the conservative one in the edge contact cases (**Figure 3-6C-E**). With head oscillation ($f = 2$ Hz), compared to without ($f = 0$ Hz), the measured forces and torques better matched the conservative ones in x direction, improving to $\varepsilon_x = 5\% \pm 4\%$ from $8\% \pm 3\%$ ($P = 0.0012$, Student's t-test), and β direction, improving to $\varepsilon_\beta = 17\% \pm 7\%$ from $31\% \pm 12\%$ ($P < 0.001$, Student's t-test), but no significant improvement was found in α direction ($P = 0.45$, Student's t-test) (**Figure 3-6F**).

These results showed that active head oscillation improves landscape gradient estimation in edge contact cases and landscape reconstruction. Further discussion on why the active head oscillation does not improve conservative torque estimation in α direction is in Section 3.6.8.

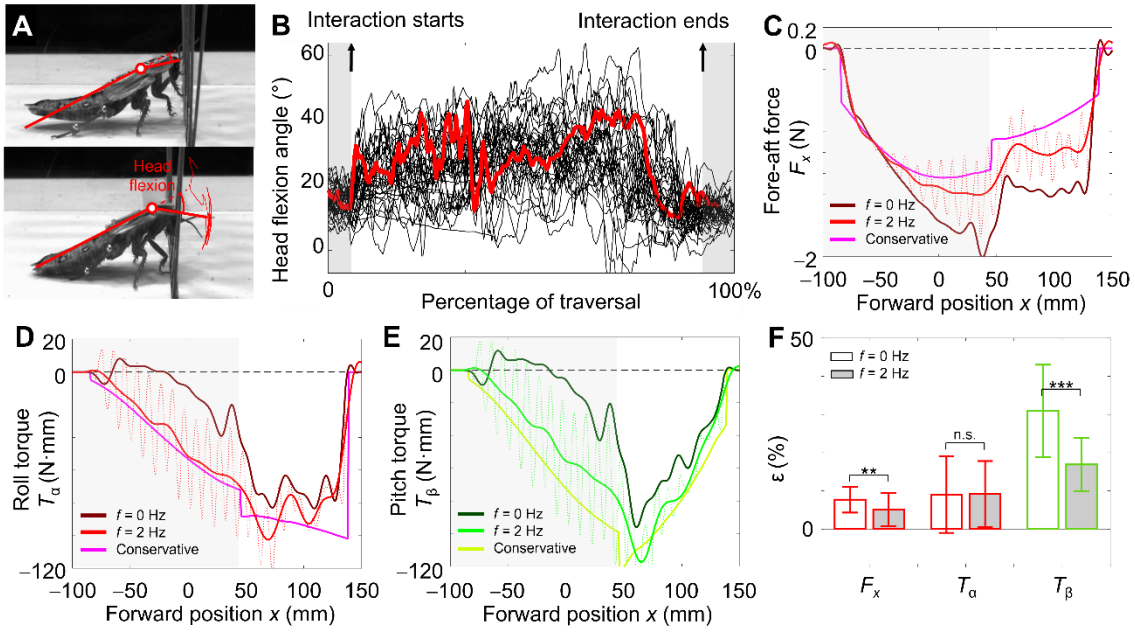

Figure 3-6: Head oscillations modulated sensed contact forces and torques. (**A**) Snapshots of a cockroach oscillating its head while traversing cluttered large obstacles. Head flexion angle was defined as the relative pitch angle between the animal's head and thorax. Red curve shows representative head oscillation from a trial. (**B**) Head flexion angle as a function of traversal progress when a cockroach traverses large, cluttered obstacles. Curves are individual trials. Thick, red curve is from the single trial in (A). White and gray backgrounds show the cockroach physically interacting with the obstacles or otherwise, separately. The cockroach oscillated its head in a larger amplitude when it physically interacted with the obstacles than otherwise. (**C**) Fore-aft force F_x, (**D**) roll torque T_α, and (**E**) pitch torque T_β as functions of forward position x from a representative trial. As the total roll torque (sum from both beams) was near zero, we show the forces and torques from contact with the right beam only for better comparison. In the case with head oscillation (f = 2Hz), thin, dashed curves are original, unfiltered data (see Section 3.7.4), thick, solid curves are further processed by zero-phase digital filtering using a six-order Butterworth filter with a cut-off frequency of the corresponding head oscillation frequency for better comparison. Gray shows edge contact phase. (**F**) Relative error ε of using fore-aft force F_x, roll torque T_α, and pitch torque T_β as the landscape gradients in edge contact cases. White and gray bars show using measured force/torques without (f = 0Hz) and with

(f = 2Hz) head oscillation, separately. Bars and error bars are means ± 1 standard deviation of the average relative error of all average trials. *** $P < 0.001$, ** $P < 0.01$, n.s.: not significant $P > 0.05$, Student's t-test. (A, B) are adapted from [226].

3.6 Discussion

3.6.1 Major findings

In summary, we built a robot capable of sensing obstacle contact forces and torques. Using a model system of grass-like beam obstacle traversal, we found that such sensing enabled the potential energy landscape gradient estimation and landscape reconstruction despite the measured forces and torques not being fully conservative. We also found that using normal forces and torques and a robotic active head oscillation improved the accuracy of landscape gradient estimation. This initial step introduces the potential energy landscape modeling to unknown, cluttered large obstacles where the robot physically interacts with them, similar to how machine vision enables robots to apply artificial potential fields to avoid sparse obstacles.

3.6.2 Benefit from custom, distributed sensors

Although reconstructing potential energy landscapes only requires total contact forces and torques, where one six-axis force and torque sensor is sufficient, we used a combination of custom distributed force and contact sensors for multiple reasons. Firstly, these custom sensors are low-cost (~$200 for all sensors and DAQ on our robot) and easy to repair (~10 min to repair one worn touch-sensitive cell) compared to a commercial sensor (~ $8,000 for a transducer, ~ 1 year repair cycle), which suits fast prototyping. Secondly, this distributed sensor design is robust against sensor damage. For example, a single touch-sensitive cell damage does not affect force sensory, and only causes a minor

error in contact point sensory information, which can also be easily mitigated from interpolation. Finally, the distributed force and contact sensors provide much richer information, such as contact force with either obstacle or local stress on the shell, that may be useful for future studies (e.g., as a robophysical model mimicking campaniform sensilla [140] on insect's exoskeleton to study how an insect leverage mechanoreception to sense and traverse obstacles. See Section 3.6.5). Moreover, compared with flexible sensory arrays [144,161–165], our hierarchical sensory strategy to have multiple distributed 3-D force sensors, each monitoring multiple contact sensors, can easily achieve a similar contact sensing resolution, and faster, more accurate, multi-axes force sensing.

3.6.3 Revealing potential energy landscape as a representation of physical interaction with the obstacles

Although a previous review summarized that the potential energy landscape approach successfully modeled the locomotor-terrain physical interaction over many model obstacles and self-righting, and suggested that the robot (and animal) can identify distinct obstacles and transition to proper modes to traverse then one-by-one [26] (proved to be practical in [111]), many problems are unsolved to keep this approach from real applications, e.g., whether the potential energy landscape modeling can be generally applied to physical interactions between any robots and any large obstacles; how to deal with the situation where the obstacles are too dense to separate (e.g., in **Figure 3-1F**). Since the contact forces and torques are ubiquitous in physical interaction with the obstacles, and we found a relation to transform contact forces and torques to a potential energy landscape (see Section 3.8.9 for another example of successfully reconstructing potential energy landscape from obstacle contact force and torque measurement using another robot), we

show that the potential energy landscape approach is applicable to all large obstacles (note that this claim does not indicate that the potential energy landscape dominated all obstacle interaction dynamics, see [26] for discussion on its limitation). Moreover, the relation also indicates that the potential energy landscape is a representation of physical interaction with the obstacles, similar to a neural network serving as a general representation of complex mathematical formulas [258,259]. This inspires further studies to leverage other data-driven approaches [260] to identify the landscape in unknown terrains, and provides simplified conceptual modeling of physical interactions with obstacles as a starting point for control strategy development (see Section 3.6.6 for an example).

3.6.4 Why and how head oscillation leads to better landscape gradient estimation

In each trial, the robot held its rotation and moved forward at a constant speed. We speculate that in that case, the system was dominated by normal forces and friction, whereas speed-dependent forces (e.g., damping forces) and inertial forces were small. In the edge contact cases**,** we speculated that the fast head oscillation made the contact friction cancel out temporally. When the robot's head was static (relative to the body), under a kinetic Coulomb friction assumption, the contact friction f was along the direction of relative velocity $\overrightarrow{v_0}$ between the body and the beam, and its amplitude depended on the normal contact force N and friction coefficient μ: $f = \mu\,|N|\frac{\overrightarrow{v_0}}{|\overrightarrow{v_0}|}$. When the robot head oscillated up and down, it added an oscillatory velocity $\pm\overrightarrow{v_{add}}$ to the original relative velocity between the body and beams, and the contact friction was along the direction of this new relative velocity as $\overrightarrow{v_1^{\pm}} = \overrightarrow{v_0} \pm \overrightarrow{v_{add}}$ for upward and downward head motion separately. When the head oscillation frequency is large enough, $\overrightarrow{v_{add}}$ dominated the

relative velocity, which made the latter roughly the same amplitude and inverse direction in the back- and forth- motion, $\overrightarrow{v_1^{\pm}} \approx \pm\overrightarrow{v_{add}}$, and so did the friction, which canceled out each other when averaged temporally. Thus, the sensed contact forces and torques were closer to the conservative forces and torques.

Note that, in the surface contact cases, a head oscillation may not significantly improve the normal direction estimation, because the actuated motion may be perpendicular to the friction direction, so the friction won't cancel out. On the other hand, we also observed that the animal's whole body had obvious body oscillation in the fore-aft and lateral direction [31,36,226]. We speculate that in a similar mechanism, these oscillations broke the friction and modulated the contact forces and torques to be closer to the landscape gradient. Further studies can test this by applying body oscillations in fore-aft and lateral directions and observing how they modulate the force and torque sensory.

3.6.5 Animal's head oscillation may allow active sensing and *local* potential energy landscape estimation

For obstacle traversal in real robotic applications and animal cases, the robot and the animal should estimate the local shape of the potential energy landscape (i.e., locally reconstruct the potential energy landscape) by estimating the conservative forces and torques and plan a prospective least-resistant path (this process could be simplified and encoded in the animal's neural network). However, unlike long-range vision or finite-range antenna sensing [261], force and torque sensing require direct contact. To estimate a potential energy landscape, a robot or an animal must move around the neighborhood of its current state and collect sensory data. However, unlike in our experiment, where the

robot freely swept a large state space and used a global algorithm (e.g., Helmholtz decomposition) to compensate for the non-conservative forces and torques, with only a rough and quick exploration in local space, the robot or the animal cannot easily extract the conservative forces and torques due to limited samples. They have leveraged other information (e.g., geometry) and motion (i.e., active sensing behavior) to obtain the conservative forces and torques in local space.

Previous biological studies in contact-based active sensing behavior [148,195,262] show that animals' force sensing inherently involves sensor motion, i.e., animals often move their sensors to enhance sensation. For example, when encountering an obstacle, an insect uses its antennas to repeatedly touch the obstacle (e.g., cockroach [150,151]) or does an antenna search and sample behavior aided by body and head rotating (e.g., stick insect [153,154]), which locates the obstacle and induces turning to avoid collision [150,154,263]; a rat actively whisks (i.e., moving the whiskers back and forth) against objects when exploring the terrain [149,155–157]. From comparative robotic studies [264–266], this probably enables the animal to extract object contours [267,268]. We speculate that similarly, the discoid cockroach's head oscillation in beam obstacle traversal [31,226] suggested a novel form of active sensing, which is useful for freely moving robots traversing cluttered large obstacles.

Although our study shows that a similar robotic head oscillation modulated force and torque sensory signals to better capture physical interaction with the obstacles (in the form of potential energy landscape gradient), whether and how the animal leverages a similar mechanism during obstacle traversal remains not understood. To test this speculation, future studies should measure the animal's muscle activity and neural signals

to first verify whether the head oscillation behavior is active or passively resulting from obstacle interaction. If it is an active behavior, studies can collect more biological observations and use robophysical models to examine the function of this behavior.

3.6.6 How a free-running robot may use force sensing to facilitate transitions

We speculate that our strategy to sense contact forces and torques to estimate landscape gradients and reconstruct the landscape will work in free-running robots. Because traversing cluttered large obstacles is highly strenuous, the robot needs to continually push against and intermittently collide with them [26], making it difficult to build up high momentum, i.e., it operates in a low-speed, small-acceleration regime, where the speed-dependent damping forces and inertial forces are likely small. Also, the robot often makes intermittent body contact with and pushes against large obstacles, likely resulting in large normal forces, whereas the associated frictional forces are usually smaller. Based on these, it is plausible that the conservative forces dominate the noisy contact forces even for a freely running robot, and our approach still applies.

Towards this, we still need to solve major additional questions. Firstly, how to filter the noisy contact forces with the obstacle to infer the landscape gradients. When a self-propelled, free-moving legged robot [111] negotiates with obstacles, the force sensory data can be substantially noisy because of friction and damping, oscillation from cyclic leg propulsion, and impulse from frequent collision with the beams. Studies can look for better mechanical design or signal processing methods to obtain the landscape gradients and reconstruct the landscape from the noisy sensory data.

Secondly, how to use sensing to reconstruct the *local* landscape near the robot's trajectory to enable a single, prior-free traversal. Future studies can adopt bio-inspired

approaches. For example, cockroaches [31,36,219,226] and ground beetles [269] often like to wedge in between obstacles like shrubs or rock cracks to go in to seek shelter. It is plausible that these animals use proprioceptive and tactile sensing [140,141] to detect or infer the obstacle resistance or resistive forces as they do so [226]. If this were the case, using such exploratory motions may allow these animals to sample contact forces and torques around their neighboring states and decide a direction with the least resistance to maneuver through/into the gaps/cracks. In other words, such animals' preference to go towards weaker spots (if they have such preference) coupled with exploratory motions for force and torque sensing may lead them to follow small potential energy gradients to ascend towards saddles and make least-resistance transitions [215,216]. We speculate that the robot can use a similar bio-inspired approach to sample around neighboring states to reconstruct a local landscape, estimate and follow the lowest gradient direction to gradually find saddles, and make least-resistance transitions to traverse obstacles. Future studies can also combine vision (or geometry detection) with force and torque sensing to enlarge local landscape detection region, and adapt other numerical algorithms for finding saddles and maximum-likelihood transition paths between local stability basins in physical chemistry [215,270–274].

Ultimately, we hope to build on this initial sensing and landscape reconstruction work to enable self-propelled, free-moving robots, during a single, prior-free traverse with substantial sensing noise, to use a range of exploratory motions to sample forces and torques around its current state, estimate and follow the lowest gradient direction and follow it to gradually find saddles, and control its self-propulsion to cross saddles to make least-resistance transitions to traverse cluttered large obstacles.

3.6.7 Full modeling of stochastic dynamics in large obstacle traversal

Building on the potential energy landscape modeling, future studies should model the robot (and animal) locomotion during cluttered large obstacle traversal as a potential energy landscape-dominated, stochastically perturbed dynamics with diffusion (i.e., Langevin dynamics [275–277]), where friction, damping, kinetic energy fluctuation, and inertia effects will also be considered [26]. The Langevin equations will greatly improve the prediction of the system dynamics, especially in the neighborhood of the saddle point, because around saddle points, the potential gradients are near zero, and the friction, damping, and oscillation will dominate the robot dynamics. Reliably producing Langevin dynamics models will improve our understanding of biological motion and create new possibilities for robot control in challenging terrains.

3.6.8 Remaining issues in this study

Currently, the distributed touch-sensory cells require the obstacle surface to be conductive (and better be grounded), which limits its access to nature. They are also worn out due to consistently rubbing against the obstacles (in ~100 trials of experiments). We should seek other touch detection mechanisms (e.g., dome switch [278]) for out-of-lab applications.

The potential energy landscape reconstruction did not show steep gradients near the barrier like the ground truth calculations (**Fig 5, iii**, around roll $\alpha = 35°$). We speculate that this was because the state space of the steep gradients was small, and insufficient samples were taken in the neighborhood. A possible solution is to obtain more samples in the region with steep gradients.

Neither using normal roll torque nor involving head oscillation improved roll torque estimation. We speculated that this was because the pitch basin was flat along the roll direction, where the conservative roll torque was near zero, and the friction-resulted torque dominated the measured roll torque. We speculate that this can be better explained using Langevin dynamics (see Section 3.6.7).

3.6.9 Envision torque sensing guiding self-righting

As the potential energy landscape modeling also reveals physics principles of self-righting of animals and robots [37,279], we foresee that torque sensing can guide better self-righting. Because the potential energy landscape of self-righting varies dramatically with the ground geometry [37], we envision that the capability of reconstructing the potential energy landscape on an unknown ground will benefit the animal or the robot by identifying the least-resistance rotating direction to apply direct perturbation to self-right. Because self-righting only involves rotational dimensions, sensing ground reactive torque is sufficient for landscape reconstruction. However, self-righting is highly dynamic and unavoidably involves fierce perturbation from wing opening and leg flailing. Therefore, the inertial effect and impulses can heavily bias the sensed ground reactive torque.

3.7 Methods

3.7.1 Potential energy landscape modeling

The system's potential energy *PE* was the sum of the gravitational potential energy of the robot PE_G and the elastic potential energy from the beams PE_E:

$$PE_G = mg(\Delta z - h), \tag{3-1}$$

$$PE_E = \tfrac{1}{2} k_1\theta_1^2 + \tau_1\theta_1 + \tfrac{1}{2} k_2\theta_2^2 + \tau_2\theta_2, \tag{3-2}$$

$$PE = PE_G + PE_E = mg(\Delta z - h) + \tfrac{1}{2} k_1\theta_1^2 + \tau_1\theta_1 + \tfrac{1}{2} k_2\theta_2^2 + \tau_2\theta_2, \quad (3\text{-}3)$$

where m was the mass of the robot, g was the gravitational acceleration, Δz was the vertical distance between the geometric center and center of mass, $\theta_{1,2}$, $k_{1,2}$, and $\tau_{1,2}$ are the deflection angles, the torsional stiffness, and the preload of the left and right beams, separately. See Section 3.8.1 for more details.

3.7.2 Robot experiment protocol

Before each trial, the robot was positioned at a distance of 200 mm (x = –200 mm) from the beams, at a height of z = 138 mm from the beams' bottom edges, roughly in the middle of the two beams (y = –6 mm) and pointing forward (body yaw $\gamma = 0°$). The robot was rotated to the desired roll and pitch angle. The beams were set vertically and moved to have a gap of 130 mm wide symmetric to the robot. The robot's head was aligned with the body (head pitch angle = 0°). All the force sensors were zeroed. Then, the robot's head started oscillating between 0° and 20° at a frequency of f (for f = 0 Hz) until the end of the fore-aft translation, and the LabVIEW program started data recording. After a random period (to randomize the head oscillation phase), the robot was moved forward at a constant speed of 20 mm·s^{-1} by a distance of 500 mm, which guaranteed the robot passed the beam obstacle area fully, and the beams were bounced back to vertical. Finally, we stopped the head oscillation and data recording and moved the robot back to its initial position for the next trial. Two cameras (Logitech C920 HD PRO, Logitech, Switzerland) synchronized by Open Broadcaster Software (OBS) recorded the experiment from the side and the isometric views at a frame rate of 30 Hz and a resolution of 960×720 pixels (**Movie 4**).

We varied the head oscillation frequency f at 0 and 2 Hz. For head oscillation frequency f, we varied the roll angle α from 0° to 40° with an increment of 5° and the pitch angle β from −10° to −40° with a decrement of 5° (note that negative pitch angle meant pitching the body upward). At each combination of head oscillation frequency f, desired roll angle α, and pitch angle β, we performed five trials, which resulted in a total of $n = 630$ trials.

Note that because the robot frames and links were not stiff, the robot's roll and pitch angles slightly changed (maximal roll angle change < 10°, maximal pitch angle change < 5°) in each trial. We measured the roll and pitch angles from IMU to account for this effect.

3.7.3 Force analyses and accuracy optimization

The measured contact forces (**Figure 3-4A**, red) are directly measured from the 3-D force sensors. The contact position (**Figure 3-4A**, orange points) was estimated as the center of the cell at the contact. Every cell on the robot shield-shaped surface (i.e., not on the edge) is a quadrilateral (**Figure 3-3D**), which is from two fractions of an ellipsoid. The center is calculated as the average of the four corners of each cell and projected to the ellipsoidal surface. The measured normal direction was defined as that of the curved surface of the shell shape at the center of the cell at contact. The normal force (**Figure 3-4A**, cyan) was the component of the measured force along the normal direction. The moment arm (**Figure 3-4A**, blue) was the distance from the robot's geometric center to the contact position. The measured or normal torque was the cross of the force arm and the measured or normal force, separately. The measured or normal torques along the roll, pitch, and yaw direction were the projections of the torque T along the roll (x'-, as yaw is zero), pitch (y-, as yaw is zero), and yaw (z-) axes, separately. The total measured and normal

forces and torques were the sum of those from the two beams. We don't define normal direction, forces, and torques in the edge contact cases. Note that in this section, we made no assumption about the obstacle geometry, any obstacle properties, or body motion. Thus, these analyses are applicable to various obstacles.

To estimate contact position and normal direction, we minimized the maximal estimation error over the entire surface. The maximal estimation errors of contact position and normal direction were assumed to be at one of the four corners. We calculated the maximal position error (defined as the maximal distance from any point on the cell to the cell center) and maximal normal direction error (defined as the maximal angle between the normal directions from any point on the cell and cell center) on each cell as sensor resolution, and revised the pattern of the sensory cells to minimize the largest resolutions of the two aspects over the entire surface.

3.7.4 Data filtering and averaging

All the data (robot positions, orientations, head oscillation angles, forces, torques, etc.) were processed by zero-phase digital filtering (i.e., "filtfilt" function in MATLAB) using a six-order Butterworth filter with a cut-off frequency of 6 Hz for head oscillation frequency f = 2Hz, 1.5 Hz for f = 0 Hz, or 0.5 Hz, or 3 Hz for f = 1 Hz, respectively (See Section 3.8.7 for head oscillation frequency selection). As the measured data are consistent using the same treatment (see Section 3.8.8 for limited exceptions), to obtain the average data over these trials, we varied x from −100 mm to 200 mm with an increment of 1 mm, and we linearly interpolated the measured data over x and then averaged them over the five repeated trials.

3.7.5 Potential energy landscape reconstruction

We used the measured contact forces and torques to estimate the vector field of landscape gradients in the x-α-β space, combining all averaged trials. Due to the slight change in the robot's roll and pitch in each trial (see Section 3.7.2), the vector field base was heterogeneous (i.e., not strictly gridded). We applied a meshless Helmholtz-Hodge decomposition (HHD) [280] on this vector field to reconstruct the potential energy landscape. Only the potential energy landscape for x from −100 mm to 100 mm was reconstructed because our landscape model did not capture the beam bouncing back, which occurred after this range. To roughly unify the input data along the three axes, we multiplied a ratio of 0.01 to the input bases $\boldsymbol{X}$ along x-axis and multiplied the reciprocals of this ratio to the input vectors $f(\boldsymbol{X})$ along x-axis so that the multiplication of the unit of the base and vectors—the potential energy—was unchanged. We chose a commonly used Gaussian kernel function $\phi_i(\boldsymbol{X}) = \exp(-\sigma r_i(\boldsymbol{X})^2)$, where $r_i(\boldsymbol{X})$ was the Euclidean distance between the base $\boldsymbol{X}$ and the i-th center in the unified x-α-β space, because this kernel function fit the expected continuous, 1-order smooth, non-periodic landscape. We generated the $k = 2000$ centers by performing k-means clustering on the input base $\boldsymbol{X}$. This kernel number k allows robust estimation results (from a preliminary test, it had no significant performance reduction with even 60% data loss). We rejected any centers close to any input base $\boldsymbol{x}$ ($< 10^{-4}$ unit) to avoid singularity in the calculation. See 3.8.5 for algorithm details.

Note that the meshless Helmholtz decomposition also involves errors in landscape reconstruction. Even when performed on the conservative forces and torques, the landscape estimation still has a relative error of $\varepsilon_{PE} = 2.1\%$ in energy and $\varepsilon_{Grad} = 12.5\%$ in gradients.

3.7.6 Comparison criteria and statistics

When comparing the measured data or reconstructed landscape with the model, we were only interested in the period when the robot interacted with the beam obstacles. Here, we defined two fore-aft positions: the attach position x_a, where the robot first contacted all the beams, and the detach position x_d, where the robot first detached from one of the beams and the beam bounced back. For each trial, the attach position x_a was identified as x at the first time frame where both the beam angles θ are bigger than a threshold of 3°; the detach position x_d was identified as x at the first time frame where either of the beam angle θ reached maximum.

To compare fore-aft force F_x, roll torque T_α, and pitch torque T_β to the model, we only chose the data from the attach position x_a to the detach position x_d. We averaged the absolute difference between the measured data and model over x and divided it by the maximal range of the model data to obtain a relative error ε:

$$\varepsilon = \frac{\overline{|y(x) - r(x)|}}{r(x)_{max} - r(x)_{min}} \times 100\%, \tag{3-4}$$

where $y(x)$ was the measured data, and $r(x)$ was the model as reference. We used this criterion instead of a traditional relative error definition because the model data had near-zero sections. To compare the measured potential energy landscape in x-α-β space to the model, we flattened the landscapes into 1-D (i.e., function "reshape" in MATLAB) and defined the relative error the same as above. To compare the measured landscape gradients in x-α-β space to the model, we first unify the data along the three axes by dividing the gradients along the x direction by 0.01 (see Section 3.7.5), then flattened the gradients into

a row of vectors (i.e., function "reshape" in MATLAB), and defined the relative error using the maximal norm of model data as the denominator:

$$\varepsilon = \frac{\overline{|y(x) - r(x)|}}{|r(x)|_{max}} \times 100\%. \quad (3\text{-}5)$$

All average data are reported as mean ± 1 standard deviation. We used Student's *t*-tests to test whether the normal direction estimation or increasing head oscillation frequencies reduced estimation errors of the landscape gradients or landscape reconstruction. All data analyses were performed using MATLAB R2021b (MathWorks, MA). All the statistical tests were performed using JMP PRO 17 (SAS Institute Inc., NC).

3.8 Supplementary Information

3.8.1 Calculating potential energy landscape of the system

To calculate the potential energy landscape from first principle as ground truth calculation, we approximated the robot's shell as its uncropped counterpart. The robot's center of mass m = 0.53 kg was assumed to be at h = 8 mm below the geometric center, similar to that of the previous study [31]. Each beam was modeled as a massless rigid rectangular plate on a preloaded Hookean torsional joint without damping. For a given robot position and orientation, each beam's deflection angle was calculated as the largest possible forward deflection angle by the body, or zero if no such angle existed. Therefore, the beam deflection angles and the elastic potential energy fully depend on the robot's position and orientation. As the system potential energy is the sum of the gravitational potential energy of the robot and the elastic potential energy from the beam, the potential energy landscape depends on the robot's position (x, y, z) and orientation (roll α, pitch β,

yaw γ). To calculate the landscape gradients, we took a central differentiation of the potential energy landscape along $\{x, y, z, \alpha, \beta, \gamma\}$ with a 10^{-4} unit perturbation.

3.8.2 Proof that obstacle contact forces and torques are negative potential energy landscape gradients

In this proof, we assume that the robot and obstacles move quasi-statically, and there is no friction or damping. The system has no kinetic energy, and the input work is all converted into potential energy:

$$W = \Delta PE, \tag{3-6}$$

where W is the input work, and ΔPE is the change of the system's potential energy. Examples of the input work are the propulsion from legs or air thrusters. As the body moves quasi-statically, the external forces and torques are balanced:

$$F_{G,q_i} + F_{OB,q_i} + F_{W,q_i} = 0, q_i \in \{x, y, z, \alpha, \beta, \gamma\}, \tag{3-7}$$

where $F_{G,\,q\mathrm{i}}$, $F_{OB,\,q\mathrm{i}}$, and $F_{W,\,q\mathrm{i}}$ are the gravitational, obstacle contact, and external input forces or torques along x, y, z, α, β, or γ axes, separately. The external input forces and torques are the partial derivatives of the input work:

$$F_{W,q_i} = \frac{\partial W}{\partial q_i}. \tag{3-8}$$

The system's potential energy PE is the integral of conservative external forces and torques along relevant degrees of freedom, $PE(X) = -\int_{X(0)}^{X} \vec{q}(\vec{X}) \cdot d\vec{X} = -\int_{X(0)}^{X} \sum_i q_i(X) dX_i$, where $\vec{X}$ = (x, y, z, roll, pitch, yaw) is the state vector, and $\vec{q}$ is the generalized force. Therefore, the negative gradients of the potential energy are the sum of gravitational and obstacle contact forces or torques:

$$\frac{\partial PE}{\partial q_i} = -\left(F_{G,q_i} + F_{OB,q_i}\right). \tag{3-9}$$

If the robot's position and orientation can be sensed, we can calculate the obstacle contact forces and torques:

$$F_{OB,q_i} = -\left(\frac{\partial PE}{\partial q_i} + F_{G,q_i}\right), q_i \in \{x, y, z, \alpha, \beta, \gamma\}. \tag{3-10}$$

i.e., the obstacle contact forces and torques are the negative potential energy landscape gradients, biased by the gravitational force and torque.

Note that although the contact forces and torques are the negative gradients of the potential energy from the obstacle ($F_{OB,q_i} = -\frac{\partial PE_{OB}}{\partial q_i}$) for this beam traversal problem, this does not apply to other obstacle traversal problems, e.g., in the bump [33], gap [34], and pillar [35] traversal, where the obstacle does not possess potential energy.

3.8.3 Potential energy landscape based on geometry

To examine whether force and torque sensing enabled a potential energy landscape reconstruction better than geometry-based sensing, we generated a potential energy landscape assuming the beams were rigidly fixed, which should be the landscape reconstructed from perfect geometry-based sensing. Here, if we still assumed that the robot only moved in *x*-α-β space, we cannot appropriately define a finite potential energy when the robot had to penetrate a beam. Instead, we assumed that the robot adjusted its vertical position *z* to avoid the beams. The robot's gravitational potential energy at the minimum possible *z* was defined as the system's potential energy.

3.8.4 Robot design and manufacturing

System design. The experiment system (**Figure 3-3A**) consisted of the robotic physical model (**Figure 3-3B**), a fore-aft sliding structure (outside **Figure 3-3A**) that actuated the robot to move along the fore-aft (x-axis) and vertical (z-axis) directions, and two flexible beams (**Figure 3-3A**, green), whose bases moved along the lateral (y-axis) direction. The robot had a body and a head (**Figure 3-3B**). The body consisted of a frame, a gyroscope mechanism, and links to control rotation. The head consisted of a frame, two pieces of front shell, two custom 3-axis force sensors (**Figure 3-3B**, magenta), and a custom data acquisition board (DAQ, **Figure 3-3B**, green).

The shell was cropped from a shield-shaped counterpart (**Figure 3-3B**, semi-translucent green), whose geometric centers were at the robot's origin at zero head angle. The shell was separated from the middle, which ensured that each part of the front shell only contacted one of the beams. Only the beam-contactable area and a small outer margin were reserved. To best compare with the previous study [31], the axe lengths of the shell's counterpart were kept the same as the previous design.

The two beams were made and characterized using the same method as in [31]. Each beam was a rigid acrylic plate (30 mm width × 200 mm height) attached to the base via a 3-D printed torsional spring joint. The beams only allowed forward deflection. We chose to use the stiffest beams in [31] to maximize the force sensors' signal-to-noise ratio.

Actuation. The robot was actuated to rotate along roll and pitch directions (Euler angle follows the Tait-Bryan convention) and oscillate its head. To control the robot to rotate to the desired roll and pitch angles, we designed a gyroscope mechanism centered at the robot's origin of the body frame and added two servo motors (DYNAMIXEL XC330-

M288-T, ROBOTIS Co., South Korea) to separately control the roll (**Figure 3-3A**, **B**, red) and pitch angles (**Figure 3-3A**, **B**, blue). To enable head oscillation, we connected the body frame and the head frame via a servo motor (DYNAMIXEL XC330-M288-T, **Figure 3-3A**, **B**, pink) and used its encoder to record the head oscillation angle with a precision of 0.1°. The fore-aft sliding structure's motion and beam bases' motions were each powered by a servo motor (DYNAMIXEL XM430-W210-T, ROBOTIS Co., South Korea) via a custom gear-rack mechanism, and their motors' encoders measured the displacements with a precision of 0.01 mm. All the servo motors were commanded and reported their rotation angles to a microcontroller (OpenCM 9.04, ROBOTIS Co., South Korea) at a frequency of 50 Hz.

Data acquisition. To obtain contact forces with the obstacles, the load cells with a labeled range of ± 20 N and a precision of ± 0.004 N (BF-02088B, HK Bingf Sci. & Technol. Corp., China) in the custom 3-D force sensor were read by the load cell amplifier chips (HX711, Avia Semiconductor, China) on the DAQ board. To obtain contact position, the touch sensory cells were connected to capacitive touch sensor chips (MPR121, Freescale Semiconductor, TX) on the DAQ board via a single wire and a pull-up resistor. When a cell contacted the grounded beam surface, the capacitive touch sensor detected the touch as a voltage drop. To monitor robot's rotation, we installed an inertial measurement unit (IMU, **Figure 3-3B**, cyan, BNO055, Adafruit Industries, NY) on the robot body and connected it with the DAQ board. Preliminary tests showed that the IMU provided accurate rotation measurements with errors < 8° and < 2° for roll and pitch directions, separately. All the contact forces and positions and robot rotation sensory data were gathered by a microcontroller (Teensy 4.0, PJRC, OR) on the DAQ board at a frequency of 50 Hz.

The robot was attached to the hanging frame via a custom 3-D force sensor to monitor the hanging and propelling force. This force sensor consists of three load cells (5kg load cell, ShangHJ, China) serially connected and orthogonal to each other. With the load cell amplifier chip (HX711) along the lab *x*-, *y*-, or *z*-axis, with a labeled range of ± 50 N and a precision of ± 0.02 N. To measure the beam deflection angles, we attached a potentiometer (100 K Ohm Potentiometer, HiLetgo, China) to each beam's rotational joint via a parallel four-bar linkage. The two end terminals were powered at 5 Volt, and the voltage at the wiper was measured to calculate the rotation angle with a precision of 0.3°. The force sensory data from the top sensor and the beam angles were collected by a microcontroller (Arduino Mega, Arduino, Italy) at a frequency of 50 Hz.

Sensor calibration. See Section 3.7.3 for load cell calibration. Because the bias shifted every time the DAQ restarted, we zeroed all force sensors before each trial of experiments. We characterized the torsional stiffness and preload of the beams by measuring the restoring torque about the joint as a function of joint deflection angle using a 3-axis force sensor (Optoforce OMD-20-FG, OnRobot, Denmark), similar to [31]. The torsional stiffness and preload of either beam were calculated from the slope and the intercept of the linear fit of the torque as a function of the deflection angle, which was 285 $N \cdot mm \cdot rad^{-1}$ and 91 N·mm for the left beam and 324 $N \cdot mm \cdot rad^{-1}$ and 77 N·mm for the right beam.

Visualization. We used a LabVIEW program to bidirectionally communicate with the microcontrollers and record experimental data at a frequency of 50 Hz. The LabVIEW graphical user interface (GUI) allowed us to check all the sensory information including the robot's position, orientation, head oscillation angle, force amplitudes, and contact

positions on each piece of front shell, propelling force, and the beams' positions and deflection angles. It also allowed manual control to the system's actuation in real time and conducting automatic pre-programmed experiments.

3.8.5 Meshless Helmholtz-Hodge decomposition

The idea of Helmholtz-Hodge decomposition [257] is to consider the vector field as a sum of a gradient vector field (i.e., curl-free) and a solenoidal vector field (i.e., divergence-free):

$$f(\boldsymbol{X}) = g(\boldsymbol{X}) + r(\boldsymbol{X}) = -\nabla\Phi(\boldsymbol{X}) + \nabla \times A(\boldsymbol{X}), \tag{3-11}$$

where $\boldsymbol{x}$ is the independent variable vector, or the base of vectors (e.g., $\boldsymbol{X} = [x, \alpha, \beta]$ in our case), g($\boldsymbol{X}$) is the gradient vector of a scalar potential $\Phi(\boldsymbol{X})$, $r(\boldsymbol{X})$ is the solenoidal vector, which is a curl of the vector potential $A(\boldsymbol{X})$. We used the scalar potential Φ as the estimated potential energy landscape.

In meshless Helmholtz-Hodge decomposition [280], the scalar potential $\Phi(\boldsymbol{X})$ and the vector potential $A(\boldsymbol{X})$ were approximated as a linear combination of the kernel functions ϕ of a group of scattered points (centers):

$$\Phi = \sum_{i=1}^{k} a_i \phi_i\,, \tag{3-12}$$

$$\mathrm{A} = \sum_{i=1}^{k} [b_{i,1}\phi_i, b_{i,2}\phi_i, b_{i,3}\phi_i]^T = \sum_{i=1}^{k} (\phi_i I) b_i\,, \tag{3-13}$$

where k is the number of centers, ϕ_i is the kernel function at the i-th center, a_i and $b_i = [b_{i,1}, b_{i,2}, b_{i,3}]^T$ are its coefficients of the linear combination, and I is a 3×3 identity matrix. At a

given base $\boldsymbol{X}$, the gradients $f_g(\boldsymbol{X})$ and solenoidal $f_s(\boldsymbol{X})$ vector field are represented by the gradients of kernel function:

$$f_g(\boldsymbol{x}) = \sum_{i=1}^{k} a_i \nabla \phi_i = (\nabla \phi)^T a, \tag{3-14}$$

where $\nabla \phi := [\nabla \phi_1, \dots, \nabla \phi_k]^T, a := [a_1, \dots, a_k]^T$,

$$f_s(\boldsymbol{X}) = \sum_{i=1}^{k} \nabla \times \phi_i I b_i = (\nabla \times \phi I)^T b, \tag{3-15}$$

where $\nabla \times \phi I := \begin{bmatrix} \nabla \times \phi_1 I \\ \dots \\ \nabla \times \phi_k I \end{bmatrix}_{3k \times 3}, b := \left[b_{1,1}, b_{1,2}, b_{1,3}, \dots, \dots, \dots, b_{k,1}, b_{k,2}, b_{k,3}\right]^T$.

We speculated that the meshless landscape reconstruction algorithm that we applied suits applications of a legged mobile robot that moves on cluttered terrain. In these cases, because the robot's motion emerges from its self-propelled interaction with the obstacles, the robot cannot fully control and systematically vary its translations and rotations. The sensed force data can be heterogeneously scattered in the state space (i.e., not on a meshed grid) and sometimes missing in time series, which hinders applying reconstruction algorithms that need evenly gridded data [281–285]. In contrast, the meshless algorithm handles the fragmented sensor data and allows for reconstructing the landscape locally in the state space, which is sufficient for most state-feedback controllers (see Section 3.6.6 for details).

3.8.6 More accurate normal direction measurement allows better landscape gradient estimation

In the main text, we showed that using normal forces and torques improves the estimation of conservative ones compared with directly using the measured ones. Here, we hypothesize that more accurate normal direction measurement further improves the estimation. To test this, we obtained the normal direction from modeling), obtained the measured force component along this direction and their resulting torques (mentioned as semi-measured normal forces and torques). We found that in surface contact cases, compared to the measured normal forces and torques, the semi-measured ones further improved matching in β direction to $\varepsilon_\beta = 5\% \pm 3\%$ from $19\% \pm 8\%$ ($P < 0.001$, Student's *t*-test) but no significant improvement in the *x* direction ($P = 0.07$, Student's *t*-test) (**Figure 3-7**).

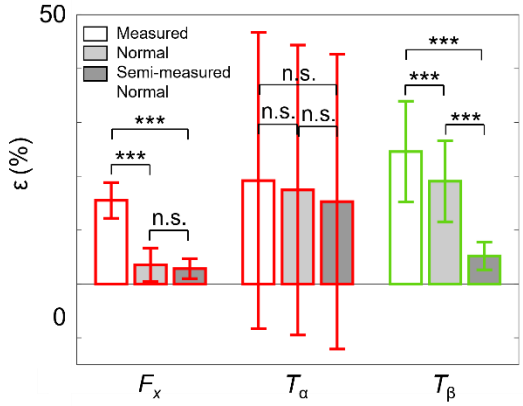

Figure 3-7: Relative error ε of using fore-aft force *Fx*, contact force roll torque T_α, and pitch torque T_β as the landscape gradients in surface contact cases. White, light gray, and dark gray bars show measured, measured normal, and semi-measured normal forces/torques, separately. Bars and error bars are means ± 1 standard deviation of the average relative error of all average trials. *** $P < 0.001$, n.s.: not significant $P > 0.05$, Student's *t*-test.

Further studies can try to improve the accuracy of normal direction measurement by designing and manufacturing touch-sensitive cell patterns of smaller spatial resolution and involving vision combine this with obstacle geometry detection to assist normal direction estimation.

3.8.7 Head oscillation frequency selection

We selected the robot's head oscillation frequency based on the observed animal behavior [226]. When exploring and negotiating the beams, the discoid cockroach oscillated its head within a highly variable frequency (**Figure 3-6A, B**). To obtain its average oscillation frequency, we separated each head oscillation cycle into two phases—the downstroke, where the head pitched downward relative to the body (increasing head angle), and the raising phase, where the head angle decreased. We defined the head oscillation amplitude as the maximal range of head angles. Average head oscillation angular velocity was this amplitude divided by the duration of each phase. The mean amplitude over each attempt and mean average head oscillation angular velocity over each attempt were 15° ± 9° and 145° ± 100° $\cdot s^{-1}$ in the lowering phases and 16° ± 10° and 150° ± 90° $\cdot s^{-1}$ in the raising phases for all the observed head oscillation cycles [226]. Using these data, we calculated the average head oscillation frequency to be roughly 5 Hz for the animals. Because the animal traversed the beam obstacle in 4 ± 1 seconds from initial to final contact [226] while the robot traversed in roughly 10 seconds, the robot head oscillation frequency was chosen to be 2 Hz so that both oscillated about the same ~20 number of cycles during traversal.

We also used two other lower oscillation frequencies, 0.5 Hz and 1 Hz, to test how oscillation frequency affects the conservative force and torque (i.e., landscape gradient) estimation in edge contact cases. We observed that for both low head oscillation frequencies (f = 0.5, 1 Hz), the estimations were not improved or even worse than without head oscillation (f = 0 Hz) ($P < 0.001$, Student's t-test) (**Figure 3-8**). We speculate that, as the head oscillation frequency was low, the relative velocity between the robot and the obstacle at the contact, i.e., the direction of frictional forces, was not governed by the oscillatory motion. So, the frictions from back-and-forth motion did not cancel out each other when averaged temporally. See Section 3.6.4 for explanations.

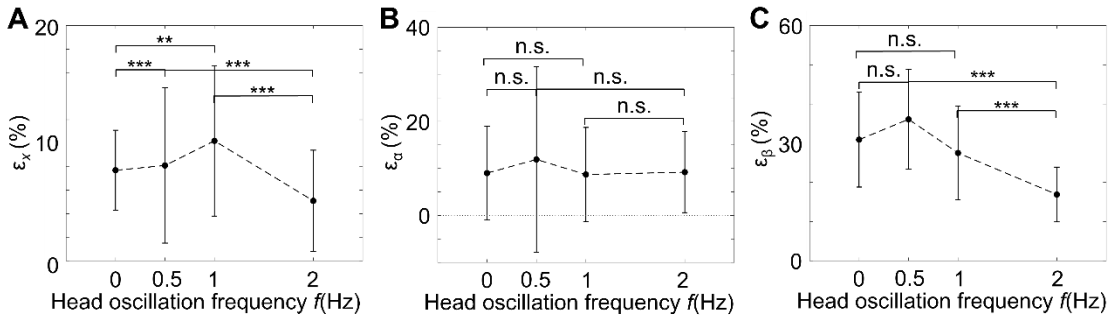

Figure 3-8: Relative error of potential energy landscape gradient estimation and landscape reconstruction with various head oscillation frequencies. (**A**, **B**, and **C**) are relative error ε_x, ε_α, and ε_β of using (A) fore-aft force Fx, (B) roll torque T_α, and (C) pitch torque T_β as the landscape gradients, separately. See Section 3.7.6 for the definition of relative error. Lines and error bars are means ± 1 standard deviation of the average relative error of all average trials. *** $P < 0.001$, ** $P < 0.01$, n.s.: not significant $P > 0.05$, Student's t-test. Brackets and asterisks show comparisons described in Section 3.8.7.

3.8.8 Various force sensing data observed in repeated experiments

Although our data showed consistency for repeated experiments (x-average coefficient of variation = 2% ± 1% for F_x, 2% ± 2% for T_α, 3% ± 3% for T_β. See how we

averaged the repeated trials in Section 3.7.4, we also found that the result was various of some roll and pitch combinations when the head oscillation was involved (maximal coefficient of variation = 20% ± 9% for F_x, 24% ± 6% for T_α, 27% ± 5% for T_β), probably due to the random starting phase of the head oscillation (see Section 3.7.2 and Section 3.7.4). These trials [1] were mostly (86%) of the roll and pitch combination near the separatrix. We carefully observed the video recording of these trials and speculated that some were caused by head-oscillation-induced pitch-to-roll transition or sudden beam bouncing back.

3.8.9 Successful adapted to sensing and landscape reconstruction strategies to another robot

To test whether our strategies to sense obstacle contact forces and torques to estimate the potential energy landscape gradient and reconstruct the landscape hold for other robots, besides the shield-shaped robot (**Figure 3-3A**), we also designed and built a rounded (i.e., without sharp edges) ellipsoidal robot of the same size (**Figure 3-9A, B**), and conducted the same experiment, where it systematically varied roll and pitch angles and was pushed through the beam obstacles, but only without head oscillation.

To sense contact forces and torques, the robot was embedded with the same custom 3-D force sensors (**Figure 3-9B**, magenta). The pattern of the touch sensory cell distribution was carefully re-designed (**Figure 3-9C**) to achieve high sensory accuracy (position resolution < 11 mm, normal direction resolution < 15°) (**Figure 3-9D**). Especially,

[1] For f = 2 Hz, {α, β} = {35°, 10°}, {30°, 20°}. For f = 0.5 Hz, {α, β} = {35°, 10°}. For f = 1 Hz, {α, β} = {35°, 10°}, {40°, 15°}, {40°, 25°}, {30°, 20°}. See Section 3.8.9 for experiments where f = 0.5 Hz and 1 Hz.

because the normal direction changes dramatically around the equator (increasing by 107° over a 50 mm arc length around z' = 0 mm), the touch sensory cells were designed to be shortened along z' direction to maintain a small normal direction resolution.

For this ellipsoidal body shape, the measured forces and torques well matched the conservative forces and torques (i.e., negative landscape gradients), with a small relative error of ε_x = 12% ± 4% in the x direction, ε_α = 12% ± 11% in the roll direction, and ε_β = 26% ± 10% in the pitch direction. The reconstructed landscape and its gradients also well matched the ground truth calculation from first-principle calculations using the rounded ellipsoidal robot, with a low relative error of ε_{PE} = 8.6% in potential energy and ε_{Grad} = 13.8% in gradients (**Figure 3-9E**). All the estimation errors are similar to or even smaller than that of the shield-shaped robot.

These observations suggested that our obstacle contact force and torque sensing and potential energy landscape reconstruction strategies also adapt to other robot shapes (i.e., universality). Further studies should try to apply these strategies to more robot shapes and obstacle types as verification.

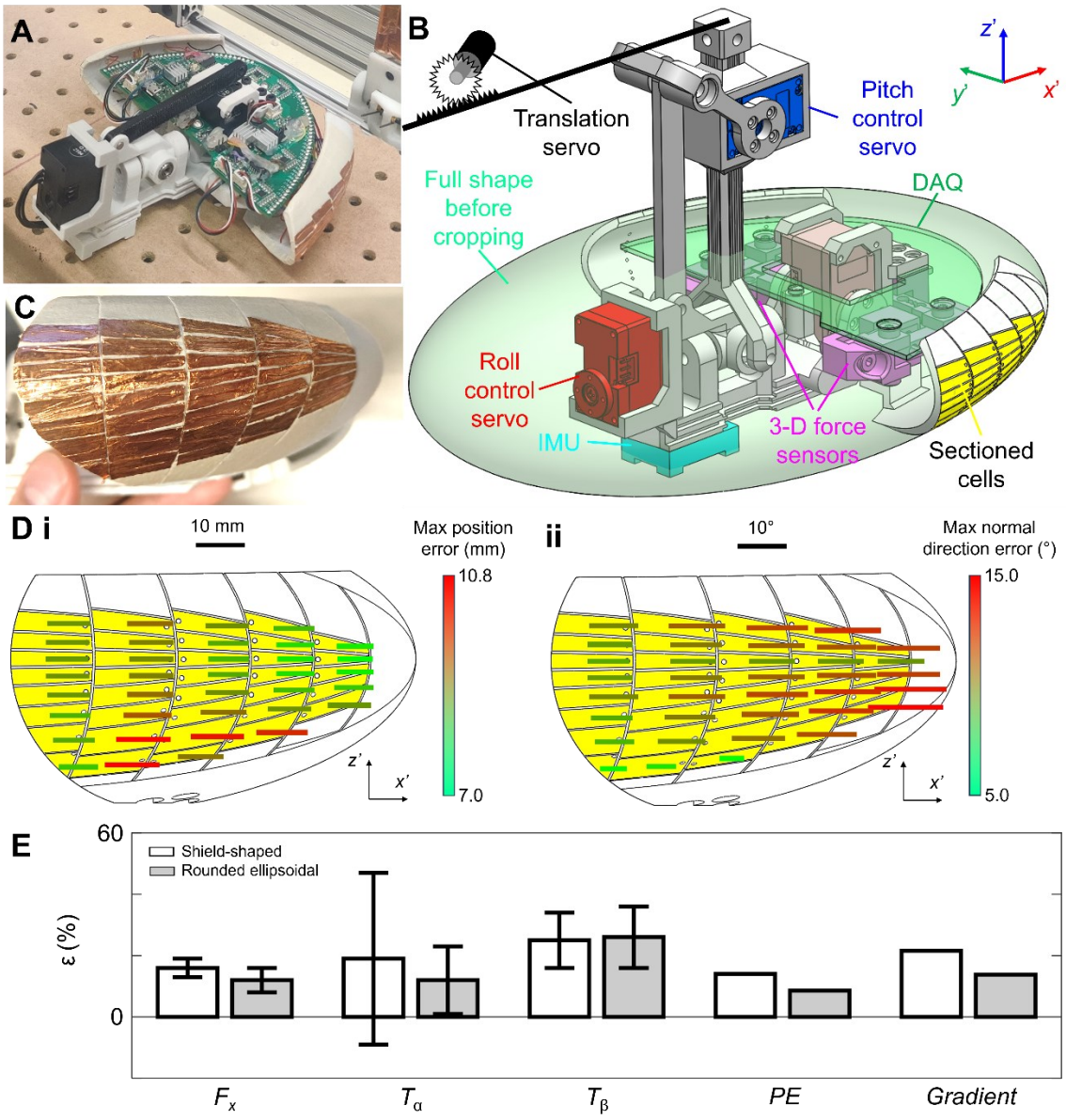

Figure 3-9: The same force and torque sensing and landscape reconstruction strategies were applied to a rounded ellipsoidal robot with no sharp edges. (**A**) Photo of the rounded ellipsoidal robot. (**B**) CAD model of the robot. The robot shell was cropped from a full ellipsoidal shape (translucent green). Other features are the same as in **Figure 3-3B**. (**C**) Touch sensory cells detecting contact positions. The cells were designed to be shortened along *z*' direction. (**D**) Maximal (i) position and (ii) normal direction errors of each touch-sensitive cell. The pattern of the cell is from robot side view. *x*'- and *z*'-axes show robot body frame. Because the left and right shells are mirrored, only the right shell

is presented. Bar rooting at the center of a cell shows error on that cell, whose height and color show error magnitude. (**E**) Relative error ε of using fore-aft force *Fx*, contact force roll torque T_α, and pitch torque T_β as the landscape gradients, and using reconstructed landscape (*PE*) and its gradients to estimate the ground truth. White and gray bars show using shield-shaped robot (**Figure 3-3A**) and (A) rounded ellipsoidal robot, separately. Bars and error bars are means ± 1 standard deviation of the average relative error of all average trials.

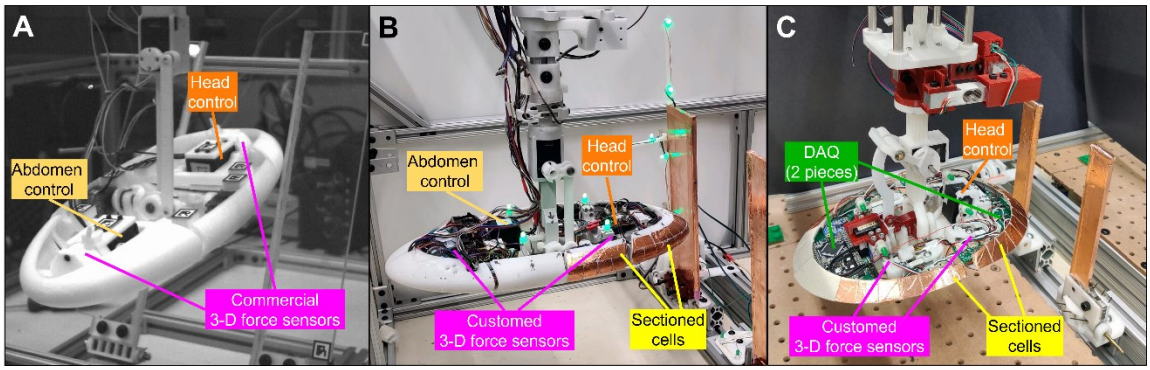

Figure 3-10: Iterative development of sensor-instrumented robot to enable force and contact measurement. (**A**) The first iteration. The robot was capable of head and abdomen oscillation and contact force sensing using commercial 3-D force sensors. This robot cannot sense the contact position nor separate the contact force with either beam, because the commercial 3-D force sensors were too bulky to place multiple of them in the confined space near the head. (**B**) The second iteration. Small, low-cost, custom-made 3-D force sensors were used. The head, body, and abdomen were separated from the middle so that the force sensors could individually sense the contact force from either beam. Sectioned cells were planted on the robot's head and front body surfaces to enable contact position sensing. The robot often suffered from signal loss issues due to the long wiring to a DAQ board that was far from it. (**C**) The third iteration. To make the robot the same size and shape as in the previous study [31], the body and abdomen were merged, and the shell was designed to be shield-shaped. Customed DAQ boards (2 pieces) were deployed to reduce wiring and signal transmission issues. The robot was damaged once the gap between the head and body was caught by a beam.

Chapter 4 Bio-inspired control strategy for least-resistance obstacle traversal

4.1 Author contributions

Yaqing Wang and Chen Li designed research; Yaqing Wang and Xiyuan Wang set up simulation environment. Xiyuan Wang confirmed simulation resembled reality; Yaqing Wang developed algorithm; Yaqing Wang performed simulation; Yaqing Wang analyzed data; and Yaqing Wang and Chen Li wrote this chapter.

4.2 Acknowledgment

We thank Shai Revzen, Ioannis Kevrekidis, and Anastasia Georgiou for discussions on saddle-finding algorithms; Floris Van Breugel and Benjamin Cellini for discussions on observability recovery; Dan Negrut, Radu Serban, and Luning Bakke for ProjectChrono simulation software support; Qihan Xuan and Daniel Zhan for suggestions on simulation design. This work was supported by a Beckman Young Investigator Award from Arnold and Mabel Beckman Foundation for Chen Li, a Career Award at the Scientific Interface from Burroughs Wellcome Fund for Chen Li, and a Bridge Grant from Johns Hopkins University Whiting School of Engineering for Chen Li.

4.3 Summary

Insects like cockroaches excel at traversing complex 3-D terrains with cluttered large obstacles, outperforming even the most advanced robots. They achieve this by transitioning across locomotor modes. Previous studies discovered that such locomotor mode transitions correspond with barrier-crossing transitions on a potential energy landscape resulting from physical interaction between the animal/robot and obstacles. If an animal/robot crosses barriers near saddle points, it encounters the least resistance. However, potential landscape-based control studies largely focused on finding minima and maxima, whereas the traditional saddle-seeking methods assumed perfect knowledge of the landscape or did not control a physical agent to cross saddles. Here, we developed a bio-inspired control strategy for seeking and crossing saddle points on the potential energy landscape for least-resistance obstacle traversal. We tested it in a simulation of a self-propelled ellipsoidal robot (similar to cockroaches) traversing grass-like beam obstacles. Inspired by cockroaches' behavior of wedging into cracks between cluttered obstacles to go in, the simulated robot physically pushed and oscillated against the obstacles to sense contact forces and torques, which provided sufficient estimates of landscape gradients. This allowed the robot to reconstruct a local piece of landscape and estimated the direction to a nearby saddle point. Inspired by cockroaches' and flying insects' behaviors of frequent crosswind turning when identifying a plume direction, the simulated robot turned when the saddle point direction was not detectable. Our strategy enabled the robot to traverse the beam obstacles resembling a cockroach with increased probability and reduced time and energy costs. Varying parameters in our strategy gave various performances, which allowed the strategy to adapt to different needs. Our work not only merged the potential

energy landscape modeling in robotic planning and control, which further enlarged accessible terrain and facilitated critical applications, but also inspired new understandings of animals' planning and control logic of obstacle traversal.

4.4 Introduction

Many applications require mobile robots to navigate in complex terrains full of cluttered, large obstacles, such as search and rescue in earthquake rubble [27], environmental monitoring in mountain boulders and forest debris [28], and planetary exploration through large Martian and Lunar rocks [29]. One common approach for 2-D navigation on the ground floor is avoiding obstacles [253] using artificial potential fields (also called navigation functions) [95,96] (**Figure 4-1A**). Usually, robots use vision to detect obstacles. Then, they construct an artificial potential field (**Figure 4-1B**), which usually has a global minimum at the goal point to attract the robot, and artificially defined high potential regions around the obstacles to keep them away. For sparse obstacles, where the high potential regions from obstacles do not overlap, robots usually can follow a gradient descent path [97] to reach the goal while avoiding all obstacles. For slightly denser obstacles, where the high potential regions from some adjacent obstacles overlap, there is no gap between them for a gradient descent path. Following such a path from the starting point may lead to entrapment at a local minimum basin formed by the high-potential regions around the obstacles. To avoid entrapment, robots can perform global optimization strategies (e.g., particle swarm optimization [286], simulated annealing [287], etc.) on the artificial potential field to find a collision-free trajectory to the global minimum and follow it to reach the goal. Robots can also facilitate other strategies to avoid obstacles [98].

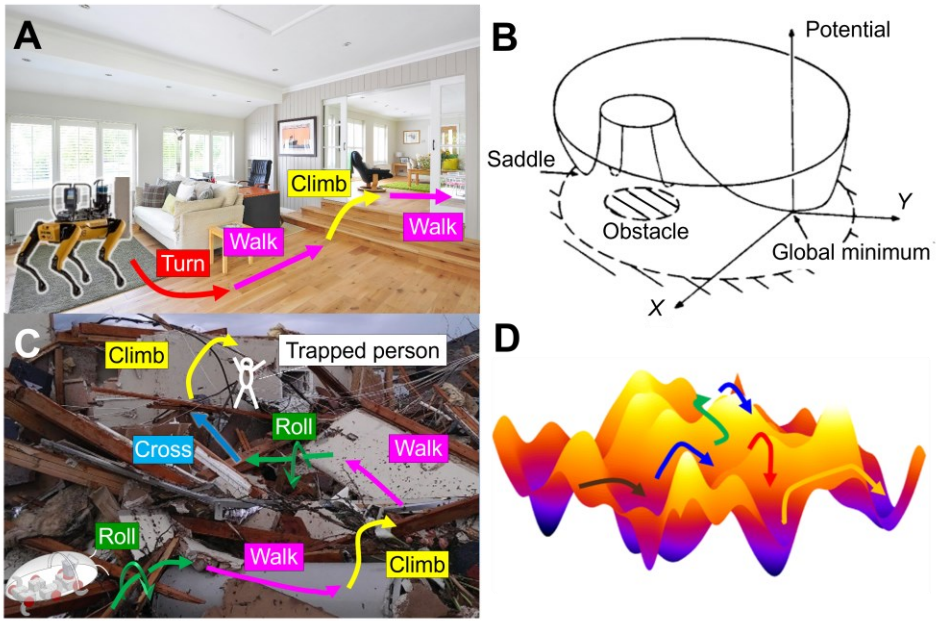

Figure 4-1: Envisioned potential energy landscape approach to enabling legged obstacle traversal to complement obstacle avoidance based on artificial potential functions. (**A**) A legged robot navigates indoors by avoiding large obstacles. (**B**) Artificial potential field approach for obstacle avoidance. (**C**) Envisioned traversal of cluttered large obstacles (e.g., earthquake rubble for search and rescue). (**D**) Potential energy landscape approach for obstacle traversal. (A) Image courtesy of Pixabay on Pexels and Boston Dynamics. (B-D) Adapted from [26,31,95].

However, robot navigations based on the artificial potential field approach fail in terrains with densely cluttered (spacing ~ or < body size), large (~ or > body size) obstacles (**Figure 4-1C**), where a collision-free trajectory to the goal point simply may not exist. To traverse such obstacles, robots must physically interact with (e.g., climb over, squeeze through, push over) them, which leads to multiple challenges: physical interaction with obstacles often requires large 3-D rotations [26], which is dangerous (e.g., robots may flip over when losing stability) and strenuous [31]. The robots cannot easily accumulate kinetic energy due to the continuous collision with the obstacles. Also, the urgency in applications

often requires the robot to reduce traversal time. All of these challenges encourage the robots to control their self-propulsion to generate appropriate forces and torques and plan and follow small-resistance trajectory (i.e., not only a 2-D path on the ground but a trajectory involving both translation and rotation) to reduce time and energy cost.

Towards this vision and inspired by the high-performance traversal of animals through densely cluttered obstacles, our lab established a new potential energy landscape modeling approach to explain and predict the locomotor modes and transitions. Potential energy landscapes emerged from the physical interaction of robots (and animals) with large, diverse obstacles that present distinct locomotor challenges [26,31,33–36,226]. Analogous to artificial potential fields for geometry-based obstacle avoidance, these real potential energy landscapes (**Figure 4-1D**) provide a physics-based foundation for robots to plan and control locomotor transitions (**Figure 4-1C**) to traverse obstacles (for a review, see [26]).

Without laboriously analyzing contacts and forces and composing and solving system dynamics equations based on Newton's Second law, the potential energy landscapes give a bird's-eye view to understand how to traverse obstacles with the least resistance. Physical interaction with obstacles results in stereotyped locomotor modes that lead to successful traversal or entrapment. These locomotor modes correspond to attractive basins on potential energy landscapes (the real potential energy over the robot's 3-D position and rotation). To traverse the obstacles, the robot (or animal) must propel to destabilize itself, escape from the basins of entrapment, and reach the basins of traversal on the potential energy landscape. Such transitions require overcoming the potential energy barriers separating these basins.

For each barrier-crossing transition, the least-resistance trajectory is the gradient minimal curve (i.e., the gradient extremal curve [216], which always follows the minimal gradient direction). Because the landscape gradients (i.e., conservative forces and torques) dominate the locomotor-terrain physical interaction and match the contact forces and torques [288], minimizing the gradients also minimizes the resistive forces and torques. Especially as a gradient extremal curve passes through saddle points, the least-resistance trajectory crosses the energy barrier at the saddle point (lowest energy point along a barrier).

To find the gradient minimal directions or saddle points on a potential energy landscape, the most straightforward approach is to obtain a large enough piece of the local landscape around the saddle point. A previous study demonstrated that a robot could reconstruct the potential energy landscape using the landscape gradients estimated from its obstacle contact forces and torques sensed during physical interaction with obstacles [288]. However, this requires the robot to physically visit every state in that piece of landscape to collect sensing data because force and torque sensing require direct contact (i.e., not remote). We propose to use more efficient methods to obtain the gradient minimal directions or saddle points**.**

Many existing strategies can identify the least-resistance path on a landscape without deliberately calculating a whole piece of it. For example, one can optimize an existing path between two minima on the landscape (a straight link between them should be suffice) to obtain the least-resistance path using methods such as dynamic programming or Pontryagin's minimum principle [205], ant colony optimization [206], and genetic algorithms [207]. Also, many strategies developed in computational chemistry can find

saddle points (i.e., saddle-seeking) [208]. For example, one can exhaustively explore the whole initial minimum basin to find the saddle point, such as the metadynamics method [209], the adaptive biasing force method [210], etc. One can also trace a curve between the two minima and minimize the energy along it, such as the nudged elastic band method and its variants [211–213]. One can also approach a saddle point from a minimum following a continuous curve, such as following Newton trajectories [214], orthogonal trajectories [215], gradient extremals [208,216], dimer method trajectories [217], gentlest ascent dynamics [218], etc.

Despite these methods, we still propose a new strategy to let robots identify the gradient extremal direction on the potential energy landscape and cross the energy barrier near the saddle point to traverse obstacles with the least-resistance. The existing methods do not apply to robots that want to traverse an unknown obstacle in one trial. Specifically, some strategies visit the states that do not form a continuous curve in space [206,207,211–213], which requires the robot to be able to obtain the potential energy of a remote state. Some strategies require strictly following a curve incompatible with robot dynamics [208,214–218]. The other strategies exhaustively explore the minimum basin, which is heavily time- and energy-consuming [209,210].

Surprisingly, animals were observed to make locomotor transitions by crossing the barrier at the saddle point on the potential energy landscape. This suggested that the animals' sensing and control strategy resulted in saddle-seeking behavior despite not having the concept of the potential energy landscape. Specifically, to traverse cluttered beam obstacles with gaps narrower than their body width and too stiff to push across, discoid cockroaches often transitioned from a strenuous pitch mode (pushing forward

against the beams with large body pitching, **Figure 4-2A**, blue) to a much easier roll mode (rolling into beam gaps and maneuvering through, **Figure 4-2A**, red) [31,36,226]. When the system trajectories were viewed on the potential energy landscape over the body roll-pitch space (**Figure 4-2B**), this pitch-to-roll transition corresponded to a transition from a pitch basin to a roll basin [31,226]. This barrier crossing usually happened near the saddle point (pitch angle error = 3° ± 11°, only 6% ± 22% of the animal's body pitch range. **Figure 4-2C**. Data from [226]).

We speculated that animals estimated the least-resistance direction by sensing the contact forces with the obstacles, enhanced by exploratory motions. The discoid cockroaches repeatedly oscillated their heads and rubbed their pronotums against the beam edges [226] (**Figure 4-2D**), seemingly to try to wedge their heads into the obstacle gap (also for shrubs and rock cracks [31,36,219,226]). Insects can use proprioceptive and tactile sensing [140,141] to detect or infer the obstacle's resistive forces. It is plausible that they used such exploratory motions to sample contact forces (and resulting torques) around its position (and orientation) to search for a least-resistance direction for a quick escape into the gaps or cracks.

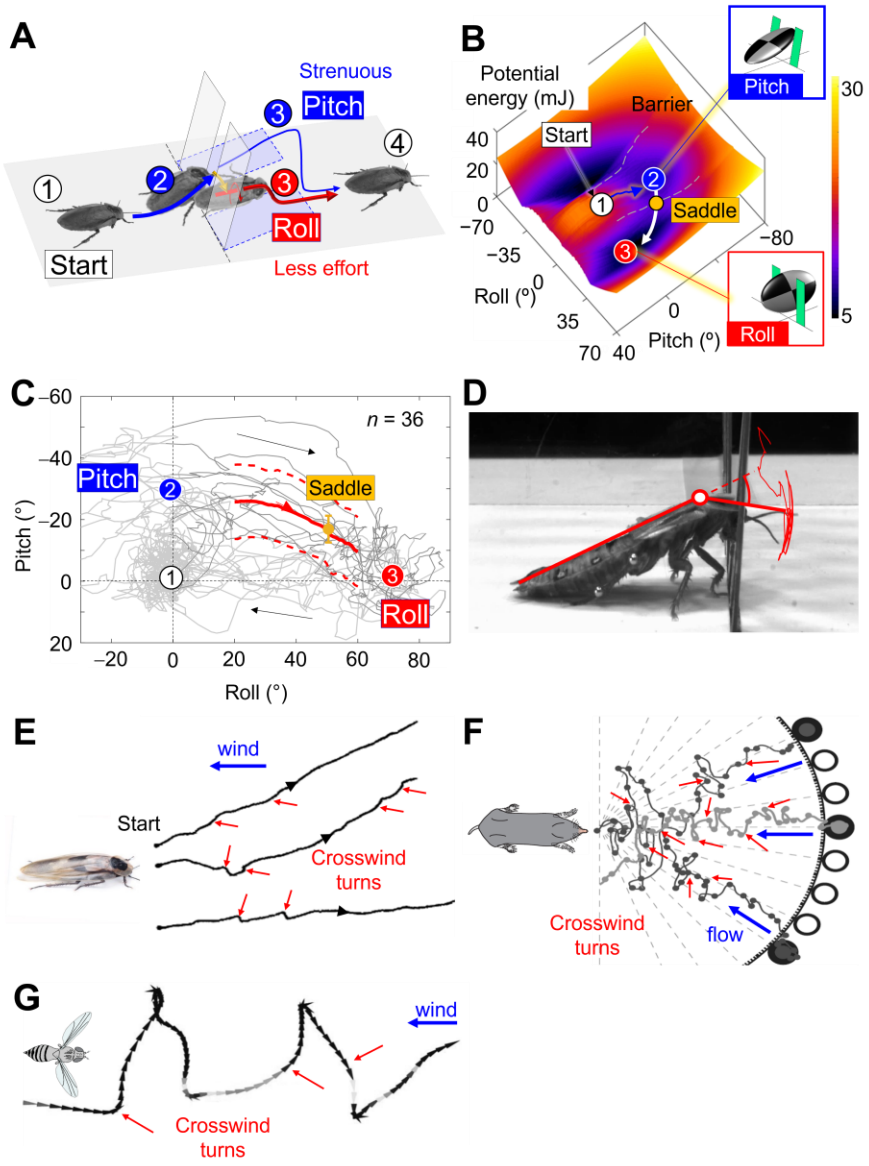

Figure 4-2: Inspiring biological behaviors. (**A**) Cockroaches traversed cluttered grass-like beams with small gaps (< body width). They used a strenuous pitch mode (blue) or a less strenuous roll mode (red). (**B**) Potential energy landscape of (A) over roll-pitch cross-section when the cockroaches were close to the beams. A pitch basin (blue) corresponding to the pitch mode in (A) and left- and right-roll basins (red) corresponding to the roll mode in (A) on the landscape are separated by potential energy barriers (gray dashed curves). The least-resistance path from the pitch to the roll basin crosses the barrier (gray) at the saddle point (orange). (**C**) The discoid cockroach transitioned from the pitch to the roll mode by crossing the energy barrier at the saddle point on the potential energy landscape.

(**D**) Cockroaches repeatedly oscillated their heads and rubbed the pronotums against the beam edges when negotiating the beams. Head flexion angle was defined as the relative pitch angle between the animal's head and thorax. Red curve shows representative head oscillation from a trial. (**E**) Trajectory of a cockroach tracking stimuli in air currents. (**F**) Trajectory of an eastern American mole's head tracking odorants. (**G**) Trajectory of a fruit fly tacking a plume in air currents. In (E-G), animals exhibited significant crosswind turning oblique to the wind directions. (A, B, D-G) Adapted from [31,185,187,189,226].

Although robots can obtain the gradient minimal direction from force sensing, this force sensing motion has a potential conflict with the motion to follow the gradient minimal direction. Animals also frequently encounter similar problems reconciling competing motion demands from sensing and locomotion. They use two strategies (not the only two) to solve this conflict. Firstly, they separate the time into "explore" and "exploit" phases for sensing and locomotion demands [195]. Secondly, they conduct crosswind turns to enhance sensing. For example, cockroaches [185,186], moles [187], and flying insects (fruit flies [188–190] and moths [191]) generate a motion that is oblique to the overall desired direction (i.e., a crosswind turn relative to a plume of sex pheromone or food odor) (**Figure 4-2E-G**), hypothetically to maintain the detectability of the desired direction [192–194].

All these animal behaviors inspired a control strategy that enables robots to physically interact with obstacles and traverse them. Inspired by the cockroaches' exploratory motions, we propose the robot should similarly sample contact forces and torques around neighboring states to reconstruct a local landscape and estimate and follow the gradient minimal direction to make least-resistance mode transitions to traverse obstacles. Inspired by cockroaches', moles', and flying insects' crosswind turns, we propose the robot should generate an appropriate self-propelled movement that is oblique

to the gradient minimal direction in a temporally separated phase to maintain the detectability of the desired direction. This control strategy provides robots with a new method to find and follow a least-resistance path to transition between locomotor modes and traverse unknown terrain**.**

To test the control strategy, we used a simulated model system of an ellipsoidal robot traversing a pair of grass-like beam obstacles. Our simulation resembled a physical robotic system [31,288], which was a robophysical model of a cockroach traversing grass-like obstacles [31]. We directly added the force and torque controls to the robot's translational and rotational motion and applied our strategy to these controls. We simulated this system using physics-based software and evaluated the robot's obstacle traversal performance. We hypothesized that (1) this strategy facilitates a high performance in locomotor transition and obstacle traversal; (2) adjusting the parameters in the strategy makes the robot behave differently to adapt to various requirements; (3) this bio-inspired strategy leads to a robot's motion that resembles animal behavior. To test the first hypothesis, we simulated the robot both with and without our strategy applied and evaluated their performance. To test the second hypothesis, we systematically varied multiple key parameters in the strategy and analyzed their effects on the performance. To test the third hypothesis, we compared the robot trajectory and behavior (with our strategy applied) to the animals'.

4.5 Methods

In this section, we first introduce our bio-inspired control strategy. Then, we elaborate on how we applied this strategy to our simulated model system that enabled the

robot to traverse the obstacles. And finally, we elaborate on how we analyzed the robot's performance under various conditions.

4.5.1 A new bio-inspired control strategy

To transition between locomotor modes, the robot should destabilize and escape from one local minimum basin to reach another on the potential energy landscape. To transition with the least resistance, the robot should follow a gradient minimal curve on the landscape. We propose the robot should first identify the gradient minimal direction. If the robot can identify this direction, it should follow and converge in that direction by generating a force (we call approach force). Or it should recover the detectability of such direction by generating either a force (we call oscillation force) to oscillate in the state space or a force (we call sideway force) to move in a direction that is oblique to the gradient minimal direction.

Identifying gradient minimal direction. We suppose the robot's state is attracted within a basin on a well-conditioned (at least 2^{nd}-order smooth) 2-D potential energy landscape (i.e., system's potential energy E as a function of robot state coordinate (x_1, x_2)). The robot can only obtain its coordinate (position and rotation angles) and contact force with the obstacles (i.e., landscape gradients with minor errors) with a limited bandwidth. We propose that the robot should first identify the gradient minimal direction by estimating an "infinite-small" local potential energy landscape, approximated using its 2^{nd}-order Taylor expansion:

$$E(x_1 + \delta x_1, x_2 + \delta x_2)$$

$$= E(x_1, x_2) + \left(\frac{\partial E}{\partial x_1}\right)_{(x_1,x_2)} \delta x_1 + \left(\frac{\partial E}{\partial x_2}\right)_{(x_1,x_2)} \delta x_2 + \frac{1}{2}\left(\frac{\partial^2 E}{\partial x_1^2}\right)_{(x_1,x_2)} \delta x_1^2$$

$$+ \frac{1}{2}\left(\frac{\partial^2 E}{\partial x_2^2}\right)_{(x_1,x_2)} \delta x_2^2 + \left(\frac{\partial^2 E}{\partial x_1 \partial x_2}\right)_{(x_1,x_2)} \delta x_1 \delta x_2,$$

$$= a_1 + a_2 \delta x_1 + a_3 \delta x_2 + \frac{1}{2} a_4 \delta x_1^2 + \frac{1}{2} a_5 \delta x_2^2 + a_6 \delta x_1 \delta x_2, \quad (4\text{-}1)$$

where the unknown variables $a_{1\text{-}6}$ are the 0th-, 1st- and 2nd-order coefficients. The gradients G and Hessian matrix H (i.e., matrix of second derivatives) of this landscape are:

$$G(x_1 + \delta x_1, x_2 + \delta x_2) = \begin{bmatrix} a_2 + a_4 \delta x_1 + a_6 \delta x_2 \\ a_3 + a_6 \delta x_1 + a_5 \delta x_2 \end{bmatrix}, \quad (4\text{-}2)$$

$$H(x_1 + \delta x_1, x_2 + \delta x_2) = \begin{bmatrix} a_4 & a_6 \\ a_6 & a_5 \end{bmatrix}. \quad (4\text{-}3)$$

The simplest way to obtain the 2nd-order coefficients is to do numerical finite differentiation (i.e., taking small equal-distant intervals around a point and computing the difference in function values), such as central finite difference over the gradient. However, due to stochastic physical interaction with obstacles, the robot cannot freely sample gradients over perfect equal-distant intervals around the current state. It must use its short memory of sensed gradients on its history trajectory. We propose that the robot should use an estimator inspired by the Savitzky-Golay filter [289]. The idea of the Savitzky-Golay filter is to fit successive sub-sets of adjacent data points with a low-degree polynomial by the method of linear least squares. Rearranging **Equation 4-2** and stacking the most recent k (k is the sample size) measurements, we obtain:

$$\underbrace{\begin{bmatrix} 1 & 0 & x_{1,1} & 0 & x_{2,1} \\ 0 & 1 & 0 & x_{2,1} & x_{1,1} \\ & & \vdots & & \\ & & \vdots & & \\ 1 & 0 & x_{1,k} & 0 & x_{2,k} \\ 0 & 1 & 0 & x_{2,k} & x_{1,k} \end{bmatrix}}_{C} \begin{bmatrix} a_2 \\ a_3 \\ a_4 \\ a_5 \\ a_6 \end{bmatrix} = \begin{bmatrix} G_1 \\ \vdots \\ G_k \end{bmatrix}, \tag{4-4}$$

where the ($x_{1,\,i}$, $x_{2,\,i}$) and G_i are the ith most recent sensed state coordinate and landscape gradients. From this, we obtain the pseudo-inverse of the matrix $\boldsymbol{C}$ on the left-hand side and multiply it with the right-hand side to obtain the coefficients $a_{1\text{-}6}$, which gives the local landscape (**Equation 4-1**) and its Hessian matrix H (**Equation 4-3**). Note that for our model system, the potential energy landscape was not static but evolved as the robot moved forward. So, this estimator was modified to compensate for the fore-aft translation. See Section ***S2*** for the details.

The gradient minimal direction is the eigenvector of the smaller eigenvalue of the Hessian matrix. Because the Hessian matrix is symmetric (**Equation 4-3**), its two eigenvalues ($d_1 > d_2$) should be real, which ensures that they are comparable (i.e., complex numbers are not comparable).

Examining the detectability of gradient minimal direction. We speculate that the robot fails to guarantee the correctness of the estimated gradient minimal direction in two cases. In the first case, both eigenvalues are similar. The robot may take the larger eigenvalue as the smaller one due to estimation error from the noisy landscape gradient sensing and obtain a direction perpendicular to the gradient minimal direction. We define the first failure case as occurring when both eigenvalues share the same sign. Because the landscape is well-conditioned (2-order smooth), the Hessian matrix's eigenvalues should be continuous. So, this case happens near the minima (where the eigenvalues are both

positive, $d_1 > d_2 > 0$) and maxima (where the eigenvalues are both negative, $d_2 < d_1 < 0$) on the potential energy landscape. We define these continuous regions as minimum and maximum neighborhoods, separately, and the rest regions on the landscape as saddle neighborhoods, where saddles exist ($d_1 > 0 > d_2$).

In the second case of failure, the matrix $\boldsymbol{C}$ in **Equation 4-4** is ill-defined, which hinders the estimation of coefficients $a_{1\text{-}6}$. This occurs when the most recent trajectory is too straight, which makes the third and fourth columns of matrix $\boldsymbol{C}$ approximately linearly dependent. We define the second failure case as occurring when the condition number of the matrix $\boldsymbol{C}$ in **Equation 4-4** is larger than an empirical threshold.

Generating approach force to follow and converge in the gradient minimal direction. We propose that the robot should generate an approach force to follow and converge in the gradient minimal direction in the saddle neighborhood. Here, we call this direction a climb direction (**Figure 4-3A,** red arrow) and the direction perpendicular to it a converge direction (**Figure 4-3A,** blue arrow). Intuitively, approaching a saddle point resembles climbing along a mountain valley (**Figure 4-3B**), where the gradient minimal curve is the valley path. To traverse the mountain with the least effort, travelers should ascend along the valley (i.e., climb direction, **Figure 4-3B**, blue arrow) to overcome the barrier while descending along the direction perpendicular to the valley (i.e., converge direction, **Figure 4-3B**, red arrow) to stay close to the valley path. Similarly, we propose that the approach force F_{app} should steer the robot to ascend along the climb direction (**Figure 4-3A,** blue arrow) and descend along the converge direction (**Figure 4-3A,** red arrow) at the same time. It is from a 1-order autoregressive process to have time consistency [290],

$$\overrightarrow{F_{app}(t+\delta t)} = \varphi_{app} \cdot \overrightarrow{F_{app}(t)} + \left(w_{climb} \cdot \overrightarrow{G_{climb}(t)} + w_{converge} \cdot \overrightarrow{G_{converge}(t)}\right), \quad (4\text{-}5)$$

where φ_{app} is the autoregressive coefficient, G_{climb} and $G_{converge}$ are components of the landscape gradients in the climb and converge directions, and w_{climb} and $w_{converge}$ are the climb and converge weights. Intuitively, the range for the climb and converge weight should be $w_{climb} > 0$ to let the approach force point to the same direction as the landscape gradients (i.e., ascending) and $w_{converge} > -1$ to let the minimum and saddle still be attractive in the converge direction. Moreover, the range for the climb and converge weight should be $w_{climb} \geqslant 1$ so that the approach force is sufficient to compensate for the landscape gradient and let the system state ascend along the climb direction, and $w_{converge} \geqslant 0$ so that the minimum and saddle are not less attractive than without this approach force in the converge direction.

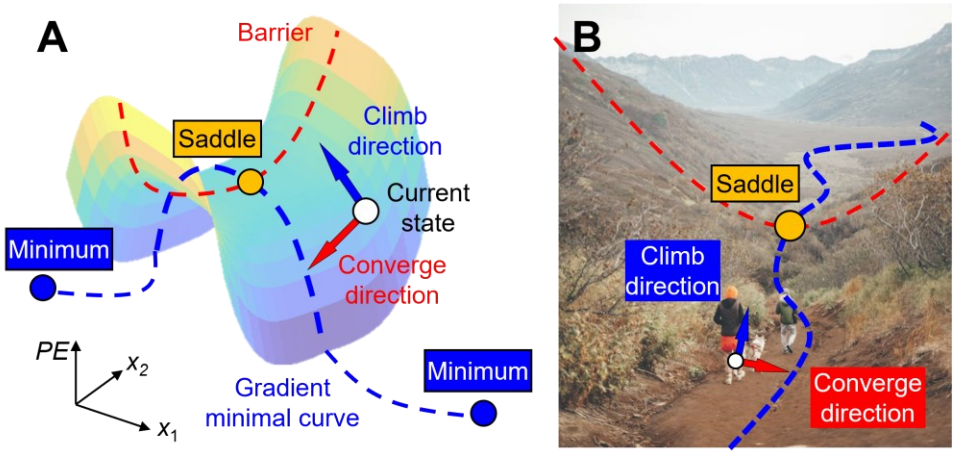

Figure 4-3: Following and converging to the gradient minimal direction. (**A**) Barrier-crossing direction on the potential energy landscape in a saddle neighborhood. White, blue, and orange points show the current state, minima (out of this saddle neighborhood region), and the saddle point. To cross the barrier (red dashed curve), the state should do a gradient ascend along the climb direction (blue arrow) to approach the barrier while doing a gradient descent along the converge direction (red arrow) to converge to the gradient minimal (blue dashed curve) at the same time. (**B**) A metaphor of barrier crossing using a mountain climbing example. To climb over a mountain effectively, travelers go to the saddle point

(orange) instead of climbing up large barriers (red dashed curve). Similarly, travelers should do a gradient ascend along the climb direction to approach the barrier and a gradient descent along the converged direction to keep in the path (as gradient minimal). (B) Image courtesy of Roman Odintsov on Pexels.

Generating oscillation force to reach saddle neighborhood. We propose that the robot should generate an oscillation force to reach the saddle neighborhood in the first case of failure to detect gradient minimal directions. In the minimum neighborhood, the robot cannot ensure to obtain the correct gradient minimal direction. It should search for saddle neighborhoods using random, isotropic oscillation (e.g., Brownian motion) to enlarge its search area and probabilistically enter a saddle neighborhood. The oscillation force F_{osc} is also from a 1-order autoregressive process [290],

$$\overrightarrow{F_{osc}(t+\delta t)} = \varphi_{osc} \cdot \overrightarrow{F_{osc}(t)} + n_{osc} \cdot \overrightarrow{\epsilon_{osc}(t)}, \tag{4-6}$$

where φ_{osc} is the autoregressive coefficient, n_{osc} is the oscillation amplitude, and $\epsilon_{\text{osc}}(t) \sim N(0, \boldsymbol{I})$ is a unit, uncorrelated white noise vector following a zero-mean Gaussian distribution ($\boldsymbol{I}$ is an identity matrix).

To probabilistically enter a saddle neighborhood, the amplitude of the oscillation force (controlled by the oscillation amplitude n_{osc}) should be sufficiently large to accumulate enough potential energy. This process may be both time- and energy-consuming. To improve the probability of reaching a saddle neighborhood, the definition of minimum neighborhoods is further modified to shrink the minimum neighborhood and enlarge the saddle neighborhood. The modified minimum neighborhood was defined as the region where both Hessian matrix's eigenvalues are above a threshold ($d_1 > d_2 \geqslant n_{\text{shrink}} \times d_{2,\text{min}}$), where $d_{2,\text{min}}$ is the smaller eigenvalue e_2 at the local minimum (or practically, the

observed largest d_2), and n_{shrink} ($0 \leqslant n_{\text{shrink}} \leqslant 1$) is the shrink coefficient to determine the shrinkage of the minimum neighborhood. Specifically, when $n_{\text{shrink}} = 0$, the modified minimum neighborhood is the same as the original (**Figure 4-4A, B**); when n_{shrink} increases from 0 to 1, the modified minimum neighborhood shrinks towards the local minimum point (**Figure 4-4C**); when $n_{\text{shrink}} = 1$, the local minimum is on the edge of the minimum neighborhood (**Figure 4-4D**).

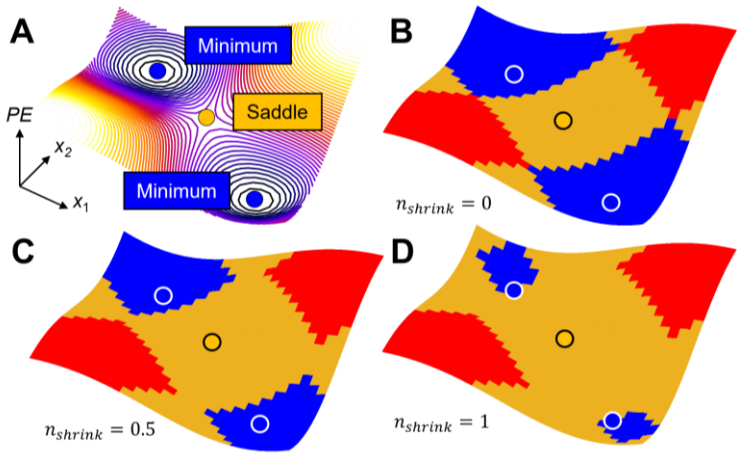

Figure 4-4: Modified saddle neighborhoods are enlarged as the shrink coefficient increases. (**A**) A simple 2-D potential energy landscape as an example. (**B**) The landscape is partitioned into minimum (blue), maximum (red), and saddle (orange) neighborhoods. Blue and orange points show minima and saddle points. (**C, D**) As the shrink coefficient n_{shrink} increases, the modified saddle neighborhoods are enlarged, "swallowing" the modified minimum neighborhoods.

In a maximum neighborhood, similarly, the robot should return to a saddle or minimum neighborhood at first. We propose that the robot should not generate control forces to naturally drift out of this neighborhood under the obstacle contact forces and torques.

Generating sideway force to recover the detectability of the gradient minimal direction. We propose that the robot should generate a sideway force in the second case of failure to recover the detectability of the gradient minimal direction by moving perpendicular to the current velocity. This sideway motion oblique to gradient minimal direction makes the columns of matrix $\boldsymbol{C}$ linearly independent. The sideway force F_{side} is also from a 1-order autoregressive process [290],

$$\overrightarrow{F_{side}(t+\delta t)} = \varphi_{side} \cdot \overrightarrow{F_{side}(t)} + \sigma_{side} \cdot \overrightarrow{v_{side}(t)} \cdot \epsilon_{side}(t), \tag{4-7}$$

where φ_{side} is the autoregressive coefficient, σ_{side} is the sideway force level, v_{side} is a unit vector that is perpendicular to the current robot velocity, and $\epsilon_{\text{side}}(t) \sim N(0, 1)$ is a unit white noise following a zero-mean Gaussian distribution.

The control force F_{ctrl} is the sum of approach force F_{app}, oscillation force F_{osc}, and sideway force F_{side} (note that the three forces are generated separately, but they can be non-zero at the same time due to the autoregressive process),

$$F_{ctrl}(t) = F_{osc}(t) + F_{app}(t) + F_{side}(t). \tag{4-8}$$

To summarize, to make a least-resistance transition from one basin to another basin on the potential energy landscape, the robot should follow a gradient minimal curve (strictly following is not required). To do this, the robot should first estimate the local potential energy landscape using a custom estimator. The robot should check if the estimation of this gradient minimal direction is reliable. If so, the robot should generate an approach force to steer the system to follow and converge in such a direction. If not, the robot should generate either an oscillation force to reach the saddle neighborhood or a sideway force to recover the detectability of such a direction based on the failure cases. See Section ***S1*** for the pseudo-algorithm.

4.5.2 Model system and simulation

To test the first hypothesis that this control strategy facilitates a high performance in locomotor transition and obstacle traversal, we verified the usefulness of our strategy by applying it in a simulated model system of a robot traversing grass-like beam obstacles (**Figure 4-5A**). This system was a simulated model of a physically robotic system previous studies [31,288] (**Figure 4-5B, C**). To traverse the beams, the robot should strenuously physically interact with the beams and transition between locomotor modes [31], which our control strategy should facilitate.

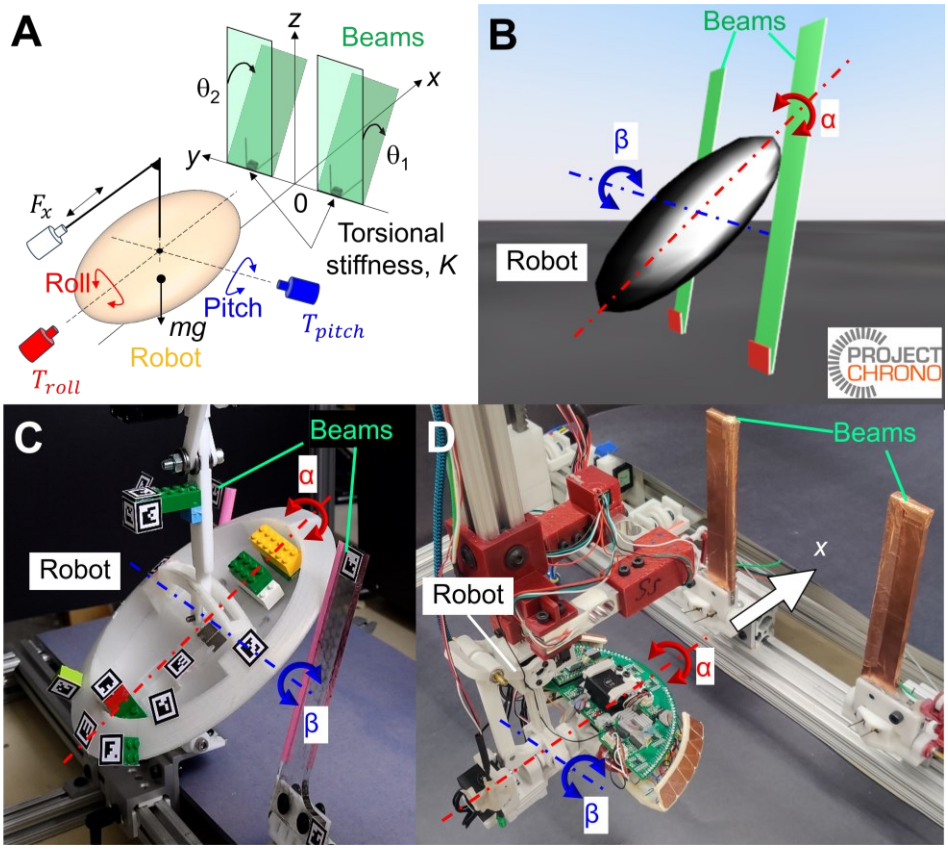

Figure 4-5: Model system of a robot traversing grass-like beam obstacles and its potential energy landscape. (**A**) Schematic of the simulated system. The robot body was a rigid, bottom-heavy ellipsoid actuated by fore-aft linear (white), roll (red), and pitch (blue) rotational motors. The beams were rigid rectangular plates with springs of torsional

stiffness K at the base, whose deflection angles were $\theta_{1,2}$. (**B**) Visualization of the simulated system in ProjectChrono. (**C** and **D**) Physical robotic models of the simulated robot used in previous experiments [31,288]. (C, D) Adapted from [31,288].

To observe how our control strategy led to locomotor transitions, we first introduce the model system, locomotor modes, the potential energy landscape of the model system, and simulation protocols.

Model system. The robot is a bottom-heavy ellipsoid hanging above the ground (**Figure 4-5A**, orange), whose motion is confined to the fore-aft translation (x) and roll (α) and pitch (β) rotations (**Figure 4-5A**, black, red, and blue, separately), defined as dimensions of the system states. The robot is actuated along the three dimensions by a direct-driven force/torque motor, mimicking leg propulsion while isolating control within each dimension. The beam obstacles (**Figure 4-5A**, green) are two thin, rigid rectangular blocks attached to the ground via Hookean torsional joints.

Locomotor modes and transitions. To traverse the beams, the robot should transition from (what we call) the pitch mode, where the robot tries to push down the beams, and it pitches up due to the resistive forces from the beams, to (what we call) the roll mode, where the robot rolls and maneuver through the gap between the beams.

Potential energy landscape. The robot physically interacting with the obstacles (**Figure 4-6A**) results in a potential energy landscape (**Figure 4-6B**). The potential energy of the system is the sum of the gravitational potential energy from the robot and the elasticity potential energy from the beams, which is a function of the system states (x, α, β). The sum of gravitational forces, obstacle contact forces, and their resulting torques roughly match the landscape gradients [288]. When the robot is distant from the beams

(**Figure 4-6A, i**), the potential energy landscape has a global (start) minimum at zero roll and zero pitch (**Figure 4-6B, i,** white), because the robot is bottom-heavy, and all potential energy of the system is from the gravitational potential energy of the robot. As the robot moves to the beams (**Figure 4-6A, ii**), the initial minimum transforms to the pitch minimum (**Figure 4-6A, ii,** blue), while two roll minima (**Figure 4-6A, ii,** red) emerge, corresponding to the pitch and roll modes, separately. The robot should transition from the pitch (**Figure 4-6A, iii**) to toll mode (**Figure 4-6A, iii'**) to traverse the beams, corresponding to escaping from the pitch minimum basin and reaching the roll minimum basin (**Figure 4-6A, iii**) on the potential energy landscape.

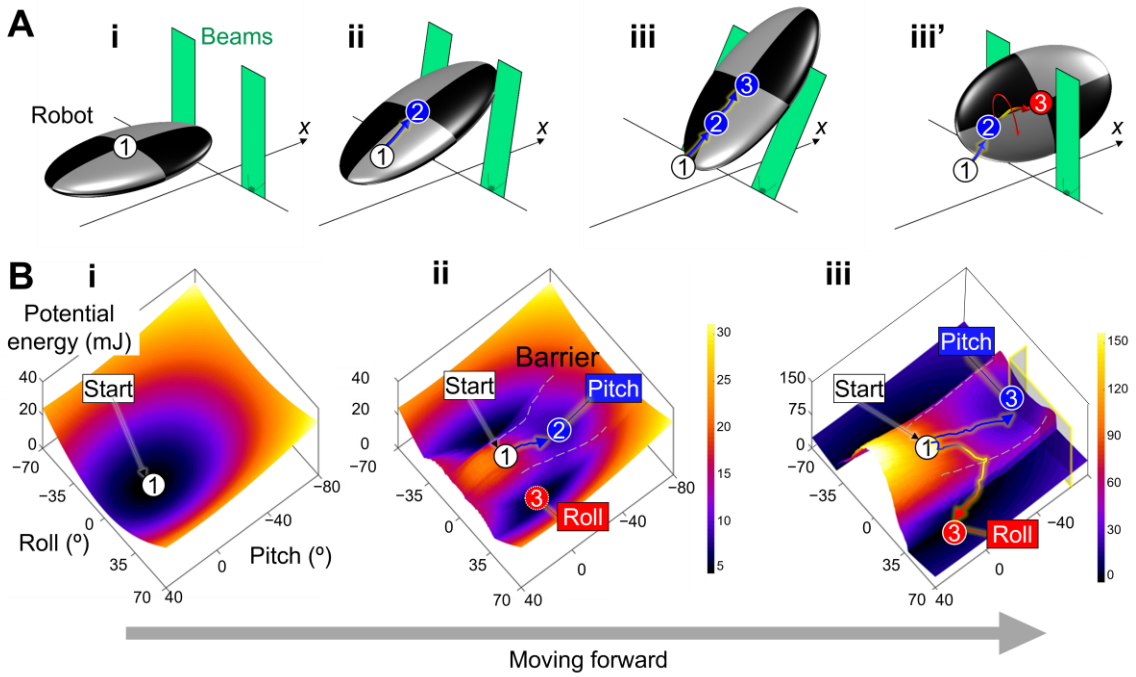

Figure 4-6: Locomotor transitions and potential energy landscape of the model system. (**A**) Schematics of the robot's body (checkered) interacting with two beams. After coming close to the beams (**i**), the body interacts with beams either using the pitch mode (**ii, iii**) or transitioning to the roll mode (**iii'**). (**B**) Snapshots of the potential energy landscape over roll-pitch space. Before physically interacting with the beams (**i**), the

landscape has a global basin. During interaction **(ii**, **iii)**, a pitch basin and left- and right-roll basins emerge on the landscape, separated by potential energy barriers (gray dashed curves). The start, pitch, or roll locomotor mode (white, blue, or red circles in (D)) emerges as the system is attracted to the global, pitch, or roll basin (white, blue, or red circle in (E)), separately. Arrows on the landscape show examples of state trajectory. Adapted from [31].

As animals use both mechanical feedback and sensory feedback when interacting with obstacles [4], we propose that our simulated robot should do the same. So, we design the motor to provide both "mechanical" and "control" forces and torques. To mimic the mechanical feedback control, the mechanical forces and torques are always designed to compensate 80% of the external forces and torques of the robot (i.e., the sum of gravitational forces, sensed obstacle contact forces, and their resulting torques) without delay. To mimic sensory feedback control, the control forces and torques are determined by the sensed robot state, velocity, and obstacle contact forces and torques. Specifically, the fore-aft control force is from a proportional-only controller to regulate forwarding velocity,

$$F_{x,active} = P_x\big(v_r - v_x(t)\big), \tag{4-9}$$

where P_x is the proportional gain, and v_r is the reference forwarding velocity. Because the beam stiffness is high, the maximum forwarding propulsive force (**Equation 4-9**, with forwarding velocity being zero) does not allow the robot to traverse by staying in pitch mode. The robot can only traverse using the roll mode (**Figure 4-6A, iii'**). The roll and pitch control torques are calculated from our control strategy (here, the control from our strategy are torques as generalized forces), where the remaining 20% of the external torques are used as the measured landscape gradients (i.e., only 20% of the original potential energy landscape is effective). All the control forces and torques on the robot are

updated at f = 50 Hz (i.e., having a delay between sensing and control), which was proven to be a practical sensory frequency [288].

Simulation protocol. Initially, the robot was at a distance in front of the beams (x = −100 mm, **Figure 4-6A, i**) so that it did not contact them. The robot was moved forward at a constant speed with the P-only controller. After it hit the beams, it slowed down due to the resistance from the beams. The robot was considered to be trapped in pitch mode (**Figure 4-6A, ii, iii**) when the robot's velocity was smaller than the threshold. When trapped, the robot generated control torques in roll and pitch directions calculated from our control strategy. Meanwhile, the robot obtained the trapping time t_{trap}, defined as the latest time span of being trapped. As the trapping time increased, the robot gradually increased its oscillation amplitude n_{osc} and shrink coefficient n_{shrink}, which asymptotically converged to their maximal values,

$$n_{osc} = n_{osc,max} \cdot \left(1 - \exp\left(-\lambda_{osc} \cdot t_{trap}\right)\right), \tag{4-10}$$

$$n_{shrink} = 1 - \exp\left(-\lambda_{shrink} \cdot t_{trap}\right), \tag{4-11}$$

where $n_{\text{osc,max}}$ was the maximal oscillation amplitude, λ_{osc} was the converge rate of oscillation amplitude, λ_{shrink} was the converge rate of shrink coefficient, also called the haste level, because it represented how urgent the robot wanted to escape the minimum neighborhood. The robot was considered to successfully traverse the beams if it reached enough distance ahead of the beams (x = 200 mm) within T = 100 seconds or failed to traverse otherwise.

The system was built and simulated in ProjectChrono [291], a physics-based modeling and simulation software. Compared to physical robot experiments, the simulation facilitated obtaining a large number of trials to examine the probabilistic behavior of the

robot (also in [39,237]). To reduce the sim-to-real gap [106,292,293], we carefully validated the simulation by conducting the same robotic control as in two previous experiments (i.e., the robot was moved forward at a constant speed and oscillated in the vertical direction of various frequencies with free rotation as in [31]; the robot was rotated to various roll and pitch angles and moved forward at a constant speed while sensing contact forces and torques with fixed rotation as in [288]) and compared the transversal probability and obstacle contact forces and torques. See Section ***S3*** for details. Also, to match the real system, we measured the friction coefficient between the physical robot and beam obstacles in [288] ($\mu = 0.2$). We did not add noise to the sensory data because the measured contact forces and torques obtained from the ProjectChrono simulation already contained noise, approximately F_{noise} (N) ~ $N(0, 13)$, T_{noise} (N·mm) ~ $N(0, 11)$, which gave a rough signal-to-noise ratio of 10. To reduce the effect from sensory noise, the robot applied an average filter with a time window of 0.02 s on the sensed contact forces and torques. See **Table 4-1** for the parameters and settings.

4.5.3 Examining the effects of parameters on performance

To test the second hypothesis that adjusting the parameters in the strategy makes the robot behave differently to adapt to various requirements, we varied the parameters and examined how they affected the robot's performance using our control strategy. We focused on four parameters: climb weight w_{climb}, converge rate w_{converge}, haste level λ_{shrink}, and maximal oscillation amplitude $n_{\text{osc,max}}$. We speculated that the first two parameters modifying the approach torque affected the speed and precision of following the gradient minimal direction, and the last two parameters modifying the minimum neighborhood size

and the oscillation torque affected the escaping speed and search area in the pitch basin. These affected the total transition speed and energy cost.

To first obtain the overall performance of our strategy, we fixed parameters (w_{climb} = 1.2, w_{converge} = 1.0, λ_{shrink} = 0.04, $n_{\text{osc,max}}$ = 1.0) and performed n = 1000 trials as **the** "Default" data group. To understand the functions of climb weight w_{climb} and converge rate w_{converge}, we systematically varied the climb weight w_{climb} from 1.2 to 2.0 with an increment of 0.2, and the converge rate w_{converge} within {-1.0, -0.5, 0.0, 0.5, 1.0, 2.0, 3.0, 4.0} while fixing the haste level λ_{shrink} = 0.04, and maximal oscillation amplitude $n_{\text{osc,max}}$ = 1.0, and performed 100 trials for each combination, which resulted in n = 4000 trials as the "Variation A" data group. To understand the functions of haste level λ_{shrink} and maximal oscillation amplitude $n_{\text{osc,max}}$, we systematically varied the haste level λ_{shrink} from 0.02 to 0.10 with an increment of 0.02, and the maximal oscillation amplitude $n_{\text{osc,max}}$ within {0.25, 0.5, 1.0, 2.0, 4.0}, while fixing the climb weight w_{climb} = 1.2 and converge rate w_{converge} = 1.0, and performed 100 trials for each combination, which resulted in n = 2500 trials as the "Variation B" data group.

To compare the performance with our control strategy to that without, we also conducted simulations where the robot did not use our strategy but only attempted to accumulate momentum and cross the barrier using kinetic energy fluctuation from oscillation (similar to [31]). Here, the control torque was only from oscillation $F_{\text{ctrl}}(t) = F_{\text{osc}}(t)$, and the oscillation amplitude was always maximal (i.e., $\lambda_{\text{shrink}} \to +\infty$, $n_{\text{osc}} \equiv n_{\text{osc,max}}$). We systematically varied the maximal oscillation amplitude $n_{\text{osc,max}}$ within {0.25, 0.5, 1.0, 2.0, 4.0}, and performed 100 trials for each combination, resulting in n = 500 trials as the "Control" data group.

4.5.4 Analyses and statistics

To test the first hypothesis, we quantified its performance using the traversal probability, traversal time, and energy cost. The energy cost was calculated as the integration of power from the three motors over time, which was the force/torque multiplied by the displacement if it was positive and zero if otherwise [237]. We also calculated saddle-seeking time (defined as the time span of the robot being in the saddle neighborhood before crossing the barrier) and accuracy (quantified by the error, defined as the pitch angle difference between the barrier-crossing point and the saddle point) to quantify the saddle-seeking performance, and escaping time (defined as the time span of the robot being in the pitch minimum neighborhood) to quantify minimum-neighborhood-escaping performance.

To test the second hypothesis, we tested whether monotonic relationships existed between the parameters and the robot's performance. To test if the climb and converge weights affected saddle-seeking performance, we calculated the Spearman's rank correlation between the climb weight and the saddle-seeking time and between the converge weight and the standard deviation of the saddle-seeking error in Variation A group. To test if the haste level and maximal oscillation amplitude affected the minimum-neighborhood-escaping performance, we calculated the Spearman's rank correlation between the two and the escaping time in Variation B group.

To test if the simulated robot correctly estimated the gradient minimal directions from sensed forces and torques, we theoretically calculated gradient minimal directions as the ground truth calculation and compared it with the simulated robot's estimation.

We also examined how the climb weight modulated self-propulsion that controlled the simulated robot motion besides the physical interaction with the obstacles. Because the approach torque was only determined by the potential energy landscape assuming perfect estimation of the landscape gradients (**Equation 4-5**), it was also a function of the robot's states, which could be considered as the gradient of an (artificial) control potential landscape (similar to [96]). The effect from both physical interaction with the obstacles and the approach torque was captured by an effective potential landscape, which was the sum of the real potential energy landscape and the artificial control potential landscape. To obtain the effective potential landscape, for each fixed climb weight of $w_{\text{climb}} = \{0, 1, 2\}$ with a fixed converge rate $w_{\text{converge}} = 0$, we first obtain the control potential landscape by applying a Helmholtz-Hodge decomposition [288,294] on the vector field of approach torques. Then, we added it to the potential energy landscape and obtained the effective potential landscape. With this effective potential landscape, we examined how the approach torque modified the attraction of minima and saddle points.

All the analyses except for statistical tests were performed using MATLAB R2021b (MathWorks, MA). Statistical tests were performed using JMP PRO 18 (SAS Institute Inc., NC).

4.6 Results

4.6.1 Simulated robot achieved high performance traversing obstacles

Our control strategy enabled a simulated robot to perform a pitch-to-roll transition on the potential energy landscape, resulting in a high obstacle traversal performance. The robot was always initially trapped around the pitch minimum $(\alpha, \beta) = (0.0° \pm 0.1°, -59.0°$

± 0.2°) at x = 40.2 mm ± 0.3 mm, where the propulsive force and the torque from the robot's gravity balance the beam resistance in fore-aft and pitch directions. Due to the high stiffness of the beam and limited propulsion, the robot could not use a pitch mode (**Figure 4-6A, iii**) to traverse. It must transition to the roll mode (**Figure 4-6A, iii'**) by crossing the barrier separating the pitch and roll basins (**Figure 4-6B, ii, iii,** gray) to traverse.

Our control strategy facilitated the pitch-to-roll transition. When the simulated robot did not use our control strategy but only generated a random oscillation (Control group), it did not traverse the obstacles (probability = 0% for all oscillation levels we tested) because it did not transition to the roll mode. In contrast, when using our strategy (Default group), the robot always traversed the obstacles (probability = 100%), with a small traversal time (83 ± 10 s) and energy cost (444 ± 43 mJ), because it transitioned from the pitch to roll mode. The maximum potential energy accumulation (233 ± 45 mJ) was much smaller than the needed potential energy accumulation using a pitch mode (379 mJ), calculated as the potential energy increase if both beam obstacles did not bounce back. These supported our first hypothesis that our strategy facilitates a high performance in locomotor transition and obstacle traversal.

4.6.2 Control forces led to a saddle-seeking behavior

Using our control strategy, the simulated robot showed a saddle-seeking behavior on the potential energy landscape (**Figure 4-7A**). The three control forces achieved their desired functions. Specifically, the approach force steered the system state to follow the gradient minimal curve and cross the barrier near the saddle point. Before crossing the barrier, the approach force (**Figure 4-7B, cyan**) approximately pointed toward the gradient

minimal direction) (**Figure 4-7C, i**) because the estimated gradient minimal direction matched the ground truth calculation (direction error = 0° ± 31° in Default group) (**Figure 4-7C, ii**). As a result, the robot's state crossed the barrier near the saddle point (**Figure 4-7A**) (distance to saddle point = 1.4° ± 1.2° in Default group).

The oscillation force perturbed the system state to escape from the minimum neighborhood. The probability density of the robot's state gradually diffused (**Figure 4-7D**), indicating that the search area for an escape from the pitch minimum neighborhood was gradually enlarged. As a result, the robot reached a state distant from the pitch minimum when it escaped from the minimum neighborhood (maximal distance = 9° ± 2° in Default group).

The sideway force effectively recovered the detectability of the gradient minimal direction. After the sideway force was triggered, the condition number still increased but was bounded (maximal condition number = 55 ± 42 of all triggers in Default group) and reduced below the threshold quickly (condition number = 16 ± 12 at 0.3 s after the sideway force was triggered in Default group) (**Figure 4-7E**), which indicated that the sideway force recovered the detectability of the gradient minimal direction.

All of these supported our first hypothesis that our control strategy facilitated a high performance in locomotor transition and obstacle traversal.

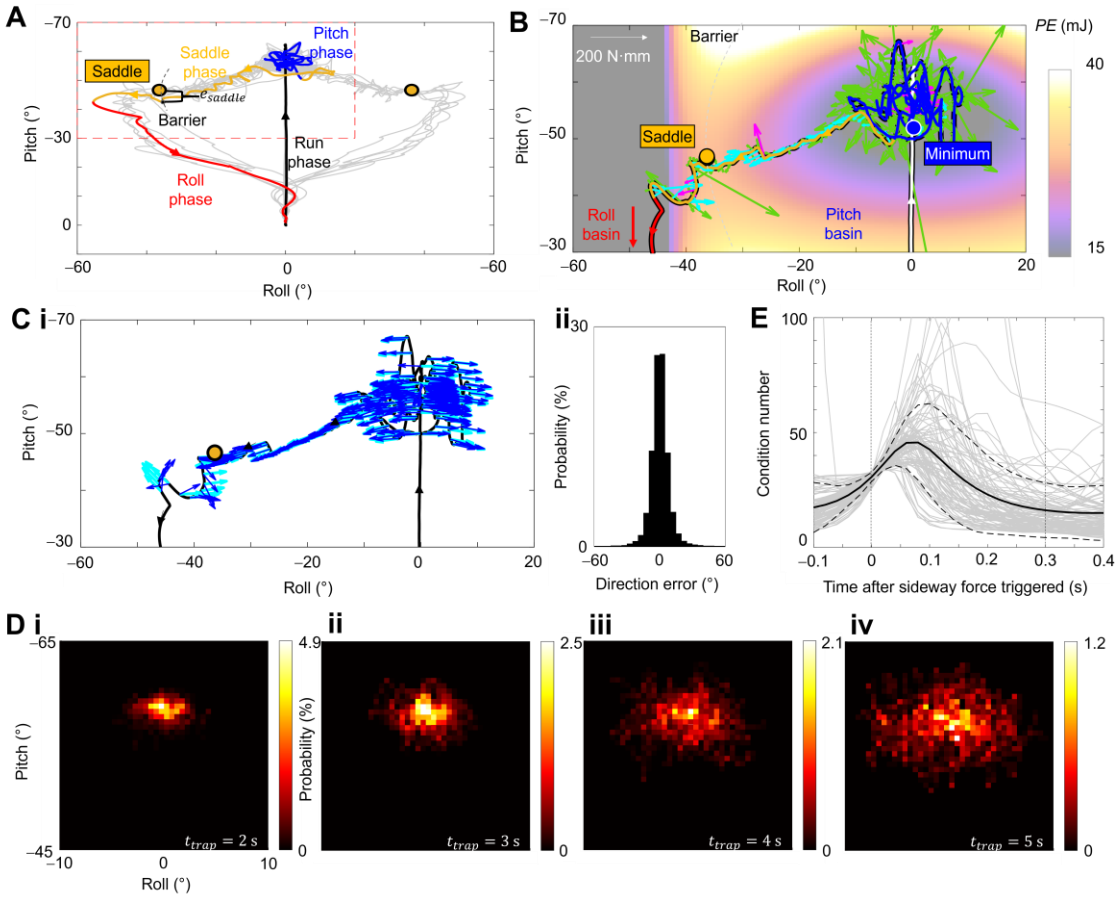

Figure 4-7: Obstacle traversal performances. (**A**) Simulated robot's trajectory in roll-pitch space, showing the robot transitioned from pitch to roll mode to traverse obstacles. Black, blue, orange, and red curves are one simulated robot trajectory, representing the robot moving close to the beams, in pitch minimum, saddle, and roll minimum neighborhoods, separately. Arrows show their directions. Gray solid curves are trajectories from 10 other randomly selected trials. Orange points are saddle points on the energy barrier (gray dashed curve). (**B**) Applied active forces in the representative trial in (A). Trajectory of the robot moving close to the beams (black in A) is changed to white for better visualization. Cyan, green, and magenta arrows are approach torque F_{app}, oscillation torque F_{osc}, and sideway torque F_{side}, separately. Background is the potential energy landscape snapshot. Blue and orange points are the pitch minimum and saddle point. Gray dashed curve is the energy barrier. (**C**) (**i**) Estimated gradient minimal direction (blue)

matched with ground truth calculation (cyan) in the representative trial in (A). (**ii**) The distribution of the direction estimation error. In (B and C), the roll-pitch space is zoomed in the red dashed box in (A), and control torques and gradient minimal directions are shown in every five control loops for a clear demonstration. (**D**) Probability density distribution of robot's state in pitch neighborhood. (**i-iv**) are from trap time t_{trap} = 2–5 s. (**E**) Condition number of matrix $\boldsymbol{C}$ as a function of time after the sideway force was triggered. Solid and dashed curves show average ± 1 standard deviation of all triggers. Gray curves show data from 100 random triggers.

4.6.3 Parameters modulated performance

Parameter variation modulated the robot's saddle-seeking and minimum-neighborhood escaping performances. We observed that a higher climb weight increased saddle-seeking speed. In Variation A group where the climb weight w_{climb} was varied, as the climb weight increased, the saddle-seeking time significantly decreased **(Figure 4-8A)** ($\rho = -0.69$, $P < 0.001$, Spearman's rank correlation), indicating that the saddle-seeking speed increases.

We observed that a higher converge weight increased trajectory convergence. In Variation A group where the converge weight $w_{converge}$ was varied, as the converge weight increased, the trajectory divergence (quantified as the standard deviation of saddle-seeking error) decreased **(Figure 4-8B)** ($\rho = -0.88$, $P < 0.001$, Spearman's rank correlation).

We observed that a higher haste level increased escaping speed, but a higher oscillation amplitude did not. In Variation B group where the maximal oscillation amplitude $n_{osc,max,}$ and the haste level λ_{shrink} was varied, as the haste level increased, the escaping time decreased **(Figure 4-8C)** ($\rho = -0.64$, $P < 0.001$, Spearman's rank correlation).

However, no clear trend of the escaping time was observed as the oscillation amplitude increased **(Figure 4-8D)** (P = 0.53, Spearman's rank correlation).

All of these supported our second hypothesis that adjusting the parameters in the strategy made the robot behave differently.

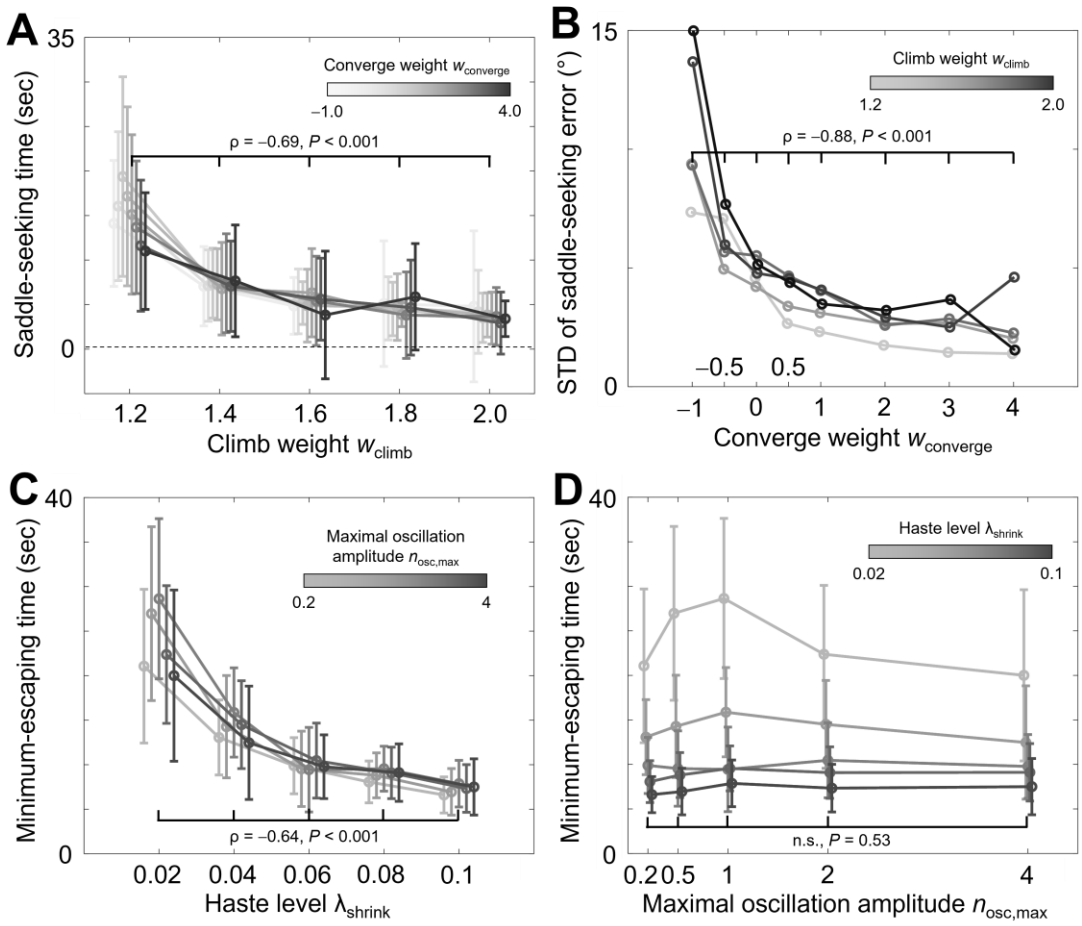

Figure 4-8: Saddle-seeking and obstacle traversal performance varies with the parameters. (**A**) Saddle-seeking time and (**B**) standard deviation of error as functions of climb w_{climb} and converge weight $w_{converge}$. (**C** and **D**) Escaping time as a function of (C) haste level λ_{shrink} and (D) maximal oscillation amplitude $n_{osc,max}$. Curves and error bars are average ± 1 standard deviation of all trials. Statistics are from Spearman's rank correlation.

4.6.4 Robotic motion resembled animal behavior

To elaborate on how our control strategy led to a robotic motion (**Figure 4-9A**) that resembled animal behavior (**Figure 4-9B**), we first describe the animal behavior [31,36,226] while speculating the animal's logic for motion planning and control. Shortly after hitting the beams, the animal passively pitched their body up due to the resistance from the beam (**Figure 4-9A, i**). We speculated that the animal kept applying the same control as it approached the flat ground due to control hysteresis (i.e., not switched to another control for interacting with obstacles in time). This was evident by some cockroaches even flipping over after they hit the beams [36]. After hitting the beams and stopping, the animal often initially kept using the pitch mode to try to push down the beams and traverse, but then started oscillating its body in both roll and pitch rotations (**Figure 4-9A, ii**). We speculated that the animal initially trusted the default pitch mode. However, as the animal kept being trapped and not escaping, it gradually lost its faith in this pitch mode. It became more eager to move/escape by finding and reaching another locomotor mode (not had to be the roll mode). This urgency explained why sometimes the animal did not traverse the obstacle but fled sideways or climbed on the beam to traverse [36]. Finally, the animal rolled its body into the beam gap (**Figure 4-9A, iii**) before the pitch-to-roll transition barrier was lower than the kinetic energy fluctuation level from body oscillation [31]. This may because instead of using the oscillation to make locomotor transition in a passive, stochastic manner, the animal identified a possible transition direction (in state space) with a small resistance, generating directional self-propulsion to make the transition.

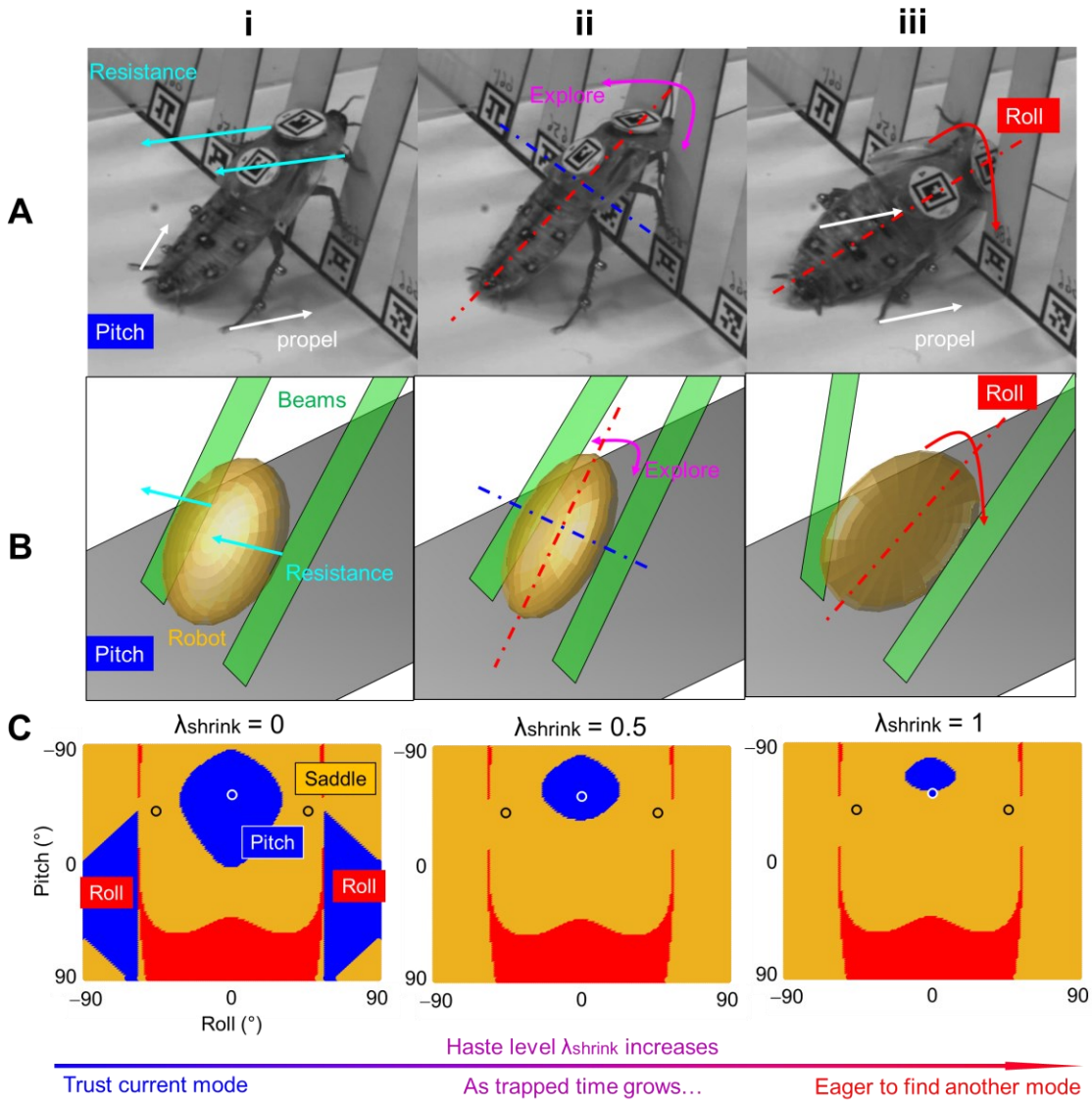

Figure 4-9: Bio-inspired strategy leads to a robotic motion that resembles animal behavior. (**A**) A cockroach traversed grass-like beam obstacles. The animal (**i**) used the pitch mode, (**ii**) explored for another mode, and (**iii**) transitioned to the roll mode. (**B**) A simulated robot traversed beam obstacles, showing similar (**i**) pitch mode, (**ii**) exploration, and (**iii**) roll mode motion as the animal. (**C**) Evolution of pitch minimum and saddle neighborhoods on the potential energy landscape where the robot state crossed the barrier (x = 58 mm). Blue, red, and orange regions are minimum, maximum, and saddle neighborhoods. Blue and orange points are pitch minimum and saddle points. Haste level (**i**) $\lambda_{shrink} = 0$, (**i**) $\lambda_{shrink} = 0.5$, (**i**) $\lambda_{shrink} = 1$. (A) Adapted from [226].

We observed that the simulated robot's motion resembled a cockroach's behavior in traversing the grass-like beam obstacles (**Figure 4-9B**, also **Movie 5**). The robot also pitched its body up after hitting the beams due to the delay in applying our control strategy (**Figure 4-9B, i**). After hitting the beams and stopping, the robot was also trapped in pitch mode, and gradually oscillated in a stochastic matter (**Figure 4-9B, ii**). This showed that the robot gradually lost faith in the current locomotor mode and became more and more eager to escape the current one and change to another, as indicated by the expanding search area (**Figure 4-7D**) and expanding saddle neighborhoods (**Figure 4-9C**). Finally, when the robot state was still away from transition barrier but already in the saddle neighborhood, it generated a directional approach force to steer to cross the barrier around the saddle point (**Figure 4-9B, iii**).

This similarity between the animal's and robot's motion supported our third hypothesis that our bio-inspired control strategy leads to a robot's motion that resembles animal behavior.

4.7 Discussion

4.7.1 Major achievements

In summary, we proposed a new bio-inspired control strategy. Based on the potential energy landscape approach served as a model for robot-obstacle physical interaction [26,288], such strategy enabled the robot to transition between locomotor modes and traverse the obstacles with the least-resistance path. This was achieved by following a gradient minimal direction on the potential energy landscape while maintaining the detectability of that direction. Using a simulated robot traversing grass-like beam

obstacles, we verified the usefulness of this strategy and examined the parameters' functions. This was an initial step to finally enable a physical robot to traverse large obstacles and complex 3-D terrains using sensory feedback control, which advanced robots still struggle to do [15,20].

4.7.2 Similarities between the animal's and robot's control

We speculate that the similarities between the animal's and robot's motion were from the similar requirements between the cockroach's hurriedly escaping and the robot traversing unknown obstacles, which resulted in similar planning and control logic. Firstly, they both wanted to traverse unknown obstacles in the first trial. If the animal failed to traverse the obstacles quickly and was trapped by them, it may result in a fatal outcome (e.g., being spotted by a predator and killed). Similarly, if a robot was trapped by the obstacle or flipped over during physical interaction with the obstacle, it usually could not recover by itself, which usually resulted in being abandoned and a costly failure [20,295]. This hindered many saddle-seeking strategies based on trial-and-error (e.g., dynamic programming [205], ant colony optimization [206], genetic algorithms [207], nudged elastic band method and its variants [211–213], etc.) to be applied. Secondly, they had no prior knowledge about the obstacles. This meant that the potential energy landscapes from (or, more generally, the physical interactions with) the obstacles were not known in advance, and the animal or robot should sense and "learn" the interactions. Note that the grass-like obstacles in previous experiments [31,36,226] were custom-made and definitely not fully unknown to cockroaches. Thirdly, they both (mainly) sensed noisy contact forces and torques and planned and modulated actuation using sensory feedback in a limited bandwidth. When physically interacting with beam obstacles, the cockroach sensed the

obstacle contact forces and positions using groups of campaniform sensilla and sensory hairs embedded in its exoskeleton [140,141,235] and generated feedback control [4]. However, this required ~100 ms to complete a control loop (6–40 ms for the sensory delay [116] and 47 ms for the neuromuscular delay [74]). Also, their antennae were usually not useful because they did not contact the obstacles during the physical interaction (**Figure 4-9A**). Similarly, in our robotic model system, the robot sensed the obstacle contact forces and torques at 50 Hz [288]. We speculated that in both cases, the conflict between high obstacle contact forces/torques (which might result in high acceleration) and limited sensory-control bandwidth required the animal and robot to use mechanical feedback control other than the sensory feedback control [4] to maintain stability. Finally, the obstacle traversal and locomotor transitions for both animal and robot were strenuous and urgent, while the animal's and robot's actuations were both limited. This made it difficult to accumulate high momentum and urged both animal and robot to find the least-resistance path to transition.

Although the insects were expected not to understand the concept of potential energy landscape to guide obstacle traversal, they might be able to identify a natural obstacle (e.g., grasses, shrubs, etc.), roughly estimate its properties, and identify the least-resistance direction through evolution and its own development [296]. Future studies should measure animal neural and muscle signals and collect more biological observations to verify and better understand animal control strategies in identifying the least-resistance direction. Similarly, robots may also facilitate vision and artificial intelligence techniques to identify common obstacles and roughly estimate their properties based on an online shared library, which may help estimate the (local) landscape [237].

4.7.3 Comparison between our strategy and other saddle-seeking algorithms

Our strategy has many similarities with some existing saddle-seeking strategies, such as following gradient extremal [208], dimer method [217], and gentlest ascent dynamics [218]. When approaching the saddle point, all these strategies aim to minimize the amplitude of the gradients (which indicated small resistance forces in our case). This requires the algorithm to estimate the gradient minimal direction [218], resulting in trajectories that strictly follow or converge to the gradient minimal curve.

Compared to other algorithms, our strategy is more practical for robot dynamics and answers the motivation of saddle-seeking behavior. Because the other strategies are proposed for abstracted mathematical problems (mainly in physical chemistry), they lack consideration of robotic dynamics and needs. (1) Most other strategies do not consider the dynamics, inertial effect, and stochasticity when a robot physically interacts with obstacles, so they either do not give continuous trajectories (e.g., dynamic programming [205], ant colony optimization [206], genetic algorithms [207], and the nudged elastic band method and its variants [211–213]), or may give impractical trajectories that contain sharp turns (e.g., following Newton trajectories [214], orthogonal trajectories [215], gradient extremals [208,216], dimer method trajectories [217], and gentlest ascent dynamics [218]). We solved this problem by applying control in the external forces and torques. (2) Nearly all other strategies assumed that the Hessian matrices can be obtained analytically or calculated numerically by sampling gradient at adjacent points and using a central difference scheme (e.g., dynamic programming [205], ant colony optimization [206], genetic algorithms [207], the nudged elastic band method and its variants [211–213], the metadynamics method [209], the adaptive biasing force method [210], following Newton

trajectories [214], orthogonal trajectories [215], gradient extremals [208,216], dimer method trajectories [217], and gentlest ascent dynamics [218]), which is impractical for a robot on an unknown potential energy landscape. We solved this problem by sampling the obstacle contact forces and torques as the landscape gradients along the robot's trajectory and using a custom estimator. We also involved an oscillation force and a sideway force to recover the detectability of the gradient minimal direction when necessary. (3) Nearly all strategies are only applicable to fixed landscapes (same examples as in (2)). We solved this problem using a modified estimator for the gradient minimal directions (see Section ***S2***). (4) None of the other strategies motivate saddle-seeking behavior. In our bio-inspired strategy, the saddle-seeking process was triggered when the robot was trapped in the current locomotor mode for a prolonged duration, which still allowed the robot some time to try the default mode (e.g., traversing using the pitch mode was easier than using the roll mode if the beams were flimsy [31]). Adjusting parameters such as climb weight w_{climb}, converge rate w_{converge}, and haste level λ_{shrink} also allowed the robot to present rich behaviors showing different urgencies and saddle-seeking accuracies for various applications.

4.7.4 Climb weight controlled morphing of the effective potential landscape

The climb weight modulated the attraction of minima and saddle points dramatically. We elaborate on this using the effective potential landscape, which evolved as the climb weight varied. A bifurcation occurred at the climb weight $w_{\text{climb}} = 1.0$, where the effective potential landscape gradient was zero along the climb direction. For $w_{\text{climb}} < 1.0$, the amplitude of the approach torque was smaller than the original landscape gradient in the climb direction, which resulted in the effective potential landscape gradient being the same direction as the potential energy landscape gradient in such direction. Here, the

minima and saddle points on the potential energy landscape (**Figure 4-10A**) were still minima and saddle points on the effective potential landscape. However, the transition barrier was lower (**Figure 4-10B**).

For $w_{\text{climb}} = 1.0$, the amplitude of the approach torque equaled the potential energy landscape gradients in the climb direction, which resulted in the effective potential landscape gradient being zero in such direction. Here, the flow curve crossing minima and saddle points on the potential energy landscape became an equipotential curve on the effective potential landscape (**Figure 4-10C**), where the system's dynamics were dominated by oscillation and noise in this direction. The robot might generate a small oscillation force to explore along this curve to easily transition between minimum basins on the potential energy landscape.

For $w_{\text{climb}} > 1.0$, the amplitude of the approach force was larger than the potential energy landscape gradients in the climb direction, which resulted in the effective potential landscape gradient being in the opposite direction as the potential energy landscape gradient in such direction. Here, the saddle points on the potential energy landscape transformed to minima, and the minimum transformed to a saddle point on the effective potential landscape (**Figure 4-10D**). The system automatically drifted to the saddle point and crossed the barrier on the potential energy landscape.

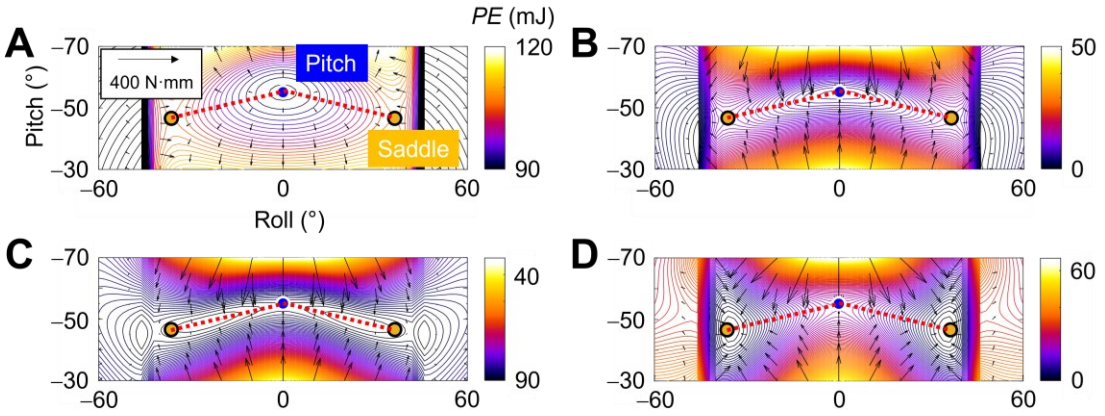

Figure 4-10: Comparison of the potential energy landscape and the effective potential landscapes from various climb weights. (**A**) Potential energy landscape. (**B-D**) Effective potential landscapes from climb weight of (B) w_{climb} = 0.5, (C) w_{climb} = 1, and (D) w_{climb} = 2. The landscapes were obtained at x = 58 mm. Arrows are landscape gradients. Blue and orange points are pitch minimum and saddle points. Red dot curves are gradient minimal trajectories.

All these explained how the approach torque steered the simulated robot to transition to the roll mode and traverse the obstacles. Ideally, when w_{climb} = 1.0, the noise force should occasionally steer the system state to cross the barrier and transition. However, it was never observed in our preliminary tests. We speculated that this was due to the delay from the control loop and estimation error in the climb direction (though both are small) that made the approach force never exactly cancel out the potential energy landscape gradients in the climb direction.

4.7.5 Future directions

We propose to develop neural networks to estimate gradient minimal directions. Although our estimator that directly used the contact forces and torques as the potential energy landscape gradients already yielded a gradient minimal direction estimation that matched the ground truth calculation (**Figure 4-7C**), it contained heavy calculations (e.g.,

obtaining the pseudo-inverse of matrix $\boldsymbol{C}$ in **Equation 4-4**) for onboard microcontrollers. This hinders applying this control strategy to physical robots. To enable estimating gradient minimal directions with light-loaded calculation, we propose to develop a long short-term memory neural network estimator [297] (similar to that developed in [298]). The neural network should be able to estimate such directions from measured forces and torques directly through simple forward propagation, which is affordable for microcontrollers and facilitates physical robotic experiments.

We propose to use active sensing behavior to recover the detectability of the gradient minimal directions. The need to sense environmental interaction physics and traverse obstacles may place competing demands on the robot's locomotion similar to the animals [195]. Instead of conducting an extra phase to generate motion that benefits sensing besides the desired motion, we envision involving an active sensing motion over another degree of freedom other than the existing ones that may resolve this motion conflict. Curiously, the discoid cockroach often exhibited up/down head oscillations (more than on flat ground [226]) while pushing against large obstacles. We speculate that such motions resembled a local sweep in the body rotational space without physically moving the body, which had no interference with the locomotion for obstacle traversal. Future studies can use mathematical derivations and robophysical models to examine how the forces and torques measured from motion in the extra dimension (e.g., from head oscillation) can be transformed into the original dimensions (e.g., body rotation) to estimate the local landscape.

We propose to use Langevin dynamics to model the stochastic physical interaction between robots and obstacles. When physically interacting with the obstacles, the robot's

dynamics are not only governed by the potential energy landscape and self-propulsion but also affected by damping, stochasticity, and inertial effects [39,288], which should be captured by Langevin dynamics [275–277]. The defusing and stochastic nature of Langevin systems is also observed in our simulation (**Figure 4-7D**). So, we propose to use Langevin dynamics to better understand the robot-obstacle physical interaction system, which inspires more control strategies to traverse large obstacles.

Finally, a few issues in this study remain to be resolved or refined. Firstly, despite the strategy being able to guide a robot to cross a barrier via the saddle point on the potential energy landscape, the strategy could not identify whether the barrier was already crossed. As a result, instead of instantly "turning off" the control force to finish the mode transition, the robot state oscillated around the saddle point for a short period. We speculate that the robot should be able to identify barrier crossing by monitoring the change in the sign of the potential energy landscape gradients along the climb direction, which should reverse after crossing the barrier. Secondly, whether this strategy is effective on a rugged potential energy landscape with multiple small local minimum basins remains unknown. We speculate that the strategy can either let the robot escape from them individually or use a large enough sample size for the custom estimator to ignore these small basins. Thirdly, we still lack rigorous mathematical proof of completeness (i.e., being able to find a locomotor transition if one exists) and optimality in minimizing the resistive forces and torques of our strategy. To do this, we should first capture the full dynamics of the physical interaction using Langevin dynamics. Lastly, we have not yet tested the strategy's robustness against sensory noise and large friction. We currently use the friction coefficient measured from a physical robotic system and the default sensory noise in ProjectChrono.

We should systematically vary the sensory noise level and the friction coefficient in the simulation and observe the changes in the robot's performance in traversing obstacles.

4.8 Supplementary Information

4.8.1 Pseudo-algorithm

---

begin

while not reach goal **and not** reach time threshold

estimate landscape Hessian matrix H using last k measured gradients;

if cond(C) > *thresh* **then** %% gradient minimal direction not detectable

get current velocity v;

output sideway force $F_{\text{side}} \perp v$;

else then

$d_1 \leftarrow$ larger eigenvalue of H;

$d_2 \leftarrow$ smaller eigenvalue of H;

$d_{2,\min} \leftarrow \min$ (d2, $d_{2,\min}$);

if $d_2 > n_{\text{shrink}} \times d_{2,\min}$ **then** %% in modified minimum neighborhood

$t_{\text{trap}} = t_{\text{trap}} + dt$;

modify n_{osc} and n_{shrink};

output oscillation force F_{osc};

else if $d_1 < 0$ **then** %% in maximum neighborhood

output no force;

else then %% in modified saddle neighborhood

get climb and converge directions;

get gradients along climb and converge directions;

---

output approach force F_{app};

end if

end if

end while

end

4.8.2 Modified gradient minimal direction estimator for evolving landscape

The gradient minimal direction estimator was modified to adapt to an evolving landscape, where the landscape evolved as the robot's fore-aft translation (x) changed besides rotation (roll α and pitch β). We approximated the local landscape E using its 2nd-order Taylor expansion:

$$
\begin{aligned}
&E(x+\delta x, \alpha+\delta\alpha, \beta+\delta\beta) \\
&\quad = E(x,\alpha,\beta) + \left(\frac{\partial E}{\partial x}\right)_{(x,\alpha,\beta)}\delta x + \left(\frac{\partial E}{\partial \alpha}\right)_{(x,\alpha,\beta)}\delta\alpha + \left(\frac{\partial E}{\partial \beta}\right)_{(x,\alpha,\beta)}\delta\beta \\
&\quad + \frac{1}{2}\left(\frac{\partial^2 E}{\partial x^2}\right)_{(x,\alpha,\beta)}\delta x^2 + \frac{1}{2}\left(\frac{\partial^2 E}{\partial \alpha^2}\right)_{(x,\alpha,\beta)}\delta\alpha^2 + \frac{1}{2}\left(\frac{\partial^2 E}{\partial \beta^2}\right)_{(x,\alpha,\beta)}\delta\beta^2 \\
&\quad + \left(\frac{\partial^2 E}{\partial x \partial \alpha}\right)_{(x,\alpha,\beta)}\delta x\delta\alpha + \left(\frac{\partial^2 E}{\partial x \partial \beta}\right)_{(x,\alpha,\beta)}\delta x\delta\beta + \left(\frac{\partial^2 E}{\partial \alpha \partial \beta}\right)_{(x,\alpha,\beta)}\delta\alpha\delta\beta, \\
&= a_1 + a_2\delta x + a_3\delta\alpha + a_4\delta\beta + \frac{1}{2}a_5\delta x^2 + \frac{1}{2}a_6\delta\alpha^2 + \frac{1}{2}a_7\delta\beta^2 \\
&\qquad + a_8\delta x\delta\alpha + a_9\delta x\delta\beta + a_{10}\delta\alpha\delta\beta. \qquad (4\text{-}12)
\end{aligned}
$$

The gradients G and Hessian matrix H of this potential energy function over the roll-pitch section were:

$$
G_{rp}(x+\delta x, \alpha+\delta\alpha, \beta+\delta\beta) = \begin{bmatrix} a_3 + a_8\delta x + a_6\delta\alpha + a_{10}\delta\beta \\ a_4 + a_9\delta x + a_{10}\delta\alpha + a_7\delta\beta \end{bmatrix}, \qquad (4\text{-}13)
$$

$$H_{rp}(x+\delta x, \alpha+\delta\alpha, \beta+\delta\beta) = \begin{bmatrix} a_6 & a_{10} \\ a_{10} & a_7 \end{bmatrix}. \quad (4\text{-}14)$$

Rearranging **Equation 4-13** and stacking the most recent k measurements, we obtain:

$$\underbrace{\begin{bmatrix} 1 & 0 & \delta\alpha_1 & 0 & \delta x_1 & 0 & \delta\beta_1 \\ 0 & 1 & 0 & \delta\beta_1 & 0 & \delta x_1 & \delta\alpha_1 \\ & & & \vdots & & & \\ & & & \vdots & & & \\ 1 & 0 & \delta\alpha_k & 0 & \delta x_k & 0 & \delta\beta_k \\ 0 & 1 & 0 & \delta\beta_k & 0 & \delta x_k & \delta\alpha_k \end{bmatrix}}_{C} \begin{bmatrix} a_3 \\ a_4 \\ a_6 \\ a_7 \\ a_8 \\ a_9 \\ a_{10} \end{bmatrix} = \begin{bmatrix} G_{rp,1} \\ \vdots \\ G_{rp,k} \end{bmatrix}. \quad (4\text{-}15)$$

From this, we obtained the pseudo-inverse of the matrix ***C*** on the left-hand side and multiplied it with the right-hand side to obtain the coefficients $a_{6,\ 7,\ 10}$, which gave the Hessian matrix H_{rp} in the roll-pitch section.

4.8.3 Validation of model system simulation

We validated the simulation by conducting the same robotic control as in two previous experiments [31,288], and compared the transversal probability and obstacle contact forces and torques. Specifically, to mimic the control in [31] **(Figure 4-5C)**, we disabled the motors (i.e., allowing the robot to rotate freely) and added a forced vertical oscillation of the amplitude and various frequencies (f = 0 – 6 Hz) the same as in [31], and conducted n = 100 trials of simulation for each frequency. We observed that the pitch-to-roll mode transition probability in our simulation matched that in the previous experiment ($P \geqslant 0.34$, Fisher's exact test) (**Figure 4-11A**). To mimic the control in [288] (**Figure 4-5D**), we set the robot to various roll (α = 0° – 40°) and pitch (β = –40° – –10°) combinations, the same as in [288] and fixed the robot rotation, and conducted n = 100 trials of simulation for each rotation. We observed that the measured obstacle contact

forces and torques in our simulation matched that in the previous experiment (**Figure 4-11B**), with a small relative error of 5% ± 7% in *x* direction, 7% ± 9% in roll direction, and 7% ± 5% in pitch direction (see definition of relative error in [288]).

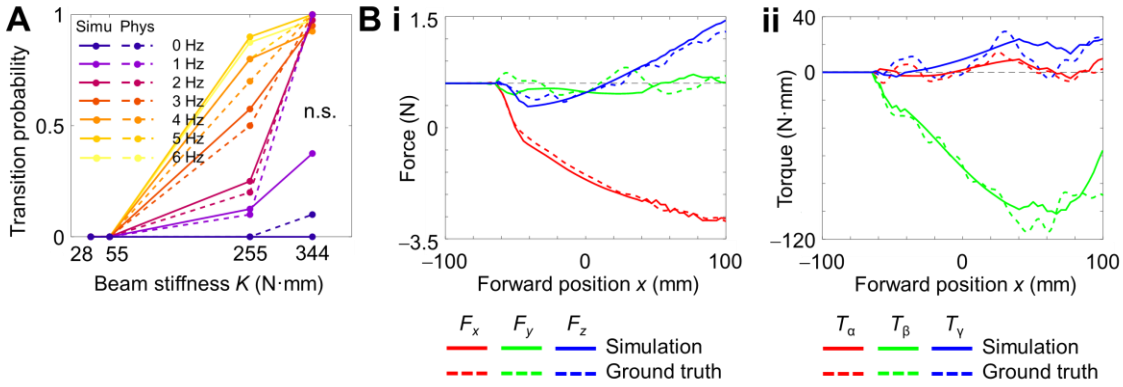

Figure 4-11: Simulation results matched the physical systems. (**A**) Comparison of pitch-to-roll mode transition probability between simulation (solid curves) and physical system in [31] (dashed curves). (**B**) Comparison of measured (**i**) forces in fore-aft (red), lateral (green), and vertical (blue) directions and (**ii**) torques in roll (red), pitch (green), and yaw (blue) directions from a representative trial in simulation (solid curves) and physical system in [288].

Table 4-1 Parameters of model system and simulation

Robot	Mass (g)	1000
	Length (mm)	236
	Width (mm)	170
	Thickness (mm)	66
	Distance between CoM and CoG (mm)	8
	Height z (mm)	138
	Damping in x ($N \cdot mm^{-1}$)	0.1
	Damping in roll ($N \cdot mm \cdot sec \cdot rad^{-1}$)	1
	Damping in pitch ($N \cdot mm \cdot sec \cdot rad^{-1}$)	6
Beam	Lateral distance (mm)	130
	Length (mm)	300
	Width (mm)	30
	Thickness (mm)	2
	Stiffness K ($N \cdot mm \cdot rad^{-1}$)	300
Control	Desired forward velocity ($mm \cdot sec^{-1}$))	20
	Proportional control gain P_x	0.08
	Velocity threshold of being trapped	1.5
	Autoregressive coefficient of approach force φ_{app}	0.5
	Autoregressive coefficient of oscillation force φ_{osc}	0.3
	Converge rate of oscillation λ_{osc}	0.1
	Autoregressive coefficient of sideway force φ_{sid}	0.6
	Sideway force level σ_{sid}	[3, 3]
	Filter sample number k	30
	Condition number threshold	33

Chapter 5 Conclusion

5.1 General remarks

In this dissertation, we combined biological and robotic studies to investigate how a locomotor (animal/robot) should physically interact with terrains and traverse them, using a model system of a cockroach and a cockroach-inspired legged robot traversing cluttered, large obstacles as a pair of grass-like beams.

Previous studies in our lab [26] revealed that, to traverse complex terrain, the locomotor should transition from the current locomotor mode to one that leads to a successful traversal (e.g., from pitch to roll mode in the model system). The lab also established a potential energy landscape modeling based on first principles that describes and predicts such stochastic locomotor transition. However, as is often the case in initial investigations, many interesting topics had not been studied, such as understanding whether and how adjustments can facilitate transitions, how to obtain potential energy landscapes of unknown terrains, and how this modeling guides a robot to traverse obstacles with feedback control.

Our study focused on bridging this knowledge gap by further developing the potential energy landscape modeling theory and involving actuation and adjustments, sensing, and planning and control strategies. We showed that this modeling can further explain some biological adjustments in strenuous locomotion, and this theory and related bio-inspired strategies can facilitate a robot to identify and modulate its physical interaction with obstacles to traverse them. Our work expanded the applications of potential energy landscape modeling, leading to advancements in biology and robotics [299].

5.2 Specific accomplishments

- Captured the detailed kinematics of cockroaches traversing grass-like beam obstacles and quantified multiple adjustments on the animals' heads, abdomens, and legs. Found that the cockroaches oscillated their heads more when negotiating with the beams, oscillated their abdomens more after rolling into the beam gaps, used their legs differentially more when pitching up against the beams, and tucked their legs inward more after rolling into the beam gaps (Chapter 2).
- Discovered the usefulness of the animals' adjustments. Added head and legs to the simplest model of the cockroach traversing beam obstacles to examine whether the leg tucking-in and head oscillation affect the shape of the potential energy landscape and transition barrier. Found that the leg tucking-in significantly reduced the animals' pitch-to-roll transition barrier; the head oscillation did not significantly affect the animals' pitch-to-roll or roll-to-deflect transition barriers (Chapter 2).
- Designed and built a robot capable of sensing physical interaction with the beam obstacles. The robot sensed the contact forces using custom 3-D force sensors and estimated the resulting torques by sensing the contact position using touch-sensitive cells on the surface. Controlled the robot to move into and interact with beams while measuring contact forces and torques (Chapter 3).
- Discovered that the contact forces and resulting torques with the obstacles are roughly the potential energy landscape gradients. The normal forces and resulting torques matched better with the potential energy landscape gradients, which equaled conservative forces and torques (Chapter 3).

- Reconstructed the potential energy landscape from contact force and torque sensing in unknown obstacles. The robot swept a rectangular region in the state space by varying its rotational angles. The potential energy landscape reconstructed from Helmholtz decomposition matched ground truth calculations (Chapter 3).
- Developed a practical, bio-inspired, potential energy landscape-based control strategy that enabled robots to perform a single, prior-free obstacle traversal with the least effort. The least-resistance path was the gradient minimal curve on the potential energy landscapes. The robot used continuous force and torque sensing to identify the gradient minimal direction and followed and converged to this direction to achieve least-resistance locomotor mode transitions. The robot also generated active oscillations and sideway turnings to enhance the detectability of such directions. Validated the control strategy in a simulation of a robot traversing beam obstacles using ChronoEngine (Chapter 4).
- Discovered the effect of key parameters in the strategy on the traversal performance of the simulated robot. Especially, a higher climb weight increased the speed of reaching the saddle point yet reduced the accuracy. A higher converge weight increased trajectory convergence to the gradient minimal curves. A higher haste level increased the escape speed from the initial basin (Chapter 4).
- Discovered two robotic active sensing behaviors. In particular, head oscillations modulated contact force and torque sensing when negotiating with the obstacles, making the sensed data closer to the potential energy landscape gradients (Chapter 3). Sideway tuning enhanced the estimation of the shape of the local potential energy landscape, facilitating the estimation of the least-resistance directions (Chapter 4).

5.3 Future directions

With limited time and personal strength, many natural extensions of this thesis have not been studied thoroughly. Here, we elaborate on our envisioned studies towards a better understanding of how animals and robots should physically interact with complex terrain in biology, robotics, and physics aspects (**Figure 1-4**).

5.3.1 Biology

Using neural tools to examine whether adjustments are from feedback control. Animal's motion merged from physical interaction with the terrain (i.e., passive) and can be modulated by both neural sensory feedback and mechanical feedback controls [4]. It is challenging to determine the contribution of the three aspects and the usefulness of control (if it exists) from only the kinematics (Chapter 2). On the other hand, neural signals like muscle action potentials provide clear and direct evidence of the existence or absence of neural and mechanical feedback control [23,74]. We should test whether the biological adjustments we claimed in Chapter 2 are generated by feedback control by measuring these neural signals. Then, we should combine the results with the potential energy landscapes or other models to understand their usefulness.

Understanding biological sensory fusion. Animals combine multiple sensory pathways (e.g., vision, mechanosensing, electrosensing) to sense the environments and modulate locomotion [300–303]. When cockroaches traverse complex terrain, they not only sense the resistive forces and torques from the terrain (similar to the robots in Chapters 3 & 4) from mechanosensing, but also sense the terrain geometry from vision and antennae [137,138,152,222]. We should understand how the animals fuse these vision- and contact-

based sensory signals to get the geometry and force information, which may inspire sensor fusion strategies for robotics.

Arenas that precisely monitor physical interaction with obstacles. Although force plates or photoelastic substrate techniques can already sense ground contact forces, as mentioned in Section 1.2.5, such tools cannot provide enough information on the physical interaction between animals and cluttered terrain. Especially, the traditional force plates measure the overall forces instead of the contact forces with each obstacle. Photoelastic substrates are usually restricted to flat surfaces and cannot provide precise measurements compared to load cell-based sensors. We propose developing biological experiment arenas that precisely monitor physical interaction with obstacles. To do this, we should separate the ground and obstacles into small, gridded sections (e.g., 1 mm × 1 mm grids) and measure the 3-D contact forces on each section using a 3-axis force sensor (similar to custom force sensors in Chapter 3). One challenge is the conflict between the numerous sensors and limited space. We propose to distribute the force sensors away from the arena and link the gridded terrain sections and the force sensors via levers, similar to the keyboard structure of a mechanical typewriter. With these arenas, the contact force and position sensing between each animal body part or appendage and each obstacle can be obtained with controlled precision. These tools enable us to obtain precise ground contact forces and resulting torques, which facilitates verifying more hypotheses (e.g., the differential leg use of cockroaches (Chapter 2) generated a roll torque).

5.3.2 Robotics

From a recent quantification and comparison between animals' and robots' locomotion performances (mainly on running) [304], robots are better than animals in

nearly all subsystems, including power, frame strength, actuation, sensing, and control. Yet, animals still outrun robots in overall performance because of the challenge of integrating the robotic subsystems. However, we argue that in traversing complex terrain, the sensing, actuation, and control robotic subsystems are still not comparable to their biological counterparts and need further development to achieve higher locomotion performance. Here, we propose several future directions.

Bio-inspired force and torque sensors for real-world terrain. Although current robotic visual sensors can tie to even the most sophisticated biological counterparts, robotic mechanoreceptors (e.g., force and touch sensors) that are of great importance in monitoring physical interaction with terrains (Chapter 3) always fail to compare to the animals. They are quantitatively fewer in number and type and less in area of distribution [140,304,305]. We propose that robots should have adequate, even redundant, force and touch sensors of various kinds and ranges [306] on their surface to monitor physical interaction. Especially, we propose to develop a bio-inspired surface sensor cluster that measures contact force, mimicking a campaniform sensillum cluster. Campaniform sensilla are biological membranes on the insect's exoskeleton. They are sensitive to mechanical deformation. They often form clusters and have various orientations (**Figure 5-1**), which allows them to sense the forces of various directions and be robust against damage [142]. We propose to develop robotic sensor clusters mimicking the campaniform sensillum clusters to achieve surface force sensing.

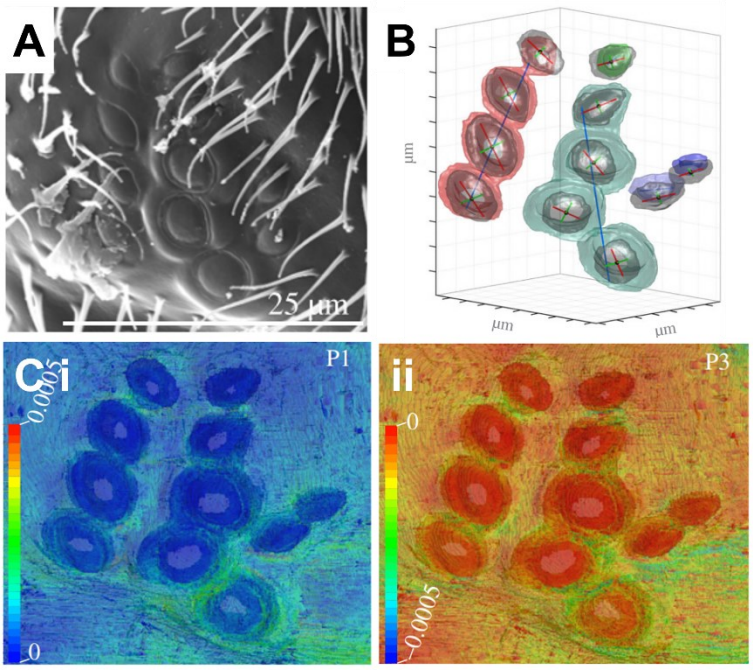

Figure 5-1: Campaniform sensillum cluster. (**A**) Scanning electron microscopy image of the campaniform sensillum cluster. (**B**) A cluster of campaniform sensilla with various orientations. The red and green directions are the main axes of their caps. (**C**) Strain of campaniform sensillum caps in (**i**) most tensile and (**ii**) most compressive cases. Adapted from [142].

Neural network estimator for least-resistance directions. The current method to obtain the least-resistance directions (i.e., the gradient minimal directions) on potential energy landscapes (i.e., it needs to obtain a pseudo-inverse of a roughly 30 × 7 matrix) is computationally heavy for microcontrollers (Chapter 4), which hinders applying the strategy to real-world experiments. Also, the method treats each measurement from a short history equally, which contradicts the intuition that the more recent data should have a larger effect on the estimation result. To address this, we propose to build a long short-term memory (LSTM) neural network estimator [297] to obtain the least effort directions.

Unlike traditional model-based analyses, which rely heavily on detailed knowledge of system dynamics and is often difficult to obtain inputs of the dynamics equations (such as system states) in highly nonlinear systems [192,194], a neural network can derive the desired information directly from measured data through simple forward propagation [298]. This process is computationally efficient, even for microcontrollers. Moreover, the network's training process automatically optimizes the impact of measurements on the estimation results, adapting to the time series data. We propose training this neural network estimator using massive data from simulation (Chapter 4), which will be used to calculate the least-resistance directions and evaluate its detectability. This neural network estimator may allow robots to make real-time decisions, facilitating real-world experiments.

Applying the control strategy on a free-running legged robot. Compared to the tethered robots (Chapters 3 & 4), applying our control strategy (Chapter 4) on a free-running legged robot to enable real-world obstacle traversal can be very challenging, aside from the need to process noisy force sensory data. Here, we list two other challenges to achieving such a goal.

Firstly, handling high-dimensional motion. In systems from previous studies, the potential energy landscapes are usually presented as a function of the state in two principal dimensions (pitch and yaw angles in bump [33] and gap traversal [34], pitch and bearing angles in pillar traversal [35], roll and pitch angles in beam traversal [31,226,227] and ground self-righting [11,37–39]). However, such decisions of principal dimensions are all based on the empirical experience of researchers who have long-time observations of related biological and robotic motions and are even based on trying-on-errors. Generally, a rigid, single-segment robot's trajectory involves six dimensions, usually considered as

three translational and three rotational. Adjustments (e.g., head oscillation, tail actuation) add more dimensions. Dimension explosion makes the landscape difficult to analyze and visualize. The robot should apply the strategy in the principal dimensions to transition between locomotor modes and traverse obstacles. Here, we provide four criteria about when a dimension can be "squeezed" (i.e., being less important). (1) The system is neutrally identical along one dimension. Examples include lateral displacement in bump and gap traversal and horizontal displacements in flat ground self-righting [11,33,34,37–39]. (2) The system quickly converges to a landscape local minimum in other dimensions that is continuous in one dimension. This case is similar to treating a river as a one-dimension curve by squeezing the lateral dimension into the midline. Examples include vertical displacements in all the cases above except for robotic beam traversal [11,31,33–35,37–39,226]. (3) A dimension forced to follow a trajectory or couple with another dimension. Examples include translational displacements in robotic beam traversal [31,227]. (4) The dimension along the observed trajectory. Squeezing in such a dimension helps understand the motion in other dimensions along the trajectory. Examples include the lateral displacement and yaw angles in the biological beam traversal [31,226]. (5) motion coupled by transmission mechanism or neural control. Although these criteria can help reduce the dimensions, we can easily spot a "chicken and egg dilemma": the robot can only know that one dimension can be "squeezed" by examining that dimension or after having a rich experience traversing the terrain. We need practical methods to solve this dilemma and enable effective dimensional deduction.

Secondly, lack of methods to generate effective propulsion. The direct-drive (DD) robotic legs [19,73,307,308] achieve high transparency, mechanical robustness and

efficiency, and actuation bandwidth [19]. They also allow direct leg torque monitoring and control [73,79]. However, robotic legs naturally provide noisy, dimension-correlated, substrate-dependent propulsions. Although the reaction force of legged motion on the rigid ground [21,309,310] or yielding terrain [32,311] is modeled, we still don't know the fundamental principles of generating desired propulsion by contacting arbitrary obstacles. We need models and methods to let robots generate controlled, precise, and frequently changing propulsions like animals [9] (Chapter 4).

5.3.3 Physics Models

Capturing full dynamics using Langevin equations. We propose to use Langevin equations [275–277] to capture the full dynamics of a physical interaction with obstacles:

$$\underbrace{m\ddot{X}(t)}_{\text{Inertial effect}} = \underbrace{-\nabla PE(X)}_{\text{Potential gradient}} + \underbrace{f(X,t)}_{\text{Damping}} + \underbrace{\eta(t)}_{\text{Randomness}} + \underbrace{F_{ext}(t)}_{\text{External forces}} \quad (5\text{-}1)$$

Langevin dynamics captures not only the natural drift of a system (in the potential gradient term) like the potential energy landscapes, but also frictions and damping, stochasticity, inertial effects, etc. The simulation results of a robot physically interacting with beam obstacles (Chapter 4) have already demonstrated the stochastic, diffusive nature of physical interaction systems (**Figure 4-7D**), suggesting Langevin dynamics. However, instead of having a simple, isolated viscous damping term as common in microscopic particle motion, the friction between locomotors and terrains from the macroscopic physical interaction is usually difficult to model and also affects the normal forces (which is the gradient term in the ideal case, Chapter 3). This makes the Langevin equations difficult to compose. We speculate that we can initially use Langevin dynamics with

common viscous damping assumption as a rough estimate and further augment the model to adapt to the macro-scale locomotion.

Using data-driven methods to obtain potential energy landscapes in unknown terrains. Aside from using contact force and torque measurements to reconstruct the potential energy landscape (Chapter 3), another possible approach to obtaining the landscape of an unknown terrain is using data-driven methods. Suppose the stochastic locomotor-terrain physical interaction is modeled using Langevin dynamics (previous paragraph), we may use data-driven methods to obtain the potential term in the Langevin equations to obtain the landscape. Especially, we can launch naïve animals and self-propelled, feedforward-controlled robots [312] in the terrain and let them stochastically interact with it. Then, we can obtain their trajectories and use classical statistical data-driven methods [120] and machine learning-based approaches [313,314] to identify the potential term in the Langevin equation as the potential energy landscape. This approach should be preferred over the one proposed in Chapter 3 for animal experiments because measuring the contact position and force on an animal is usually challenging [52,169–171].

Using existing knowledge base to obtain potential energy landscapes in unknown terrains. We already know the potential energy landscape of various types of obstacles [26], and this knowledge base can be further expanded and accumulated with more studies using theoretical modeling [26], real-world robotic experiments (Chapter 3 and previous paragraph), or knowledge and experiences from other robots. Benefiting from this large knowledge base, we may obtain the potential energy landscape of a known terrain by identifying the distinct obstacles on it from multiple abstracted types [26] and combining their landscapes to form a new one. However, the landscapes from different obstacle types

are on different dimensions (e.g., roll, pitch, yaw, bearing dimensions in **Figure 1-3D**), so they cannot be simply patched together. We should carefully combine the individual landscapes according to their dimensions and the obstacle distribution. Also, with only remote sensing (e.g., visual scanning), obtaining the obstacle's full geometry and precise physical properties is still hard. We propose launching robots to approach the obstacle and use active perception to identify these properties [237,315].

Using potential energy landscapes to model flexibility and mechanical intelligence. Cockroaches with jointed exoskeletons have huge body flexibility that can facilitate locomotion, e.g., crawl through crevices smaller than their natural thickness [10], which all our robots fail to do. Many mobile robots already have jointed, compliant bodies and appendages that facilitate navigation in cluttered and confined spaces [10,64,65,316,317] (**Figure 5-2**). We speculate these robots' locomotion can also be captured using the potential energy landscape modeling. Because the compressions are usually from the folding of 1-D elastic joints, the additional elastic potential energy to the system can be calculated.

Aside from flexibility, many passive morphologies and mechatronic systems show "mechanical intelligence" [318,319] that automatically leads to a favorable result from physical interaction (e.g., stable grasping [320,321], dynamic stability [21,22,46], transition to a model leading to success [35,36], etc.). We speculate that potential energy landscape modeling is a promising tool for understanding robotic flexibility and mechanical intelligence, as it usually emerges from physical interaction without control. Studies should continue seeking these from bio-inspiration to simplify robotic modulation of physical interaction.

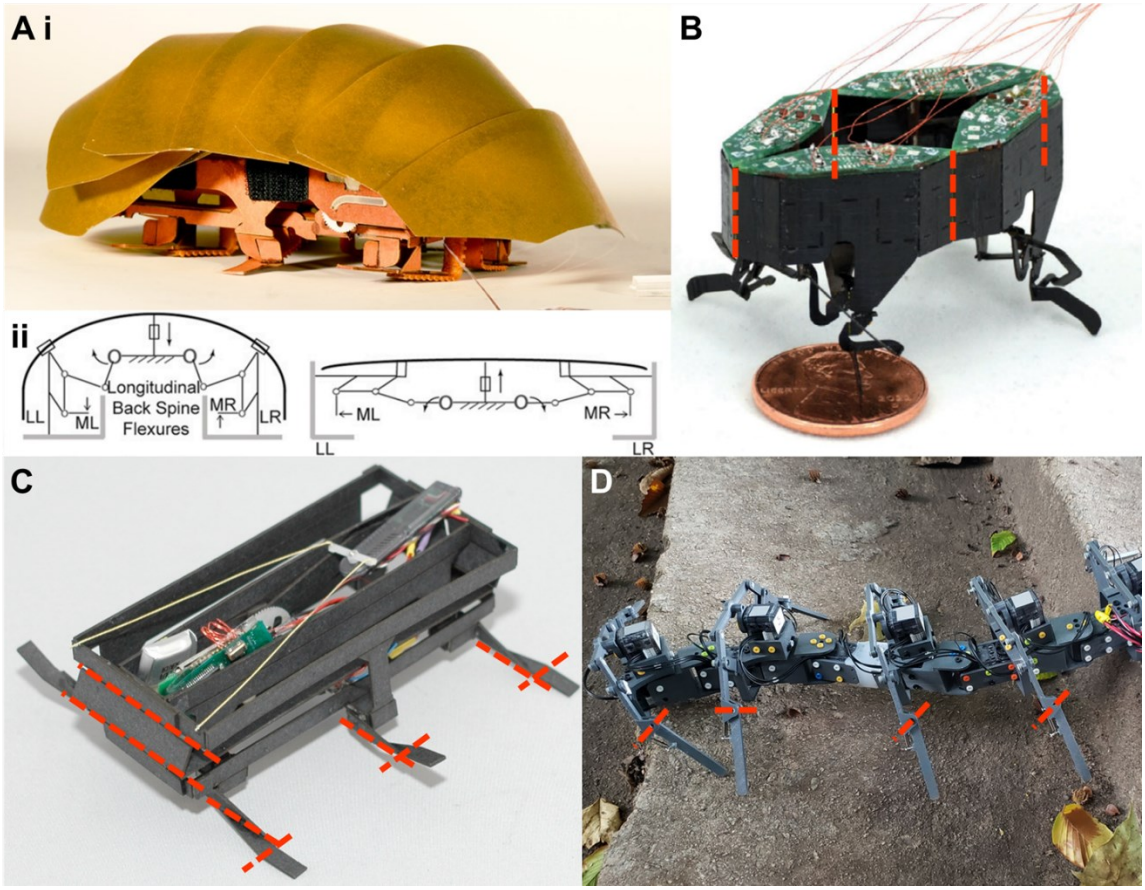

Figure 5-2: Example robots with compliant bodies and appendages that navigate cluttered terrain and confined spaces. There are 10^1 to 10^2 elastic joints on each robot that enable body and leg compliance. Dashed red lines show some of them. (**A**) (I) CRAM robot and (ii) its structure schematics. (**B**) CLARI robot. (**C**) DASH robot. (**D**) A centipede robot. Adapted from [10,65,316,317].

Developing new models for physical contact. Potential energy landscapes can only capture limited scenarios of physical interaction with complex terrain. It is only effective in a "potential energy landscape-dominated regime of locomotion," where large potential energy barriers are comparable to or exceed kinetic energy and/or mechanical work generated by each propulsive cycle or motion [26]. It also emphasizes the stochastic physical contact (e.g., collision) with obstacles [31,35,36] and the existence and usefulness

of stochasticity and large oscillation [31,38,39,322]. These hinder its applications of less stochasticity, such as mammal locomotion where the obstacle contact is usually at a foot or a paw, stable, and long-lasting (e.g., we struggled in applying this modeling to a rat jumping across a gap [323] and a mountain goat climbing a cliff [324]), surgical robotics, etc. These limitations encourage us to revise current models, clarify their effective ranges, and develop new animal/robot physical interaction models with obstacles under other conditions or requirements.

5.4 Final thoughts

When working on the projects shown in this dissertation and witnessing the other projects (with snakes, amphibious fishes, spiders, etc.) in Dr. Chen Li's lab, I have always been fascinated by and appreciated the beauty of biological locomotion more. Initially, I thought they were only fun to watch, but now, I observe them more out of scientific curiosity. These studies also taught me that scientific research should not (only) focus on "showing off skills." Small, simple, "quick and dirty" (quote from Dr. Chen Li) robots, tools, and tests are sufficient to make a big difference. I have learned, yet I still need to learn more about balancing fun and rigor in research with limited time, personal strength, and funding. I am still interested in biological and robotic locomotion and look forward to hearing about updates and offering help on the ongoing and future projects related to those above.

Appendix

Below are some additional attempts that are not mentioned in the main context. However, we would still show them there because they either inspired and led the projects above or had flaws we pointed out to help other researchers avoid the same mistakes.

A.1 Optimal trajectory for a cockroach traversing beam obstacles

This section was submitted as a project report for the course "Applied Optimal Control" in Fall 2020, authored by Yaqing Wang and Boyang Xiao. We re-used the article in this chapter with slight format changes under CC BY 4.0 and with permission from all authors.

A.1.1 Author contributions

Yaqing Wang designed research; Boyang Xiao transformed the potential energy landscape into a polynomial; Yaqing Wang conducted optimization; and Yaqing Wang and Boyang Xiao wrote the paragraph.

A.1.2 Acknowledgment

We want to acknowledge the Terradynamics Lab at Johns Hopkins University for providing the topic of this study and landscape data and Professor Marin Kobilarov for inspiring guidance.

A.1.3 Summary

Cockroaches are amazingly good at traversing complex terrain. A recent study showed that to traverse beam obstacles, a cockroach often transitioned from the pitch mode (pitching up its body and trying to push through) to the roll mode (rolling into a beam gap and traversing) for easier traversal. A potential energy landscape approach was used to explain this phenomenon. As the cockroach approached the beam, a "pitch basin" emerged at zero roll and finite pitch on the potential energy landscape. A "roll basin" emerged at near-zero pitch and over 50° roll, which was lower than the pitch basin. The cockroach often escaped from the pitch basin and reached the roll basin.

Here, we tested whether we could understand how animals optimized their trajectories. We optimized the trajectory based on the potential energy landscape using heuristic cost functions and compared the result with measured animal trajectories from the physical experiments. We found that the optimized trajectory was similar to an animal using a pitch mode without manually interfering with the optimization process. However, when we forced the trajectory to enter the roll basin on the landscape, the optimized trajectory was similar to an animal using a roll mode and cost less than the previous one. We speculated that the trajectory using a pitch mode was at a local minimum of the optimization process. Suppose the animal actively made adjustments from neural feedback to induce pitch-to-roll transition, it must have the intelligence to know that it should seek other locomotor modes rather than stay in the default one (also Chapter 4).

A.1.4 Method

Model landscape. In the simplest model of the cockroach traversing beams in [31], the animal was modeled as a rigid ellipsoid, and the beams were modeled as rigid plates with torsional springs at the bottom. The potential energy was the sum of the body and beam's gravitational potential energy and beam elastic energy. The beam stiffness we selected was 2.5 (we omitted all units in section A.10), which was stiff for the animal. The system's potential energy is fully determined by animal forwarding displacement X, body *roll*, and body *pitch*, which is history-independent. To generate this landscape, we swept X (range [−24.2, 33], interval 0.2), *roll* (range [−π, π], interval π/36), and *pitch* (range [−π, π], interval π/36) and calculated the 3-D gridded potential energy as a landscape (287 × 73 × 73). The landscape in the roll-pitch cross-section evolves as X increases (**Figure 5-3**).

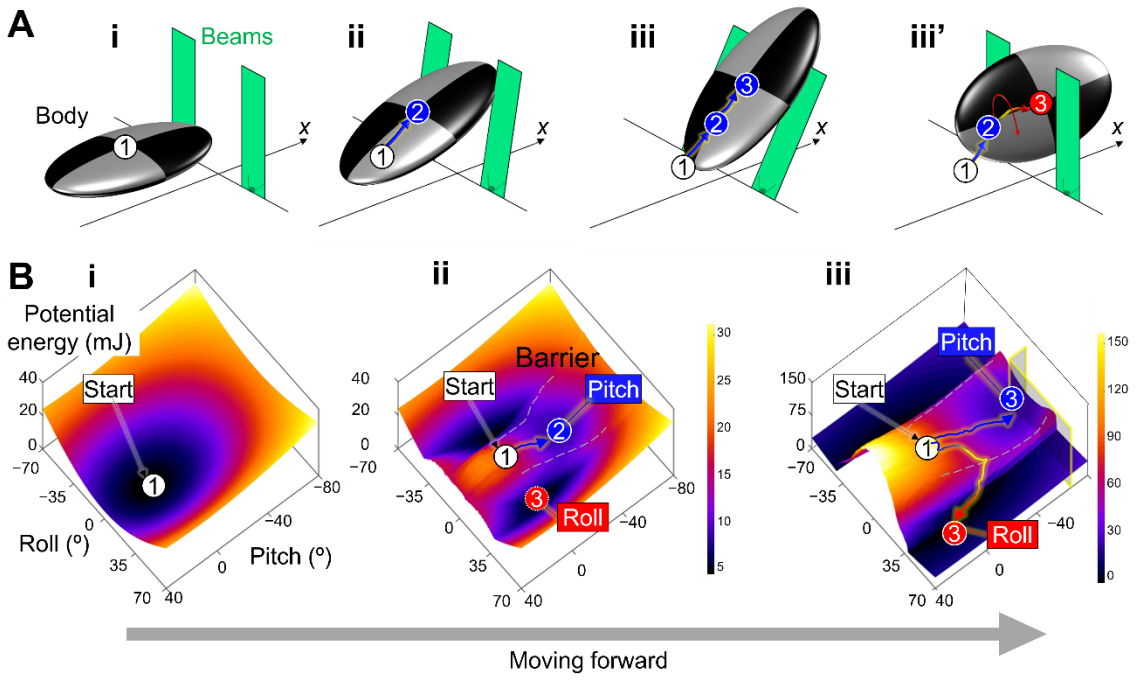

Figure 5-3: Potential energy landscape evolving as a cockroach traversing beams. Adapted from [31].

The original landscape defined in the model is not analytical and is non-smooth. To enable optimization, we used 15th-degree polynomial of the original potential energy landscape for optimal trajectory. In polynomial regression [325], the *X*, *roll*, and *pitch* were the inputs, and the potential energy was the output. To reduce the variance, we chose ridge regression as our regression method. The coefficient for ridge regression was:

$$\hat{\beta} = (\mathrm{A}^{\mathrm{T}}\mathrm{A} + \lambda I)^{-1}\mathrm{A}^{\mathrm{T}}PE, \tag{5-2}$$

where A is a N × M matrix with the polynomial terms (N = 287 × 73 × 73 is the number of data points, M is the number of terms in a 15th-degree, 3-variable polynomial), ($\lambda \geq 0$) is a complexity parameter. The polynomial could be expressed as:

$$f(X, roll, pitch) = \hat{\beta}^{\mathrm{T}}x, \tag{5-3}$$

where *x* contains all the terms of the polynomial.

Cost function. We hypothesized that the cost function that the cockroach should minimize (note: we did not claim that cockroaches considered in this way) was the potential energy it would accumulate. We defined the cost function as:

$$J = \frac{1}{2}\int_0^{t_f} [(PE - r)^2(t) + u^T R u]dt\,, \tag{5-4}$$

where t_f is the fixed final time, *r* is the global minimum of *PE*, *u* is input, and *R* is the weight of input, which was very small as 0.0005).

Optimization tool and settings. We used ACADO for MATLAB [326] as the optimization tool. We selected direct multiple shooting with a step size 288 and a KKT tolerance 1e-8. To simplify the dynamics, the animal moved forward at a constant speed. The body roll and pitch velocity were directly changed by inputs ($\dot{X} = 1, \dot{roll} = u_1, \dot{pitch} = u_2$). We set necessary limitations to *roll* and *pitch*, and limitations to the input according to

the maximal roll and pitch velocity observed in animal experiments ($roll \in [-\pi, \pi]$, $pitch \in [-\pi, \pi]$, $|u_1| \leq 2\pi/9$, $|u_2| \leq \pi/5$). We set the *roll* and *pitch* to be zero at the start and the end ($t_f = 57$, $X(0) = -24.2$, $roll(0) = roll(t_f) = 0$, $pitch(0) = pitch(t_f) = 0$).

A.1.5 Results

Landscape fitting. The 15th-degree polynomial reproduces the original landscape (**Figure 5-4A, B**) with a fitting error of 0.00 ± 0.06 (mean ± s.d.).

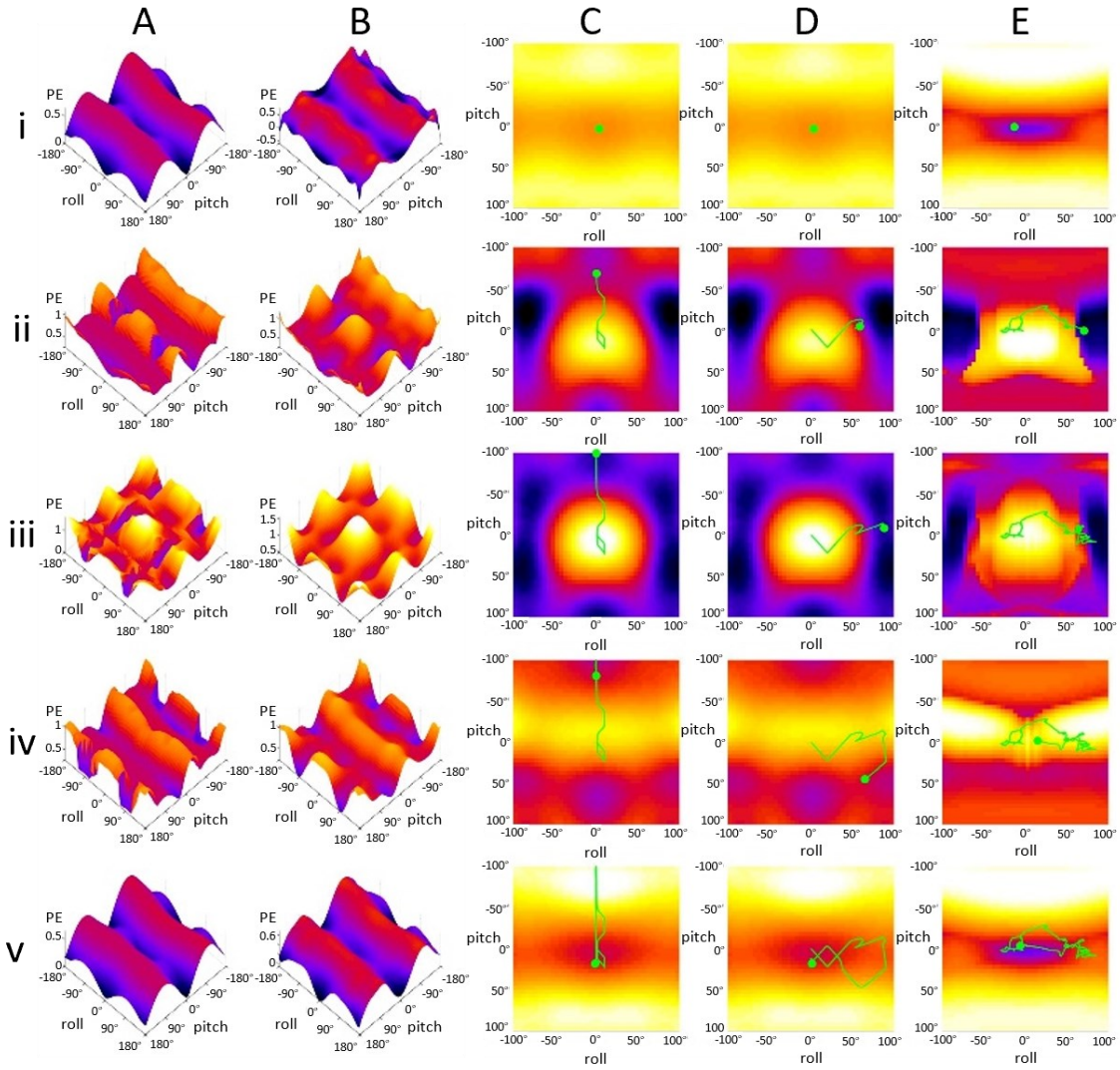

Figure 5-4: Potential energy landscapes in roll-pitch cross-section and trajectories. (**A**) Original landscape. (**B**) Polynomial. (**C**) Pitch mode trajectory on polynomial. (**D**) Roll

mode trajectory on polynomial. (**E**) A typical animal trajectory on the original landscape. (**i**) $X = -24$. (**ii**) $X = -12$. (**iii**) $X = 0$. (**iv**) $X = 12$. (**v**) $X = 24$. In (C, D, and E), green lines are the trajectory projections, and green dots are the current state projections.

Optimal trajectory. We observed the pitch mode as optimal without further manual intervention for optimization. Initially, the animal state started at zero *roll* and *pitch* (**Figure 5-4C, i**). It first pitched up and moved to the pitch basin (**Figure 5-4C, ii**), with about $-\pi/2$ in *pitch* and zero *roll*. Then, it stayed in the pitch basin (**Figure 5-4C, iii**), and returned to the origin at the end (**Figure 5-4C, iv & v**).

We observed the roll mode as optimal when we set the trajectory to deliberately cross a fixed point at ($X = 0$, $pitch = -\pi/18$, $roll = \pi/2$). Initially, the state started at zero *roll* and *pitch* (**Figure 5-4D, i**). It first pitched up (~ 15°) and rolled to the roll basin (**Figure 5-4D, ii**), with about $\pi/2$ in *roll* and zero *pitch*. Then, it stayed in the roll basin (**Figure 5-4D, iii**) and pitched down (~ 45°), and returned to the origin at the end (**Figure 5-4D, iv & v**).

Roll mode was more favored than pitch mode. The pitch mode accumulated more cost than the roll mode at X from −19.0 to −12.6, −10.2 to 0.4, and 12.0 to 20.6 (**Figure 5-5A**), resulting in a higher final cost than the roll mode. So, the roll mode was more favored in the sense of having a smaller cost.

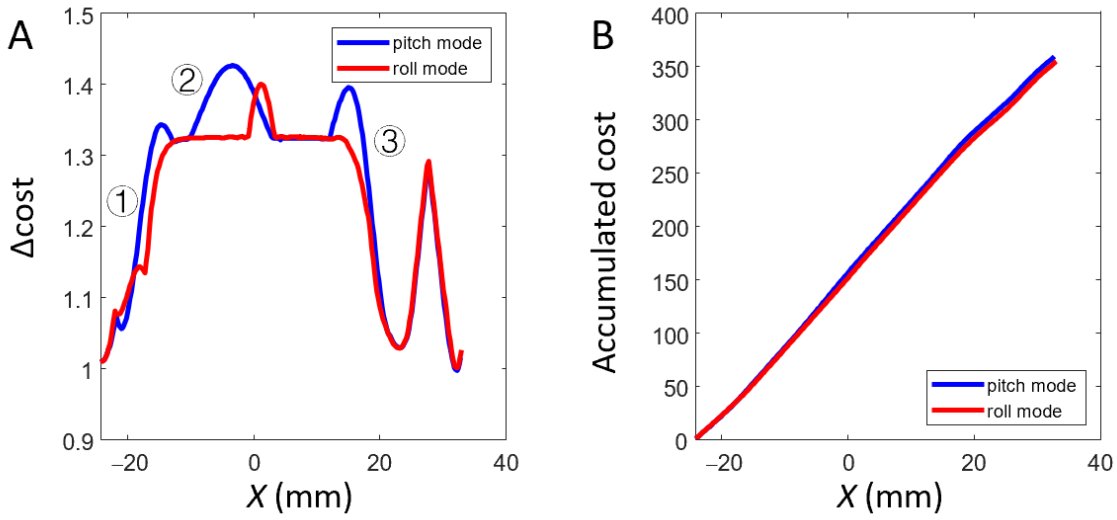

Figure 5-5: Cost in optimization. (**A**) Δcost as a function of *X*. (**B**) Accumulated cost as a function of *X*.

A.1.6 Discussion

Roll mode had a similar trajectory to that in animal experiments. Compared to the trajectory in roll mode, a typical animal trajectory measured from the experiment (**Figure 5-4E**) also started near the origin, went to the roll basin, and went back to the origin in a clockwise trajectory. So, the trajectory of roll mode was similar to that in the animal experiment.

Conclusion. In our study, we looked for the optimal trajectory of a cockroach traversing a layer of beams, and we optimized the 15^{th}-degree polynomial fitting of the original landscape. We observed pitch and roll mode trajectories and found that the roll mode trajectory was similar to those observed in an animal experiment.

A.2 Seeking saddle points using first return time

A.2.1 Author contributions

Yaqing Wang conducted the research and wrote the paragraph under the supervision of Chen Li and Shai Revzen.

A.2.2 Introduction

Previous studies showed that stereotyped locomotor modes are local minimum basins on the potential energy landscape [26]. To transition from one mode to another with a minimal potential energy barrier, animals or robots need to seek the saddle point between the two basins (Chapter 4).

Here, we sought the saddle point of a landscape using the first return time. Our algorithm did not need prior knowledge of the landscape. It only requested local information about the landscape in the process.

A.2.3 Method

For an energy landscape $J = J(X)$ (**Figure 5-6A**), we defined the dynamics of the system as gradient descending dynamics (i.e., $\dot{X} = -G(X)$, where $G(X) = \nabla J(X)$ was the gradient of the landscape). We defined the contour(s) of an energy level h_0 as H: $J(X) = h_0$. We defined the first return time $\tau(X)$ (**Figure 5-6B**) as the first time that the state started from X fell on H:

$$\tau(X) = \int_{X}^{X_{final}@H} \frac{\left|\overrightarrow{dX}\right|}{|G(X)|}. \tag{5-5}$$

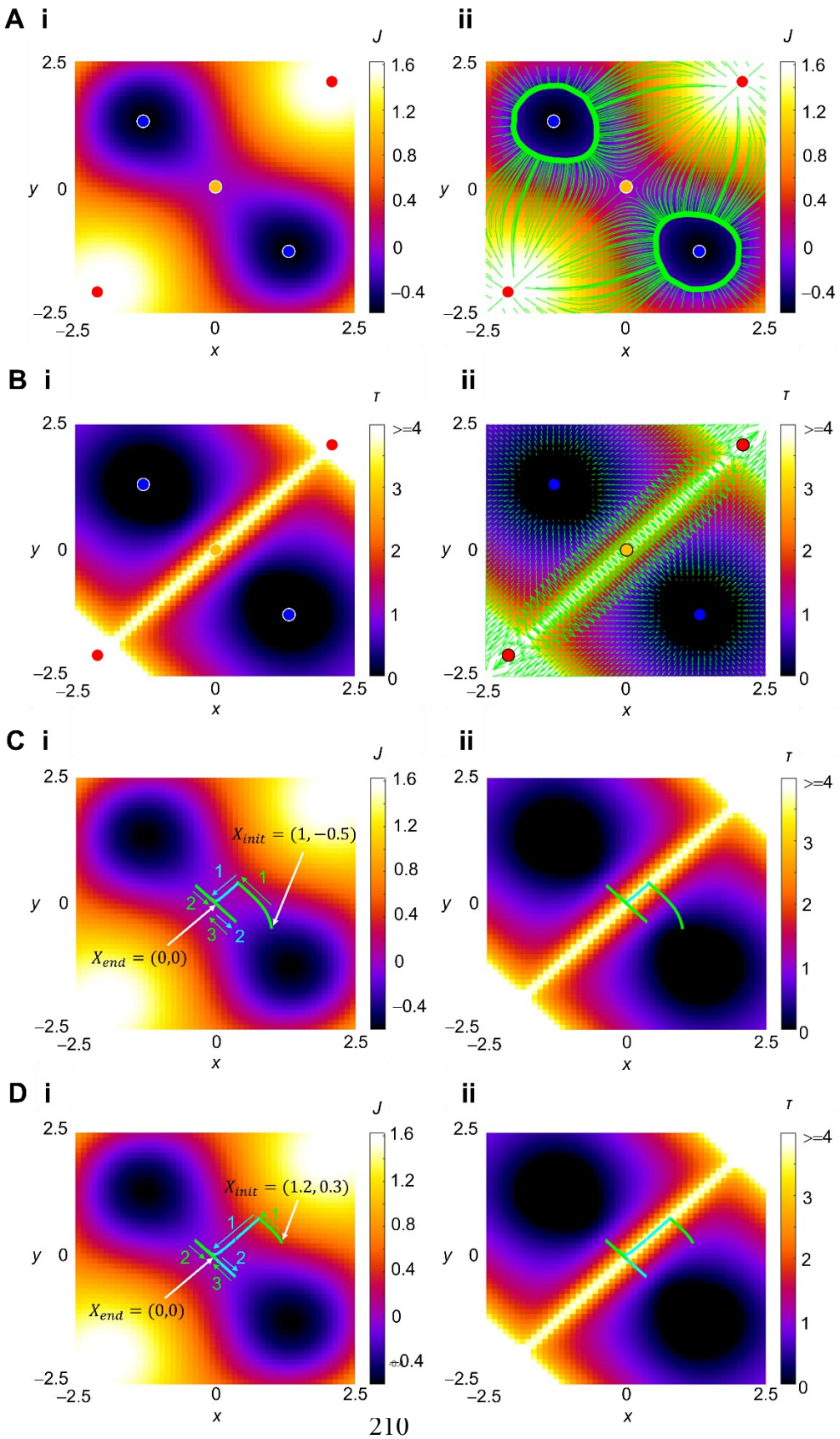
A i
ii
B i
ii
C i
ii
D i
ii
J
τ
2.5
0
−2.5
y
x
1.6
1.2
0.8
0.4
−0.4
>=4
3
2
1
$X_{init} = (1, -0.5)$
$X_{end} = (0,0)$
$X_{init} = (1.2, 0.3)$
$X_{end} = (0,0)$

Figure 5-6: Potential energy and first-return-time landscapes. (**A**) Potential energy landscape. (**i**) Potential energy J as a function of variable (x, y). (**ii**) Flow field of potential energy landscape. Thin green curves show landscape flow. Thick green curves are H: $J = h_0$. Background is the same as (i). (**B**) First-return-time landscape. (**i**) First return time τ as a function of variable (x, y). Region of $\tau > 4$ is saturated. (**ii**) Gradient of first-return-time landscape. Green arrows show landscape gradient direction and magnitude. Background is the same as (i). In (A, B), blue, red, and orange points are local minima, maxima, and saddle points, respectively. (**C and D**) are two successful demos that located the saddle point at (0,0) from (C) $X_{\text{init}} = (1, -0.5)$ and (D) $X_{\text{init}} = (1.2, 0.3)$. Green curves show routes from the procedure (1) gradient ascend on first-return-time landscape, and cyan curves show routes from the procedure (2) gradient descend on potential energy landscape. Numbers and arrows on curves show iteration number and direction.

To find a saddle point on a potential energy landscape, we first (1) optimized state X to increase the first return time $\tau(X)$ (**Figure 5-6C, D,** green curves) (i.e., did gradient ascend on first return time landscape), then (2) followed the flow of energy landscape to try to locate the saddle point (**Figure 5-6C, D,** cyan curves) (i.e., did gradient descend on potential energy landscape), and then (3) repeat (1 & 2) to finally locate the saddle point.

The basic rationale of this method was that on a "nice" surface, each flow curve on the landscape should start from a divergent pole (local maxima or infinite) and end at a convergent pole (local minima or infinite). As the surface was "nice," the gradient near the critical points (minima, maxima, saddle points) was near zero. Therefore, the flow speed was low near a critical point like a saddle point, meaning more time was needed. Using an iso-energy (contour) curve (H: $J = h_0$) to crop the end of every flow, the first return time measured how close a sub-curve had a part close to a saddle point. To the limit, the initial points (which form the edge between two basins) that guided the flow to a saddle point

gave an infinite first return time. Therefore, maximizing the first return time, the animal or robot found a point close enough to the basin edge. Following its flow and repeating these two processes, the saddle point between the two basins was found.

We made our demo on a "nice" potential energy landscape (**Figure 5-6A, i**):

$$J(x, y) = \sin x \cdot \sin y + 0.1(x^2 + y^2), \tag{5-6}$$

where x and y were variables, and J was the potential energy. M_1 = (1.2979, –1.2979) and M_2 = (–1.2979, 1.2979) were two local minima, and S = (0, 0) was the saddle point between the basins (**Figure 5-6A, B,** blue and orange points). We set h_0 to be –0.3 J. All the information about the landscape was initially unknown to the animal or robot.

A.2.4 Results and Discussion

Here, we tested our algorithm from two initial states, X_0 = (1, –0.5) (**Figure 5-6C**) and X_0 = (1.2, 0.3) (**Figure 5-6D**). We observed that after 2~3 iterations, in both cases, the algorithm located the saddle point from the initial states, which showed that our method was useful, general, and converged fast.

Despite the achievement, this algorithm assumed that the system's dynamics were deterministic, which was against the schochastic nature of the system of an animal or a robot physically interacting with the complex terrain. This algorithm also required the animal or robot to perform multiple trials, which was against the requirement of a quick traversal. All these encouraged us to find a new method to seek the saddle point on the potential energy landscape to achieve the least-resistance traversal (Chapter 4).

A.3 Other efforts

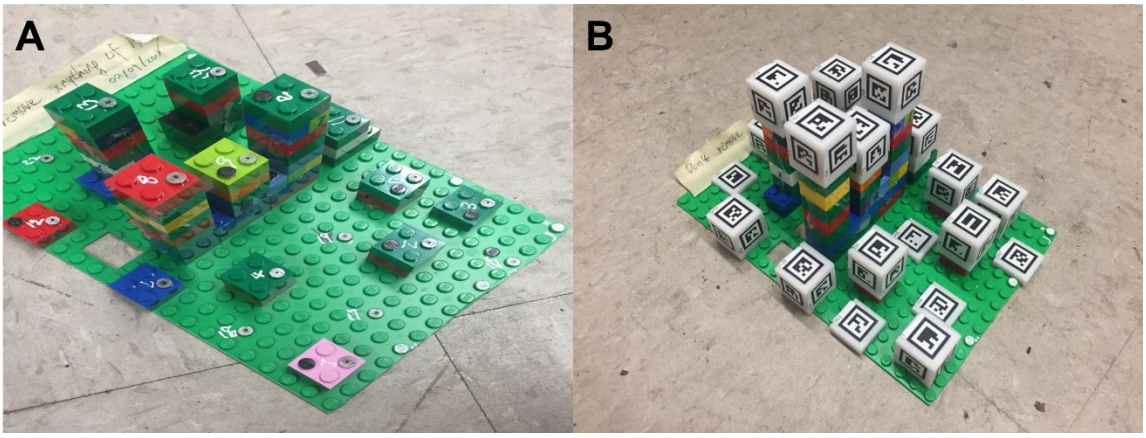

Figure 5-7: 3-D calibration object for camera calibration. (**A**) Manual calibration object. This object facilitated camera calibration (in Chapter 2) by providing points (black dots) with easily obtainable world and camera view coordinates. The world coordinates were calculated from the LEGO structure. The camera view coordinates were manually digitized. (**B**) Automated calibration object. Compared to (A), the camera view coordinates of points (replaced by the center of tags) are automatically digitized using BEEtags [231]. Although (B) required no laborious manual digitization compared to (A), it has a higher calibration error. Because camera calibrations were not frequently required (e.g., we performed six calibrations over 300 trials of animal experiments), we still recommend using a manual calibration object as in (A). (B) Adapted from [26].

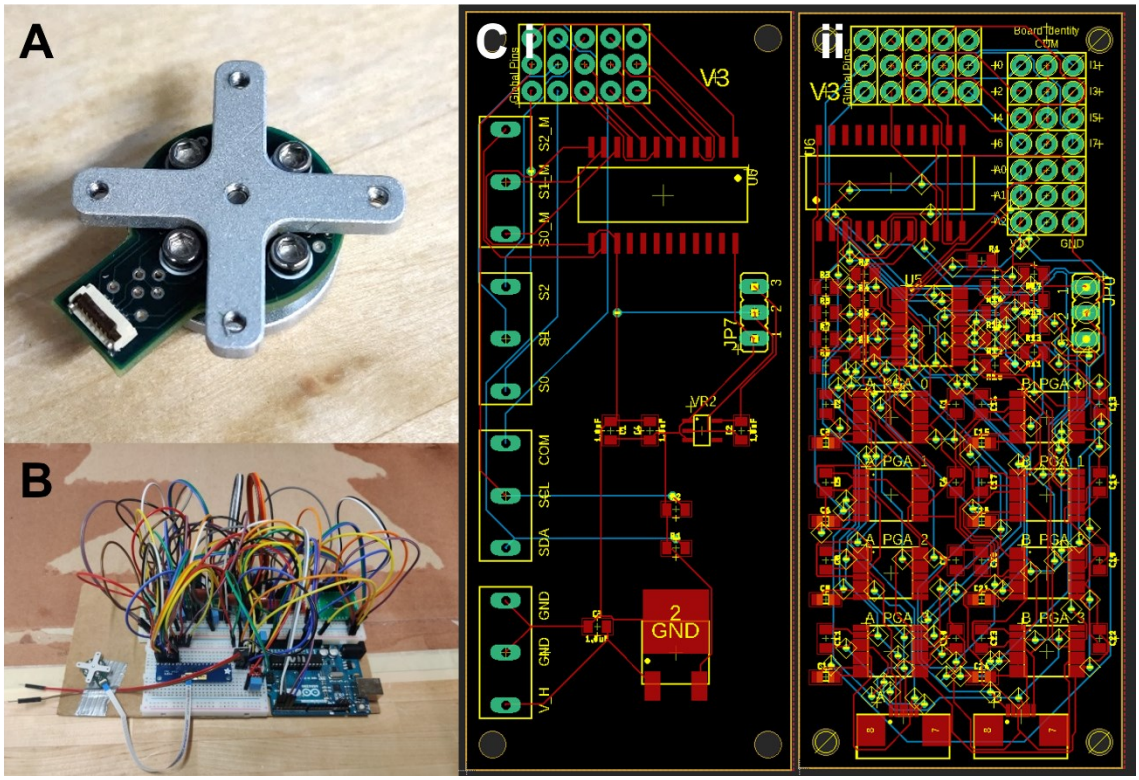

Figure 5-8: A small, custom 3-axis force sensor and its DAQ boards. (**A**) A force sensor modified from [327]. A PCB board (green) was sandwiched between two steel plates. The deformation on the PCB board was measured with the stain gauges on the PCB board to infer the 3-axis forces. (**B**) A prototype of a custom DAQ board. (**C**) An integrated DAQ board design for multiple sensors. (**i**) Base board with ports for power and communication with microcontrollers. (**ii**) Expansion board. Each board enabled two more force sensors, as shown in (A). The integrated DAQ board should be multiple expansion boards stacked on a base board. From our testing, the force sensor only provided an accurate and consistent signal when the force was applied vertically to the PCB board, and the force sensor was damaged frequently. We speculated that because the PCB board in the force sensor was "crispy" and heterogeneous, impulses might easily generate plastic deformation that damaged the sensor. We should use force sensors that are more robust against impulses (Chapter 3). We acknowledge Prof. Jeremy Brown and Jacob Carducci from the HAMR Lab at Johns Hopkins University for offering the documents and files of the original design in [327].

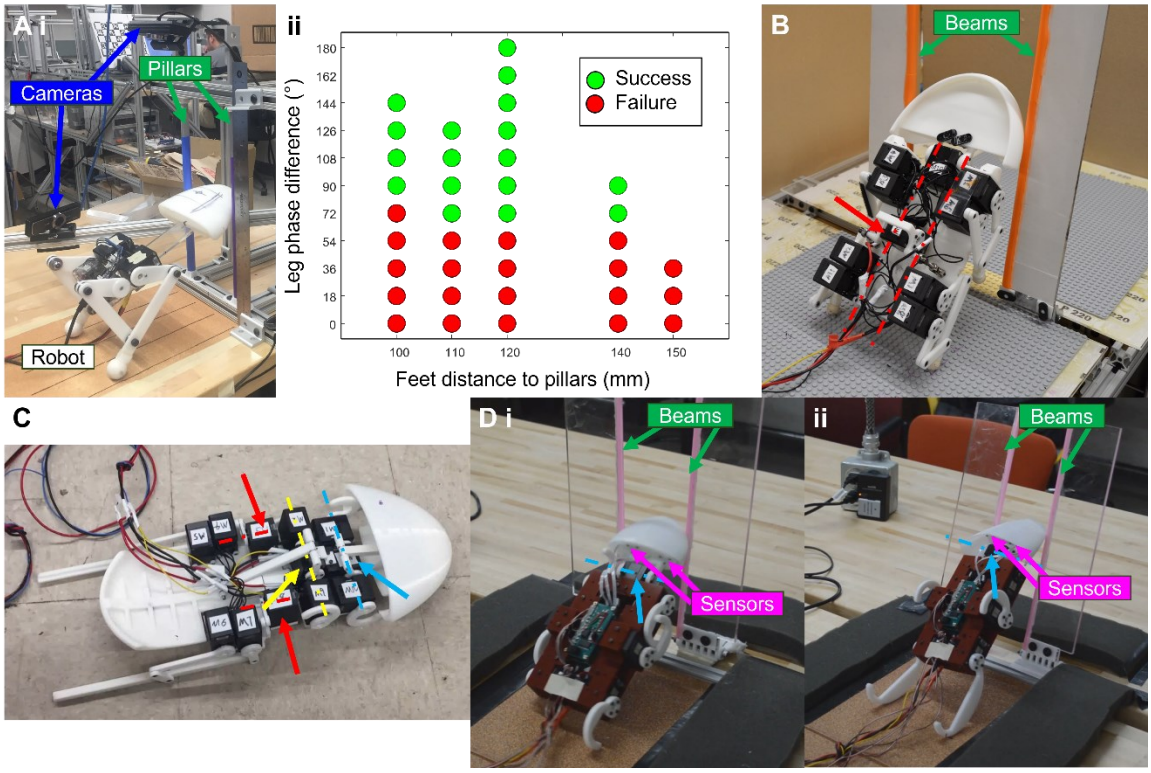

Figure 5-9: Multiple legged robots to understand the effect of leg actuation in obstacle traversal performance. (**A**) (**i**) A two-legged robot attempted to traverse two pillars (green) with a gap smaller than the head width. The robot legs are Minitaur-like [104]. The robot's feet tracked a prescribed circular trajectory. The robot successfully traversed the pillars if its head moved in the gap and beyond the pillar plane. (**ii**) We systematically varied the initial feet distance from the pillar and the leg phase difference. The robot could traverse the pillar when the legs were out of phase. (**B**) A robot upgraded from (A) by adding front legs and a crouch ability (red). (**C**) A robot upgraded from (B) by adding head (cyan) and abdomen (yellow) oscillation abilities. The hind legs were lengthened, mimicking a cockroach. (**D**) A legged robot attempted to traverse beams. This robot would sense contact force on its head using sensors (magenta, **Figure 5-8**). The robot has either (**i**) normal C-shaped legs or (**ii**) long C-shaped legs. Experiments with these robots found that it was hard to generate effective and desired propulsive forces and torques when physically interacting with obstacles, especially when using the C-shaped legs commonly used for running on flat ground. We proposed skipping this problem using a tethered robot (Chapters 3 & 4).

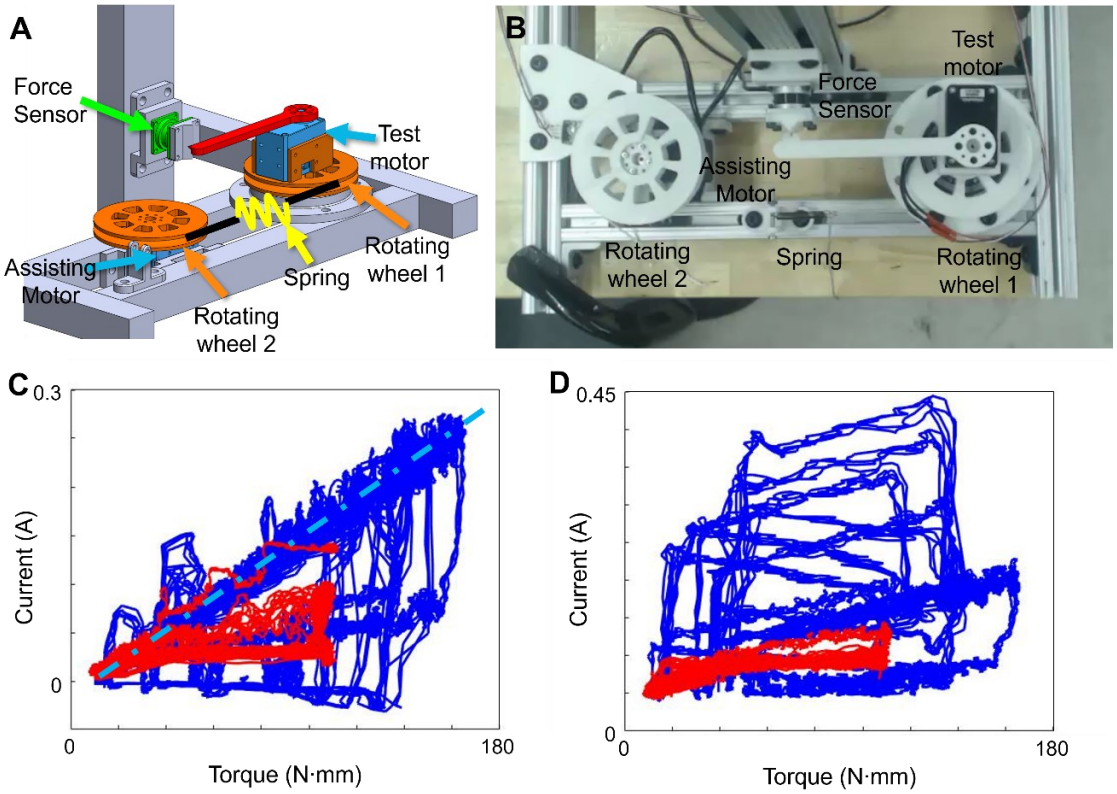

Figure 5-10: Servo motor characterization. We tried to find a relationship between the servo motor's (Dynamixel XM430-W210-T) current (either the current of the inner bare motor or the total current) and the applied torque. (**A**) A motor calibration tool. The test motor (cyan, right) was tested under various rotational speeds (including being static). The assisting motor (cyan, left) and the spring generated applied torque. The applied torque was measured using a force sensor (green) of a known force arm (red). (**B**) Top view of the physical tool in (A). (**C and D**) The current of (C) the inner bare motor and (D) the servo motor changed with torque. All the loop cycles were clockwise. The current of the inner bare motor was obtained from the servo motor readouts. Blue and red are from a rotating or static servo motor separately. The only obvious linear relationship was between the current of the inner bare motor and the applied torque when the motor rotated in the same direction as the applied torque (C, cyan). We speculates that unlike a direct-drive motor design, the gear box of a servo motor involved frictions and backlash, and the power was also consumed for motor control aside from generating torque. This study partially encouraged us to directly obtain the contact force from force sensors instead of obtaining it from motor signals (Chapter 3).

References

List of supplementary movies

Movie 1: Cockroach Flexed its Head and Abdomen while Traversing Beams. Top: zoomed top (left) and side (right) views. White points with red, magenta, cyan, green, and orange edges are the origins of thorax frame, head frame, abdomen frame, middle point of thorax-head joint, and middle point of the thorax-abdomen joint, respectively. Solid and dotted arrows show $+x$ and $+x$' direction of body (red), head (magenta), and abdomen (cyan) frames, respectively. Head and abdomen flexion are the angles between body $+x$' direction and head or abdomen $+x$ direction. Bottom left: isometric view. Bottom right: head and abdomen flexion as a function of time.

Link: https://youtu.be/bc4hdj_a1_A.

Movie 2: Cockroach Actively Adjusts its Hind Legs while Traversing Beams. Top left: zoomed top view. White points with thick blue, red, and black edges are the left and right tibia-tarsal joints and origin of thorax frame, respectively. White points with thin blue and red edges are the projections of the tibia-tarsal joints into the body coronal plane. Total leg sprawl is the angle between the dashed blue and red lines. Top right: zoomed mirrored side view. White points with blue, red, and black edges are tibia-tarsal joints and their projections to body coronal plane, respectively. Leg height of left and right hind legs is opposite value of the length of the blue and red lines, respectively. Bottom left: isometric view. Note that this view is mirrored to better show leg motion. Bottom right: Leg sprawl (top) and leg height (bottom) as a function of time. Blue and red are for left and right hind legs, respectively.

Link: https://youtu.be/_MCw9r2t70M.

Movie 3: Evolution of Potential Energy Landscape and Transition Barriers of Cockroach Traversing Beams. Part 1. Pitch-to-roll transition on pitch-roll cross section. Part 2. Roll-to-deflect transition on yaw cross section. Top left: model of cockroach

traversing beam obstacles at head flexion $\beta_h = 15°$ with hind legs neglected. Top right: potential energy landscape pitch-roll cross section (part 1) or yaw cross section (part 2) along the average animal trajectory. Blue, red, and purple dots are pitch, roll, and deflect local minima, respectively. Orange dots are saddle points. Green curves are imaginary routes. Bottom left: Potential energy along the imaginary route. Bottom right: Potential energy barrier as a function of forward position x.

Link: https://youtu.be/gLd5n9rSg90.

Movie 4: Force sensing to reconstruct potential energy landscapes for cluttered large obstacle traversal. Part 1 & 2. Robotic experiment and real-time data visualization of a robot with a (1) static or (2) oscillating head traversing beams. Top left: video recording. Bottom left: Measured contact force in fore-aft (red), lateral (green), and vertical (blue) directions. Right: LabVIEW GUI showing real-time data acquisition, including robot rotation, beam angles, contact forces (both total and separated), and contact position. Part 3. Potential energy landscape evolves as robot moves forward. Top left: potential energy landscape reconstructed from force and torque sensing. Top right: ground truth calculation. Bottom right: the full potential energy landscape. The reconstructed potential energy landscape is a small section in the white rectangular region.

Link: https://youtu.be/iWsrin7ysr0.

Movie 5: Bio-inspired control for least-resistance obstacle traversal. Left: Animation of the robot traversed the beam obstacles in (top) isometric view and (bottom) side view. Right: the robot's state trajectory and control torques projected on the potential energy landscape (in the background).

Link: https://youtu.be/b-GxTxVCgrA.

Movie 6: Recording of Yaqing Wang's defense presentation.

Link: https://youtu.be/lJ1mdX5i-94.

Bibliography

[1] Alexander R M (2002) *Principles of Animal Locomotion* (Princeton University Press)

[2] Biewener A and Patek S (2003) *Animal Locomotion* (Oxford University Press)

[3] Tinbergen N (1955) *The Study of Instinct* (Clarendon Press)

[4] Dickinson M H, Farley C T, Full R J, Koehl M A R, Kram R and Lehman S (2000) How Animals Move: An Integrative View *Science* **288** 100–6

[5] Holmes P, Full R J, Koditschek D and Guckenheimer J (2006) The Dynamics of Legged Locomotion: Models, Analyses, and Challenges *SIAM Rev.* **48** 207–304

[6] Lock R J, Burgess S C and Vaidyanathan R (2013) Multi-modal locomotion: from animal to application *Bioinspir. Biomim.* **9** 011001

[7] Low K H, Hu T, Mohammed S, Tangorra J and Kovac M (2015) Perspectives on biologically inspired hybrid and multi-modal locomotion *Bioinspir. Biomim.* **10** 020301

[8] Goldman D I, Chen T S, Dudek D M and Full R J (2006) Dynamics of rapid vertical climbing in cockroaches reveals a template *J. Exp. Biol.* **209** 2990–3000

[9] Hunt N H, Jinn J, Jacobs L F and Full R J (2021) Acrobatic squirrels learn to leap and land on tree branches without falling *Science* **373** 697–700

[10] Jayaram K and Full R J (2016) Cockroaches traverse crevices, crawl rapidly in confined spaces, and inspire a soft, legged robot *Proc. Natl. Acad. Sci.* **113** E950–7

[11] Li C, Wöhrl T, Lam H K and Full R J (2019) Cockroaches use diverse strategies to self-right on the ground *J. Exp. Biol.* **222** jeb186080

[12] Raibert M H (1986) *Legged Robots That Balance* (MIT press)

[13] Saranli U, Buehler M and Koditschek D E (2001) RHex: A Simple and Highly Mobile Hexapod Robot *Int. J. Rob. Res.* **20** 616–31

[14] Raibert M, Blankespoor K, Nelson G and Playter R (2008) BigDog, the Rough-Terrain Quadruped Robot *IFAC Proc. Vol.* **41** 10822–5

[15] Rahman-Jones I and Singleton T (2024) Bye, robot: Atlas HD retires after 11 years of jumps, flips and falls *Br. Broadcast. Corp.* https://www.bbc.com/news/articles/ck7ly07gmx4o

[16] Bouman A, Ginting M F, Alatur N, Palieri M, Fan D D, Touma T, Pailevanian T, Kim S-K, Otsu K, Burdick J and Agha-Mohammadi A (2020) Autonomous Spot: Long-Range Autonomous Exploration of Extreme Environments with Legged Locomotion *IEEE/RSJ International Conference on Intelligent Robots and Systems* (IEEE) pp 2518–25

[17] Hurst J (2019) Walk this way: To be useful around people, robots need to learn how to move like we do *IEEE Spectr.* **56** 30–51

[18] Hutter M, Gehring C, Jud D, Lauber A, Bellicoso C D, Tsounis V, Hwangbo J, Bodie K, Fankhauser P, Bloesch M, Diethelm R, Bachmann S, Melzer A and Hoepflinger M (2016) ANYmal - a highly mobile and dynamic quadrupedal robot *IEEE/RSJ International Conference on Intelligent Robots and Systems* vol 2016-Novem (IEEE) pp 38–44

[19] Kenneally G, De A and Koditschek D E (2016) Design Principles for a Family of Direct-Drive Legged Robots *IEEE Robot. Autom. Lett.* **1** 900–7

[20] Guizzo E and Ackerman E (2015) The hard lessons of DARPA's robotics challenge [News] *IEEE Spectr.* **52** 11–3

[21] Blickhan R and Full R J (1993) Similarity in multilegged locomotion: Bouncing like a monopode *J. Comp. Physiol. A* **173** 509–17

[22] Kuo A D (2007) The six determinants of gait and the inverted pendulum analogy: A dynamic walking perspective *Hum. Mov. Sci.* **26** 617–56

[23] Biewener A A and Daley M A (2007) Unsteady locomotion: integrating muscle function with whole body dynamics and neuromuscular control *J. Exp. Biol.* **210** 2949–60

[24] Couzin-Fuchs E, Kiemel T, Gal O, Ayali A and Holmes P (2015) Intersegmental coupling and recovery from perturbations in freely running cockroaches *J. Exp. Biol.* **218** 285–97

[25] Revzen S, Burden S A, Moore T Y, Mongeau J-M and Full R J (2013) Instantaneous kinematic phase reflects neuromechanical response to lateral perturbations of running cockroaches *Biol. Cybern.* **107** 179–200

[26] Othayoth R, Xuan Q, Wang Y and Li C (2021) Locomotor transitions in the potential energy landscape-dominated regime *Proc. R. Soc. B Biol. Sci.* **288** rspb.2020.2734

[27] Murphy R R (2014) Disaster robotics *Springer Handbook of Robotics* ed B Siciliano and O Khatib (MIT press)

[28] Angelini F, Angelini P, Angiolini C, Bagella S, Bonomo F, Caccianiga M, Santina C Della, Gigante D, Hutter M, Nanayakkara T, Remagnino P, Torricelli D and Garabini M (2023) Robotic Monitoring of Habitats: The Natural Intelligence Approach *IEEE Access* **11** 72575–91

[29] Li C and Lewis K (2023) The Need for and Feasibility of Alternative Ground

Robots to Traverse Sandy and Rocky Extraterrestrial Terrain *Adv. Intell. Syst.* **5** 2100195

[30] Guizzo E and Ackerman E (2015) DARPA Robotics Challenge: A Compilation of Robots Falling Down: Gravity is a bad thing for robots *IEEE Spectr.*

[31] Othayoth R, Thoms G and Li C (2020) An energy landscape approach to locomotor transitions in complex 3D terrain *Proc. Natl. Acad. Sci.* **117** 14987–95

[32] Li C, Zhang T and Goldman D I (2013) A Terradynamics of Legged Locomotion on Granular Media *Science* **339** 1408–12

[33] Gart S W and Li C (2018) Body-terrain interaction affects large bump traversal of insects and legged robots *Bioinspir. Biomim.* **13** 026005

[34] Gart S W, Yan C, Othayoth R, Ren Z and Li C (2018) Dynamic traversal of large gaps by insects and legged robots reveals a template *Bioinspir. Biomim.* **13** 026006

[35] Han Y, Othayoth R, Wang Y, Hsu C-C, de la Tijera Obert R, Francois E and Li C (2021) Shape-induced obstacle attraction and repulsion during dynamic locomotion *Int. J. Rob. Res.* **40** 939–55

[36] Li C, Pullin A O, Haldane D W, Lam H K, Fearing R S and Full R J (2015) Terradynamically streamlined shapes in animals and robots enhance traversability through densely cluttered terrain *Bioinspir. Biomim.* **10** 046003

[37] Othayoth R and Li C (2021) Propelling and perturbing appendages together facilitate strenuous ground self-righting *eLife* **10** 1–23

[38] Xuan Q and Li C (2020) Coordinated Appendages Accumulate More Energy to Self-Right on the Ground *IEEE Robot. Autom. Lett.* **5** 6137–44

[39] Xuan Q and Li C (2020) Randomness in appendage coordination facilitates

strenuous ground self-righting *Bioinspir. Biomim.* **15** 065004

[40] Koditschek D E, Full R J and Buehler M (2004) A principled approach to bio-inspired design of legged locomotion systems *Unmanned Ground Vehicle Technology VI* vol 5422 pp 86–100

[41] Iida F and Ijspeert A J (2016) Biologically Inspired Robotics *Mechanical Engineering* pp 2015–34

[42] Aguilar J, Zhang T, Qian F, Kingsbury M, McInroe B, Mazouchova N, Li C, Maladen R, Gong C, Travers M, Hatton R L, Choset H, Umbanhowar P B and Goldman D I (2016) A review on locomotion robophysics: the study of movement at the intersection of robotics, soft matter and dynamical systems *Reports Prog. Phys.* **79** 110001

[43] Ijspeert A J (2014) Biorobotics: Using robots to emulate and investigate agile locomotion *Science* **346** 196–203

[44] Gravish N and Lauder G V. (2018) Robotics-inspired biology *J. Exp. Biol.* **221** 1–8

[45] Full R J and Koditschek D E (1999) Templates and anchors: neuromechanical hypotheses of legged locomotion on land *J. Exp. Biol.* **202** 3325–32

[46] Blickhan R (1989) The spring-mass model for running and hopping *J. Biomech.* **22** 1217–27

[47] Cavagna G A, Heglund N C and Taylor C R (1977) Mechanical work in terrestrial locomotion: two basic mechanisms for minimizing energy expenditure *Am. J. Physiol. Integr. Comp. Physiol.* **233** R243–61

[48] Full R J, Farley C T and Winters J M (2000) Musculoskeletal Dynamics in

Rhythmic Systems: A Comparative Approach to Legged Locomotion *Biomechanics and Neural Control of Posture and Movement* (Springer New York) pp 192–205

[49] Farley C T, Glasheen J and Mcmahon T A (1993) Running Springs: Speed and Animal Size *J. Exp. Biol.* **185** 71–86

[50] Blickhan R and Full R J (1987) Locomotion Energetics of the Ghost Crab: II. Mechanics of the Centre of Mass During Walking and Running *J. Exp. Biol.* **130** 155–74

[51] Farley C T and Ko T C (1997) Mechanics of Locomotion in Lizards *J. Exp. Biol.* **200** 2177–88

[52] Full R J and Tu M S (1990) Mechanics of six-legged runners *J. Exp. Biol.* **148** 129–46

[53] Goswami A, Thuilot B and Espiau B (1996) Compass-Like Biped Robot Part I : Stability and Bifurcation of Passive Gaits *INRIA* RR-2996

[54] Coleman M J (2010) Dynamics and stability of a rimless spoked wheel: a simple 2D system with impacts *Dyn. Syst.* **25** 215–38

[55] Ghigliazza R M, Altendorfer R, Holmes P and Koditschek D (2005) A Simply Stabilized Running Model *SIAM Rev.* **47** 519–49

[56] Geyer H and Saranli U (2017) Gait Based on the Spring-Loaded Inverted Pendulum *Humanoid Robotics: A Reference* (Springer Netherlands) pp 1–25

[57] Shemer N and Degani A (2014) Analytical control parameters of the swing leg retraction method using an instantaneous SLIP model *IEEE/RSJ International Conference on Intelligent Robots and Systems* (IEEE) pp 4065–70

[58] Geyer H, Seyfarth A and Blickhan R (2005) Spring-mass running: simple

approximate solution and application to gait stability *J. Theor. Biol.* **232** 315–28

[59] Wisse M and van der Linde R Q (2007) Passive Dynamic Walking *Springer Tracts in Advanced Robotics* vol 34 pp 7–24

[60] Ikemata Y, Yasuhara K, Sano A and Fujimoto H (2008) A study of the leg-swing motion of passive walking *IEEE Int. Conf. Robot. Autom.* 1588–93

[61] Collins S, Ruina A, Tedrake R and Wisse M (2005) Efficient Bipedal Robots Based on Passive-Dynamic Walkers *Science* **307** 1082–5

[62] Schroer R T, Boggess M J, Bachmann R J, Quinn R D and Ritzmann R E (2004) Comparing cockroach and Whegs robot body motions *IEEE International Conference on Robotics and Automation* vol 4 (IEEE) pp 3288–93

[63] Kim S, Clark J E and Cutkosky M R (2006) iSprawl: Design and Tuning for High-speed Autonomous Open-loop Running *Int. J. Rob. Res.* **25** 903–12

[64] Haldane D W, Peterson K C, Garcia Bermudez F L and Fearing R S (2013) Animal-inspired design and aerodynamic stabilization of a hexapedal millirobot *IEEE International Conference on Robotics and Automation* (IEEE) pp 3279–86

[65] Birkmeyer P, Peterson K and Fearing R S (2009) DASH: A dynamic 16g hexapedal robot *IEEE/RSJ International Conference on Intelligent Robots and Systems* (IEEE) pp 2683–9

[66] Jayaram K, Shum J, Castellanos S, Helbling E F and Wood R J (2020) Scaling down an insect-size microrobot, HAMR-VI into HAMR-Jr *IEEE International Conference on Robotics and Automation* (IEEE) pp 10305–11

[67] Park J, Kim K-S and Kim S (2014) Design of a cat-inspired robotic leg for fast running *Adv. Robot.* **28** 1587–98

[68] Griffin T M and Kram R (2000) Penguin waddling is not wasteful *Nature* **408** 929

[69] Griffin T M (2002) *Biomechanics of penguin walking: Waddling work does not explain expensive locomotion* (University of California, Berkeley)

[70] Schmitt J and Holmes P (2000) Mechanical models for insect locomotion: dynamics and stability in the horizontal plane - II. Application *Biol. Cybern.* **83** 517–27

[71] Garcia M, Chatterjee A and Ruina A (2000) Efficiency, speed, and scaling of two-dimensional passive-dynamic walking *Dyn. Stab. Syst.* **15** 75–99

[72] Grizzle J W, Hurst J, Morris B, Park H-W and Sreenath K (2009) MABEL, a new robotic bipedal walker and runner *American Control Conference* (IEEE) pp 2030–6

[73] Bledt G, Powell M J, Katz B, Di Carlo J, Wensing P M and Kim S (2018) MIT Cheetah 3: Design and Control of a Robust, Dynamic Quadruped Robot *IEEE/RSJ International Conference on Intelligent Robots and Systems* (IEEE) pp 2245–52

[74] Sponberg S and Full R J (2008) Neuromechanical response of musculo-skeletal structures in cockroaches during rapid running on rough terrain *J. Exp. Biol.* **211** 433–46

[75] Spence A J, Revzen S, Seipel J, Mullens C and Full R J (2010) Insects running on elastic surfaces *J. Exp. Biol.* **213** 1907–20

[76] Spagna J C, Goldman D I, Lin P-C, Koditschek D E and Full R J (2007) Distributed mechanical feedback in arthropods and robots simplifies control of rapid running on challenging terrain *Bioinspir. Biomim.* **2** 9–18

[77] Choi S, Ji G, Park J, Kim H, Mun J, Lee J H and Hwangbo J (2023) Learning quadrupedal locomotion on deformable terrain *Sci. Robot.* **8** 1–14

[78] Qian F, Lee D, Nikolich G, Koditschek D and Jerolmack D (2019) Rapid In Situ

Characterization of Soil Erodibility With a Field Deployable Robot *J. Geophys. Res. Earth Surf.* **124** 1261–80

[79] Wu X A, Huh T M, Mukherjee R and Cutkosky M (2016) Integrated Ground Reaction Force Sensing and Terrain Classification for Small Legged Robots *IEEE Robot. Autom. Lett.* **1** 1125–32

[80] Garcia Bermudez F L, Julian R C, Haldane D W, Abbeel P and Fearing R S (2012) Performance analysis and terrain classification for a legged robot over rough terrain *IEEE/RSJ International Conference on Intelligent Robots and Systems* (IEEE) pp 513–9

[81] Ordonez C, Shill J, Johnson A, Clark J and Collins E (2013) Terrain identification for RHex-type robots *Unmanned Systems Technology XV* vol 8741 p 87410Q

[82] Wangbo J E H, Ee J O L, Osovitskiy A L D, Ellicoso D A B, Ee J O L, Sounis V A T, Oltun V L K, Utter M A H, Hwangbo J, Lee J, Dosovitskiy A, Bellicoso D, Tsounis V, Koltun V and Hutter M (2019) Learning agile and dynamic motor skills for legged robots *Sci. Robot.* **4** 1–14

[83] Ijspeert A J (2008) Central pattern generators for locomotion control in animals and robots: A review *Neural Networks* **21** 642–53

[84] Lee J, Hwangbo J, Wellhausen L, Koltun V and Hutter M (2020) Learning quadrupedal locomotion over challenging terrain *Sci. Robot.* **5** eabc5986

[85] Faigl J and Čížek P (2019) Adaptive locomotion control of hexapod walking robot for traversing rough terrains with position feedback only *Rob. Auton. Syst.* **116** 136–47

[86] Bjelonic M, Kottege N, Homberger T, Borges P, Beckerle P and Chli M (2018)

Weaver: Hexapod robot for autonomous navigation on unstructured terrain *J. F. Robot.* **35** 1063–79

[87] Bellegarda G and Ijspeert A (2022) CPG-RL: Learning Central Pattern Generators for Quadruped Locomotion *IEEE Robot. Autom. Lett.* **7** 12547–54

[88] Clifton G, Stark A Y, Li C and Gravish N (2023) The bumpy road ahead: the role of substrate roughness on animal walking and a proposed comparative metric *J. Exp. Biol.* **226** jeb245261

[89] Kohlsdorf T and Biewener A A (2006) Negotiating obstacles: running kinematics of the lizard Sceloporus malachiticus *J. Zool.* **270** 359–71

[90] Penn D and Jane Brockmann H (1995) Age-biased stranding and righting in male horseshoe crabs, Limulus polyphemus *Anim. Behav.* **49** 1531–9

[91] Domokos G and Várkonyi P L (2008) Geometry and self-righting of turtles *Proc. R. Soc. B Biol. Sci.* **275** 11–7

[92] Weldon P J and Hoffman D L (1979) Kick and Thrust Foot Movements in the Righting and Escape Behavior of Marine Prosobranch Gastropods (Mollusca: Gastropoda) *Z. Tierpsychol.* **50** 387–98

[93] Frantsevich L I and Mokrushov P A (1980) Turning and righting in Geotrupes (Coleoptera, Scarabaeidae) *J. Comp. Physiol. A* **136** 279–89

[94] Pellis V C, Pellis S M and Teitelbaum P (1991) A descriptive analysis of the postnatal development of contact-righting in rats (Rattus norvegicus) *Dev. Psychobiol.* **24** 237–63

[95] Rimon E and Koditschek D E (1992) Exact robot navigation using artificial potential functions *IEEE Trans. Robot. Autom.* **8** 501–18

[96] Khatib O (1986) Real-Time Obstacle Avoidance for Manipulators and Mobile Robots *Int. J. Rob. Res.* **5** 90–8

[97] Tsitsiklis J, Bertsekas D and Athans M (1986) Distributed asynchronous deterministic and stochastic gradient optimization algorithms *IEEE Trans. Automat. Contr.* **31** 803–12

[98] Arslan O and Koditschek D E (2020) Sensor-Based Reactive Navigation in Unknown Convex Sphere Worlds *Springer Proceedings in Advanced Robotics* vol 13 pp 160–75

[99] Park H-W, Wensing P and Kim S (2015) Online Planning for Autonomous Running Jumps Over Obstacles in High-Speed Quadrupeds *Robotics: Science and Systems XI* (Robotics: Science and Systems Foundation) pp 1–9

[100] De A and Koditschek D E (2018) Vertical hopper compositions for preflexive and feedback-stabilized quadrupedal bounding, pacing, pronking, and trotting *Int. J. Rob. Res.* **37** 743–78

[101] Moore E Z, Campbell D, Grimminger F and Buehler M (2002) Reliable stair climbing in the simple hexapod "RHex" *IEEE International Conference on Robotics and Automation* vol 3 (IEEE) pp 2222–7

[102] Wenger G J, Johnson A M, Taylor C J and Koditschek D E (2015) Semi-autonomous exploration of multi-floor buildings with a legged robot *Unmanned Systems Technology XVII* vol 9468 p 94680B

[103] Ilhan B D, Johnson A M and Koditschek D E (2018) Autonomous legged hill ascent *J. F. Robot.* **35** 802–32

[104] Topping T T, Kenneally G and Koditschek D E (2017) Quasi-static and dynamic

mismatch for door opening and stair climbing with a legged robot *IEEE International Conference on Robotics and Automation* (IEEE) pp 1080–7

[105] Ren Z and Johnson A (2018) Toward Robust Stair Climbing of the Quadruped using Proprioceptive Sensing *C. Robot. Inst. Summer Sch. Work. Pap. J.*

[106] Tan J, Zhang T, Coumans E, Iscen A, Bai Y, Hafner D, Bohez S and Vanhoucke V (2018) Sim-to-Real: Learning Agile Locomotion For Quadruped Robots *Robotics: Science and Systems XIV* (Robotics: Science and Systems Foundation)

[107] Shafiee M, Bellegarda G and Ijspeert A (2024) ManyQuadrupeds: Learning a Single Locomotion Policy for Diverse Quadruped Robots *IEEE International Conference on Robotics and Automation* (IEEE) pp 3471–7

[108] Cheng X, Shi K, Agarwal A and Pathak D (2024) Extreme Parkour with Legged Robots *IEEE International Conference on Robotics and Automation* (IEEE) pp 11443–50

[109] Hoeller D, Rudin N, Sako D and Hutter M (2024) ANYmal parkour: Learning agile navigation for quadrupedal robots *Sci. Robot.* **9**

[110] Luo S, Li S, Yu R, Wang Z, Wu J and Zhu Q (2024) PIE: Parkour With Implicit-Explicit Learning Framework for Legged Robots *IEEE Robot. Autom. Lett.* **9** 9986–93

[111] Mi J, Wang Y and Li C (2022) Omni-Roach: A Legged Robot Capable of Traversing Multiple Types of Large Obstacles and Self-Righting *International Conference on Robotics and Automation* (IEEE) pp 235–42

[112] Berman G J (2018) Measuring behavior across scales *BMC Biol.* **16** 23

[113] Brown A E X and de Bivort B (2018) Ethology as a physical science *Nat. Phys.* **14**

653–7

[114] Nathan R, Getz W M, Revilla E, Holyoak M, Kadmon R, Saltz D and Smouse P E (2008) A movement ecology paradigm for unifying organismal movement research *Proc. Natl. Acad. Sci.* **105** 19052–9

[115] Blaesing B and Cruse H (2004) Stick insect locomotion in a complex environment: climbing over large gaps *J. Exp. Biol.* **207** 1273–86

[116] Ritzmann R E, Harley C M, Daltorio K A, Tietz B R, Pollack A J, Bender J A, Guo P, Horomanski A L, Kathman N D, Nieuwoudt C, Brown A E and Quinn R D (2012) Deciding Which Way to Go: How Do Insects Alter Movements to Negotiate Barriers? *Front. Neurosci.* **6** 1–10

[117] Bramble D M and Lieberman D E (2004) Endurance running and the evolution of Homo *Nature* **432** 345–52

[118] Shepard E L C, Wilson R P, Rees W G, Grundy E, Lambertucci S A and Vosper S B (2013) Energy Landscapes Shape Animal Movement Ecology *Am. Nat.* **182** 298–312

[119] Diedrich F J and Warren W H (1995) Why change gaits? Dynamics of the walk-run transition. *J. Exp. Psychol. Hum. Percept. Perform.* **21** 183–202

[120] Wilshin S, Haynes G C, Porteous J, Koditschek D, Revzen S and Spence A J (2017) Morphology and the gradient of a symmetric potential predict gait transitions of dogs *Biol. Cybern.* **111** 269–77

[121] Onuchic J N and Wolynes P G (2004) Theory of protein folding *Curr. Opin. Struct. Biol.* **14** 70–5

[122] Dill K A, Ozkan S B, Shell M S and Weikl T R (2008) The Protein Folding Problem

Annu. Rev. Biophys. **37** 289–316

[123] Dill K A and MacCallum J L (2012) The Protein-Folding Problem, 50 Years On *Science* **338** 1042–6

[124] Kelso J A S (2012) Multistability and metastability: understanding dynamic coordination in the brain *Philos. Trans. R. Soc. B Biol. Sci.* **367** 906–18

[125] Mason M T, Rodriguez A, Srinivasa S S and Vazquez A S (2012) Autonomous manipulation with a general-purpose simple hand *Int. J. Rob. Res.* **31** 688–703

[126] Owaki D, Goda M, Miyazawa S and Ishiguro A (2017) A Minimal Model Describing Hexapedal Interlimb Coordination: The Tegotae-Based Approach *Front. Neurorobot.* **11** 1–13

[127] Owaki D and Ishiguro A (2017) A Quadruped Robot Exhibiting Spontaneous Gait Transitions from Walking to Trotting to Galloping *Sci. Rep.* **7** 277

[128] Haynes G C and Rizzi A A (2006) Gaits and gait transitions for legged robots *IEEE International Conference on Robotics and Automation* vol 2006 (IEEE) pp 1117–22

[129] Shao Y, Jin Y, Liu X, He W, Wang H and Yang W (2022) Learning Free Gait Transition for Quadruped Robots Via Phase-Guided Controller *IEEE Robot. Autom. Lett.* **7** 1230–7

[130] Gay S, Santos-Victor J and Ijspeert A (2013) Learning robot gait stability using neural networks as sensory feedback function for Central Pattern Generators *IEEE/RSJ International Conference on Intelligent Robots and Systems* (IEEE) pp 194–201

[131] Righetti L and Ijspeert A J (2008) Pattern generators with sensory feedback for the control of quadruped locomotion *IEEE International Conference on Robotics and*

Automation (IEEE) pp 819–24

[132] Owaki D, Kano T, Nagasawa K, Tero A and Ishiguro A (2013) Simple robot suggests physical interlimb communication is essential for quadruped walking *J. R. Soc. Interface* **10** 20120669

[133] Shafiee M, Bellegarda G and Ijspeert A (2023) DeepTransition: Viability Leads to the Emergence of Gait Transitions in Learning Anticipatory Quadrupedal Locomotion Skills *arXiv* 2306.07419 [cs.RO]

[134] Mintchev S and Floreano D (2016) Adaptive Morphology: A Design Principle for Multimodal and Multifunctional Robots *IEEE Robot. Autom. Mag.* **23** 42–54

[135] Mongeau J-M, Sponberg S N, Miller J P and Full R J (2015) Sensory processing within antenna enables rapid implementation of feedback control for high-speed running maneuvers *J. Exp. Biol.* **218** 2344–54

[136] Demir A, Samson E W and Cowan N J (2010) A tunable physical model of arthropod antennae *IEEE International Conference on Robotics and Automation* (IEEE) pp 3793–8

[137] Camhi J M and Johnson E N (1999) High-frequency steering maneuvers mediated by tactile cues: antennal wall-following in the cockroach *J. Exp. Biol.* **202** 631–43

[138] Cowan N J, Lee J and Full R J (2006) Task-level control of rapid wall following in the American cockroach *J. Exp. Biol.* **209** 3043–3043

[139] Krakauer J W, Ghazanfar A A, Gomez-Marin A, MacIver M A and Poeppel D (2017) Neuroscience Needs Behavior: Correcting a Reductionist Bias *Neuron* **93** 480–90

[140] Tuthill J C and Wilson R I (2016) Mechanosensation and Adaptive Motor Control

in Insects *Curr. Biol.* **26** R1022–38

[141] Tuthill J C and Azim E (2018) Proprioception *Curr. Biol.* **28** R194–203

[142] Dinges G F, Bockemühl T, Iacoviello F, Shearing P R, Büschges A and Blanke A (2022) Ultra high-resolution biomechanics suggest that substructures within insect mechanosensors decisively affect their sensitivity *J. R. Soc. Interface* **19** 20220102

[143] Pringle J W S (1938) Proprioception In Insects *J. Exp. Biol.* **15** 114–31

[144] Sundaram S, Kellnhofer P, Li Y, Zhu J-Y, Torralba A and Matusik W (2019) Learning the signatures of the human grasp using a scalable tactile glove *Nature* **569** 698–702

[145] Mongeau J-M, Demir A, Lee J, Cowan N J and Full R J (2013) Locomotion- and mechanics-mediated tactile sensing: antenna reconfiguration simplifies control during high-speed navigation in cockroaches *J. Exp. Biol.* **216** 4530–41

[146] Solomon J H and Hartmann M J (2006) Robotic whiskers used to sense features *Nature* **443** 525–525

[147] Nelson M E and MacIver M A (2006) Sensory acquisition in active sensing systems *J. Comp. Physiol. A Neuroethol. Sensory, Neural, Behav. Physiol.* **192** 573–86

[148] Prescott T J, Diamond M E and Wing A M (2011) Active touch sensing *Philos. Trans. R. Soc. B Biol. Sci.* **366** 2989–95

[149] Zweifel N O and Hartmann M J Z (2020) Defining “active sensing” through an analysis of sensing energetics: homeoactive and alloactive sensing *J. Neurophysiol.* **124** 40–8

[150] Baba Y, Tsukada A and Comer C M (2010) Collision avoidance by running insects: Antennal guidance in cockroaches *J. Exp. Biol.* **213** 2294–302

[151] Okada J and Toh Y (2006) Active tactile sensing for localization of objects by the cockroach antenna *J. Comp. Physiol. A Neuroethol. Sensory, Neural, Behav. Physiol.* **192** 715–26

[152] Staudacher E M, Gebhardt M and Dürr V (2005) Antennal Movements and Mechanoreception: Neurobiology of Active Tactile Sensors *Advances in Insect Physiology* vol 32 pp 49–205

[153] Schütz C and Dürr V (2011) Active tactile exploration for adaptive locomotion in the stick insect *Philos. Trans. R. Soc. B Biol. Sci.* **366** 2996–3005

[154] Berendes V and Dürr V (2022) Active tactile exploration and tactually induced turning in tethered walking stick insects *J. Exp. Biol.* **225** jeb243190

[155] Hartmann M J Z (2001) Active sensing capabilities of the rat whisker system *Auton. Robots* **11** 249–54

[156] Bush N E, Solla S A and Hartmann M J (2016) Whisking mechanics and active sensing *Curr. Opin. Neurobiol.* **40** 178–88

[157] Hartmann M J Z (2011) A night in the life of a rat: Vibrissal mechanics and tactile exploration *Ann. N. Y. Acad. Sci.* **1225** 110–8

[158] Hirai K, Hirose M, Haikawa Y and Takenaka T (1988) The development of Honda humanoid robot *IEEE International Conference on Robotics and Automation* vol 2 (IEEE) pp 1321–6

[159] Qinghua Li, Takanishi A and Kato I A biped walking robot having a ZMP measurement system using universal force-moment sensors *IEEE/RSJ International Conference on Intelligent Robots and Systems* (IEEE) pp 1568–73

[160] Wu Z and Revzen S (2025) In-Situ Calibration of Six-Axis Force/Torque

Transducers on a Six-Legged Robot *J. Dyn. Syst. Meas. Control* **147** 1–17

[161] Roberts P, Zadan M and Majidi C (2021) Soft Tactile Sensing Skins for Robotics *Curr. Robot. Reports* **2** 343–54

[162] Ramesh D, Fu Q and Li C (2022) SenSnake: A snake robot with contact force sensing for studying locomotion in complex 3-D terrain *International Conference on Robotics and Automation* (IEEE) pp 2068–75

[163] Yao G, Xu L, Cheng X, Li Y, Huang X, Guo W, Liu S, Wang Z L and Wu H (2020) Bioinspired Triboelectric Nanogenerators as Self-Powered Electronic Skin for Robotic Tactile Sensing *Adv. Funct. Mater.* **30** 1–9

[164] Zhu M, Lou M, Abdalla I, Yu J, Li Z and Ding B (2020) Highly shape adaptive fiber based electronic skin for sensitive joint motion monitoring and tactile sensing *Nano Energy* **69** 104429

[165] Kamegawa T, Akiyama T, Suzuki Y, Kishutani T and Gofuku A (2020) Three-Dimensional Reflexive Behavior by a Snake Robot with Full Circumference Pressure Sensors *IEEE/SICE International Symposium on System Integration* (IEEE) pp 897–902

[166] Cowan N J, Ma E J, Cutkosky M and Full R J (2005) A Biologically Inspired Passive Antenna for Steering Control of a Running Robot *Robotics Research. The Eleventh International Symposium* (Springer Berlin Heidelberg) pp 541–50

[167] Qian F and Goldman D (2015) The dynamics of legged locomotion in heterogeneous terrain: universality in scattering and sensitivity to initial conditions *Robotics: Science and Systems XI* vol 11 (Robotics: Science and Systems Foundation)

[168] Heglund N C (1981) A Simple Design for A Force-Plate to Measure Ground Reaction Forces *J. Exp. Biol.* **93** 333–8

[169] Harris J K (1978) A photoelastic substrate technique for dynamic measurements of forces exerted by moving organisms *J. Microsc.* **114** 219–28

[170] Harris J and Ghiradella H (1980) The Forces Exerted on the Substrate By Walking and Stationary Crickets *J. Exp. Biol.* **85** 263–79

[171] Full R J, Yamauchi A and Jindrich D L (1995) Maximum single leg force production: cockroaches righting on photoelastic gelatin *J. Exp. Biol.* **198** 2441–52

[172] Hunt L T, Daw N D, Kaanders P, MacIver M A, Mugan U, Procyk E, Redish A D, Russo E, Scholl J, Stachenfeld K, Wilson C R E and Kolling N (2021) Formalizing planning and information search in naturalistic decision-making *Nat. Neurosci.* **24** 1051–64

[173] Tarsitano M S and Jackson R R (1997) Araneophagic jumping spiders discriminate between detour routes that do and do not lead to prey *Anim. Behav.* **53** 257–66

[174] O'Keefe J and Nadel L (1979) The cognitive map as a hippocampus *Behav. Brain Sci.* **2** 520–33

[175] Behrens T E J, Muller T H, Whittington J C R, Mark S, Baram A B, Stachenfeld K L and Kurth-Nelson Z (2018) What Is a Cognitive Map? Organizing Knowledge for Flexible Behavior *Neuron* **100** 490–509

[176] Tolman E C (1948) Cognitive maps in rats and men. *Psychol. Rev.* **55** 189–208

[177] Jacobs L F (2012) From chemotaxis to the cognitive map: The function of olfaction *Proc. Natl. Acad. Sci.* **109** 10693–700

[178] Jeffery K J (2007) Self-localization and the entorhinal–hippocampal system *Curr.*

Opin. Neurobiol. **17** 684–91

[179] Redish A D (2016) Vicarious trial and error *Nat. Rev. Neurosci.* **17** 147–59

[180] Mugan U and MacIver M A (2020) Spatial planning with long visual range benefits escape from visual predators in complex naturalistic environments *Nat. Commun.* **11** 3057

[181] Spence K W (1936) The nature of discrimination learning in animals. *Psychol. Rev.* **43** 427–49

[182] Deneubourg J L, Pasteels J M and Verhaeghe J C (1983) Probabilistic behaviour in ants: A strategy of errors? *J. Theor. Biol.* **105** 259–71

[183] Goss S, Beckers R, Deneubourg J L, Aron S and Pasteels J M (1990) How Trail Laying and Trail Following Can Solve Foraging Problems for Ant Colonies *Behavioural Mechanisms of Food Selection* (Berlin, Heidelberg: Springer Berlin Heidelberg) pp 661–78

[184] Aguilar-Argüello S, Gerhard D and Nelson X J (2019) Risk assessment and the use of novel shortcuts in spatial detouring tasks in jumping spiders *Behav. Ecol.* **30** 1488–98

[185] Bell W J and Kramer E (1979) Search and anemotactic orientation of cockroaches *J. Insect Physiol.* **25** 631–40

[186] Bell W J and Tobin T R (1982) Chemo-orientation *Biol. Rev.* **57** 219–60

[187] Catania K C (2013) Stereo and serial sniffing guide navigation to an odour source in a mammal *Nat. Commun.* **4** 1441

[188] Barrows W M (1907) The reactions of the Pomace fly, Drosophila ampelophila loew, to odorous substances *J. Exp. Zool.* **4** 515–37

[189] Van Breugel F and Dickinson M H (2014) Plume-tracking behavior of flying drosophila emerges from a set of distinct sensory-motor reflexes *Curr. Biol.* **24** 274–86

[190] Stupski S D and van Breugel F (2024) Wind gates olfaction-driven search states in free flight *Curr. Biol.* 1–15

[191] Kennedy J S (1983) Zigzagging and casting as a programmed response to wind-borne odour: a review *Physiol. Entomol.* **8** 109–20

[192] van Breugel F (2021) A Nonlinear Observability Analysis of Ambient Wind Estimation with Uncalibrated Sensors, Inspired by Insect Neural Encoding *IEEE Conference on Decision and Control* (IEEE) pp 1399–406

[193] van Breugel F, Jewell R and Houle J (2022) Active anemosensing hypothesis: how flying insects could estimate ambient wind direction through sensory integration and active movement *J. R. Soc. Interface* **19** 20220258

[194] Cellini B, Boyacioğlu B and Van Breugel F (2023) Empirical Individual State Observability *IEEE Conference on Decision and Control* pp 8450–6

[195] Biswas D, Lamperski A, Yang Y, Hoffman K, Guckenheimer J, Fortune E S and Cowan N J (2023) Mode switching in organisms for solving explore-versus-exploit problems *Nat. Mach. Intell.* **5** 1285–96

[196] Choset H, Lynch K M, Hutchinson S, Kantor G A and Burgard W (2005) *Principles of Robot Motion: Theory, Algorithms, and Implementations* (MIT Press)

[197] Kavraki L E, Svestka P, Latombe J-C and Overmars M H (1996) Probabilistic roadmaps for path planning in high-dimensional configuration spaces *IEEE Trans. Robot. Autom.* **12** 566–80

[198] Hsu D, Latombe J-C and Motwani R (1999) Path planning in expansive configuration spaces *Int. J. Comput. Geom. Appl.* **09** 495–512

[199] LaValle S (1998) Rapidly-exploring random trees: A new tool for path planning *Comput. Sci. Dep. Iowa State Univ.* TR 98-11

[200] Kuffner J J and LaValle S M (2000) RRT-connect: An efficient approach to single-query path planning *IEEE International Conference on Robotics and Automation* vol 2 (IEEE) pp 995–1001

[201] LaValle S M and Kuffner J J (2001) Randomized Kinodynamic Planning *Int. J. Rob. Res.* **20** 378–400

[202] Agarwal P K, Kavraki L E and Mason M T (1998) OBPRM: An Obstacle-Based PRM for 3D Workspaces *Robotics: The Algorithmic Perspective* (A K Peters/CRC Press) p 14

[203] Dijkstra E W (1959) A note on two problems in connexion with graphs *Numer. Math.* **1** 269–71

[204] Hart P, Nilsson N and Raphael B (1968) A Formal Basis for the Heuristic Determination of Minimum Cost Paths *IEEE Trans. Syst. Sci. Cybern.* **4** 100–7

[205] Kirk D E (2004) *Optimal control theory: An introduction* (Dover Publications, Inc)

[206] Dorigo M, Maniezzo V and Colorni A (1996) Ant system: optimization by a colony of cooperating agents *IEEE Trans. Syst. Man, Cybern. Part B* **26** 29–41

[207] Holland J H (1992) Genetic Algorithms *Sci. Am.* **267** 66–72

[208] Georgiou A, Vandecasteele H, Bello-Rivas J M and Kevrekidis I (2023) Locating saddle points using gradient extremals on manifolds adaptively revealed as point clouds *Chaos An Interdiscip. J. Nonlinear Sci.* **33** 123108

[209] Laio A and Parrinello M (2002) Escaping free-energy minima *Proc. Natl. Acad. Sci.* **99** 12562–6

[210] Darve E, Rodríguez-Gómez D and Pohorille A (2008) Adaptive biasing force method for scalar and vector free energy calculations *J. Chem. Phys.* **128** 144120

[211] Olender R and Elber R (1996) Calculation of classical trajectories with a very large time step: Formalism and numerical examples *J. Chem. Phys.* **105** 9299–315

[212] Jónsson H, Mills G and Jacobsen K W (1998) Nudged elastic band method for finding minimum energy paths of transitions *Classical and Quantum Dynamics in Condensed Phase Simulations* (World Scientific) pp 385–404

[213] E W, Ren W and Vanden-Eijnden E (2002) String method for the study of rare events *Phys. Rev. B* **66** 052301

[214] Hirsch M and Quapp W (2004) Reaction Pathways and Convexity of the Potential Energy Surface: Application of Newton Trajectories *J. Math. Chem.* **36** 307–40

[215] Smith C M (1990) How to find a saddle point *Int. J. Quantum Chem.* **37** 773–83

[216] Schlegel H B (1992) Following gradient extremal paths *Theor. Chim. Acta* **83** 15–20

[217] Henkelman G and Jónsson H (1999) A dimer method for finding saddle points on high dimensional potential surfaces using only first derivatives *J. Chem. Phys.* **111** 7010–22

[218] Weinan E, Zhou X, E W and Zhou X (2011) The gentlest ascent dynamics *Nonlinearity* **24** 1831–42

[219] Bell W J, Roth L M and Nalepa. C A (2007) *Cockroaches: ecology, behavior, and natural history* (John Hopkins University Press)

[220] Jindrich D L and Full R J (2002) Dynamic stabilization of rapid hexapedal locomotion. *J. Exp. Biol.* **205** 2803–23

[221] Jayaram K (2015) *Robustness of Biological and Bio-inspired Exoskeletons* (University of California, Berkeley)

[222] Harley C M, English B A and Ritzmann R E (2009) Characterization of obstacle negotiation behaviors in the cockroach, Blaberus discoidalis *J. Exp. Biol.* **212** 1463–76

[223] Ritzmann R E, Pollack A J, Archinal J, Ridgel A L and Quinn R D (2005) Descending control of body attitude in the cockroach Blaberus discoidalis and its role in incline climbing *J. Comp. Physiol. A* **191** 253–64

[224] Watson J, Ritzmann R and Pollack A (2002) Control of climbing behavior in the cockroach, Blaberus discoidalis . II. Motor activities associated with joint movement *J. Comp. Physiol. A Sensory, Neural, Behav. Physiol.* **188** 55–69

[225] Sponberg S, Libby T, Mullens C H and Full R J (2011) Shifts in a single muscle's control potential of body dynamics are determined by mechanical feedback *Philos. Trans. R. Soc. B Biol. Sci.* **366** 1606–20

[226] Wang Y, Othayoth R and Li C (2022) Cockroaches adjust body and appendages to traverse cluttered large obstacles *J. Exp. Biol.* **225** jeb243605

[227] Wang Y, Xu L and Li C (2024) Sensing environmental interaction physics to traverse cluttered obstacles *arXiv* 2401.13062 [cs.RO]

[228] Zheng B, Xuan Q and Li C (2022) A Minimalistic Stochastic Dynamics Model of Cluttered Obstacle Traversal *IEEE Robot. Autom. Lett.* **7** 5119–26

[229] Li C, Kessens C C, Fearing R S and Full R J (2017) Mechanical principles of

dynamic terrestrial self-righting using wings *Adv. Robot.* **31** 881–900

[230] Kram R, Wong B and Full R J (1997) Three-dimensional kinematics and limb kinetic energy of running cockroaches. *J. Exp. Biol.* **200** 1919–29

[231] Crall J D, Gravish N, Mountcastle A M and Combes S A (2015) BEEtag: A Low-Cost, Image-Based Tracking System for the Study of Animal Behavior and Locomotion ed G F Gilestro *PLoS One* **10** e0136487

[232] Mathis A, Mamidanna P, Cury K M, Abe T, Murthy V N, Mathis M W and Bethge M (2018) DeepLabCut: markerless pose estimation of user-defined body parts with deep learning *Nat. Neurosci.* **21** 1281–9

[233] Hedrick T L (2008) Software techniques for two- and three-dimensional kinematic measurements of biological and biomimetic systems *Bioinspir. Biomim.* **3** 034001

[234] Cormen T H, Leiserson C E, Rivest R L and Stein C (2009) *Introduction to algorithms* (MIT press)

[235] Delcomyn F, Nelson M E and Cocatre-Zilgien J H (1996) Sense organs of insect legs and the selection of sensors for agile walking robots *Int. J. Rob. Res.* **15** 113–27

[236] Field L H and Matheson T (1998) Chordotonal Organs of Insects *Advances in Insect Physiology* vol 27 pp 1–228

[237] Xuan Q and Li C (2024) Environmental force sensing helps robots traverse cluttered large obstacles *Bioinspir. Biomim.* **19** 016002

[238] Sanderson D and Jackson C F (1912) *Elementary Entomology* (Boston, MA)

[239] Theunissen L M and Dürr V (2013) Insects Use Two Distinct Classes of Steps during Unrestrained Locomotion ed H G Krapp *PLoS One* **8** e85321

[240] Wöhrl T, Reinhardt L and Blickhan R (2017) Propulsion in hexapod locomotion: How do desert ants traverse slopes? *J. Exp. Biol.* **220** 1618–25

[241] Li J, Orrego S, Pan J, He P and Kang S H (2019) Ultrasensitive, flexible, and low-cost nanoporous piezoresistive composites for tactile pressure sensing *Nanoscale* **11** 2779–86

[242] Mongeau J-M, Sponberg S N, Miller J P and Full R J (2015) Sensory processing within antenna enables rapid implementation of feedback control for high-speed running maneuvers *J. Exp. Biol.* **218** 2344–54

[243] Sponberg S, Spence A J, Mullens C H and Full R J (2011) A single muscle's multifunctional control potential of body dynamics for postural control and running *Philos. Trans. R. Soc. B Biol. Sci.* **366** 1592–605

[244] Spirito C P and Mushrush D L (1979) Interlimb Coordination During Slow Walking in the Cockroach: I. Effects of Substrate Alterations *J. Exp. Biol.* **78** 233–43

[245] Pearson K G and Iles J F (1973) Nervous Mechanisms Underlying Intersegmental Co-Ordination of Leg Movements During Walking in the Cockroach *J. Exp. Biol.* **58** 725–44

[246] Schilling M and Cruse H (2020) Decentralized control of insect walking: A simple neural network explains a wide range of behavioral and neurophysiological results *PLOS Comput. Biol.* **16** e1007804

[247] Okada J, Kanamaru Y and Toh Y (2002) Mechanosensory Control of Antennal Movement by the Scapal Hair Plate in the American Cockroach *Zoolog. Sci.* **19** 1201–10

[248] Stamper S A, Roth E, Cowan N J and Fortune E S (2012) Active sensing via

movement shapes spatiotemporal patterns of sensory feedback *J. Exp. Biol.* **215** 1567–74

[249] Moss C F, Bohn K, Gilkenson H and Surlykke A (2006) Active Listening for Spatial Orientation in a Complex Auditory Scene *PLoS Biol.* **4** e79

[250] Wessnitzer J and Webb B (2006) Multimodal sensory integration in insects—towards insect brain control architectures *Bioinspir. Biomim.* **1** 63–75

[251] Wehner R (2020) *Desert Navigator : The Journey of an Ant* (Harvard University Press)

[252] Sober S J and Sabes P N (2005) Flexible strategies for sensory integration during motor planning *Nat. Neurosci.* **8** 490–7

[253] Koditschek D E (2021) What Is Robotics? Why Do We Need It and How Can We Get It? *Annu. Rev. Control. Robot. Auton. Syst.* **4** 1–33

[254] Wooden D, Malchano M, Blankespoor K, Howardy A, Rizzi A A and Raibert M (2010) Autonomous navigation for BigDog *IEEE International Conference on Robotics and Automation* (IEEE) pp 4736–41

[255] Bajcsy R, Aloimonos Y and Tsotsos J K (2018) Revisiting active perception *Auton. Robots* **42** 177–96

[256] Qian F and Goldman D (2015) Anticipatory control using substrate manipulation enables trajectory control of legged locomotion on heterogeneous granular media *Micro- and Nanotechnology Sensors, Systems, and Applications VII* vol 9467 (SPIE) p 94671U

[257] Bhatia H, Norgard G, Pascucci V and Bremer P T (2013) The Helmholtz-Hodge decomposition - A survey *IEEE Trans. Vis. Comput. Graph.* **19** 1386–404

[258] Cybenko G (1989) Approximation by superpositions of a sigmoidal function *Math. Control. Signals, Syst.* **2** 303–14

[259] Hornik K, Stinchcombe M and White H (1989) Multilayer feedforward networks are universal approximators *Neural Networks* **2** 359–66

[260] Bishop C M (2006) *Pattern Recognition and Machine Learning* (springer)

[261] Okada J and Toh Y (2000) The role of antennal hair plates in object-guided tactile orientation of the cockroach (Periplaneta americana) *J. Comp. Physiol. A Sensory, Neural, Behav. Physiol.* **186** 849–57

[262] Biswas D, Arend L A, Stamper S A, Vágvölgyi B P, Fortune E S and Cowan N J (2018) Closed-Loop Control of Active Sensing Movements Regulates Sensory Slip *Curr. Biol.* **28** 4029-4036.e4

[263] Othayoth R, Strebel B, Han Y, Francois E and Li C (2022) A terrain treadmill to study animal locomotion through large obstacles *J. Exp. Biol.* **225** jeb243558

[264] Schultz A E, Solomon J H, Peshkin M A and Hartmann M J (2005) Multifunctional whisker arrays for distance detection, terrain mapping, and object feature extraction *IEEE Int. Conf. Robot. Autom.* **2005** 2588–93

[265] Solomon J H and Hartmann M J Z (2010) Extracting object contours with the sweep of a robotic whisker using torque information *Int. J. Rob. Res.* **29** 1233–45

[266] Emnett H, Graff M and Hartmann M (2018) A Novel Whisker Sensor Used for 3D Contact Point Determination and Contour Extraction *Robotics: Science and Systems* vol 14 (Robotics: Science and Systems Foundation)

[267] Huet L A, Rudnicki J W and Hartmann M J Z (2017) Tactile sensing with whiskers of various shapes: Determining the three-dimensional location of object contact

based on mechanical signals at the whisker base *Soft Robot.* **4** 88–102

[268] Huet L A, Emnett H M and Hartmann M J Z (2022) Demonstration of three-dimensional contact point determination and contour reconstruction during active whisking behavior of an awake rat *PLoS Comput. Biol.* **18** 1–28

[269] Thiele H-U (1977) *Carabid beetles in their environments: a study on habitat selection by adaptations in physiology and behaviour* (Springer Science & Business Media)

[270] Henkelman G, Jóhannesson G and Jónsson H (2008) Methods for Finding Saddle Points and Minimum Energy Paths *Theoretical Methods in Condensed Phase Chemistry* (Dordrecht: Kluwer Academic Publishers) pp 269–302

[271] Bello-Rivas J M, Georgiou A, Vandecasteele H and Kevrekidis I G (2023) Gentlest Ascent Dynamics on Manifolds Defined by Adaptively Sampled Point-Clouds *J. Phys. Chem. B* **127** 5178–89

[272] Zhang L, Ren W, Samanta A and Du Q (2016) Recent developments in computational modelling of nucleation in phase transformations *npj Comput. Mater.* **2** 16003

[273] Quapp W, Hirsch M, Imig O and Heidrich D (1998) Searching for saddle points of potential energy surfaces by following a reduced gradient *J. Comput. Chem.* **19** 1087

[274] Bello-Rivas J M, Georgiou A, Guckenheimer J and Kevrekidis I G (2023) Staying the course: iteratively locating equilibria of dynamical systems on Riemannian manifolds defined by point-clouds *J. Math. Chem.* **61** 600–29

[275] Pastor R W (1994) Techniques and Applications of Langevin Dynamics Simulations *The Molecular Dynamics of Liquid Crystals* (Springer Netherlands) pp

85–138

[276] Jordan M I (2019) Dynamical, symplectic and stochastic perspectives on gradient-based optimization *Proceedings of the International Congress of Mathematicians (ICM 2018)* (World Scientific) pp 523–49

[277] Cheng X, Yin D, Bartlett P and Jordan M (2020) Stochastic gradient and langevin processes *International Conference on Machine Learning* vol 119 (PMLR) pp 1810–9

[278] Li S, Dutta B, Cannon S, Daymude J J, Avinery R, Aydin E, Richa A W, Goldman D I and Randall D (2021) Programming active cohesive granular matter with mechanically induced phase changes *Sci. Adv.* **7** 1–12

[279] Li C (2024) Recent Progress in the Physical Principles of Dynamic Ground Self-Righting *Integr. Comp. Biol.* **64** 674–93

[280] Patane G (2022) Meshless Approximation and Helmholtz-Hodge Decomposition of Vector Fields *IEEE Trans. Vis. Comput. Graph.* **28** 1328–41

[281] Razafindrazaka F H, Poelke K, Polthier K and Goubergrits L (2019) A Consistent Discrete 3D Hodge-type Decomposition: implementation and practical evaluation *arXiv* 1911.12173 [math.NA]

[282] Lemoine A, Caltagirone J P, Azaïez M and Vincent S (2015) Discrete Helmholtz–Hodge Decomposition on Polyhedral Meshes Using Compatible Discrete Operators *J. Sci. Comput.* **65** 34–53

[283] Deriaz E and Perrier V (2006) Divergence-free and curl-free wavelets in two dimensions and three dimensions: Application to turbulent flows *J. Turbul.* **7** 1–37

[284] Guo Q, Mandal M K and Li M Y (2005) Efficient Hodge-Helmholtz decomposition

of motion fields *Pattern Recognit. Lett.* **26** 493–501

[285] Nguyen D Q, Fedkiw R and Jensen H W (2002) Physically based modeling and animation of fire *Annual conference on Computer graphics and interactive techniques* (ACM) pp 721–8

[286] Kaveh A (2017) Particle Swarm Optimization *Advances in Metaheuristic Algorithms for Optimal Design of Structures* (Springer International Publishing) pp 11–43

[287] Kirkpatrick S, Gelatt C D and Vecchi M P (1983) Optimization by Simulated Annealing *Science* **220** 671–80

[288] Wang Y, Xu L and Li C (2024) Force sensing to reconstruct potential energy landscapes for cluttered large obstacle traversal *arXiv* 2401.13062 [cs.RO]

[289] Savitzky A and Golay M J E (1964) Smoothing and Differentiation of Data by Simplified Least Squares Procedures. *Anal. Chem.* **36** 1627–39

[290] Box G E P, Jenkins G M, Reinse G C and Ljung G M (2015) *Time series analysis: forecasting and control* (John Wiley & Sons)

[291] Tasora A, Serban R, Mazhar H, Pazouki A, Melanz D, Fleischmann J, Taylor M, Sugiyama H and Negrut D (2016) Chrono: An Open Source Multi-physics Dynamics Engine *High Performance Computing in Science and Engineering* pp 19–49

[292] Choi H, Crump C, Duriez C, Elmquist A, Hager G, Han D, Hearl F, Hodgins J, Jain A, Leve F, Li C, Meier F, Negrut D, Righetti L, Rodriguez A, Tan J and Trinkle J (2021) On the use of simulation in robotics: Opportunities, challenges, and suggestions for moving forward *Proc. Natl. Acad. Sci.* **118** 1–9

[293] Chebotar Y, Handa A, Makoviychuk V, Macklin M, Issac J, Ratliff N and Fox Di (2019) Closing the Sim-to-Real Loop: Adapting Simulation Randomization with Real World Experience *International Conference on Robotics and Automation* (IEEE) pp 8973–9

[294] Hatton R L and Choset H (2011) Geometric motion planning: The local connection, Stokes' theorem, and the importance of coordinate choice *Int. J. Rob. Res.* **30** 988–1014

[295] Arvidson R E, Bell J F, Bellutta P, Cabrol N A, Catalano J G, Cohen J, Crumpler L S, Des Marais D J, Estlin T A, Farrand W H, Gellert R, Grant J A, Greenberger R N, Guinness E A, Herkenhoff K E, Herman J A, Iagnemma K D, Johnson J R, Klingelhöfer G, Li R, Lichtenberg K A, Maxwell S A, Ming D W, Morris R V., Rice M S, Ruff S W, Shaw A, Siebach K L, de Souza P A, Stroupe A W, Squyres S W, Sullivan R J, Talley K P, Townsend J A, Wang A, Wright J R and Yen A S (2010) Spirit Mars Rover Mission: Overview and selected results from the northern Home Plate Winter Haven to the side of Scamander crater *J. Geophys. Res. Planets* **115** 1–19

[296] Safaie M, Chang J C, Park J, Miller L E, Dudman J T, Perich M G and Gallego J A (2023) Preserved neural dynamics across animals performing similar behaviour *Nature* **623** 765–71

[297] Graves A (2012) Long Short-Term Memory *Supervised Sequence Labelling with Recurrent Neural Networks* (Springer Berlin Heidelberg) pp 37–45

[298] Cellini B, Stupski S, Houle J and van Breugel F (2024) Sensorimotor strategies for wind direction estimation in flying insects *The Society for Integrative and*

Comparative Biology p 52

[299] Yang G-Z, Bellingham J, Dupont P E, Fischer P, Floridi L, Full R, Jacobstein N, Kumar V, McNutt M, Merrifield R, Nelson B J, Scassellati B, Taddeo M, Taylor R, Veloso M, Wang Z L and Wood R (2018) The grand challenges of Science Robotics *Sci. Robot.* **3** 1–14

[300] Roth E, Hall R W, Daniel T L and Sponberg S (2016) Integration of parallel mechanosensory and visual pathways resolved through sensory conflict *Proc. Natl. Acad. Sci.* **113** 12832–7

[301] Oie K S, Kiemel T and Jeka J J (2002) Multisensory fusion: simultaneous re-weighting of vision and touch for the control of human posture *Cogn. Brain Res.* **14** 164–76

[302] Sutton E E, Demir A, Stamper S A, Fortune E S and Cowan N J (2016) Dynamic modulation of visual and electrosensory gains for locomotor control *J. R. Soc. Interface* **13** 20160057

[303] Yeh H, Yang Y, Biswas D and Cowan N J (2024) Illumination mediates a switch in both active sensing and control in weakly electric fish *bioRxiv* 10.15.618597

[304] Burden S A, Libby T, Jayaram K, Sponberg S and Donelan J M (2024) Why animals can outrun robots *Sci. Robot.* **9** 1–10

[305] Corniani G and Saal H P (2020) Tactile innervation densities across the whole body *J. Neurophysiol.* **124** 1229–40

[306] Gautschi G (2002) Piezoelectric Sensors *Piezoelectric Sensorics* (Springer Berlin Heidelberg) pp 73–91

[307] Bay H, Tuytelaars T and Van Gool L (2006) SURF: Speeded Up Robust Features

Technical Reports (ESE) pp 404–17

[308] Seok S, Wang A, Otten D and Kim S (2012) Actuator design for high force proprioceptive control in fast legged locomotion *IEEE/RSJ International Conference on Intelligent Robots and Systems* (IEEE) pp 1970–5

[309] Mochon S and McMahon T A (1980) Ballistic walking *J. Biomech.* **13** 49–57

[310] Geyer H, Seyfarth A and Blickhan R (2006) Compliant leg behaviour explains basic dynamics of walking and running *Proc. R. Soc. B Biol. Sci.* **273** 2861–7

[311] Zhang T and Goldman D I (2014) The effectiveness of resistive force theory in granular locomotion *Phys. Fluids* **26** 101308

[312] Aydin Y O, Rieser J M, Hubicki C M, Savoie W and Goldman D I (2019) Physics approaches to natural locomotion: Every robot is an experiment *Robotic Systems and Autonomous Platforms* (Elsevier) pp 109–27

[313] Dietrich F, Makeev A, Kevrekidis G, Evangelou N, Bertalan T, Reich S and Kevrekidis I G (2023) Learning effective stochastic differential equations from microscopic simulations: Linking stochastic numerics to deep learning *Chaos An Interdiscip. J. Nonlinear Sci.* **33** 023121

[314] Murphy K P (2012) *Machine learning: a probabilistic perspective* (MIT Press)

[315] Krotkov E Active perception for legged locomotion: every step is an experiment *IEEE International Symposium on Intelligent Control* (IEEE Comput. Soc. Press) pp 227–32

[316] Kabutz H and Jayaram K (2023) Design of CLARI: A Miniature Modular Origami Passive Shape-Morphing Robot *Adv. Intell. Syst.* **5** 2300181

[317] Chong B, He J, Li S, Erickson E, Diaz K, Wang T, Soto D and Goldman D I (2023)

Self-propulsion via slipping: Frictional swimming in multilegged locomotors *Proc. Natl. Acad. Sci.* **120** 1–11

[318] Blickhan R, Seyfarth A, Geyer H, Grimmer S, Wagner H and Günther M (2007) Intelligence by mechanics *Philos. Trans. R. Soc. A Math. Phys. Eng. Sci.* **365** 199–220

[319] Sitti M (2021) Physical intelligence as a new paradigm *Extrem. Mech. Lett.* **46** 101340

[320] Roderick W R T, Cutkosky M R and Lentink D (2021) Bird-inspired dynamic grasping and perching in arboreal environments *Sci. Robot.* **6** eabj7562

[321] Zhang H, Sun J and Zhao J (2019) Compliant Bistable Gripper for Aerial Perching and Grasping *International Conference on Robotics and Automation* vol 2019-May (IEEE) pp 1248–53

[322] Zhou Z, Wang Y, Hawkes E and Li C (2024) Rubble traversal experiments of a vine robot *Bulletin of the American Physical Society* p D38.00010

[323] Lashkari S G, Wilkinson M G, Krishnan B, Knierim J J and Cowan N J (2020) Decision-Making and Path Planning for Jumping Rats *Dynamic Walking*

[324] Lewinson R T and Stefanyshyn D J (2016) A descriptive analysis of the climbing mechanics of a mountain goat (Oreamnos americanus) *Zoology* **119** 541–6

[325] Hastie T, Tibshirani R and Friedman J H (2009) *The elements of statistical learning: data mining, inference, and prediction.* (Springer New York)

[326] Houska B, Ferreau H J and Diehl M (2011) ACADO toolkit—An open-source framework for automatic control and dynamic optimization *Optim. Control Appl. Methods* **32** 298–312

[327] Carducci J, Olds K, Krakauer J W, Xu J and Brown J D (2022) Novel Planar Strain Sensor Design for Capturing 3-Dimensional Fingertip Forces from Patients Affected by Hand Paralysis *Sensors* **22** 7441

Vita

Yaqing Wang was born in Beijing, China on October 17th, 1996. He received his B. Eng degree in Mechanical Engineering and B.B.A in Business & Administration from Tsinghua University, Beijing, China in 2019, and the M.S.E degree in Robotics from the Johns Hopkins University, Baltimore, MD, USA in 2023, where he is currently pursuing his Ph.D. degree in Mechanical Engineering. His research is focused on understanding principles of physical interaction of animals and robots with their environment during locomotion. He has published his research in *Journal of Experimental Biology*.